Detection of a giant molecule with a trapped ion cloud

Adrien Poindron

Aix*Marseille université
Socialement engagée

NNT/NL : 2022AIXM0087/010ED352

THÈSE DE DOCTORAT

Soutenue à Aix-Marseille Université
le 29 mars 2022 par

Adrien Gilles POINDRON

Detection of a giant molecule with a trapped ion cloud

Discipline
Physique et Sciences de la Matière

Spécialité
Optique, Photonique et Traitement d'image

École doctorale
Physique et Sciences de la Matière (ED 352)

Laboratoire
Physique des Interactions Ioniques et Moléculaires (PIIM)

Composition du jury

Rodolphe ANTOINE, DR CNRS Institut Lumière Matière, Villeurbanne	Examinateur
Laurence CHARLES, Pr. AMU Institut de Chimie Radicalaire, Marseille	Présidente
Laurent HILICO, Pr. Université d'Evry Laboratoire Kastler-Brossel, Paris	Rapporteur
Stefan WILLITSCH, Pr. Université de Bâle, Bâle, Suisse	Rapporteur
Martina KNOOP, DR CNRS PIIM, Marseille	Directrice de thèse
Jofre PEDREGOSA-GUTIERREZ, MCF AMU PIIM, Marseille	Co-Directeur de thèse

PIIM Physique des Interactions Ioniques et Moléculaires

cnrs dépasser les frontières

SATT SUD-EST ACCÉLÉRONS LE TRANSFERT DE TECHNOLOGIES

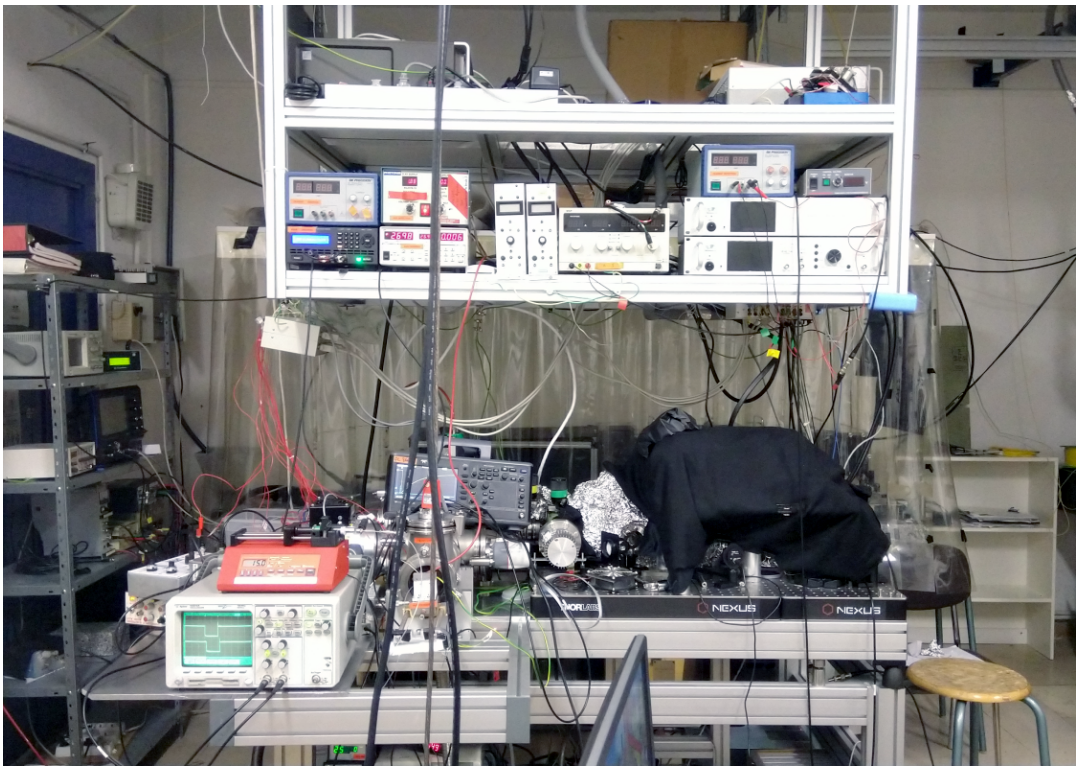

(A) The `GiantMol` laboratory.

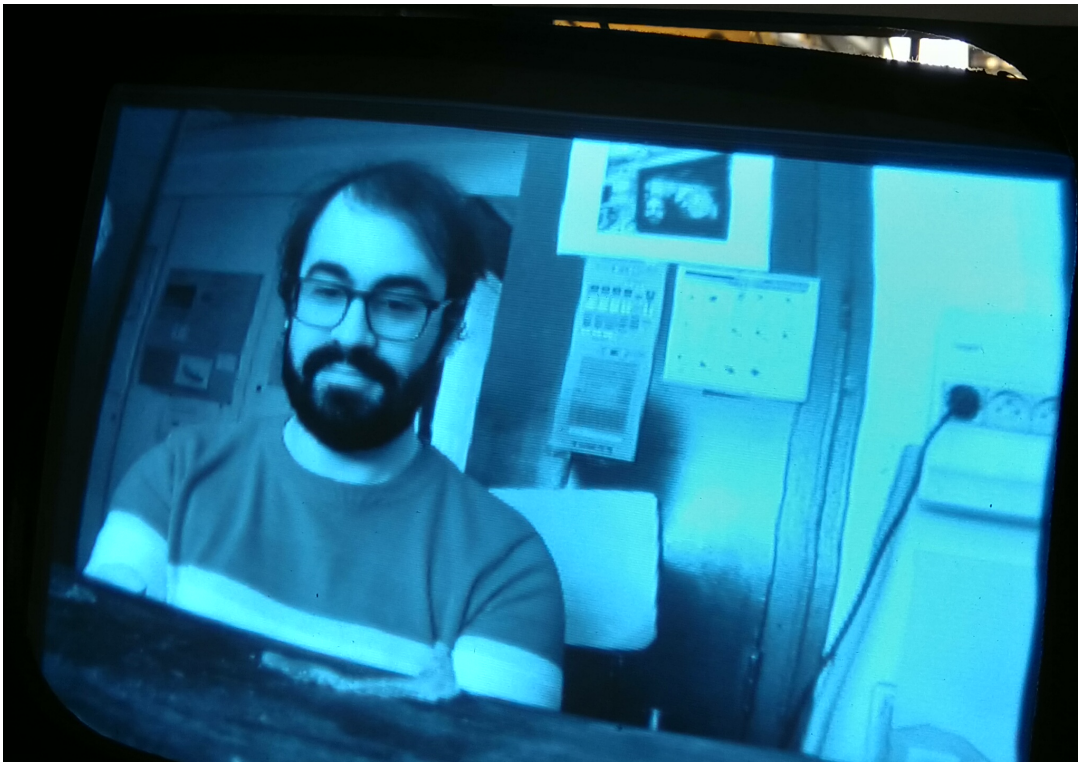

(B) Adrien Poindron.

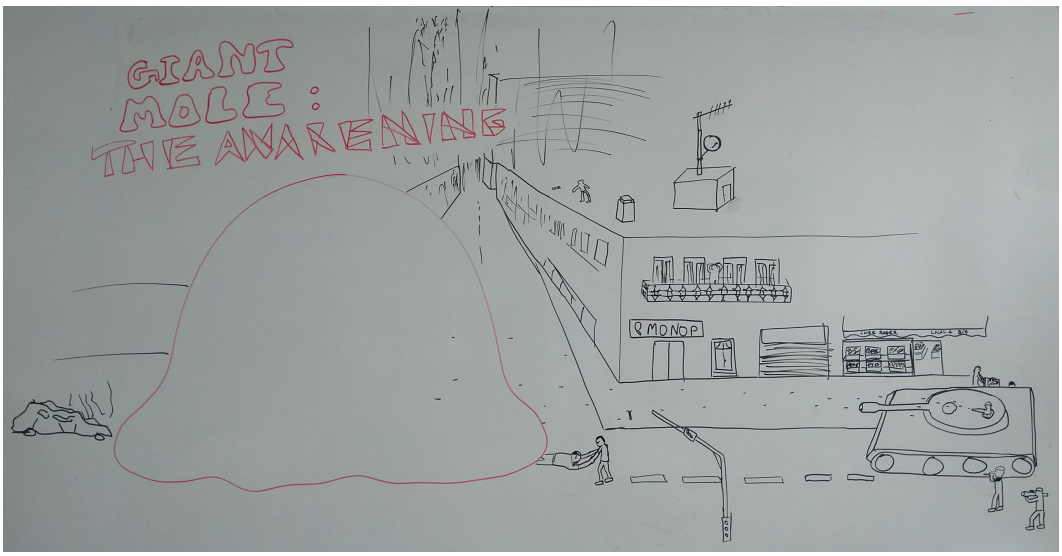

(c) `GiantMol`, the awakening. 10/10/2019.

Affidavit

Je soussigné, Adrien Poindron, déclare par la présente que le travail présenté dans ce manuscrit est mon propre travail, réalisé sous la direction scientifique de Martina Knoop et Jofre Pedregosa-Gutierrez, dans le respect des principes d'honnêteté, d'intégrité et de responsabilité inhérents à la mission de recherche. Les travaux de recherche et la rédaction de ce manuscrit ont été réalisés dans le respect à la fois de la charte nationale de déontologie des métiers de la recherche et de la charte d'Aix-Marseille Université relative à la lutte contre le plagiat.

Ce travail n'a pas été précédemment soumis en France ou à l'étranger dans une version identique ou similaire à un organisme examinateur.

Fait à Marseille le 29/12/21

I, undersigned, Adrien Poindron, hereby declare that the work presented in this manuscript is my own work, carried out under the scientific direction of Martina Knoop et Jofre Pedregosa-Gutierrez, in accordance with the principles of honesty, integrity and responsibility inherent to the research mission. The research work and the writing of this manuscript have been carried out in compliance with both the french national charter for Research Integrity and the Aix-Marseille University charter on the fight against plagiarism.

This work has not been submitted previously either in this country or in another country in the same or in a similar version to any other examination body.

Marseille 29/12/21

List of publications and participation to conferences

Articles in journals with peer review

1. 2021 : A. Poindron et al. “Non-destructive detection of large molecules without mass limitation”. *The Journal of Chemical Physics* 154.18 2021, p. 184203. DOI: 10.1063/5.0046693

Conferences, posters and presentations

1. 2019, poster : "Giant molecule detection with a laser-cooled ion cloud", Congrès de la Société Française de Physique (SFP), Nantes, 08-12 July 2019.
2. 2020, talk : "Non-destructive detection of molecules without mass limitation", Early Career Conference in Trapped Ions (ECCTI), CERN, 13-17 January 2020.
3. 2021, talk : "Détection d’ions moléculaires par un nuage d’ions piégés"[1], Société française d’optique (SFO), Dijon, 05-09 July 2021.

Cultural and transdisciplinary activities, scientific mediation

1. 2018-2019 : animation of physics stands for the general public on the themes of optics and states of matter (manipulations with liquid nitrogen), Carpentras and Caromb (Vaucluse, France).

Responsibilities

1. 2016-2018 : elected to the board of the physics department of Aix-Marseille University.
2. 2019-2021 : elected to the board of the Physics and Material Sciences doctoral school (ED 352) at Aix-Marseille University.

[1] Detection of a molecular ion by a trapped ion cloud.

Avant-propos

J'ai rejoint le laboratoire PIIM en tant que stagiaire durant mon année de M2 en 2018 et j'ai eu l'immense chance d'obtenir par la suite un financement pour y faire ma thèse. En 2022 je termine enfin ce long travail de recherche durant lequel j'ai cotoyé un environnement riche et stimulant. Je ne compte pas le nombre de choses que j'ai apprises, tant à propos de mon sujet de recherche, qu'à propos de la physique en général, la science, les scientifiques, et moi-même. Cette expérience vécue de l'intérieure montre à quel point la recherche est une activité vivante qui n'a de portée concrète qu'actualisée, non pas pour elle-même dans une démarche de préservation, mais bel et bien dans un esprit créateur. Cette créativité implique tant des innovations sur l'objet que sur le sujet. Bien entendu tout ceci s'applique à bon nombre d'activités humaines, mais à ceux qui se demanderaient à quoi cela peut-il bien servir de se poser de nouvelles questions, je dirais que les questions sont une dimension essentielle des activités *humaines*, et que se questionner, user de son esprit librement, est intrinsèquement humaniste.

Les paradoxes étant inévitables, je ne fais à présent pas le choix de les contourner. Ce document contient, outre cet avant-propos, un résumé en français de ma thèse, puis la thèse en elle-même écrite en anglais. Cette dernière est composée d'une introduction, trois parties, puis une conclusion. Quatre annexes se trouvent ensuite après le corps du texte. Puis la bibliographie arrive à la suite. En fin de document je vous invite à consulter un index qui vous permettra de naviguer dans ce même document à partir de mots clés.

Puisque j'ai l'occasion de m'adresser au lecteur durant ces quelques paragraphes, je me permets à présent d'introduire deux idées. Tout d'abord j'aimerais citer Alfred Korzybski, connu pour son aphorisme «La carte n'est pas le territoire qu'elle représente»et qui pour moi permet de prendre un recul critique important devant toute situation. Ici j'insiste sur ce point car ce document *reflète* certaines dimensions du travail que j'ai accompli durant ma thèse, il se veut synthétique et reproductible, mais à l'image de la carte et du territoire, la thèse n'est pas le travail de doctorat ! Aussi si je devais donner quelques conseils aux futurs et actuels doctorants je dirais ceci. La science est une chose extrememement complexe, abstraite, qui avance grâce au travail de recherche qui, lui, est concret, humain, quotidien. C'est la base de votre travail et il est essentiel d'obtenir de la matière avant de l'interpréter. Alors au début les choses sont confuses et semblent chaotiques, anarchiques, et c'est normal. Soyez patients, ayez confiance en votre méthode, laissez vous traverser par les doutes et la peur. N'hésitez pas à communiquer, interagir avec des gens extérieurs. Mais gardez à l'esprit qu'il reviendra à vous de mettre de l'ordre dans tout ça. Puis ne vous comparez pas aux autres : chaque thèse est unique, et ne vous comparez surtout pas aux «anciens»qui ont dix, vingt, trente … ans d'expérience, une culture et des

habitudes différentes des votres. Personne ne vous dira jamais qu'est ce que c'est que faire une thèse, ce qui est attendu, car c'est extremement compliqué et je crois bien que c'est l'objet de la chose : découvrir la recherche telle qu'elle se fait, avec son rythme varié, tantôt dilaté tantôt contracté. Tout ceci ne doit pas être un prétexte à l'exploitation des doctorants qui de par leur naïveté sont plus susceptibles de l'accepter. Chaque doctorant est celui qui maîtrise le mieux son sujet, quoi qu'en pensent les autres. Choisissez bien votre environnement et soyez sûrs de vous.

Je suis infiniment reconnaissant aux gens qui m'ont permis d'accomplir ce travail et de vivre cette aventure humaine qu'est le doctorat. Je voudrais commencer par remercier Martina et Jofre qui m'ont accordé leur entière confiance et ont toujours montré de la patience et de la bienveillance lors de nos très nombreuses interactions. Je veux aussi remercier l'ensemble des personnes que j'ai cotoyé durant mon doctorat et avec lesquels ça a toujours été un plaisir de travailler. Je vous remercie tous pour votre bonne humeur, votre aide et le partage de vos connaissances. Je pense à tous ceux qui partagent le même couloir, Aurika, Caroline, Didier, Gaëtan, Guillaume, Marie, Michel et Fernande, mais aussi les autres chercheurs, Jennifer, Alejandro, Eric, Alexandre, Olivier. Je veux en particulier remercier Caroline qui a consacré un temps significatif à mes travaux de recherche et sans qui ce travail n'aurait pas été le même, et encore Claude et Christophe qui ont aussi contribué à faire avancer l'expérience `GiantMol` sur laquelelle j'ai passé tant de temps. Je n'oublie pas non plus les nombreux chercheurs qui sont passés dans cette équipe, notamment les doctorants me précédants et avec qui j'ai pu beaucoup échanger : Mathieu, Cyril et Marylise. Il y a aussi les chercheurs confirmés, Marius, Rémy et Grégoire, dont j'ai pu bénéficier de la connaissance et de la bonne humeur. Je suis aussi très reconnaissant aux membres du jury d'avoir bien voulu évaluer mon travail et le reconnaître comme digne d'un doctorat. Je veux aussi remercier Walter Wissdorf, chercheur de l'université de Wuppertal, avec qui j'ai pu échanger durant ma rédaction de thèse et qui m'a aidé à comprendre le fonctionnement de la source électrospray et les enjeux concernant l'écoulement du flux dans mon prototype.

Un doctorat ne se prépare pas dans une bulle coupée du monde, et je voudrais remercier tous ceux qui m'ont accompagné pendant ces longues années d'étude. Il convient tout d'abord de remercier tous mes colocataires, ceux avec qui j'ai commencé l'aventure du doctorat, et tous les autres qui ont suivi, tous ayant décliné, l'un après l'autre, patiemment, la proposition pourtant alléchante de se voir offrir les frais d'inscription au doctorat de leur choix. Ce n'est pas faute de s'y être pris à deux. Durant le confinement j'ai eu la chance de cohabiter *pacifiquement* avec Patryk[2], personne de grande qualité. Dans la même veine il convient aussi de remercier le LAMA, petit groupe constitué de personnes de bon aloi et dont l'acronyme rend spirituellement hommage à Lise, Astrid et MArtin[3], aussi doctorants et personnes tout à fait admirables. En particulier je veux remercier Astrid qui fait preuve de beaucoup de patience avec moi malgré mon caractère facétieux. Il me faut

[2] A prononcer Patrèk en roulant le r.

[3] En fait pour être exact je dois dire que le dernier A, c'est moi, mais je ne vais quand même pas me péter les bretelles aussi ouvertement.

aussi remercier ma mère qui a toujours été là et sans qui rien de tout cela ne serait possible. Tout comme mon frère, qui est une source d'inspiration insoupçonnée. Que serait aussi cette période de ma vie sans les amis de l'internet ? Il me paraît indispensable de reconnaître volontiers que si les galéjades sont mon passe temps favori c'est toujours mieux en compagnie de gens qui peuvent en comprendre les *subtilités*. Je pense notamment à Brice, Christophe, Mohammed, tous les acharnés du clic. Loin de moi l'idée que ce qui vient toujours plus tard doive être considéré dans l'ombre de ce qui précède, avec moins de considération que ce dont j'ai déjà évoqué la substance précédemment. Au rang des éléments qui ont fait indéniablement mon quotidien durant cette aventure collective, ce trek de l'esprit, il y a l'appel indiscible de la création pour elle-même, dans le mystère de la nuit ; dans l'angle mort de la liberté, reigne un espace où même l'esprit le plus aguerri ne peut jamais saisir le tissu même de la réalité, un lieu où les règles sont à (re)découvrir au fur et à mesure que l'on avance. Là, tous sont égaux devant le néant pour une ultime confrontation avec ce qu'ils découvriront bien après n'être qu'eux-même. Tous ? Non. S'il est admis que c'est un fardeau que l'esprit humain soit capable de se poser des questions auxquelles il ne peut apporter de réponses, c'est négliger que la réponse peut venir ailleurs que de l'esprit, du moins le notre, si ce n'est d'autre part tout simplement. L'enthousiaste bande radiophonique qui a concrétisé plus de 100 émissions libres[4], soit le double en heures, me voit bien humblement lui addresser mes reverences les plus respectueuses. Malgré les conditions hasardeuses que nous avons traversé, rien ne nous aura empêché de continuer. J'adresse mes plus chaleureux remerciements à Thibault qui n'a de cesse de m'inspirer au quotidien et dont la créativité est un prodigieux puits sans fond dont la destination, que lui seul en perce le secret, émane jusque chez nous à la manière d'un pétrichor transformant la moindre fraction de réalité en une indiscible évidence. Ja m'arrête là pour les métaphores, et finalement je souhaite remercier tout le monde une dernière fois, et dédier ces dernières lignes à la mémoire des oubliés, de tout ce dont le secret gît au sein des choses.

Maintenant, c'est à vous de travailler : je vous propose de trouver la petite plaisanterie[5] que j'ai glissé dans ce manuscrit. Cherchez bien car il y en a bien une !

[4] Radio La Fin Du Monde, sur Radio Galère, 88.4 FM.
[5] Sans incidence.

Contents

DÉTECTION D'UNE MOLECULE GÉANTE AVEC UN NUAGE D'IONS PIÉGÉS : RÉSUMÉ DÉTAILLÉ EN FRANÇAIS

Fr.1 Introduction

Les nouveautés abordées dans cette thèse concernent l'utilisation d'un nuage d'ions piégés refroidis par laser comme détecteur de macromolécules chargées. Le travail présenté dans ce manuscrit s'inscrit clairement dans une thématique interdisciplinaire. Le cadre théorique sur lequel s'appuie ce travail est principalement issu des deux domaines suivants.

Tout d'abord, la **spectrométrie de masse** qui sert de toile de fond générale dans laquelle la problématique est inscrite. Il s'agit du domaine dédié à l'identification et la détection des molécules.

Deuxièmement, le **piégeage** et le **refroidissement par laser** d'un **nuage d'ions**, pour lequel nous introduisons dans ce travail une nouvelle finalité en tant que détecteur non destructif d'ions moléculaires.

Le principe de l'expérience, appelée par la suite `GiantMol`, est illustré par la figure Fr.1. La présence d'un **ion moléculaire** géant est déterminée par **l'interaction** avec un **ensemble d'ions** piégés et refroidis par laser. La **fluorescence** de cet ensemble, induite par le refroidissement laser, peut être suivie, et on s'attend à ce que dans certaines conditions le passage de l'ion moléculaire déclenche une **modification détectable de la fluorescence** du nuage d'ions, ce qui constitue le signal de détection.

Alors que nos simulations numériques (partie III) fournissent déjà une preuve de concept pour ce principe, l'expérience `GiantMol` est toujours en cours de développement. Ailleurs, des montages expérimentaux sont déjà exploités afin de suivre la collision d'une molécule avec un ensemble d'ions Ca^+ piégés, avec un contrôle précis de l'énergie de collision [Wil08]. En dehors de la spectrométrie de masse, la bibliographie illustre également comment la plateforme que nous proposons peut être l'occasion de réaliser plusieurs autres mesures liées à l'interaction entre l'espèce piégée et la molécule dans le contexte de la chimie ou de la physique en général [Wil12; Ber06; Cap12]. Du point de vue numérique, `GiantMol` peut également être l'occasion de développements indépendants du contexte de la spectrométrie de masse (partie III), et de nombreux autres travaux montrent que des

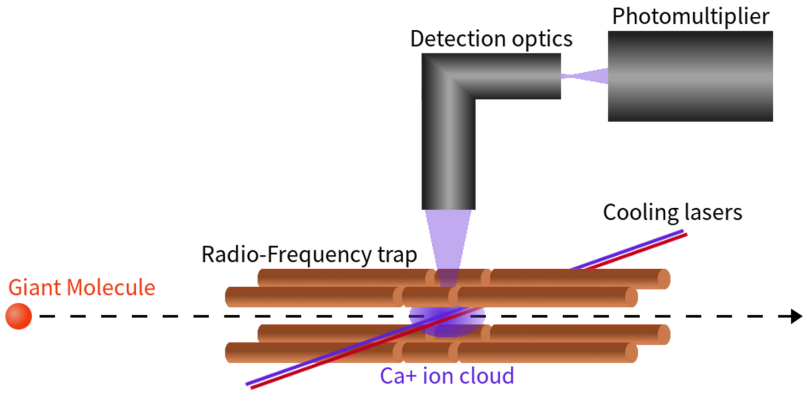

Figure Fr.1: Principe de `GiantMol` : injection d'un analyte dans un nuage d'ions piégés et refroidis par laser et mesure de la fluorescence.

montages similaires présentent un intérêt dans d'autres contextes tels que les plasmas et le pouvoir d'arrêt [Bus06], le chauffage dans les pièges [Ryj05; Nam14] ou la manipulation de l'antimatière [Hil14].

Le projet de `GiantMol` provient de la confrontation de plusieurs champs relevant de la physique, de la physico-chimie et de la chimie. L'idée était de mobiliser des techniques, méthodes et points de vue de ces différentes disciplines avec pour objectif de répondre à une problématique. La question de la détection d'une molécule est ressortie de cette confrontation des disciplines et les idées initiales ont donné naissance à un brevet [Cha14]. La recherche d'intérêt auprès d'industriels et chercheurs a suivi, notamment auprès des membres des communautés de spectrométrie et des pharmacologistes. La SATT sud-est a financé le développement d'un prototype.

Premièrement, le développement d'un tel détecteur est crucial afin de combler une lacune parmi les possibilités offertes par les méthodes analytiques classiques. Deuxièmement, la configuration que nous proposons fournit une plateforme pour l'étude de l'interaction entre une particule chargée et un nuage d'ions bien contrôlé.

Ce manuscrit de thèse est organisé de la manière suivante. L'introduction résume le contexte de la chimie analytique, ses principes, ses méthodes et ses performances démontrées. Puis la partie I (LASER COOLING OF TRAPPED IONS) est consacrée à la présentation des considérations expérimentales sur les ions piégés et leur refroidissement par laser. Les développements analytiques fondamentaux sont présentés ainsi que les résultats expérimentaux. Cette partie est essentielle pour comprendre les mécanismes physiques du principe de détection. Ensuite, la partie II (THE MOLECULAR SOURCE) est consacrée à la présentation des considérations expérimentales sur la source moléculaire et le guidage des ions moléculaires chargés. Dans cette partie II, le prototype de guidage en cours de développement est décrit et testé. Cette partie résume les récents développements fondamentaux relatifs à ces dispositifs et démontre comment une particule peut être guidée pour interagir avec une cible spécifique. Ensuite, la partie III (DETECTOR BEHAVIOUR AND PROOF-OF-CONCEPT BY MOLECULAR DYNAMICS SIMULATIONS) est consacrée aux simulations numériques qui ont accompagné le développement du prototype. En particulier, les simulations numériques sont utilisées pour étudier les conditions spécifiques pour lesquelles le détecteur fournit un signal de détection observable. Des simulations numériques sont également utilisées pour étudier la physique de l'interaction d'un projectile chargé avec un ensemble d'ions piégés refroidis par laser. Chaque partie est ensuite présentée de manière similaire dans leurs introductions respectives.

Ce manuscrit de thèse propose un aperçu général d'un principe faisant appel à plusieurs disciplines. Il s'agit également de la description d'un prototype en cours de développement. Il présente des choix qui ont déjà été faits lorsque j'ai rejoint le groupe, ainsi que des développements introduits pendant ma présence, que ces développements soient analytiques ou expérimentaux. Ce travail contient un travail de recherche bibliographique afin de consolider la maîtrise des différents éléments impliqués et de proposer par la suite des améliorations au prototype. Des expériences permettant de tester et de caractériser le prototype dans son état actuel de développement sont fournies, néanmoins d'autres

idées restent encore des propositions.

Fr.1.1 Spectrométrie de masse et ses limitations actuelles

Le détecteur que nous développons avec `GiantMol` est pensé pour être utilisé dans le cadre de la **spectrométrie de masse**, dans laquelle un échantillon est vaporisé et ionisé puis accéléré et enfin détecté par un processus physique. La spectrométrie de masse est reconnue pour sa grande sensibilité, sa rapidité et sa polyvalence, ainsi que pour ses capacités d'automatisation et la large gamme de molécules qu'elle peut accepter, la rendant compatible avec de nombreux contextes comme la chimie et la biologie [Kon19; Tit00], l'environnement [DEl89; Arm08], la médecine [Dru13; Mik14] ou la sécurité alimentaire [Dan16], ce qui explique qu'elle est très répandue [Gli03].

Dans ce contexte, la détection des molécules géantes ($M > 10^6$ Da) se fait avec des techniques limitées tant en masse qu'en charge [Kei17] (Fig. Fr.2), et dont le nombre est d'autant plus faible que la masse de la macromolécule est importante. Actuellement, il n'existe pas de technique de détection non-destructive d'une molécule individuelle et chargée une seule fois. Le détecteur `GiantMol`, basé sur un nuage d'ions piégés et refroidis par laser (partie I), propose de s'affranchir de ces limitations. Il possède une plage de fonctionnement en masse débutant à partir d'un seuil aussi bas que possible – idéalement 10^6 Da – et sans limite supérieure théorique, ainsi que la capacité de détecter des molécules ayant le plus faible nombre de charges possible, et de façon non destructive.

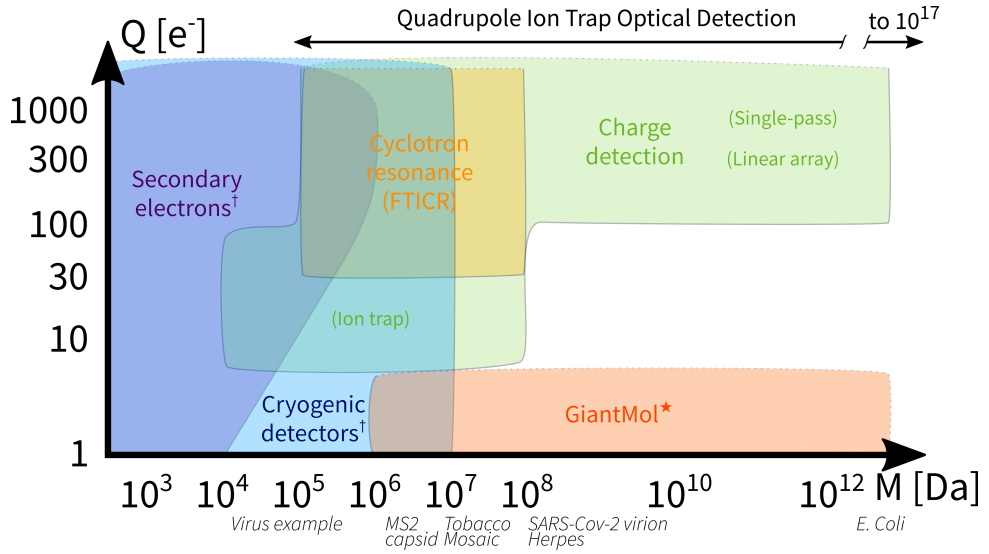

FIGURE Fr.2: Performances comparatives des techniques de spectrométrie de masse monomoléculaire en fonction de la masse et de la charge de l'ion moléculaire, d'après la revue de Keifer and Jarrold [Kei17]. Les zones colorées indiquent les plages de travail démontrées expérimentalement pour chaque méthode testée. Lorsqu'elle est délimitée par des lignes en pointillés, cela signifie que la plage continue au-delà. La détection optique en piège quadripolaire (QIT) ne dépend pas de la charge, sa portée est donc indiquée par la flèche au-dessus. L'étoile * indique qu'il s'agit d'une performance de détection *attendue* pour `GiantMol` indiquée en orange. La dague † indique que la méthode de détection est destructive. Les exemples de virus en italique sont positionnés de manière à ce que la première lettre soit alignée avec la valeur de masse correcte.

Fr.2 Refroidissement laser d'ions piégés

Fr.2.1 Piégeage des ions Ca^+

Description

Les ions Ca^+ sont confinés dans un piège linéaire quadrupolaire constitué de quatre barreaux parallèles, segmentés en trois parties longitudinalement (Fig. Fr.3). Afin de confiner radialement les ions, une tension radio-fréquence (U_{RF}, à la fréquence $\Omega/2\pi$ = 2.05 MHz) est appliquée aux paires de barreaux diagonales, en opposition de phase. Afin de confiner axialement, une tension statique (U_{DC}) est appliquée différentiellement entre les segments extérieurs et intérieurs du piège.

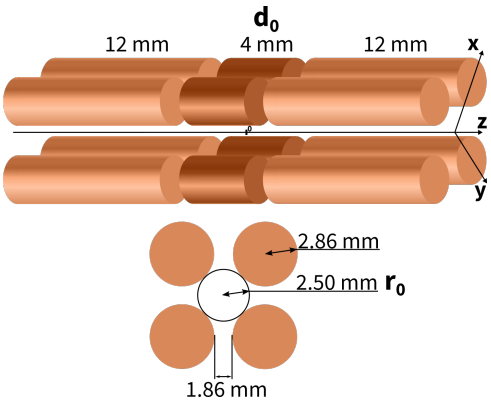

(A) Dimensions du piège. Chacun des quatre barreaux est segmenté en trois parties. Les ions sont confinés dans la partie centrale.

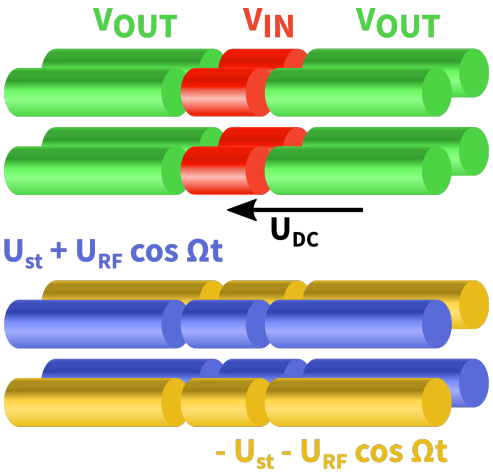

(B) Schéma d'alimentation électrique. Deux ensembles de tensions sont appliqués aux barreaux. Haut : une tension continue est appliquée entre les segments extérieurs (vert) et le segment intérieur (rouge). Bas : une tension radio-fréquence est appliquée aux paires diagonales de barreaux (bleu et jaune), en opposition de phase.

FIGURE Fr.3: Piège quadrupolaire linéaire et son alimentation électrique.

Le potentiel généré par ces tensions est indiqué par les équations 1. La stabilité d'un ion Ca^+ dans ce potentiel est régie par les tensions appliquées [Kno16]. Les paramètres de stabilités ainsi que la plage dans laquelle ils permettent de confiner sont indiqués section 1.2 (Fig. 1.4). Les mesures permettant de caractériser le piège, le mouvement des ions ainsi que leur forme sont présentés chapitre 2.

$$\Phi(x,y,z,t) = \Phi_{Rad}(x,y,t) + \Phi_{DC}(x,y,z) \tag{1a}$$

$$\Phi(x,y,z,t) = \frac{U_{st} + U_{RF}\cos\Omega t}{2r_0^2}(x^2 - y^2) + \frac{\kappa V_{DC}}{2d_0^2}(2z^2 - x^2 - y^2). \tag{1b}$$

Comportement à plusieurs ions et chauffage radio-fréquence

Le mouvement des ions dans le piège lorsqu'ils sont piégés à plusieurs est régi par les équations de Mathieu (Eq. 2) (voir McLachlan [McL47] and Knoop [Kno16]), dans lesquelles le terme de droite représente l'interaction coulombienne entre les ions, tandis que la partie gauche représente les forces confinantes appliquées.

$$\begin{cases} \dfrac{d^2}{dt^2} x_i + (\widetilde{a} - 2q\cos 2\tau)\, x_i = \dfrac{q_e^2}{4\pi\varepsilon_0 m} \displaystyle\sum_{j=1}^{N} \left(\dfrac{x_i - x_j}{\mathbf{r_{ij}^3}} \right) & \text{(2a)} \\ \dfrac{d^2}{dt^2} y_i + (\widetilde{a} - 2q\cos 2\tau)\, y_i = \dfrac{q_e^2}{4\pi\varepsilon_0 m} \displaystyle\sum_{j=1}^{N} \left(\dfrac{y_i - y_j}{\mathbf{r_{ij}^3}} \right) & \text{(2b)} \\ \dfrac{d^2}{dt^2} z_i + \omega_z^2\, z = \dfrac{q_e^2}{4\pi\varepsilon_0 m} \displaystyle\sum_{j=1}^{N} \left(\dfrac{z_i - z_j}{\mathbf{r_{ij}^3}} \right) & \text{(2c)} \end{cases}$$

Cette interaction coulombienne introduit un couplage entre les directions x, y et z du mouvement, et permet le passage de l'énergie issue du champ radio-fréquence vers le mouvement brownien des ions. Cet effet est communément appelé chauffage radio-fréquence [Nam14], il est détaillé dans le chapitre 3, sous-section 3.3. Le chauffage radio-fréquence se manifeste par un taux de chauffage ($H = \mathrm{d}T/\mathrm{d}t$) dépendant de l'amplitude du champ radio-fréquence ainsi que de la température du nuage. L'amplitude du champ-radio fréquence augmente elle-même avec l'éloignement au centre du piège, ce qui peut être utilisé à notre avantage, en augmentant l'extension radiale du nuage afin qu'il voit un champ radio-fréquence plus important et soit donc plus susceptible au chauffage radio-fréquence. Lorsque le nuage est en phase cristalline, suffisamment froid, ce chauffage devient faible et peut être combattu avec une source de refroidissement tel que le refroidissement laser. Néanmoins, si la température du nuage augmente, le chauffage peut devenir prépondérant. Un juste équilibre entre chauffage radio-fréquence et refroidissement laser peut être défini, afin que l'état cristallin soit un état d'équilibre durable, mais de telle sorte que le nuage soit suffisamment susceptible pour être grandement perturbé par l'introduction d'une perturbation telle qu'un ion moléculaire le traversant. Grace au chauffage radio-fréquence, la petite quantité d'énergie introduite par l'ion moléculaire vient déstabiliser le nuage au delà de ce dont aurait été capable la molécule seule : le chauffage radio-fréquence agit comme un amplificateur de la perturbation initiale.

Fr.2.2 Refroidissement laser

Probabilité d'excitation et fluorescence des ions

Le refroidissement laser repose sur le ralentissement des ions grâce au recul généré par l'absorption des photons par les ions (chapitre 4). L'efficacité du refroidissement laser dépend de la probabilité d'excitation d'un ion (ρ_{ee}) définie comme [And15; Nie10]

$$\rho_{ee} = \frac{1}{2}\frac{\Omega_R^2}{\Omega_R^2 + 2\Delta_\star^2 + \Gamma_t^2/2} = \frac{A/2}{A + B + \Delta_\star^2}. \tag{3}$$

La fluorescence des ions (F) soumis au refroidissement laser et manifestant une distribution de vitesse de Maxwell-Boltzmann ($MB_T(v)$) s'exprime comme

$$F = N\Gamma \int \rho_{ee}(v) \times MB_T(v)\, \mathrm{d}v. \tag{4}$$

Cette expression, représentée en bleu sur la figure Fr.5 permet de constater que la fluorescence dépend de la température, et cela au travers des deux termes inclus dans l'intégrale. La hausse de la température au delà d'un certain seuil permet donc de modifier la fluorescence au delà du seuil observable.

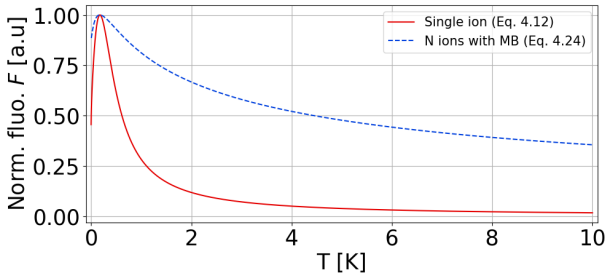

FIGURE FR.5: Signal de fluorescence calculé d'après les équations 4.14 et 4.21 pour, respectivement, un ion seul, et une collection de 1024 ions avec une distribution de vitesse de Maxwell-Boltzmann. Dans e cas d'un ion, la température est dite équivalente, calculée à partir de la vitesse selon la formule $T = mv^2/k_B$.

Fr.3 La source moléculaire

Fr.3.1 Description de la source électrospray et du guidage des ions moléculaires

L'ensemble de la source moléculaire , représenté schématiquement dans la figure Fr.5 est constitué, d'une source électrospray [Fen89] (Fig. 5.1) permettant l'ionisation et la mise en phase gazeuse des molécules à analyser, d'un ensemble capillaire/skimmer [Cam84; Wiß16] (Fig. 5.4) permettant de filtrer le solvant et de procéder à un pompage différentiel jusqu'à 10^{-6} mbar, d'un octupole permettant de guider les ions vers deux électrodes commandées (C8 et C9, Fig. 5.6) permettant de générer des paquets d'ions synchronisés. Deux MCP (Fig. 7.1) sont placés afin de procéder à des mesures de contrôles, tandis que le piège à ions, utilisé comme un détecteur de molécules est placé dans une enceinte à 10^{-9} mbar (GICD).

Fr.3.2 Mesure d'ions légers

La présence des MCP permet de tester la source moléculaire pour des petits ions. De la pyridine (79 Da) et du tryptophane (204 Da) ont pu être observés sur le plus proche des MCP, tandis que de la pyridine a pu être guidée dans le MCP au delà du piège, permettant

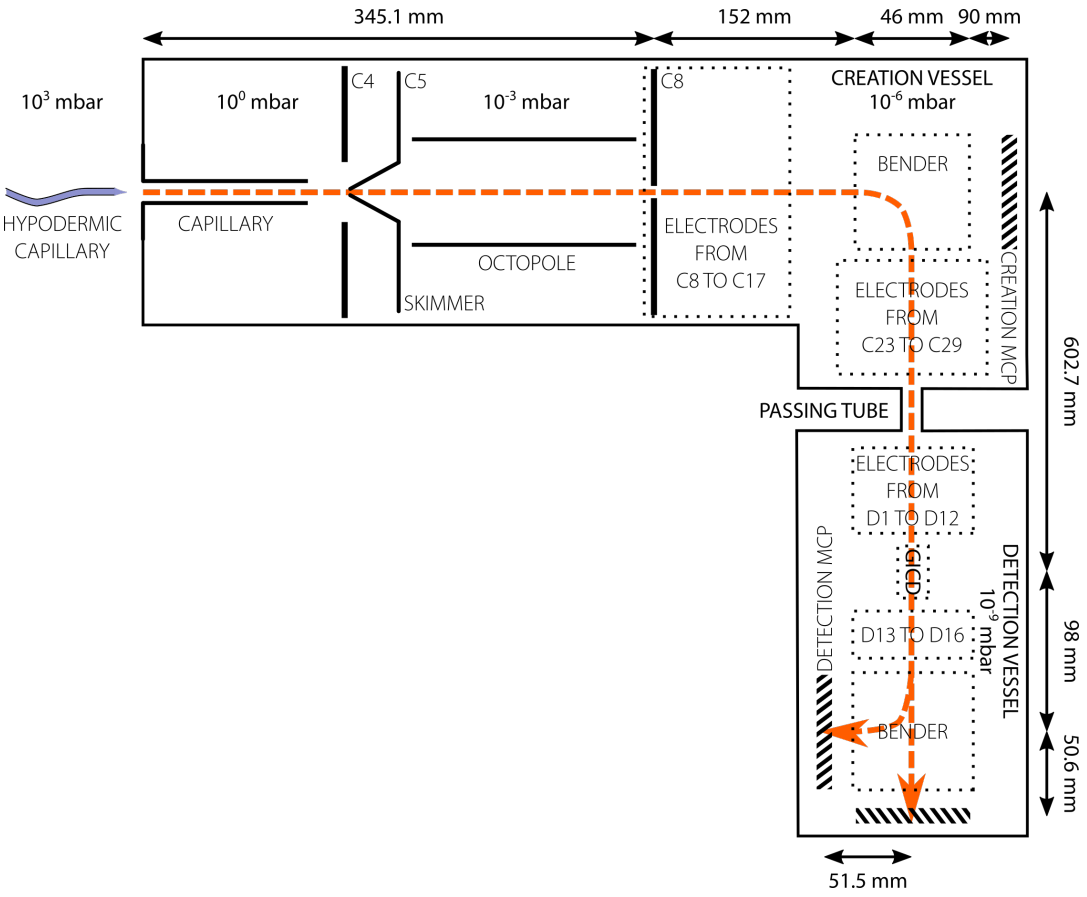

FIGURE FR.5: Schéma des électrodes de guidage des ions moléculaires depuis l'electrospray vers le GICD et les MCP. Les distances se rapportent aux dimensions du plan.

ainsi de guider un ion moléculaire à travers le piège à ions. Plusieurs difficultés ont été constatés lors de l'utilisation de la source moléculaire. Il n'a pas été possible d'observer des molécules plus lourdes que la pyridine au delà du piège. Des problèmes de stabilité de la source rendent son comportement trop imprévisible pour être utilisée fiablement pour le moment. L'analyse bibliographique menée durant cette thèse a permis d'identifier plusieurs points critiques à réviser, notamment auprès de la source électrospray et des premiers éléments, parmi lesquels le système capillaire/skimmer.

Fr.4 Comportement du détecteur et preuve de concept par des simulations de dynamique moléculaire

Fr.4.1 Description des simulations

Les simulations numériques permettent de modéliser le comportement des ions piégés et refroidis par laser en utilisant la méthode de dynamique moléculaire dans laquelle les équations du mouvement sont intégrées après avoir pris en compte les forces exercées par les différents éléments [Poi21]. Les simulations sont utilisés afin d'étudier le comportement de l'ensemble d'ions lorsqu'une molécule géante chargée (Q = 1 charge, M = 10^6 Da)

le traverse (section 9.1). Elles sont aussi utilisées afin de modéliser la dynamique des ions lorsqu'ils sont soumis au champ radio-fréquence uniquement, ce qui permet d'étudier l'effet du chauffage radio-fréquence (section 9.4).

Fr.4.2 Principaux résultats

Interaction entre l'ion moléculaire et le nuage d'ions – effet de détection

Nous montrons que l'effet de détection repose sur deux mécanismes, un premier échange d'énergie entre l'ion moléculaire et le nuage d'ion par l'intermédiaire de l'interaction coulombienne, et un second apport d'énergie à l'ensemble d'ion par l'intermédiaire du chauffage radio-fréquence devenu prépondérant suite au premier apport d'énergie.

Des simulations numériques d'interaction (dynamique moléculaire) entre la molécule géante et un nuage de 1024 ions ont été conduites pour une grande variété de conditions de confinement exposées dans la figure Fr.6. 100 simulations ont été réalisées pour chaque condition et le taux de détection (%D) est déterminé en fonction du nombre de simulations qui ont donné lieu à une différence de fluorescence observable (#D) par rapport au nombre total de simulations (100). Le taux de détection en fonction des conditions de confinement est présenté dans la figure Fr.6. La plupart des cas permettant un bon taux de réussite du détecteur ont une amplitude radio-fréquence la plus élevée (U_{RF} = 70 V, q_x = 0.65), ce qui s'explique par la présence d'un fort chauffage radio-fréquence déstabilisant le nuage une fois la molécule ayant traversé et transféré une partie de son énergie au nuage d'ions. Dans les cas où la tension de confinement axiale est faible ($U_{DC} \leq 2$) les conditions permettant le fonctionnement du détecteur sont plus souples puisqu'il fonctionne dès que l'amplitude de la radio-fréquence est supérieure ou égale à 59 V. Ceci s'explique par le rallongement du nuage lorsque la tension axiale diminue, favorisant l'interaction et l'échange d'énergie entre le nuage et l'ion moléculaire. Ainsi, plus d'énergie peut être transférée au nuage, ce qui permet au détecteur de fonctionner malgré un chauffage radio-fréquence plus faible.

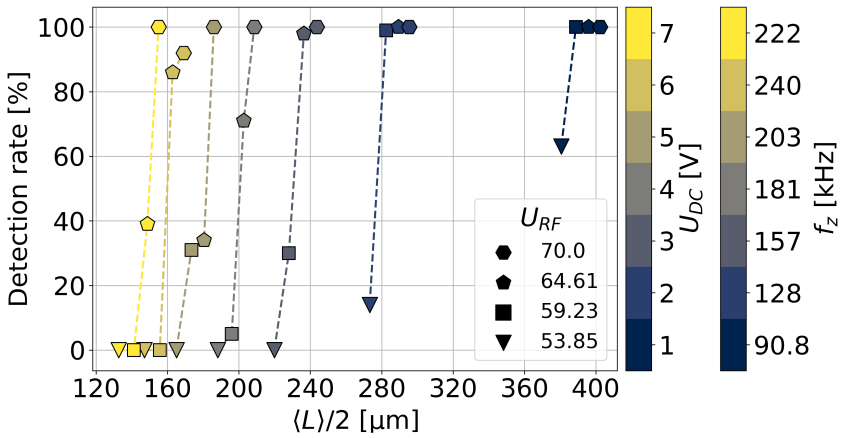

FIGURE Fr.6: Taux de détection en fonction de la demi-longueur du nuage $\langle L/2 \rangle$ et des paramètres de confinement. La forme du marqueur indique la tension radio-fréquence U_{RF}, et le code couleur indique la tension de confinement axial U_{DC}, ou les fréquences séculaires axiales équivalentes f_z. Les lignes en tirets relient les points partageant les mêmes U_{DC}.

Etude du chauffage radio-fréquence

Pour un nuage de 1024 ions, la simulation d'un nuage dans le champ de confinement a été faite pour différentes amplitudes radio-fréquence et une tension de confinement axiale U_{DC} = 7 V. Ni refroidissement laser ni injection d'un ion moléculaire n'a lieu dans ces simulations. La température du nuage d'ions est suivie au fil du temps et est caractérisée par une évolution en trois temps (Fig. 9.14). Dans un premier temps la température reste inférieure à 40 mK et évolue avec un taux de chauffage moyen de 10 K/s. Puis au bout d'un temps t_0 appelé temps critique, la température évolue brusquement ce qui est caractérisé par un taux de chauffage explosant de plusieurs ordres de grandeur : la température atteint 10 K avec un taux de 10^5 K/s. Enfin le taux de chauffage se stabilise autour de $1.5 \cdot 10^5$ K/s. L'évolution de ce temps critique en fonction de l'amplitude de la radio-fréquence U_{RF} montre une évolution en inverse de la racine de U_{RF}. La température au temps critique est présentée figure Fr.7. Cette température décroît linéairement lorsque U_{RF} augmente. Cette température est comparable à la température nécessaire à atteindre pour que le chauffage radio-fréquence domine l'évolution du nuage et créé un emballement. C'est une donnée importante afin de comprendre quel apport initial d'énergie est requis afin que l'interaction de l'ion moléculaire avec le nuage permette à la détection d'avoir lieu.

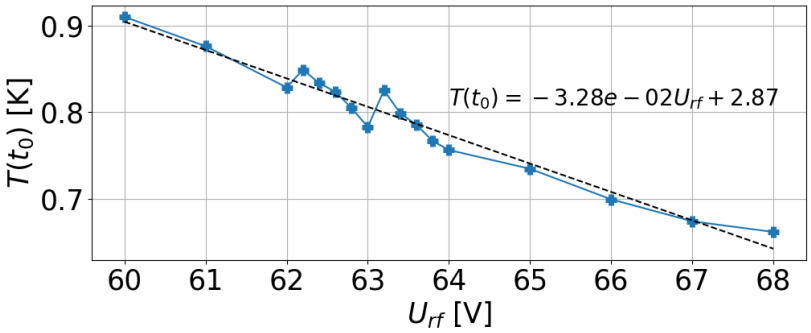

FIGURE FR.7: Température du nuage au temps critique t_0 déduit du fit, en fonction de U_{RF} pour 17 conditions différentes, en utilisant le programme `RF HEATING`. U_{DC} = 7 V, 1024 ions. La ligne en tirets est un fit linéaire dont l'équation est écrite en noir. La ligne bleue relie les points voisins entre eux.

Fr.5 Conclusion

Le travail réalisé dans cette thèse a pour but de proposer une nouvelle solution de détection non-destructive pour les molécules géantes. Actuellement, les molécules géantes de masse supérieure à 10^6 Da, comme les virus, sont détectables dans des conditions restreintes en raison de la limitation des solutions de détection. En particulier, leur détection nécessite soit une fragmentation, soit un état de charge élevé, ce qui dans les deux cas place la molécule dans un état éloigné de son état dans les systèmes biologiques. Dans ce travail, le principe que nous proposons est étudié pour permettre la détection

non-destructive d'un ion moléculaire individuel de masse 10^6 Da. Le détecteur est un ensemble d'ions Ca^+ piégés et refroidis par laser. Le signal de détection est recherché dans la fluorescence de cet ensemble d'ions. Le principe repose sur la perturbation de la fluorescence induite par l'interaction de l'ion moléculaire avec l'ensemble ionique. Afin de démontrer une détection selon ce principe, un prototype et des simulations numériques sont développés en parallèle.

Dans ce travail, ce principe est démontré par des simulations numériques. Nous démontrons également que l'effet de détection est dû à la combinaison de deux effets. Premièrement, l'énergie est transférée de la molécule chargée à l'ion via l'interaction de Coulomb, ce qui entraîne une faible augmentation de la température (environ 100 mK). Deuxièmement, un mécanisme connu sous le nom de chauffage par radiofréquence devient dominant et provoque un réchauffement rapide du nuage de plusieurs ordres de grandeur (jusqu'à 1000 K environ). Cette hausse de température au delà de la dizaine de Kelvin provoque une diminution significative de la fluorescence observable.

Ce travail présente le piégeage et le refroidissement par laser d'un ensemble d'ions, et discute des éléments importants afin de comprendre le principe de détection (partie I). Il propose également une source moléculaire et un système pour guider les ions moléculaires vers le détecteur (partie II). Les simulations numériques sont utilisées afin de reproduire l'interaction de la molécule géante avec l'ensemble des ions (partie III). Les conditions spécifiques dans lesquelles le détecteur est capable de fournir un signal de détection sont spécifiées à partir des résultats numériques. Ces résultats numériques permettent une comparaison avec les aspects fondamentaux du piégeage et du refroidissement laser inhérents au principe du détecteur, mentionnés précédemment. Les simulations numériques proposent également une discussion de cet effet de chauffage par radiofréquence qui est au cœur du mécanisme de détection, et qui peut être vu comme un amplificateur de l'apport initial d'énergie fourni par la molécule chargée qui traverse.

Les défis à surmonter pour assurer expérimentalement une détection sont nombreux. Tout d'abord, la stabilité et la reproductibilité de la source moléculaire doivent être améliorées. Ensuite, le fonctionnement de la source pour les molécules lourdes doit être réalisé. Différentes molécules de masse intermédiaires sont identifiées afin de tester le fonctionnement de la source : le Dibenzo-18-crown-6 (360 Da), la gramicidine (1 882 Da) et l'albumine de sérum bovin (66.5 kDa). Plusieurs défis non discutés dans ce manuscrit nous attendent également. Parmi eux, le contrôle minutieux de l'énergie de collision de l'ion moléculaire avec le nuage d'ions doit être maîtrisé. La position et la direction vers lesquelles la molécule entre en collision avec l'ensemble d'ions est un paramètre crucial qui doit être contrôlé. Il est essentiel de guider l'ion moléculaire le plus près possible du centre du nuage pour qu'il se déplace le long de l'axe longitudinal et interagisse le plus possible avec le nuage, notamment sans être dévié trop tôt. A propos du contrôle de l'énergie incidente de la molécule, des expériences dédiées à l'interaction d'une molécule (CH_3F) avec un nuage d'ions Ca^+ démontrent déjà la possibilité de produire un flux de molécules avec une énergie translationnelle du même ordre de grandeur que le Kelvin ($1K \approx 0.1$ meV) [Wil08], en utilisant un multipole courbé à 90 degrés.

Je souhaite aussi commenter les récentes avancées faites dans le domaine des pinces optiques et rapportées par Gieseler et al. [Gie21] dans sa revue. Notamment l'auteur indique que la manipulation des molécules biologiques dans le vide est désormais possible. La principale limite à l'utilisation de pinces optiques à ces fins sont les sources moléculaires. Ces dernières doivent être capables de projeter des molécules avec une énergie suffisamment faible pour être capturées dans le piège optique. La condition à respecter est que la vitesse des ions moléculaires soit inférieure au produit $\lambda\gamma_0$, les deux variables étant respectivement, la longueur d'onde du laser et la constante d'amortissement. L'utilisation des pinces optiques avec un nébuliseur [Ric19] ou un dispositif de désorption acoustique [Byk19] sont rapportés par Gieseler et al. [Gie21].

De plus, le succès de l'expérience dépend de la capacité à refroidir le nuage d'ions à une température basse (environ 5 mK). Néanmoins, les hautes tensions radiofréquences ($U_{RF} > 50$ V, $q_x > 0.5$) requises dans notre expérience sont la source d'un échauffement important auquel il est inhabituel de travailler et qui mettent au défi le refroidissement laser. En raison de la plus grande susceptibilité que cette haute amplitude de radiofréquence implique, elle exige également un contrôle minutieux de l'environnement de l'ensemble d'ions, et surtout un contrôle minutieux des défauts du piège et autres déséquilibres. Si les petites imperfections sont tolérables lors d'un piégeage avec une faible amplitude de radiofréquence, elles deviennent trop importantes lorsque le champ appliqué atteint des amplitudes aussi élevées.

Enfin, le travail numérique présente également quelques défis. En particulier, l'étude du chauffage par radiofréquence exige un cadre spécifique afin d'exploiter les données avec une cohérence raisonnable. En effet, en raison de la forte oscillation de la valeur des variables numériques telles que la température, il est très difficile d'exploiter leur dérivée temporelle. Alors que certains ont utilisé un modèle analytique complexe afin d'étudier le chauffage par radiofréquence dans des conditions limitées [Nam14], nous avons essayé de fournir une compréhension plus générale et universelle du chauffage par radiofréquence. En particulier, nous ne voulons pas limiter notre étude à un effet moyen, mais le considérer tout au long de l'évolution de la température, ce qui est en fait plus difficile que prévu. Cela a nécessité de remplacer la température par une forme analytique via un ajustement afin de l'étudier. Néanmoins, une approche moins analytique peut être développée afin de représenter les données avec plus de précision.

Finalement, il est important de noter que si le présent travail est orienté vers la question de savoir comment optimiser le chauffage radio-fréquence afin de maximiser le taux de chauffage, ce travail peut aussi être utilisé, à l'inverse, afin de minimiser le chauffage radio-fréquence. En effet si nous utilisons le chauffage radio-fréquence à notre avantage, c'est dans la plupart des cas un inconvénient que l'on cherche à minimiser. Les principes, arguments et outils présentés dans cette thèse peuvent servir à minimiser le chauffage radio-fréquence.

INTRODUCTION

"[Les physiciens] comprirent que la raison ne voit que ce qu'elle produit elle-même selon son projet, qu'elle devrait prendre les devants avec les principes qui régissent ses jugements d'après des lois constantes et forcer la nature à répondre à ses questions, mais non pas se laisser guider uniquement par elle pour ainsi dire à la laisse ; car, sinon, des observations menées au hasard, faites sans nul plan projeté d'avance, ne convergent aucunement de façon cohérente vers une loi nécessaire, que pourtant la raison recherche et dont elle a besoin."
– Emmanuel Kant *in* Critique de la raison pure, préface de la seconde édition.

THE novelties we deal with in this thesis concern the use of a laser-cooled trapped ion cloud as a detector for charged macromolecules. The theoretical framework upon which this work is based originates from the two following contexts.

First, mass spectrometry which serves as a general background in which the problematic is intended to be included. This is the dedicated field for identification and detection of molecules. Second, is trapping and laser cooling of an ion cloud, for which we introduce a application end in this work as a detector for molecular ions. The principle of the experiment, refereed to as `GiantMol`, is illustrated with figure In.1. The presence of a giant molecular ion can be determined by the interaction with an ensemble of trapped and laser cooled ions. The fluorescence of this ensemble, induced by the laser-cooling, can be monitored, and it is expected that, under certain conditions, the passing of the molecular ion triggers a detectable modification of the ion cloud fluorescence, which constitutes the detection signal.

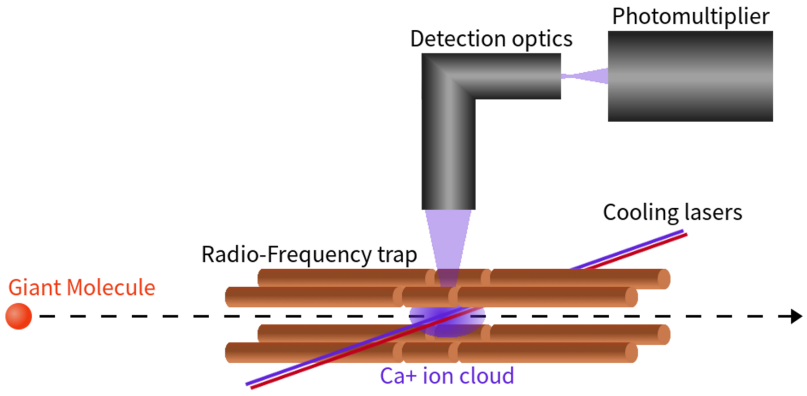

FIGURE IN.1: GiantMol principle : injection of an analyte in a laser cooled ion trap and measure of fluorescence.

The development of such a detector is crucial in order to fill a gap among the possibilities provided by classical analytical methods. Secondly the setup we propose provides a platform for the study of the interaction between a heavy charged particle and a

well-controlled ion cloud. Among the existing demonstrated solutions existing (Fig. In.5), either singly-charged molecules are detectable only below a certain mass limit using a destructive principle, or heavy molecules are detectable above a certain charge threshold. The ion cloud as a detector for charged molecules proposes the detection of individual singly-charged molecule of high mass ($> 10^6$ Da) as a goal, which would overcome the above mentioned limitations. While our numerical simulations (part III) already provide a proof-of-concept for such principle, the `GiantMol` experiment is still in development. Elsewhere, experimental setups are already operated in order to monitor the collision of a molecule with a trapped Ca^+ ion ensemble with a precise control of the collision energy [Wil08]. Apart from mass spectrometry, the bibliography also illustrates how the platform we propose can be the opportunity to carry out several other measurements related to the interaction between the trapped species and the molecule in the context of chemistry or physics in general [Wil12; Ber06; Cap12]. On the numerical point of view `GiantMol` can also be an opportunity for developments independent of the mass spectrometry context (part III), and many other works show that similar setups are of interest in other contexts such as plasmas and stopping power [Bus06], heating in traps [Ryj05; Nam14] or manipulating antimatter [Hil14].

The `GiantMol` project originates from the confrontation of several fields related to physics, physical chemistry and chemistry. The idea was to mobilise techniques, methods, point of views, from those fields with the intent to deal with a common problematic. The question of the detection of a molecule emerged from this confrontation and the initial ideas gave birth to a patent [Cha14]. Researches on the possibility of the exploitation of such a principle were made. The SATT South-East, a society dedicated to the maturation of inventions, funded the prototype and prospected among the enterprises and scientists among the communities of mass spectrometry and pharmacology.

This thesis manuscript is thus about a project involving a prototype under development. It presents major choices that were already made before I joined the group, as much as developments introduced during my presence, whether those developments are analytical or experimental. This work contains a bibliographic research work in order to consolidate the mastery of the several elements involved and later propose enhancements to the prototype. Experiments in order to test and characterise the prototype in its current development state are provided, alongside with propositions for further studies.

This thesis manuscript is organised according to the following. This introduction sums up the context of analytical chemistry, its principles, methods and demonstrated performances. Then part I (LASER COOLING OF TRAPPED IONS) is dedicated to the presentation of the experimental considerations on trapped ions and laser cooling. The analytical fundamental developments are presented as long with experimental results. This part is essential in order to understand the physical mechanisms of the detection principle. Then part II (THE MOLECULAR SOURCE) is dedicated to the presentation of the experimental considerations on the molecular source and the guiding of charged molecular ions. In this part II the guiding prototype in development is described and tested. This part is important because it summarises the recent fundamental developments relative to such devices

and demonstrates how a particle can be guided to interact with a specific target. Then part III (DETECTOR BEHAVIOUR AND PROOF-OF-CONCEPT BY MOLECULAR DYNAMICS SIMULATIONS) is dedicated to the numerical simulations that accompanied the development of the prototype. In particular the numerical simulations are used to investigate the specific conditions for which the detector provides an observable detection. Also numerical simulations are used in order to investigate the physics of the interaction of a charged projectile with a set of laser-cooled trapped ions. Each part is later introduced in a similar fashion in their respective introductions.

0.1 Definition of giant molecules and their role in biological systems

The word molecule derives from Latin molecula, itself a diminutive for the Latin moles, meaning “a mass of something”. In modern context a molecule is an assembly of two or more atoms held together by **chemical bonds**[6] [IUP97a], forming an entity with specific properties depending on its atomic composition and its structure [Win07] (See Box 0.1.1). The mass of a molecule can be as little as the one of dihydrogen – 3.35×10^{-27} kg – and can reach human comparable masses (See Frame 0.1.2).

Giant molecules, or macromolecules, are also called large molecules. When deriving from similar molecules assembled together, a molecule is called a polymer. Historically macromolecules appeared in the context of synthetic polymers. “The first experimental evidence for the existence of long polymer chains was provided by Staudinger and Fritschi who performed the polymer-analogous hydrogenation of natural rubber” [Mül04]. The term macromolecule is introduced for the first time in the work of Staudinger and Fritschi [Sta22] in 1922, and is defined as a “polymer chains containing covalent bonds between the monomeric units in the backbone”.

Box 0.1.1: Protein structure – biological and synthetic examples

A protein – Hemoglobin Hemoglobin (15 258 Da) displays a quaternary structure, resulting from the folding of the original atomic chain in a complex mechanism (Fig. In.2). The simple chain of atoms constitutes the primary structure. It locally arranges in α helixes (red subunits) and β sheets (blue subunits) by close interaction of functional groups, forming a secondary structure. Those in turn arrange in a third structure represented by the blue and red subunits. Those subunits assemble together to form the final functional quaternary structure, including the hemes represented in green.

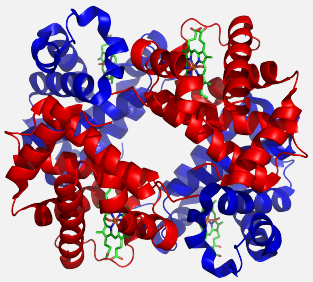

FIGURE IN.2: Structure of human hemoglobin. Green structures are hemes.

[6] The bonds can be classified as strong or weak bonds. For instance, a covalent, ionic or metallic bond is called strong, while a hydrogen bond is qualified as weak.

A synthetic polymer – Polyvinyl chloride Polyvinyl chloride is a polymer built upon monomer units as showed in Figure In.3. Objects built in PVC are a complex combination of this same monomer unit, repeating itself along the structure. This polymer can form human-sized objects such as bottles, cards, cable insulation or imitation leather. In the case of synthetic polymer the composition is much simpler than with biological molecules and there is no concept of secondary or more structure.

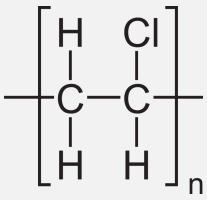

FIGURE IN.3: Unit of PVC.

Later, discoveries on biological molecules will bring new considerations on giant molecules. In 1948, Pauling [Pau48] refers to insulin and its 2000 atoms as a giant molecule. The discovery of their complex structure due to the weak bonds between functional groups (See frame 0.1.1) sets new criteria for the definition of large molecules, distinguishing them from the simpler small molecules only displaying a structure defined by the covalent bonds between atoms. The careful study of macromolecules is of major interest in biology since it is known that their complex structure and their variations depending on the environment are known to be responsible for their specific activity [Pau48; Mon65; Eat07]. For instance, desaturated hemoglobin changes conformation when binding with oxygen, favoring affinity with further oxygen atoms and allowing to deliver oxygen when the difference in partial pressure would be insufficient without this change in conformation. Again, “the configuration of antibody molecules is very closely complementary to that of the surface of the homologous antigen” [Pau48]. In particular biological macromolecules with variable conformations are the key elements in the regulation of the activity of organisms [Mon65]. Biological macromolecules can also play a role as envelope for certain organisms. For instance, the virus envelope of bacteriophage MS2 is a polymer of 180 coat proteins. Following this statement on biological functionality, a definition for a macromolecule has been settled around its ability to diffuse across cell membranes, defining the threshold between small and large molecules in the range of 500 to 900 Da [Lip04; Dou11]. Most of the small molecules used to probe functional groups, or other such as drugs, fall below this threshold.

Nowadays, biological macromolecules can be grouped in four essential categories : polysaccharides, lipids, proteins and nucleic acids – DNA and RNA. In practice, many biological macromolecules are polymers (See Frame 0.1.2) but this is not necessarily the case.

Box 0.1.2: Giant molecules and polymers

Size of a molecule Asking for the "size" of a macromolecule, it is often agreed in chemistry that the answer is given in term of mass or number or atoms. It is simpler because molecules can have very disproportionate aspect ratios. Also measuring their spatial size depends on the context. Considering a molecule, three different sizes would be relevant.

The **kinetic diameter** is related to the mean free path of the molecule in a gas

[Joo86]. It expresses the likelihood that a molecule in a gas collides with another molecule and it depends on the gas composition.
The **Van der Waals radius** is related to the ability of the molecule to chemically react with its environment [Win07]. It can be determined by considering the Van der Waals radius of each atom within the molecule. Also it is possible to consider the Van der Waals radius as the solvent accessible surface, thus it is determined by the surface swept by a spherical probe rolled over the Van der Waals surface formerly described. The probe is usually about 1.5 Å which is the size of water molecule. This size is important to consider in gas chromatography, zeolites adsorption.
Then the **covalent radius** is determined by the length of the covalent bonds formed between atoms.

Mass of a molecule A first approximation of the **mass of a molecule** is determined by its formula. Nevertheless due to the existence of atomic isotopes – i.e ^{12}C,^{13}C and ^{14}C – a given molecule can have different masses – i.e CH_4 mass can vary from 16 to 18 atomic mass units, which is observable in high-resolution mass spectrometry. Accounting for this fact the relative mass is defined as the arithmetic mean of the mass of isotopes weighted by their abundance. Since 2019 and the redefinition of SI units [BIP19], masses are given in Dalton [Da] so that 1 Da = $m(^{12}C)/12 \approx 1$ g/mol.

Monomers and polymers A polymer is a molecule composed as an assembly of a individual molecules called monomers and that can be encountered repeatedly in the polymer. Polymers can be linear, branched, form loops or have a semi-crystalline structure. They can also be a mix of several monomer units mixed together in more or less complex fashion, such as the MS2 bacteriophage capsid or RNA and DNA.

Some examples The MS2 virus capsid – casing – is a polymer of 180 copies of a coat protein [Tit00] for a total mass of 2484700 Da. The largest protein to known date is titin with a mass measured in the interval $3 - 3.7$ MDa [Opi03], it is an elastic protein composing muscles. DNA is also a macromolecule, the chromosome 1 from human genome has a mass of 156 GDa [Pio19]. In the case of DNA and RNA, the order is highly significant for the activity of the molecule. Other biopolymers such as silk, collagen or sugars can be representative of higher masses.

0.2 Principles of analytical chemistry

0.2.1 Generalities

Analytical chemistry is the field of research dedicated to the analysis of chemical substances. Analytical chemistry is often implemented in order to identify and/or characterise and/or quantify molecules in a sample. It has a broad application in all chemistry related

fields such as biology [Kon19; Tit00], environment [DEl89; Arm08], food authentication [Dan16], forensic science and drug testing [Dru13] or toxicology [Mik14].

In an analysis, the processing of a sample under investigation can be divided into three major successive steps (Fig. In.4), starting with the actual removal from the sample and ending with the production of the result. The sensibility and resolution of the whole analysis will depend on the technological choices for each of those steps. First the sample is **prepared** in order for the molecules to be manipulated out of a solution or substrate. This first step often includes, desolvatation, vaporisation, ionisation and acceleration [7]. Then secondly, the sample is manipulated in order to **discriminate** its components. Then those components are **detected**. The detector is a device providing only a signal when it receives something it is sensitive to. The results provided depend not only on the detector but on the design of the whole analyser. In particular, the purpose of a detector for large molecules is dependent on the ability of a source to produce large molecules in a state ready for measurement.

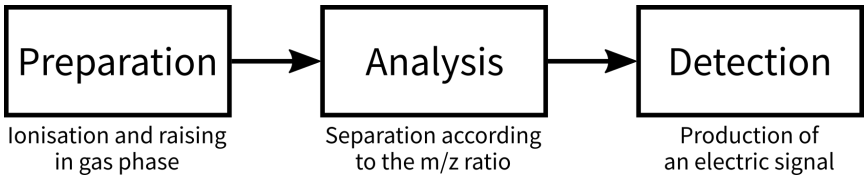

FIGURE IN.4: Diagram of any time-of-flight mass spectrometer.

Results can be sorted into two categories, depending if the analysis allow to quantify the results. In the case the analysis can provide numeric results it is said **quantitative**. If it is not possible, the analysis is said **qualitative** [Sko13]. Those quantified results can be a mass or volume then used to identify the chemical species, or a quantity related to its mass, charge state, or concentration, in order to characterize the presence of the specific species . . . At the same time, an analysis can be either **targeted** or **non-targeted** [Bal19]. In **targeted** analysis, one compound at a time is looked for, contrary to **non-targeted** analysis where a sample is analysed "as a whole" in a procedure resembling *fingerprinting*. In targeted analysis preparation and discrimination steps are often more demanding than in non-targeted analysis, because it is required to isolate a specific molecule or group of molecule from the solvent and other contaminants. In the case of a non-targeted analysis those phases are much simpler as we do not require to measure individual components, but the complexity lands on the analysis of the result where the sample is analysed as a whole. The result must then be compared with other results obtained with calibrated samples – thus the designation *fingerprinting*. Atomic absorption/emission spectroscopy (AAS and AES) are a good example of quantitative non-targeted methods.

The technological choices to fulfil each of those three steps are done accordingly to

[7] Before everything, it is often required that the raw sample undergoes **purification** in order to sort it from its original substrate. It is then prepared in an intermediate state such as in solution suitable for its further analysis.

their ability to proceed the sample under investigation. It is interesting to **combine** several techniques in order to benefit from their respective advantages. The interest for non-destructive methods is then understandable in terms of functionality provided by an apparatus combining several functions. `GiantMol` lies in the category of targeted qualitative mass spectrometry.

0.2.2 Particular families of analysis

Several families of analytical techniques can be summed up in function of their respective specificities.

A first group of methods involving **chemical reactions** can be identified. To identify and characterize biological molecules, it is useful to target a specific element within the molecules of interest, using another molecule reacting with the specific element. Molecular techniques such as genomics and proteomics use reaction between molecules at their advantage [Dan16; Pay17]. Molecules under investigation will manifest by production of a by-product, later analysed with other methods such as mass spectrometry.

Optical methods are also relevant in biology with methods such as electron or atomic force microscopy, spectroscopy or scattering [Dan16; Kon19]. While microscopy methods are destructive, other optical methods are non-destructive and non-invasive but are best suited to understand the inner structure and composition of molecules. Nuclear magnetic resonance may combine the advantages of those optical methods with a high throughput and minimal sample preparation, mostly used for food and aromatic compounds authentication [Dan16].

Mass spectrometry is on the other hand a method in which a sample is often vaporized, ionized then accelerated and detected via processes involving physical processes. For instance, the detection relies on the coulombic interaction and momentum exchange of the particle with the detector, rather than on a chemical based reaction (such as redox, acid-base, combustion …). Recognized for its high sensitivity, speed and versatility, as much as for its automation capabilities and the wide range of molecules it can accept, mass spectrometry is a very important and widespread technology, especially shining in proteomics and crucial for all other emerging '-omics' fields such as genomics [Gli03]. The interest to develop a detector usable in mass spectrometry is thus high.

0.3 Mass spectrometry for macromolecules

Nowadays, mass spectrometry (MS) is appreciated for its versatility, speed and sensitivity [Gli03]. But before MS was able to proceed giant mega-Dalton molecules, many improvements were required both on the detector and source side. Those two essential components play a key role in the capabilities of a mass spectrometer and a brief presentation of the evolution of the performances of both is presented below.

0.3.1 A detector limitation

The first particle detectors were based on photographic plates or collecting electrodes producing a small current – the Faraday cup. In mass spectrometry the number of charges to be measured can be as little as one, and a considerable amplification can be required, up to 10^8 typically [Hof05]. To achieve this requirement, several techniques were developed based on secondary electron emission. Detectors based on this principle are electron multipliers : when the incoming charged particle impinges on the detector material with enough velocity it eject a primary electron, accelerated on dynodes producing secondary electrons in cascade. The amplification gain can reach 10^8 with Micro Channel Plates (MCP) while other methods such as Photon Multiplying achieve to 10^5 [Hof05]. Nevertheless, the masses those detectors are able to detect is limited to an upper threshold. Indeed, as the mass of the charged particle increases, its velocity decreases for a given acceleration voltage and charge. As there is a limit to the voltage it is possible to apply for acceleration, it is not possible to use the above detectors for masses up to a certain limit, due to the fact that a slow collision velocity fails to produce a primary electron [Twe06]. Also, molecules can only be charged up to few hundreds of charges. See figure In.5 for a detailed review of detectors performances in single-molecule spectrometry. This problem can be circumvented by breaking the charged particle into lighter components. Nevertheless when it comes to molecule of biological interest it is essential to keep them intact and control their charge state for careful characterization in their functional state [Bas19]. Modern developments at the end of 20^{th} century leaded to few improvements using cryogenic [Hil98] or inductive detectors [Sch98] insensitive to molecular velocities [Twe06]. Nevertheless, cryogenic detectors require expensive apparatus, have a low active detection area and a long response time [Pen14]. Using other complex techniques such as cyclotron resonance (FTICR), charge detection (CDMS), it is possible to detect heavier molecules with masses up to 10^{12} Da, but only for sufficiently high charge states. Also other techniques such as Quadrupole Ion Trap Optical Detection (QIT) allow to detect bigger masses, but in very specific conditions. The performances of single-molecule spectrometry techniques are summed up in the figure In.5, from a review from Keifer and Jarrold [Kei17], dealing with the above mentioned detection techniques. Several other reviews exist, one not limited to single-molecule detection from Peng, Chou, and Patil [Pen14] or other more qualitative ones from Danezis et al. [Dan16] and Kondylis et al. [Kon19].

0.3.2 A source limitation

Mass spectrometry (MS) was settled as the modern technique we know of today in the late 1910 with the works of Dempster [Dem18] and Aston [Ast19]. Using as molecular sources electron bombardment or discharge tubes, they observe small molecules with masses up to 112 Da. Already they pointed out the fact that vaporising heavier molecules requires more heating but results in the breaking of the molecule. The heat dislocation of molecules was a huge limitation to the masses available for analysis, until the development of the so-called energy sudden ionization techniques. Fast atom/ion bombardment and plasma

desorption proposed a first improvement in the mass range available to mass spectrometry.

But this is really the development of laser desorption techniques and electrospray ionisation sources (ESI) in the late 1980 that allowed mass spectrometry to become relevant for giant molecule spectrometry. Fenn et al. [Fen89, p. 63] reports observation of proteins and oligonucleotides up to 130 kDa with an electrospray source ionisation (ESI), then reports in the early 90's masses available for intact detection up to hundreds of kDa [Fen90]. Karas et al. [Kar89] reports the observation of a 250 kDa intact protein thanks to Matrix-Assisted UV Laser Desoprtion Ionisation (MALDI). Yet, it is still reported that "polymer chemists prior to the mid-1990s had a rather skeptical opinion of mass spectrometry for polymer analysis" [Ant20], but later experiments using ESI showed the relevance of mass spectrometry for the analysis of giant mega-Dalton molecules. In 2000, with the use of an ESI, Tito et al. [Tit00] report the detection of an intact bacteriophage MS2 virus capsid with mass of 2.5 MDa. More recently, mass spectrometry techniques were used in order to detect mega-Dalton polymers [Vio16], using ESI and CDMS.

In all cases, the above mentioned heavy molecules were detectable because ESI and MALDI provided multiply-charged molecular ions. For instance in the MS2 case where a typical MCP is used, only molecular ions with a high charge state $Q \approx 120$ are reported. Nevertheless if required to detect molecular ions with few or a single charge, the above mentionned detection techniques fail. The idea of `GiantMol` is precisely to be able to benefit from singly-charged heavy molecular ions and detect them, non-destructively.

0.3.3 Detection and identification of virus

Those details emphazise the specificity of each technique and the impossibility for a universal analytical technique. We understand the need for developping multiple analytical techniques, often combined to provide the best accuracy. The review by Danezis et al. [Dan16] gives an overview of the multiple techniques used in analytical chemistry. They emphasize the sensitivity of each technique regarding the chemical species, functional groups or phase state. Related to the `GiantMol` experiment, the performances of current single-molecule mass spectrometry techniques are presented in a review from Keifer and Jarrold [Kei17], and summarised in the figure In.5. The expected privileged domain of expertise reserved to `GiantMol` is indicated so it can be located with respect to the other demonstrated techniques.

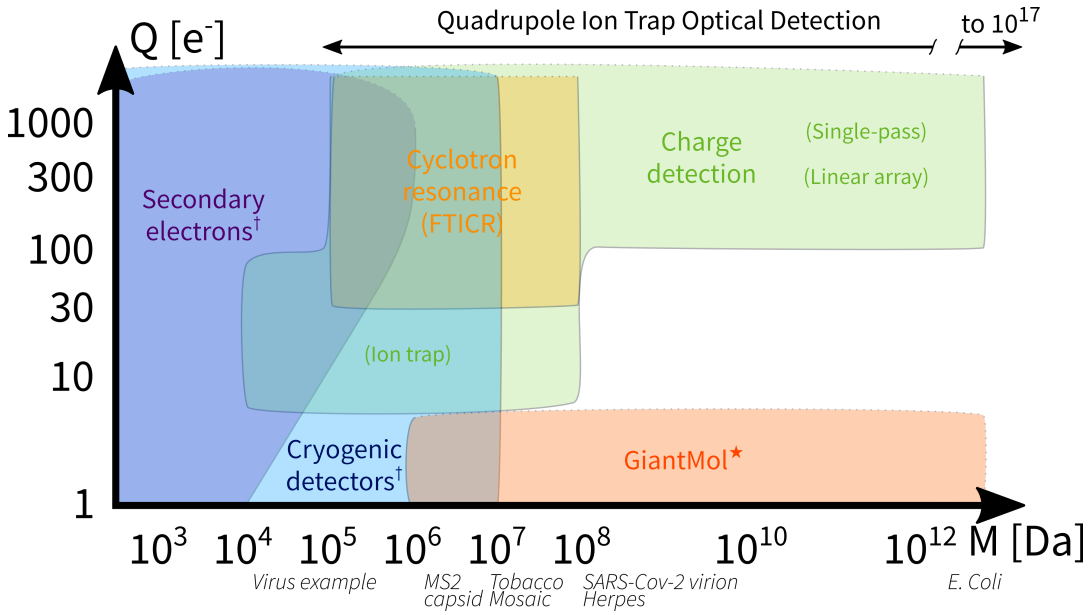

FIGURE IN.5: Comparative performances of single-molecule mass spectrometry techniques depending mass and charge of molecular ions, based on the review from Keifer and Jarrold [Kei17]. The coloured area indicate the working ranges experimentally *demonstrated* for each method tested. When it is bounded by dashed lines it indicates that the range is unbounded. Quadrupole Ion Trap Optical detection is not charge dependent thus its range is indicated with the arrow above. The star ⋆ indicates it is an *expected* detection performance, for `GiantMol` indicated in orange. The dagger † indicates the detection method is destructive. Example virus in italics are positioned so the first letter is in line with the correct mass value.

Part I

LASER COOLING OF TRAPPED IONS

Introduction

"L'expérience est un peigne que vous donne la vie quand vous êtes devenu chauve."

– Bernard Blier

In this part, the trapping and cooling of atomic and ionic species is introduced. In chapter 1 a thorough description of the quadrupole trap is carried out in which the motion of a single ion is described, in an ideal quadrupole trap and a quadrupole with axial potential. Then in chapter 2 an overview of the `GiantMol` experimental setup is given. The trap characteristics are then investigated through some measurements. The next chapter 3 highlights the modifications to the original equations (from chapter 1) it is required to carry out when dealing with an ensemble of ions. This is the opportunity to introduce the important effect known as radio-frequency heating, which is at the very heart of the detection mechanism we propose in this thesis manuscript. Some other important concepts such as aspect ratio, cloud state and phase transition are presented in this chapter. The last chapter 4 is dedicated to the thorough presentation of laser cooling, theory and experiment.

Ion trapping

Development of traps

In 1953 was designed by W. Paul the first ion trap confining in three dimensions using oscillating electric fields [Pau53; Pau58] in the range of radio-frequencies (Fig. I.1). In the late 60's, two other German teams involving Dehmelt [Deh67] and Gräff, Klempt, and Werth [Grä69] developed traps using a mix of electric and magnetic fields (Fig. I.2). Those devices allowed soon to carry out precision measurements on matter such as weighting atoms or latter frequency metrology.

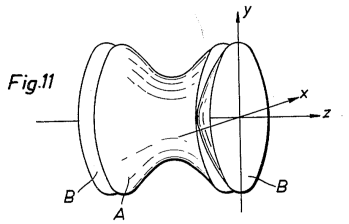

FIGURE I.1: The original design for Paul trap, with one ring electrode and two end caps.

Then in 1989, Prestage, Dick, and Maleki [Pre89] presented a new linear geometry for ion traps (Fig. I.3), inspired from the three dimensional Paul trap. This new linear design confines ions with a set of oscillating and static electric fields applied to four rods. This layout is similar to the one used as quadrupolar analyzer in mass spectrometers [Hof05, Chapter 2]. Those linear traps are of interest for metrology applications [Pre89] and have allowed to trap thousands of ions and to generate Coulomb crystals at mK temperatures

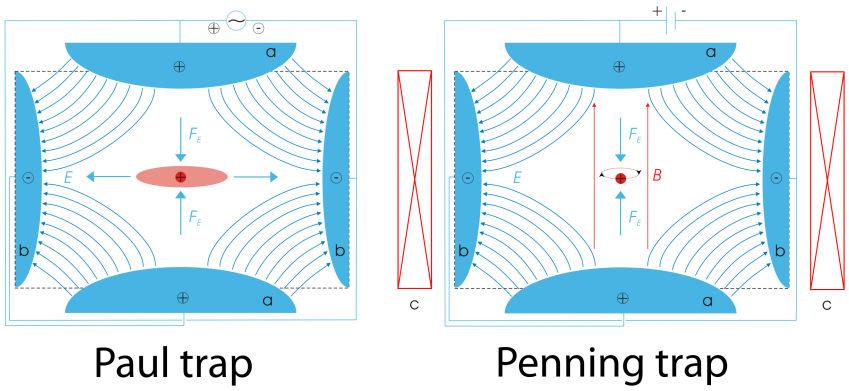

FIGURE I.2: Left : Paul Quadrupole ion trap of classical setup with a particle of positive charge (dark red), surrounded by a cloud of similarly charged particles (light red). The electric field E (blue) is generated by a quadrupole of end caps (a, positive) and a ring electrode (b). Right : Penning Trap for the storage of charged particles by the use of a constant electric field (blue), generated by a quadrupole (a, end caps) and (b, ring electrode) and a superposed constant and homogeneous magnetic field (red), generated by a surrounding cylinder magnet (c). A particle, indicated in red (here positive) is stored in between caps of the same polarity.

when coupled to laser cooling. The interest of the linear geometry is that the radio-frequency zero extends along the trap z-axis (a property often referred as strong focussing effect). It allows to have multiple ions in the node where the radio-frequency is locally negligible thus reducing the heating induced by radio-frequency. For instance it is possible to trap a small array of ions ($<$ 100 ions) along the z-axis in a linear chain [Kam17] or zig-zag conformation [Bow99; Mor04; Sch15]. Also this geometry leaves some space for the laser injection.

Related to the field of chemistry, higher order linear multipole traps are developed for guiding molecules or study chemical reactions at very low temperatures [Ger92; Ott08]. Those traps are made with more than four rods, and typical configurations have 8, 12, 16 or 22 rods. Compared to the quadrupole trap, the electric field is much weaker and more homogeneous in most of the volume. But also, the stability of the particles strongly depends on the initial conditions, which is a reason why the selectivity in mass of those higher order multipoles is bad [Sud03]. Multipoles also raise interest in the context of atomic clocks [Pre99; Pre07; Bur16]. However, it has been shown that mechanical defects leads to different potential than those predicted by the analytical equations in the error-free case, leading to local minima where the ions crystallise below a certain temperature. Such phenomena was first reported in a 22-pole trap [Ott09], and later confirmed in a 8-pole trap [Kam15; Ped18b; Ped18a]. This makes those multipoles not as much convenient than the quadrupole for the trapping of cold ions.

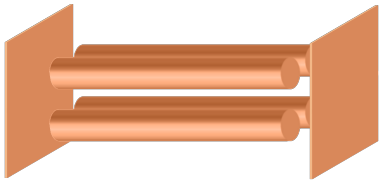

FIGURE I.3: A simple design for a quadrupole linear trap. The rods are paired diagonally and fed with an oscillating electric field. The two plates at the ends are fed with static electric field.

Also, in 2006, Seidelin et al. [Sei06] demonstrating at NIST the first stable confinement

of atomic ions in a surface-electrode trap. This innovation initiate a new standard for ion trapping and is of particular interest for quantum information systems. Later in 2014 Mehta et al. [Meh14] reports the use of a commercial 90-nm CMOS process to manufacture surface-electrode traps, which suits the miniaturization required in order to scale quantum systems to a very large number of qubits. Surface-electrodes traps at millimetre scale are also conceivable [Szy12; Tan14].

Radio-frequency heating and non-laser cooling technique

The analytical description for the motion of an individual ion is well known [Deh67; Ger92; Mar95] and refers to Mathieu equations [McL47; Cam56]. Nevertheless the equations become approximate for a greater collection of ions due to the Coulomb interaction between ions. This interaction, shifting the ions from their equilibrium trajectories in the radio-frequency field, leads to **radio-frequency heating** : energy from the radio-frequency field is transferred to the **Brownian motion** of ions [Sch00]. It is a phenomenon numerically studied since the 80's for few ions Blümel et al. [Blü89] and since the past two decades for bigger collection of ions [Ryj05]. Some references propose analytical characterizations of some aspects surrounding radio-frequency heating [Blü89; Bre90; Nam14], demonstrating that it is well understood qualitatively. But the amount of radio-frequency heating for a given set of trap parameters is not known beforehand. Experimentally, heating reduces confinement duration and precision of frequency measurements because of Doppler effect. An advance in trapped particle physics is due to the successful introduction of cooling in systems of ions. Kellerbauer et al. [Kel01], in their review "Buffer gas cooling of ion beams" state :

> The benefits of beam cooling derive from the concentration in phase space (the six-dimensional space made up of the momentum and position coordinates) that cooling of a collection of particles implies. Essentially, the smaller the volume occupied by the particles and the smaller the range of their momenta, the easier it is to detect them and to carry out precise measurements on them.

Particle cooling is thus appreciated, not only because it allows for a smaller area of confinement, but also because it reduces the spread of velocities among the trapped species, which allows for more precise frequency measurements.

Three **non-laser cooling techniques** are described by Hilico [Hil16]. First, **radiative cooling** relies on the energy a particle dissipates when it is accelerated. Nowadays this mechanism is reserved to electron and positrons for cyclotron motion dampening. Second, **resistive cooling** relies on the reciprocal influence of the charged particle over the trapping electrodes. The charged particle is cooled by dampening the image current its motion is creating in the electrode circuitry. It is mostly used to cool the axial motion in a Penning trap. The limit of this type of cooling is given by the temperature of the resonant circuit. It has been reported to cool ions down to 900 K. Third, **buffer gas cooling** implements a neutral gas (the buffer gas) colliding with the trapped ions. The principle is that

the trapped species, undergoing elastic collisions with cold buffer particles will exchange momentum and reach a thermal equilibrium. The buffer gas itself is cooled, for instance to 4.2 K with He in a cryogenic environment. Buffer gas cooling was first demonstrated by Huggett and Menasian in 1965 for Hg^+ ions confined in a Paul trap where He gas was introduced as buffer gas. The basic principles were then presented by Dehmelt [Deh67] in 1967. Nowadays, it is still of use as a cooling method [Rot05; Off08; Rot09] or for other applications such as ion bunching in high-energy physics [Kel01].

Laser cooling

Another major improvement in particle cooling is due to **LASER**[8] **cooling**. Laser cooling relies on the resonant absorption and emission of photons by the particles of interest [Wue59]. A careful arrangement of the parameters allows to reduce the temperature of the species [Hän75; Win75]. Because of the lower temperature that such cooling allows, Laser cooled ion traps are the support for multiple experimental applications ranging from few ions for quantum information [Bla08] to huge ensembles of ions for microwave metrology [Pre91]. Between those two domains are another fundamental applications such as terahertz metrology [Cha07], sympathetic cooling of molecules [Rot05] or the study of plasmas stopping power [Bus06]. Recently, we identified the interest of such system within the context of virus detection [Poi21]. When it is simply referred to laser cooling it is heard that the ion species of scientific interest is directly interacting with the laser. More specifically **Sympathetic cooling** is used to refer to a technique where a trapped species is interacting with another trapped species that is directly laser cooled. This scheme is often used in order to cool ionic or molecular species for which no laser cooling scheme is feasible. It can be used to perform high-resolution spectroscopy and frequency metrology over a particular species of interest, but also manipulate molecules in a cold state around 1 K and study chemical reactions or carry out mass spectrometry [Wil08].

Advent of laser cooling

Important landmarks related to laser cooling of trapped ions can be found in an article by Eschner et al. [Esc03b], and a review by Hecht [Hec10]. The formalization of optical cooling of atoms was carried out by Kastler [Kas50] in 1950, followed in 1974 by the work of Zeldovich [Zel74] “proposing optical pumping of a two-level system for cooling”. The next year two proposals for optical cooling came from Wineland and Dehmelt [Win75] and from Hänsch and Schawlow [Hän75], supported by latter experiments by Neuhauser et al. [Neu78], Wineland, Drullinger, and Walls [Win78], and Neuhauser et al. [Neu80]. Many interests appeared during the next twenty years, such as the manipulation of quantum states and quantum information with trapped ions proposed by Cirac and Zoller in 1995 [Cir95]. The trapping of Ca^+ becomes of interest in such a context with the initial work from Roos et al. [Roo99] in 1999.

[8] Light Amplification by Stimulated Emission of Radiation, spelled laser in the following.

Development of laser and frequency doubling

The first microwave MASER[9] is developed in 1954 [Gor54] while the first coherent laser light is obtained in May 1960 [Mai61]. Second Harmonic Generation is demonstrated with simple quartz crystal in 1961 [Fra61] and formulated in 1962 [Blo62]. The first continuous-wave solid-state laser with practical operating characteristics was developped in 1977 [Har77; Hsi77]. During the next 20 years, lasers have spread and entered the realm of mass production. Peter Moulton successfully operated a Titanium:Sapphire laser in 1982 [Mou86]. A patent [Chu88] is filed in 1988 for Lithium Borate Oxyde (LiB_3O_5), explicitly indicating its suitability for production of coherent harmonics of wavelengths below 200nm. Laser diodes for producing blue light are invented in the late 90's [Nak97; Nak00].

Application of laser-cooled and trapped ions, and work at PIIM

The laser-cooled and trapped ions are the support for numerous experimental applications ranging from quantum information with few ions [Bla08] to micro-wave metrology with huge ensembles of ions [Pre91]. In the past decades, the CIML team thoroughly explored the possibilities offered by such systems to carry out the measurement of the $3d^2D_{5/2}$ level lifetime [Kno04] and terahertz metrology [Cha07]. Phase transfer was recently developed in the context of the other experiment currently under operation in the team [Col19b]. Also developments on the manipulation of the trapped ions in radio-frequency traps were achieved, leading to publications about resonant ejection ("tickle") [Ved90] or macroscopic transport [Ped15] of ions. Trap imperfections was also a topic studied in the team [Ped18b; Ped18a].

[9] Microwave Amplification by Stimulated Emission of Radiation

Chapter 1

Description of a linear quadrupole

A solution in order to **trap** a charged particle consists of providing a **stable equilibrium position** using an **electric potential** ($\Phi(x,y,z)$). The potential Φ, through the **electric field E** from which it derives ($\mathbf{E} = -\nabla\Phi(x,y,z)$), will produce a **force** on any **charged particle** immersed in the potential. Ideally, every time the particle should move from its equilibrium position, the field would apply a **restoring force $\mathbf{F_r}$** pointing *towards* this equilibrium position, ensuring the confining of the particle in a limited three dimension space.

1.1 Potential in an ideal quadrupole trap

1.1.1 Radial ideal quadrupole potential

The description of the radial confinement inspires from the work of Campana [Cam80]. The author discuss a linear geometry (Fig. 1.1) similar to that used in our experiment. A justification for the trap's design and electric feed is given by the following computation. Also this section is intended to serve as a base for the description of quadrupole mass filter and multipole guide in mass spectrometry (see section 5.4).

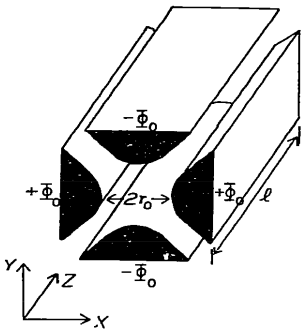

FIGURE 1.1: Linear trap design from Campana [Cam80], with hyperbolic surfaces. Φ_0 is the applied electric voltage, r_0 the inscribed radius between the electrodes, and l the length of the rods.

Let's suppose the potential produced by the trap resolvable into the sum of its components so that $\Phi(x,y,z) = \Phi(x) + \Phi(y) + \Phi(z)$. With static electric fields, this would require field lines all around the equilibrium position to converge towards this position so that $\Delta\Phi(x,y,z) \neq 0$. *This is incompatible with Gauss' law* and in particular with **Laplace equation** $\Delta\Phi(x,y,z) = \nabla(-\mathbf{E}) = 0$. This means it is impossible to provide a field trapping *simultaneously* in all directions. Nevertheless, using *electric fields alternating in time*, it is possible to produce a restoring force alternatively in each of the cardinal directions, ensuring the particle is globally trapped in a limited three dimension space at long time range. The expression for the ideal trapping field is thoroughly demonstrated in appendix A. Below is given the potential expression for the ideal quadrupole, before the more general case is treated just after, where a multipole expansion of the potential produced by the linear quadrupolar geometry is done.

The potential $\Phi_{Rad}(x,y,z)$ produced can be summed as individual contributions over the three dimensions x, y and z,

$$\Phi_{Rad}(x,y,z) = \alpha x^2 + \beta y^2 + \gamma z^2. \tag{1.1}$$

In the case of the ideal quadrupole trap, it is set

$$\alpha = -\beta = \frac{\Phi_0}{r_0^2} \tag{1.2}$$

$$\gamma = 0 \tag{1.3}$$

$$\Phi_{Rad}(x,y) = \Phi_0(t)\frac{x^2 - y^2}{r_0^2}. \tag{1.4}$$

As the voltage applied to the rods can be written as $\Phi_0(t) = U_{st} + U_{RF}\cos\Omega t$, with U_{RF} the amplitude of the alternating field applied to a rod, and U_{st} a possible offset, Ω the angular frequency of the alternating field, the potential can be expressed as

$$\boxed{\Phi_{Rad}(x,y,t) = \frac{U_{st} + U_{RF}\cos\Omega t}{2r_0^2}(x^2 - y^2).} \tag{1.5}$$

It is created by applying two alternating voltages with amplitude U_{RF} to each pair of rods, the pairs being in phase opposition. For a single particle, no coupling between x and y appear in this equation. This is due to the fact that the trap was chosen ideal and so the potential was defined since the beginning as a sum of separated contributions for each direction (Eq. 1.1). For the atomic species of interest in atomic physics, the frequency of the alternating field applied to the electrodes very often fall in the range of the radio-frequencies[1]. This is why the radial trapping field is very often referred as radio-frequency field. In order to provide the appropriate field, the surface of the electrode must comply to the potential equation 1.5. Ideally the surfaces should be hyperboloids, which is the case in the original three dimension Paul trap and the later design from Campana (Fig. 1.1). Nevertheless in order to keep the machining practical, the rods of many traps, including `GiantMol`, are cylindrical, which is proven to be satisfying provided the dimensions are well chosen (see section 1.6).

1.1.2 Multipole expansion

With no hypothesis other than the rod geometry, the Laplace equations, once solved in the case of planar 2D fields, leads to a more general form that it is possible to simplify through multipolar expansion, which consists of a Taylor expansion around point (x_0, y_0) of the potential distribution. This way then it is possible to express the solution potential Φ as a combination of complex polynomials of order $n \in \mathbb{N}$.

[1] The radio spectrum identified as radio-frequency ranges from 20 kHz to 300 GHz approximatively.

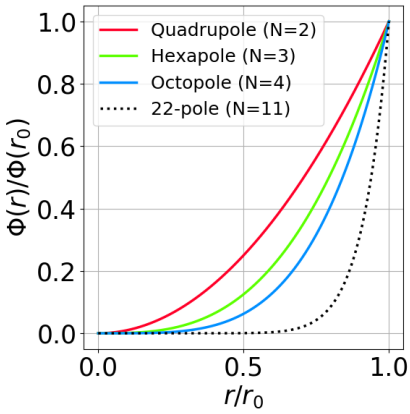

FIGURE 1.2: Four multipole shapes in radial direction for $y = 0$

$$\Phi(x,y) = A_0 + \sum_{n=1}^{\infty} \Phi_n \tag{1.6}$$

$$= A_0 + \Re\left[\sum_{n=1}^{\infty} A_n \left(x - x_0 + i(y - y_0)\right)^n\right] \tag{1.7}$$

$$= \Re\left[\sum_{n=0}^{\infty} A_n \rho^n e^{in\phi}\right] \tag{1.8}$$

with $\Re$ the real part and i the imaginary unit. This analysis of the electric field in linear quadrupoles is done in a recent article from Douglas, Frank, and Mao [Dou05], that also demonstrates the conformity of the ideal quadrupolar form with the above equation 1.5.

This expansion provides a very good approximation of the real potential only with the few first terms. In the case of the pure ideal quadrupole, $n = 2, A_2 = 1$ and $A_{i\neq 2} = 0$, the equation 1.7 leads to equation 1.5. Nevertheless, any imperfection in the trap's design geometry will introduce higher order potentials. For instance, relocating one electrode from its ideal position introduces a hexapole potential ($n = 3$) [Kon06] and changing the electrode radius introduces an octopole potential ($n = 4$) [Sud03]. Those two potential expresses as

$$\text{hexapole potential } [\ \Phi_3(x,y) = \frac{A_3^*}{r_0^3}(x^3 - 3xy^2) \tag{1.9}$$

$$\text{octopole potential } [\ \Phi_4(x,y) = \frac{A_4^*}{r_0^4}(x^4 - 6x^2y^2 + y^4). \tag{1.10}$$

Both potentials, along with the quadratic ideal one, are represented in figure 1.2, for $y = 0$. A 3D rendition of the ideal quadratic potential is provided in figure 1.3 at two specific times. The weight of the higher order potentials in the generated trapping field is weighted by coefficients $A_n = A_n^*/r_0^n$ depending on the size of the defect. Those higher order potentials are usually detrimental because they introduce coupling between x and y directions through products of the form $x^i y^j, (i,j) \in \mathbb{N}$. Perhaps some applications such as the one we propose may benefit from this coupling. In the case of the three dimensional Paul trap, the method is the same but the multipole expressions are slightly different because of the axial symmetry. Filippov and Sudakov [Fil21] provides an extensive development of the

multipolar expansion for circular electrodes (3D Paul trap) and linear geometries.

In any case, the more energy is put into higher order multipoles, the less there is in the ideal quadrupole. Such higher order anomalous potentials can be integrated in the above computation as a dampening of the pure ideal quadrupolar potential. This is done by dividing the radial potential Φ_{Rad} by a geometric constant $0 < \mathcal{L} < 1$ [Ped10].

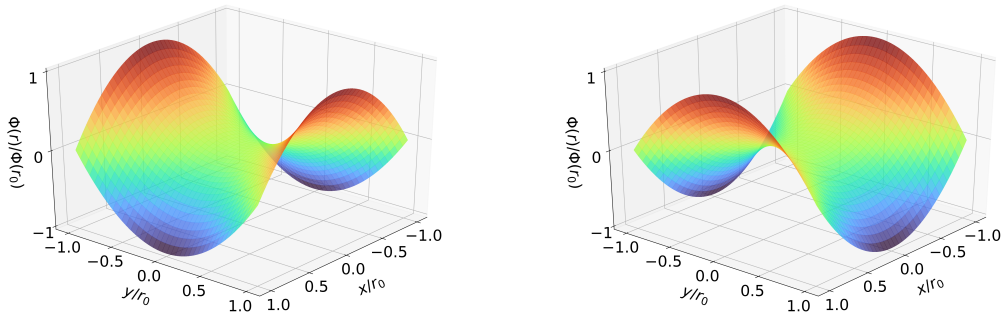

(A) Normalised quadrupolar field from equation 1.5 at $t = 0$.

(B) Normalised quadrupolar field from equation 1.5 at $t = \pi$.

FIGURE 1.3: Normalized quadrupolar field in `GiantMol` trap.

1.2 Motion equation and stability in an ideal radial potential

1.2.1 Motion equation – Mathieu equations

Considering the motion and stability of a **single charged particle** with mass m and charge q_e, immersed in the trap's field, we may integrate Newton's second law. To discuss stability, only the radial component $\Phi_{Rad}(x, y, t)$ of the trap can be considered first. The minor contribution of an axial static potential $\Phi_{DC}(x, y)$ to ion stability will be discussed later. With potential $\Phi_{Rad}(x, y, t)$, the restoring force can be computed with $\mathbf{F_{Rad}} = -q\nabla\Phi_{Rad}(x, y, t)$. Then

$$\begin{cases} \dfrac{d^2}{dt^2}x + (U_{st} - U_{RF}\cos\Omega t)\dfrac{2q_e}{mr_0^2}x = 0 & \text{(1.11a)} \\ \dfrac{d^2}{dt^2}y - (U_{st} - U_{RF}\cos\Omega t)\dfrac{2q_e}{mr_0^2}y = 0 & \text{(1.11b)} \end{cases}$$

are the equations to be integrated. Thanks to a variable change those equations can be rewritten under the form of Mathieu equation [McL47]

$$\boxed{\frac{d^2}{dt^2}u + (a_u - 2q_u\cos 2\tau)\,u = 0} \qquad (1.12)$$

with $u = x, y$, and

stability parameters

$$\boxed{a_x = -a_y \overset{\text{def}}{=} \frac{8q_e U_{st}}{mr_0^2\Omega^2}} \quad (1.13)$$

$$\boxed{q_x = -q_y \overset{\text{def}}{=} \frac{4q_e U_{RF}}{mr_0^2\Omega^2}} \quad (1.14)$$

variable change

$$\boxed{\tau \overset{\text{def}}{=} \Omega t/2} \quad (1.15)$$

$$\boxed{\frac{d^2}{d\tau^2} = \frac{4}{\Omega^2}\frac{d^2}{dt^2}} \quad (1.16)$$

1.2.2 Solution of Mathieu equations

A thorough explanation on the resolution of Mathieu equation can be found in appendix B, inspired by the extensive work from McLachlan [McL47]. Also, a synthetic description of Mathieu equation, upon which this text is based, can be found in textbooks [Maj05; Kno16].

Mathieu equation have two kinds of solutions u, unstable and stable, depending on the choice of parameters (a_u, q_u) (Fig. 1.4a), later referred as stability parameters. Stable solutions related to ions trapped in stable trajectories over time can be expressed as a sum of cos mt and sin mt functions with π and 2π periodicity [McL47], so that

$$u(\tau, q_u) = \alpha ce_\nu(\tau, q_u) + \alpha' se_{\nu+1}(\tau, q_u) \quad (1.17)$$

$$= \alpha \sum_{n=m}^{\infty} f_{\nu+1}(q_u)\cos(n+\beta)\tau + \alpha' \sum_{n=m}^{\infty} f_\nu(q_u)\sin(n+\beta)\tau \quad (1.18)$$

with $\alpha, \alpha', \in \mathbb{R}$, $f_m(q_u)$ a polynomial function of q_u, $\nu = m + \beta$ a real order so that $m \in \mathbb{N}$ an integer order, $0 < \beta(a_u, q_u) < 1$. Only terms with same parity as m and $m+1$ appear in the sum terms of, respectively, ce_m and se_{m+1}.

When the solution is stable it means that its values over time tends to 0 or are bounded spatially within a finite volume when time t tends to infinity [McL47, p. 59]. The set of parameters (a_u, q_u) for which a single particle is on a stable trajectory are represented by the blue area in figure 1.4a. In the contrary, when the parameters are chosen so the working condition is not represented in the blue stable are, the solution of the Mathieu equation – and consequently the trajectory of the particle – is coined unstable. "A solution is defined to be unstable if it tends to $\pm\infty$ as $t \to \infty$" [McL47, p. 59], or at any time reasonably small with respect to ion trapping experiments, would I add.

1.2.3 Natural/Secular oscillating frequencies

Replacing τ by its definition (Eq. 1.15) in the Mathieu functions u (Eq. 1.17), it is possible to see that $u(\tau, q_u)$ is a sum of cos and sin functions all with arguments of the form $\frac{1}{2}(m+\beta)\Omega t$, with m an integer so that $2n = m$ or $2(n+1) = m$. The solution $u(t)$ is thus characterised by an infinite sum of oscillating terms with pulsations

$$(\omega_u)_m = \frac{1}{2}(2n \pm \beta_u)\Omega \text{ and } (\omega_u)_m = \frac{1}{2}(2(n+1) \pm \beta_u)\Omega. \quad (1.19)$$

Then the smallest order term ($m = 0$)

$$\boxed{(\omega_u)_0 = \frac{\beta_u \Omega}{2}} \tag{1.20}$$

is defined as the motion secular frequency, characteristic frequency of ion confinement motion. The value for β can be determined using the following relationship

$$\beta^2 = a_u + f(\beta, a_u, q_u) + f(-\beta, a_u, q_u) \tag{1.21}$$

with the following generalised continued fractions

$$f(\beta, a_u, q_u) = \cfrac{q_u^2}{(\beta+2)^2 - a_u - \cfrac{q_u^2}{(\beta+4)^2 - a_u - \cfrac{q_u^2}{(\beta+6)^2 - a_u - \ddots}}} \tag{1.22}$$

$$f(-\beta, a_u, q_u) = \cfrac{q_u^2}{(\beta-2)^2 - a_u - \cfrac{q_u^2}{(\beta-4)^2 - a_u - \cfrac{q_u^2}{(\beta-6)^2 - a_u - \ddots}}}. \tag{1.23}$$

Details on how to solve this equation are given in the appendix B. Also, an experiment dedicated to measuring those secular frequencies through parametric excitation is described below subsection 2.3.

1.2.4 Stability domain in a linear quadrupole trap

Considering a trap with two set of rods with two radio-frequency fields, it is required to consider that the trapped ion motion is set by two Mathieu equations, one for each radial direction (x and y). So there are two stability domains in which it is required to be at the same time for the trap to be really confining the ion. Nevertheless, as the voltages are in phase opposition for each set of rods, the solutions are the same simply with a π phase difference. In term of stability domain, it is equivalent to superimposing twice the same diagram from figure 1.4a, with one of them flipped around the q axis. Also, very often in ion trapping, the trapping parameters are chosen so the solution of Mathieu equation is of order $\nu < 1$, which is the stability area near the point $(a_u, q_u) = (0, 0)$. To have a stable trajectory it is then required that the trapping parameters lie within the superimposed area of the stability diagram, so the solution for each Mathieu equation is stable. This superimposed stability diagram is represented in figure 1.4b. See appendix B for details on how to establish the stability diagram.

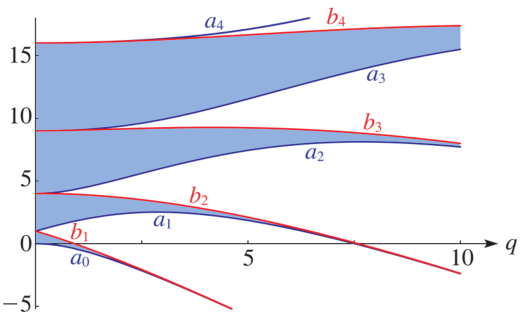

(A) The first nine characteristic values for a Mathieu equations represented in the space of stability parameters (q_u, a_u). The stability of a trapped particle is ensured as long as the stability parameters are choosen within the area bounded by the characteristic values – in blue. Adapted from Olver et al. [Olv21].

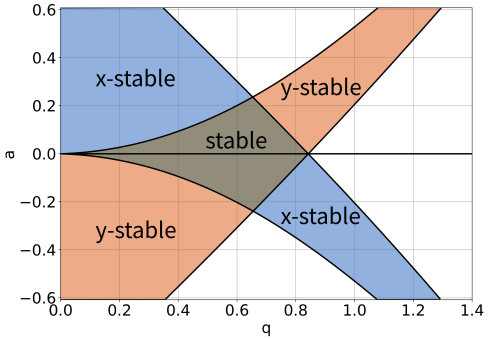

(B) Stability diagram representing the domain for which a particle is stable in the trap, depending on the stability parameters (a_u, q_u). Only the stability domain in the vicinity of the origin is represented. This stability diagram is the combination of the two stability diagrams, each for the Mathieu equation 1.12 in x and y.

FIGURE 1.4: The characteristic values of Mathieu equation and the corresponding stability domain.

1.3 Adiabatic approximation and the pseudo-potential

While the trapped ion is immersed in a radio-frequency field and its motion is thus driven by it, the above considerations on ion dynamics also highlights the existence of the secular motion. Depending on the choice of the parameters (a_u, q_u), both coexist with more or less relative amplitude. Nevertheless, there is a framework, called the adiabatic approximation, in which the radio-frequency driven motion amplitude is much lower than that of secular motion. In this approximation, the secular motion $\mathbf{R_0}(t)$ at frequency $\omega/2\pi$ is responsible for what is called the **macromotion**, while the radio-frequency driven motion $\boldsymbol{\mu}(t)$ at frequency $\Omega/2\pi$ is called **micromotion**. This adiabatic approximation is demonstrated acceptable for $|q_u| < 0.4$, $|a_u| \ll |q_u|$. In this case, the value for β can be taken as

$$\beta_a = \sqrt{\frac{q_u^2}{2} + a_u}, \tag{1.24}$$

and the secular frequency can be written as

$$\omega_u \approx \frac{\Omega}{2}\sqrt{\frac{q_u^2}{2} + a_u}. \tag{1.25}$$

For $a_u = 0$, the secular frequency can be written as

$$\omega_u \approx \sqrt{2}\frac{q_e}{mr_0^2\Omega}U_{RF}.$$

Comparing β_a with its exact value from continued fraction β (Eq. 1.21), no more than a 5% difference was observed for $q = 0.4$ (Fig. 1.5).

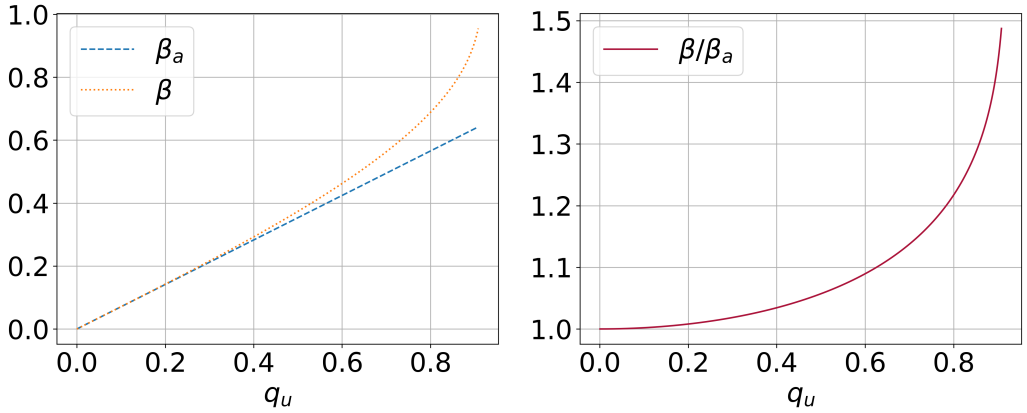

FIGURE 1.5: Comparison of two computations of β parameters, in the general case, and the adiabatic case.

The adiabatic approximation can be understood as a synonymous of gradual perturbation approximation. To have a clear idea of how this translates for a trapped ion, I could not find a better illustration than that of Griffiths [Gri18], introducing the concept by the following explanation

> Imagine a perfect pendulum, with no friction or air resistance, oscillating back and forth in a vertical plane. If I grab the support and shake it in a jerky manner, the bob will swing around in a wild chaotic fashion. But if I *very gently and steadily* move the support, the pendulum will continue to swing in a nice, smooth way, in the same plane (or one parallel to it) with the same amplitude. This *gradual change in the external conditions* characterises an adiabatic process.

This can be understood if the analogy is done as follows : the support is moved by the micromotion, and the pendulum by the macromotion. For the pendulum, everything is happening as if it was oscillating in a constant field. As do the ion in the adiabatic approximation : when the secular frequency is for much greater amplitude than that of the radio-frequency driven motion, it is possible to replace the radio-frequency potential in which the ion oscillates by a pseudo-potential. A synthetic approach is developed below but a detailed derivation can be found in appendix C.

1.3.1 Pseudo-potential derivation

Given the adiabatic approximation, the proper definition for the motion of an ion *i* in this framework starts with splitting it in two contributions, one slow contribution $\mu(t)$ that can be considered invariant during a period of the second contribution $\mathbf{R_0}(t)$, and it can be written as

$$\mathbf{u}(t) = \mathbf{R_0}(t) + \mu(t) \tag{1.26}$$

$$\mathbf{u}(t) = \mathbf{R_0}(t) - \varepsilon(t)\sin\Omega t \tag{1.27}$$

with $\varepsilon(t) = \frac{q_e}{m\Omega^2}\mathbf{E}(t)$. Immersed in a non uniform and alternating field, the charged particle would behave accordingly to the Newton's equation so that

$$m\frac{d^2}{dt^2}\mathbf{u}(t) = q_e\mathbf{E}(\mathbf{r}(\mathbf{t}))\sin\Omega t = m\varepsilon\sin\Omega t. \tag{1.28}$$

The idea is now to derivate twice the equation 1.27, in order to combine it with equation 1.28. This computation can be found in appendix C, with details about the adiabatic approximation. This leads to the following result

$$\boxed{m\frac{d^2}{dt^2}\mathbf{R_0} = -\nabla\frac{q_e^2}{4m\Omega^2}\mathbf{E_0}(\mathbf{R_0})^2 = -\nabla\Psi^*} \tag{1.29}$$

with

$$\boxed{\Psi^* = \frac{q_e^2}{4m\Omega^2}\mathbf{E_0}(\mathbf{R_0})^2} \tag{1.30}$$

the pseudo-potential.

In the pseudo-potential approximation, everything is happening as if the slow macromotion, is governed by this static pseudo-potential Ψ^*. The expression for the pseudo-potential is equivalent to the average micromotion kinetic energy over a trapping field period, so that

$$\overline{E_{kin}} = \overline{\Psi^*} = \frac{1}{2}m\overline{(\Omega\varepsilon\cos\Omega t)^2}. \tag{1.31}$$

1.3.2 Motion in the pseudo-potential

Inserting the basic decomposition (Eq. 1.26) into the Mathieu equation (Eq. 1.12), it is possible to determine a motion equation for a trapped ion in the pseudo-potential (using Eq. C.19). The solution to Mathieu equation can be written as

$$\boxed{u(t) = A_u\cos(\omega_u t + \phi_u)\left(1 - \frac{q_u}{2}\cos\Omega t\right)} \tag{1.32}$$

with $\omega_u = \beta_u\Omega/2$, A_u and ϕ_u arbitrary amplitude and phase depending on initial ion condition.

1.4 Axial potential

1.4.1 Quadratic axial potential with endcaps

The quadrupole geometry presented in section 1.2 and illustrated with figure 1.1 is not confining axially as it is wide open on its extremities. To solve this inconvenient, end electrodes polarized with static voltages are placed at each extremity of the trap. This will produce a quadratic potential along the z-axis, but unfortunately, this static axial potential will also display a non-zero component over the radial directions. The axial confining potential can be retrieved in the same manner as the radial potential, solving Laplace equations.

The axial potential is

$$\boxed{\Phi_{DC}(x,y,z) = \frac{\kappa V_{DC}}{2d_0^2}(2z^2 - x^2 - y^2).} \tag{1.33}$$

with $2d_0$ the length of the central part of the trap[2], V_{DC} the electric static potential applied between those electrodes, κ an efficiency factor accounting for the endcaps and trap design.

1.4.2 Modified quadratic potential in `GiantMol`

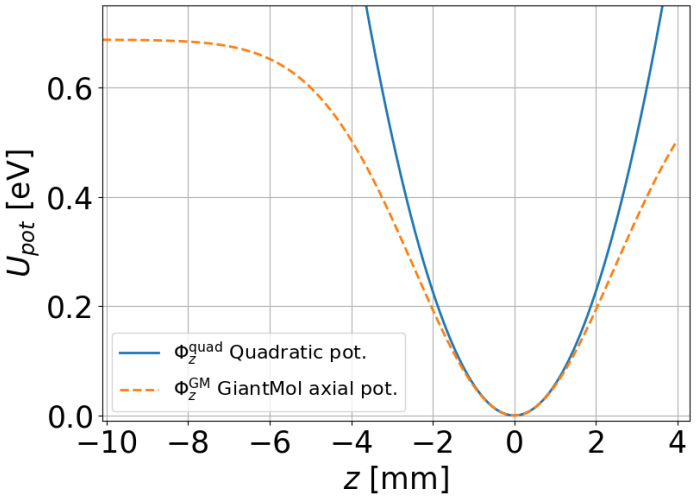

FIGURE 1.6: Comparison of theoretical ideal quadratic axial potential with the actual trap generated by the `GiantMol` geometry.

The above potential is often met in other typical ion traps with planar electrodes serving as axial endcaps, the generated potential is quadratic and obeys equation 1.33. Nevertheless, due to the fact that the axial potential is produced by the cylindrical rods themselves, the axial potential in `GiantMol` is slightly smaller from the ideal quadratic potential. A reproduction of `GiantMol` geometry in the software SIMION allows for the representation of the axial potential, and especially the retrieval of an analytical fit. The axial potential can be modelled as

$$\Phi^{\star}_{DC}(z) = U_{DC} m\omega_z^2 L^2 \left(1 - \exp\left(-\frac{z^2}{2L^2}\right)\right) \tag{1.34}$$

with $L = 2.45$mm a characteristic length given by the fit. The potential seemingly acts as a quadratic potential at its bottom centred on the trap, while it saturates to a constant value at its edges. A comparision of the axial potential with the quadratic ideal potential is showed in figure 1.6. At $z_1 = \pm 1.5$ mm[3], the modified potential $\Phi^{\star}_{DC}(z_1) = 117$ meV and the ideal quadratic potential $\Phi_{DC}(z_1) = 128$ meV. The ratio ${}^{\Phi_{DC}(z_1)}/_{\Phi^{\star}_{DC}(z_1)}$ is 1.095. At $z_1 = \pm 0.4$ mm[4], the ratio ${}^{\Phi_{DC}(z_1)}/_{\Phi^{\star}_{DC}(z_1)}$ is 1.006. In the following, when dealing with axial potential for the trapped ions, only the quadratic potential is considered, unless otherwise stated.

[2] Or the axial distance between the end electrodes if relevant.
[3] Initial position of the giant molecule in the numerical simulations.
[4] Maximum extension of the simulated clouds.

The potential energy of a charged particle immersed in such field can be written as

$$E_{pot}(x,y,z) = q\Phi_{DC}(x,y,z) = \frac{1}{2}m\omega_z^2(2z^2 - x^2 - y^2) \tag{1.35}$$

$$\omega_z = \sqrt{\frac{2\kappa q_e U_{DC}}{m d_0^2}} \tag{1.36}$$

with ω_z the natural frequency over the z-axis of the particle in the axial static potential.

1.4.3 Modified stability parameter

It is then possible to define a parameter a_z accounting for the static axial potential, in an analogous fashion to the a_u parameter accounting for the presence of a static offset in the alternating field. The parameter a_z can be defined as

$$a_z = \widetilde{a_z} \overset{\text{def}}{=} \frac{8\kappa q_e U_{DC}}{m d_0^2 \Omega^2} = \frac{4}{\Omega^2}\omega_z^2 U_{DC}. \tag{1.37}$$

In the case of `GiantMol` trap, the axial confinement is ensured by the segmented extremities of the rods. In accordance with geometry presented in figure 1.7a, a static voltage is added to the outer part of the segments (Fig. 1.7b). Here, a careful attention to the choice for the sign of V_{DC} should be paid, as it must be of the same sign of the particle charge in order to properly trap along the z-axis.

1.5 Complete 3D potential and stability parameters

1.5.1 Trapping potential

The `GiantMol` trap design is showed in figure 1.7. Making the hypothesis that the potential in any part of the trap is the sum of the potentials produced by the radial and axial potentials, we can finally write the total potential produced by our linear quadrupole trap as

$$\Phi(x,y,z,t) = \Phi_{Rad}(x,y,t) + \Phi_{DC}(x,y,z) \tag{1.38}$$

$$\Phi(x,y,z,t) = \frac{U_{st} + U_{RF}\cos\Omega t}{2r_0^2}(x^2 - y^2) + \frac{\kappa V_{DC}}{2d_0^2}(2z^2 - x^2 - y^2). \tag{1.39}$$

It appears that a convenient formulation of this combination can be done considering ion stability. The natural frequencies and stability parameters must be computed in a modified form to account for the axial trapping static potential. It is noticeable that the static potential is breaking symmetry because it introduces the same static contribution in each radial direction, while the alternating field is in phase opposition. The new trapping parameters are as follows

$$\boxed{\widetilde{a_u} \overset{\text{def}}{=} a_u - \widetilde{a_z}} \tag{1.40}$$

and the natural frequencies are as follows

$$\omega_r = \widetilde{\omega_u} = \sqrt{\omega_u^2 - \frac{1}{2}\omega_z^2} \approx \frac{\Omega}{2}\sqrt{\frac{q_u^2}{2} + a_u - \frac{1}{2}\widetilde{a_z}} \tag{1.41a}$$

$$\omega_z = \sqrt{\frac{2\kappa q_e U_{DC}}{m d_0^2}}. \tag{1.41b}$$

Because $\sqrt{x} \Rightarrow x \geq 0$, equation 1.41a implies that $\frac{q_u^2}{2} + a_u - \frac{1}{2}\widetilde{a_z} \geq 0$. In case this condition is not satisfied the trap will not confine.

Also, from those considerations, it is possible to update Mathieu equation 1.12. The reader is sent to subsection 1.2.1 for the definition of pure radial parameters. One important comment about the trajectory of the ions, considering either the analytical solution $u(\tau)$ in adiabatic approximation, or the pseudo-potential approximation, is that the trajectory of the single ion is periodical. This means that there is conservation of energy, i.e the total energy of the *single trapped ion* is constant [Ryj05]. Measurement of those natural frequencies are discussed in subsection 2.3.

1.5.2 `GiantMol` electrodes design and electric supply

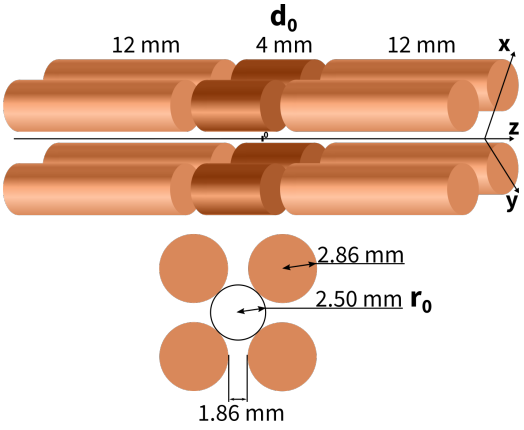

(A) Trap dimensions. Each rod is segmented in three parts. Ions are confined in the inner central part.

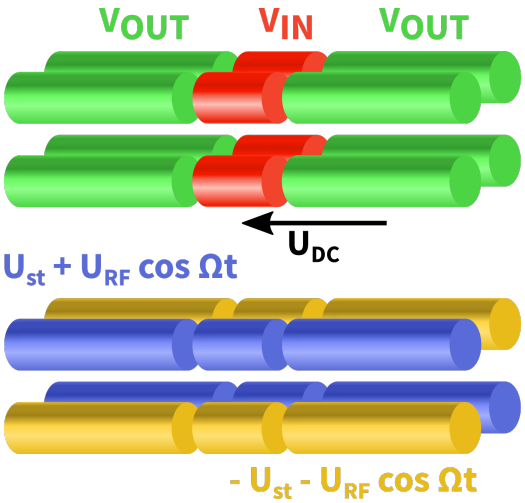

(B) Electric feed scheme. Top : a static voltage is applied differentially between outer and inner part of the trap (green and red). Bottom : a radio-frequency voltage is applied to diagonal pair of rods (blue and yellow) in phase opposition.

FIGURE 1.7: Linear quadrupole trap design and electric feed scheme.

The trap used in `GiantMol` experiment is a linear quadrupole trap supplied with electric fields. The trap is made of four cylindrical rods, segmented in three parts (Fig. 1.7). Two set of voltages are applied to the trap in order to provide radial and axial confinement. The

radial confining potential is made of a radio-frequency voltage applied to diagonal pair of rods, each of them in phase opposition. The rods are segmented so that their outer parts can be used to confine ions axially by applying a static voltage difference with respect to the central part. The rod dimensions and spacing are chosen in accordance with the remarks in subsection 1.6.1 in order to minimise the deviation from the ideal quadrupolar trapping field. Ions are stored in the short central part.

The quadrupole trap is surrounded by multiple apparatuses designed to ensure its proper working, control, and observation. In order to understand the measurements carried out, the important details on the trap environment are given in the next chapter 2.

1.6 Sources of deviation from the equations

1.6.1 Rods shape

Being cylindrical, the rods produce in most cases higher order fields whose effects are minimized by carefully choosing a geometry so that the rods radii is $r = 1.148 r_0$ [Daw76, Chapter 5, p116] (The higher order terms for potential, and the justification on why electrode surfaces should not be cylindrical, are given in section dealing with multipole expansion, page 22).

1.6.2 Segmented design

The choice of segmented rods rather than endcaps for axial confining is made in order to improve the opening along the z-axis, better for laser and molecule injection. While the central part of the trap is $z_0 = 4$ mm long, the equivalent length for the axial potential is less clear. This problematic can be circumvented by taking into account a geometric constant and applying it to the field computed as if the length was that of the central part of the trap. This geometric constant is introduced in the equation 1.33 as κ, and the variable used as trap length z_0 is the length of the central part of the trap. The careful measurement of this constant κ is an essential parameter in order to properly describe the ion motion. Furthermore, it is possible to simulate the potential in a finite element software such as SIMION. The `GiantMol` geometry has been reproduced and an expression for the axial potential retrieved. Again, with a fit it is possible to recover an equivalent length for the central part of the trap.

1.6.3 Rods asymmetry

In case the rods are not perfectly collinear, excess micromotion can appear [Ber98].

Chapter 2

Real trap design

In this chapter, a first overview of the experimental setup is given. A basic description of the trapped ions as a two level system is given, along with their environment. The fluorescence detection layout is given. First experiments in order to characterise the trap are presented.

2.1 Laser cooling for Ca^+ ions

2.1.1 Three-level cooling scheme

In our experiment, laser cooling is done on $^{40}Ca^+$ ions. This species was chosen in the past when the team was created and since then all lasers and equipments are appropriated to this species. The number 40 isotope is convenient because it is by far the most abundant of the Calcium isotopes – 96.941 % – and has no hyper-fine structure. Its energy levels are showed in figure 2.1. The used transitions are described below and their main properties summed up in table 2.1. The laser sources required to cool $^{40}Ca^+$ are at 397 nm and 866 nm wavelength and are available commercially.

In order to cool $^{40}Ca^+$ ions through resonant radiation pressure (see subsection 4.1), a transition from the ground state must be chosen. It is useful to choose the excited state with the shortest lifetime so a maximum of photons can be absorbed in a given period of time, leading to the strongest radiation pressure. The $S_{1/2} \rightarrow P_{1/2}$ is a good candidate and is the chosen transition. A 397 nm laser is used to excite the transition to the $P_{1/2}$ level with lifetime 6.904 ns [Het15]. Yet its de-excitation probability is shared between ground state $S_{1/2}$ and the meta-stable level $D_{3/2}$ in a ratio of approximately 15 : 1 [Ram13]. The $D_{3/2}$ level with lifetime 1.176 s [Kre05] is a "sink" for the ions because once in this state they do not contribute to the $S_{1/2} \rightarrow P_{1/2}$ cooling transition, thus they are not cooled any more. In order to make the ions available for the cooling transition, another laser is used to deplete the $D_{3/2}$ level. A 866 nm laser is used to serve this purpose. It is often referred as re-pumping beam, as it re-pumps atoms to the $P_{1/2}$ state. More details on laser cooling and detection can be found in chapter 4.

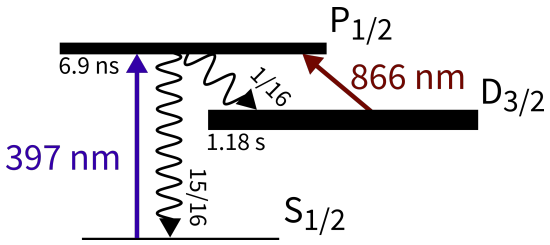

FIGURE 2.1: $^{40}Ca^{+}$ relevant energy levels for laser cooling and the appropriate laser wavelengths. The transition probabilities, given as decimal ratios are approximative.

2.1.2 Laser injection

The two lasers for ion cooling are injected in windows located around the trap, at the same level. Two windows along the z-axis allow to inject the lasers along this axis. It is possible to use windows located over axis at 30° with respect to z-axis for laser injection or any other optical requirement. More details on laser cooling and setup are given in section 4.4. Because laser cooling, ions are fluorescent at the 397 nm wavelength.

2.2 Trap environment

2.2.1 Trap electric supply

The ion trap is supplied with two Stahl-electronics® devices, HF-DR 1.5A for radio-frequency supply and BS 1-16-16 for DC supply.

2.2.2 Vacuum chamber and fluorescence detection

The trap is placed in a vacuum chamber where a pressure of 10^{-9} mbar is sustained by an Agilent Technologies® ionic pump, model Diode VacIon Plus 300. This vacuum chamber is built with several windows in order to observe the ions fluorescence. The fluorescence of the Ca^{+} ions is collected through the above window by a Nikon® Series MM (Measuring Microscopes) $\times 10$ objective with 49 mm of working distance. The objective is located 50 mm above the trap axis, collecting a light cone of 0.362 steradians, similar to the light cone the trap rods are letting go through. The image from this objective is filtered by two optical elements in a cage. A notch filter centred at 397 nm is placed before a 50/50 beam splitter. One optical path is sent to a Tucsen® camera model Dhyana 400BSI v2, and the other is sent to a Hamamatsu® photomultiplier model H10682-210. Thanks to a last lens located before the beam splitter, the whole detection apparatus provides a $\times 12 \pm 1$ optical magnification for the camera.

The collection efficiency ζ of the ion-to-photomultiplier part is the product of the efficiency of each of the three optical parts between the ions and the photomultiplier : the

TABLE 2.1: Transition properties for the 40 Ca^{+} ion.

Transition	Type	Wavelength [nm]	Frequency [THz]	Width [MHz]
$S_{1/2} \rightarrow P_{1/2}$	Electric dipole	397	755.222766 [Wan14]	21.57 [Het15]
$D_{3/2} \rightarrow P_{1/2}$	Electric dipole	866	346.000235 [Geb15]	1.482 [Het15]

collection objective and the optical path in the cage (common to both photomultiplier and camera), and the photomultiplier, so that

$$\zeta = \prod_n \eta_n \tag{2.1}$$

$$= \eta_1 \times \eta_2 \times \eta_3 \tag{2.2}$$

$$= 0.0288 \times 0.9 \times 0.305 \tag{2.3}$$

$$\zeta = 7.9 \cdot 10^{-3} \tag{2.4}$$

with $\eta_1 = 0.0288$ the collection efficiency of the objective, $\eta_2 = 0.9$ the estimated efficiency of the optics between the objective and the photomultiplier and $\eta_3 = 0.305$ the photomultiplier efficiency given at 400 nm.

2.2.3 Computer control

Several apparatuses are controlled or read with a computer. The independent trap supply units can be remotely controlled by a computer with LabVIEW ®[1] softwares. The fluorescence reading is also carried out with the same computer, on a LabVIEW ®software, also able to tune the laser frequency (piezo). The camera is read with a custom software provided with the camera by the same company.

2.3 Parametric excitation

As already explained in section 1.3, the motion of ions can be described as an infinite sum of oscillating terms (subsection 1.2.3). In order to measure the secular frequencies at which the ion cloud oscillates, it is possible to excite the cloud with a small amplitude oscillating field in the vicinity of the trap [Ved90]. This tiny excitation is called "tickle", or parametric excitation. When the excitation oscillates with a frequency close enough to one of the motion frequencies, a resonant phenomenon amplifies the ion's oscillatory motion amplitude and their fluorescence is significantly perturbed. This way it is possible to characterise and diagnose the trap, by then comparing the measured motion frequencies with the expected frequencies from equation 1.19. The determination of the geometrical factor κ in equation 1.37 can be done by comparing a spectrum measured with this method to theoretical values. Trapping potential asymmetries can be investigated and parasitic external potentials or symmetry breaking can be identified.

To properly measure frequencies through an applied tickle with a non destructive method, ions should be laser cooled in order to be fluorescent. This fluorescence should be constant over time, except when the tickle frequency is close to a motional frequency. The tickle amplitude V_{tickle} is chosen small enough to be considered as a perturbation of the trapping field $V_{tickle} < U_{DC}$. The measured frequencies are usually proportional to $n'\Omega$ and $n\omega_u$, with $n \in \mathbb{N}$, $n' = n/2$, and $u = x, y$ or z [Ved90]. They can also be a combination of

[1] https://www.ni.com/fr-fr/shop/labview.html

TABLE 2.2: Reference values for trapping potential, tickle, and fluorescence acquisition.

U_{RF} [V] | q_r	42.43 | 0.394	V_{tickle} [V]	0.7
U_{DC} [V] | a_z	$(1/-1.5/1)$ | $7.85 \cdot 10^{-3}$	$f_{tickle}\|\delta f$ [kHz]	$[0;500]\|0.1$
$\Omega/2\pi$ [MHz]	2.05	T_{int} [ms]	250

TABLE 2.3: Comparison of parameters from the voltages set during the experiment of Fig. 2.2 and the predicted values.

	Measured	Expected
$\omega_x/(2\pi)$ (kHz)	281.5	270.6
$\omega_y/(2\pi)$ (kHz)	305.9	270.6
$\omega_z/(2\pi)$ (kHz)	130.9	see footnote[a]

[a] The computation of the expected ω_z value relies on a predetermined value for κ that is obtained through potential fitting with SIMION. Otherwise determining the experimental value for κ requires to *measure* ω_z. In `GiantMol`, $\kappa = 0.227$, and for $U_{DC} = 1$ V, $\omega_z = 90807$ Hz.

secular frequencies such as $n\omega_x \pm \omega_z$ with $n = 2$ or $n = 3$, or combination of secular frequencies with the radio-frequency ($\omega_z + \Omega$ for instance). Subharmonics such as $\omega_z/2$ are also reported [Ved90]. The measured frequencies can also be linear combinations of $n_u\omega_u$ such as $\sum_u n_u\omega_u = \Omega$ [Tab12].

2.3.1 Methodology

The following analysis focuses first on the measurement of frequencies for fixed trapping voltages and cooling parameters – laser frequencies, power, alignment. The tickle frequency is applied to the electron gun Wehnelt located below the trap by an Agilent® signal generator model 33220A, with device specifications for the frequency precision of 1% and the voltage precision of 5% on the peak amplitude. The following set of parameters of tables 2.2 was first applied in order to retrieve the data presented in figure 2.2. It highlights the several parameters to control when carrying out parametric excitation frequency measurement. In such configuration, the calculated and measured (see Fig. 2.2) frequencies are as follows in table 2.3.

The tickle frequency is swept from 0 to 500 kHz, with frequency resolution $\delta f = 0.1$ kHz, and with integration time at each frequency step of $T_{int} = 250$ ms. With 250 ms of integration time the background light level is 13000 counts. No parametric resonance is detected outside from the [100;400] kHz range. Four main fluorescence drops are observed and are associated each with a secular frequency. The computation of the frequencies (Eq. 1.41) allows to associate the measured fluorescence peaks to the secular frequencies. The association of radial frequencies with axis x or y is here arbitrary, chosen to be $\omega_x < \omega_y$ [Poi18].

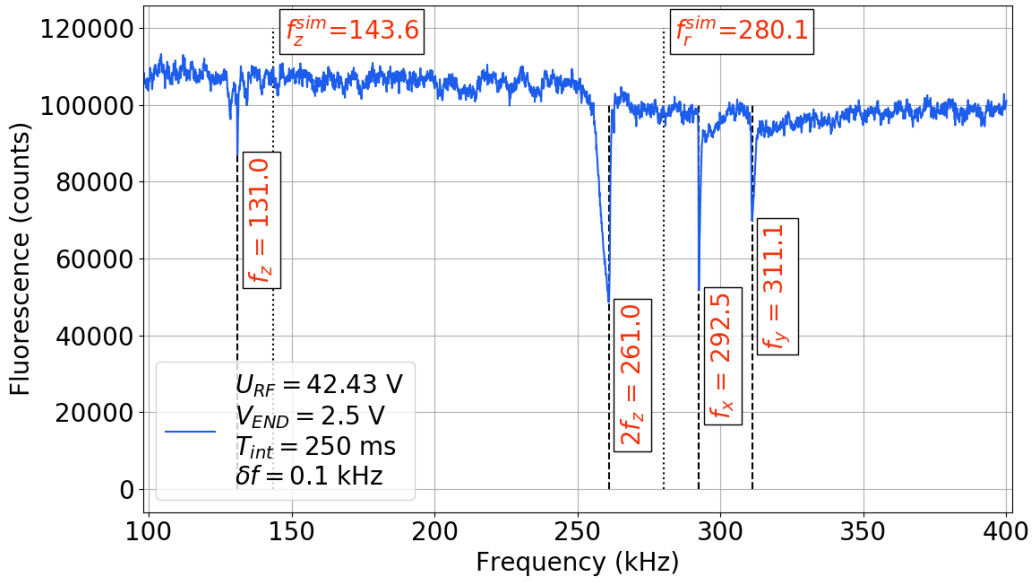

FIGURE 2.2: Tickle frequency response of a trapped ion cloud under constant trapping field amplitude. The fluorescence is integrated over 250 ms, the background light level is at 13000 counts at this integration time. The frequency resolution is δf_{tickle} = 0.1 kHz.

2.3.2 Measurement under variation of axial confinement potential

Determination of geometric factor κ with f_z

Measuring the tickle frequencies for several different axial potentials allows for the determination of the geometric factor. In figure 2.3 are represented the measured tickle frequencies for the eight different values of axial confinement tested at the beginning of this thesis [2]. The measurement of $2f_z$ as a function of U_{DC} are represented as the red elements in Fig. 2.3. As f_z depends itself on $\sqrt{\kappa U_{DC}}$ (Eq. 1.41) it is possible to carry out a square root fit $g = g_0(\kappa)\sqrt{U_{DC}}$ and retrieve the unknown κ value with the parameter g_0 given by the numerical fit. Theoretical f_z values deduced from equations 1.41 and theoretical geometric parameter deduced from SIMION $\kappa^{SIMION} = 0.270$ are represented as the dotted line. In order to speed up the measurement and ensure data consistency in regard of amplitude stability, $2f_z$ was measured so the frequency sweep could be shortened. This last statement implies $g = 2f_z$, thus $g_0(\kappa)/2$ is the right parameter to compute κ

$$f_z = \frac{1}{2\pi}\sqrt{\frac{2q_e\kappa}{md_0^2}}\sqrt{U_{DC}} \tag{2.5}$$

$$g = 2f_z = g_0(\kappa)\sqrt{U_{DC}}. \tag{2.6}$$

Comparing $g_0(\kappa)/2$ with $\frac{1}{2\pi}\sqrt{\frac{2q_e\kappa}{md_0^2}}$ leads to the following formula for κ

$$\kappa = \frac{g_0^2\pi^2 md_0^2}{2q_e}. \tag{2.7}$$

[2] May 2018

In the case of `GiantMol`, the experimental value for the geometric factor is $\kappa = 0.227$. The experimental value deviates from the geometrical value deduced from a SIMION fit by 16%.

Furthermore, when considering the measured axial frequencies, they are lower than the theoretical ones (see dotted line of Fig. 2.3). The ions behave as if the axial potential was weaker than the expected one. The effect of the space charge is expected to produce such behaviour [Ved91] because approximately a thousand ions or more were trapped. The electron gun was disabled during those tickle experiments.

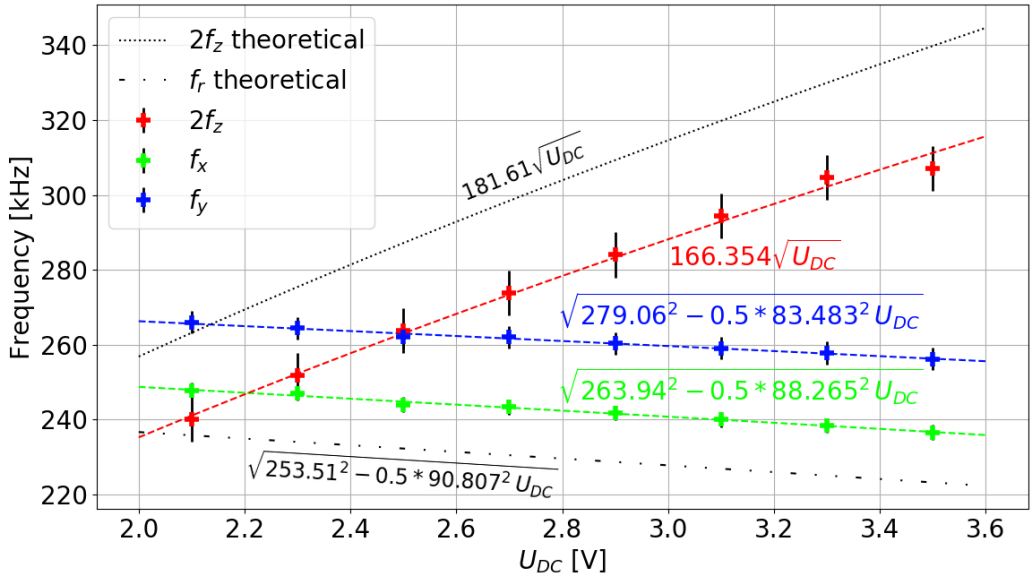

FIGURE 2.3: Measured tickle frequencies for several axial confining voltages U_{DC}. The radio-frequency is set to U_{RF} = 37.5 V amplitude, 2.045 MHz. The tickle is set to V_{tickle} = 1.5 V. The acquisition time is 100 ms per tickle frequency step. The coloured crosses are frequency measurements. Dashed lines are square root fits of the appropriate data. Please note that $2f_z$ is measured and fitted. The dotted and dot-dashed lines are expected values from formula with ideal values, in particular the expected f_z value is computed with the ideal κ^{SIMION}. The error bars are retrieved from the fluorescence peaks FWHM.

Considerations on the radial frequencies

According to equations 1.41 it is expected that the radial frequencies vary a little bit when the axial potential changes. This is due to the deconfining character of the axial field with respect to the radial field. The equations 1.41 allow to determine the expected values for f_x and f_y, considering the *real* experimental geometric factor κ (see dashdotted line of Fig. 2.3). Numerical fits of the form $h = (h_0^2 - 0.5 h_1^2 U_{DC})$ with h_0 and h_1 the fit parameters, allows for the determination of the radial frequencies.

$$f_r = \sqrt{f_u^2 - \frac{1}{2} f_z^2} \tag{2.8}$$

$$h = f_r = \sqrt{h_0^2 - \frac{1}{2} h_1 U_{DC}}. \tag{2.9}$$

Nevertheless, the two measured radial frequencies are different and both vary from the reference theoretical value. More precisely the theory underestimates the frequencies, as if the radial potential was stronger than the theoretical one. This could indicate a contact potential or any asymmetry regarding potential or rod geometry. Indeed, if a contact potential raises the electric field over one direction, the frequency is changed with respect to the frequency observed in the direction where the contact potential is different.

Also, the difference separating both radial frequencies turns out to be proportional to U_{DC}. This indicates the effect of the axial potential is not the same over each radial direction. Again this would indicate a static potential symmetry problem.

2.3.3 URF varies

Furthermore, varying the radio-frequency amplitude has allowed to control the stability of axial and radial tickle frequencies (Fig. 2.4). According to the equations 1.41, the axial frequency should not vary in that case, while the radial frequency should also depend on the amplitude of the radio-frequency field. Radio-frequency amplitudes ranging from 30.2 V to 47.6 V – q ranging from 0.28 to 0.44 – were tested. Figure 2.4 shows that the difference between both radial frequencies, f_x and f_y, reduce when the radio-frequency amplitude U_{RF} increase. This gap is at maximum 17%. The difference between the measured radial frequencies and the theoretical predicted provided the adiabatic approximation increase when the radio-frequency amplitude U_{RF} increases. The axial frequency measured remain quite constant for the values tested except the smaller one, in that case the measured axial frequency is distant from the other one by two times the error bar.

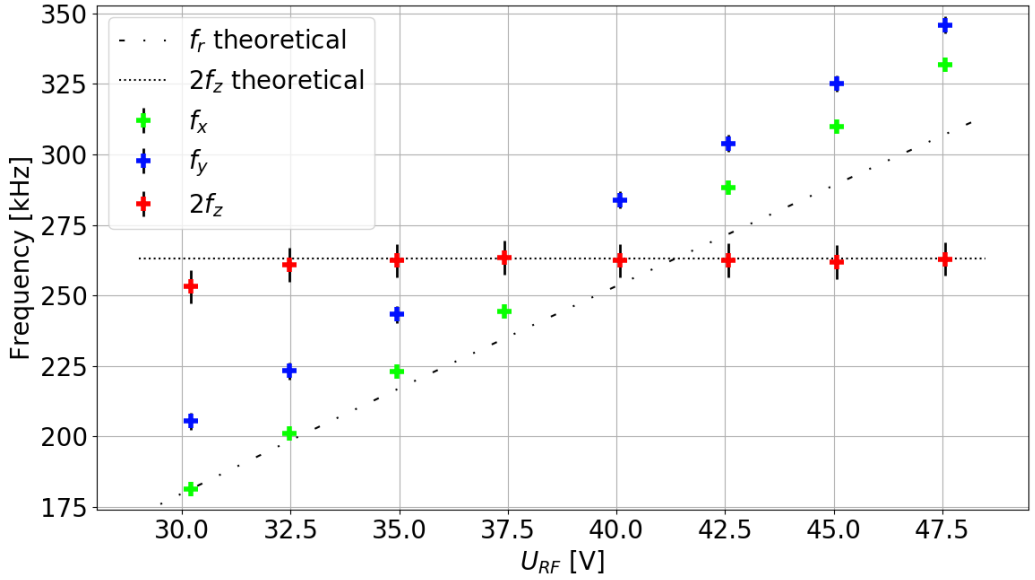

FIGURE 2.4: Measured tickle frequencies for several radial confining amplitudes U_{RF}. The axial potential is set to U_{DC} = 2.5 V amplitude, the radio-frequency $\Omega/2\pi$ = 2.045 MHz. The tickle is set to V_{tickle} = 1.5 V. The acquisition time is 100 ms per tickle frequency step. The coloured crosses are frequency measurements. Please note that $2f_z$ is measured and fitted. The black dotted and dash-dotted lines are expected values from formula with ideal values, in particular the expected f_z value is computed with the measured κ. The error bars are retrieved from the fluorescence peaks FWHM.

2.4 Contact potential correction

Supposing the trap and field are perfect, with no defect whatsoever, the ions will settle in a position of the field where the potential energy is minimised, in a radio-frequency node. Thus they will experience minimum perturbation. In the case of any defect the ions will be pushed out of this ideal position and be subject to a higher potential than expected, shaking them a little bit more, heating them. With the hypothesis that the defects can be modelled by a static potential applied in the vicinity of the ideal potential, it is possible to estimate its value. This is how a contact potential is defined. It may originate from trap's geometric imperfections or potential imbalances due to charging surrounding electrodes. Rods themselves can be coated due to calcium atoms depositing in some parts, creating surface effects modifying impedance. A top cut view of the trap and its surrounding can be seen figure 2.5. This is also the view from the above detection. Cloud images can be seen figure in 2.7 at the end of this chapter.

In order to determine the position of the ideal center of perfect potential, the ion cloud position for several trapping potentials is measured. This is done with a camera detecting the ion fluorescence under laser cooling. Details on laser cooling and detection are introduced later in this document but are not required to understand the following explanation.

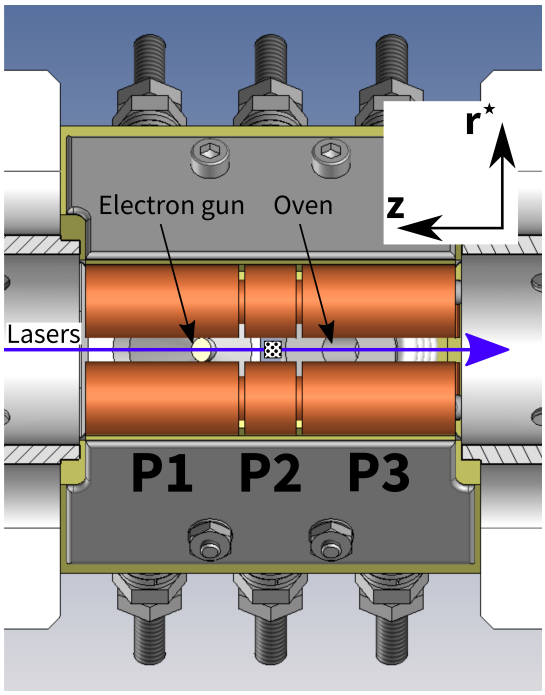

FIGURE 2.5: Top view of GiantMol ion quadrupole trap from the upper viewport where the optical detection is located. The electron gun Wehnelt and oven below the trap are visible. The laser direction is indicated with the purple arrow. The trap segment names are indicated with P signifying Part. P2 is the central segment where the ions are hosted. Laser is going from P1 to P3, while the giant molecules go from P3 to P1. The dot filled area represents the approximate detection field of view.

2.4.1 Axial contact potential

Measuring the position of the ions along the z-axis is the easiest part because of the detection axis being normal to that direction. Furthermore the potential along z-axis is a simple direct voltage, described above as the axial static confining potential. It is thus easy to change this axial potential and retrieve snapshots of ions. Then an elliptical fit (see Box 3.4.1) is carried out to retrieve the ion cloud center position, and cloud size.

Lets say the axial contact potential introduces a force $\mathbf{F_c}$ on the ions trapped in the axial potential applying a force $\mathbf{F_z} = m\omega_z^2(z - z_0)$ over the ions, where z_0 is the ideal cloud position without contact potential ($\mathbf{F_c}(z_0) = 0$). The new equilibrium created by introduction of $\mathbf{F_c}$ is such that $\mathbf{F_c} + \mathbf{F_z} = 0$. Assuming the contact potential originates from a difference of potential V_c between external segments, it is possible to consider them as the two electrodes of a capacitor. Identifying $\mathbf{F_c} = q_e V_c/(2d_0)$ to the force applied to a charge in a capacitor it is possible to write

$$z = \frac{q_e V_c}{2md_0}\frac{1}{\omega_z^2} + z_0. \tag{2.10}$$

A measurement of z against ω_z^{-2} allows to carry out a linear fit and retrieve V_c the potential applied by the equivalent capacitor. The measurement applying the above protocol are summed up in the figure 2.6. The fit retrieves the expression displayed in figure 2.6b. The value deduced for the capacitor voltage is $V_c = -89.569$ mV. The related force applies in the opposite direction of laser, from the direction of the oven.

During the above process, the radial position of the ion cloud is also retrieved and represented as $r^\star$. It is interesting to notice that this value is significantly varying with U_{DC} for the higher values tested. This indicates a potential interplay between z-axis and $r^\star$-axis, nevertheless small enough to be only visible for somewhat high U_{DC} values.

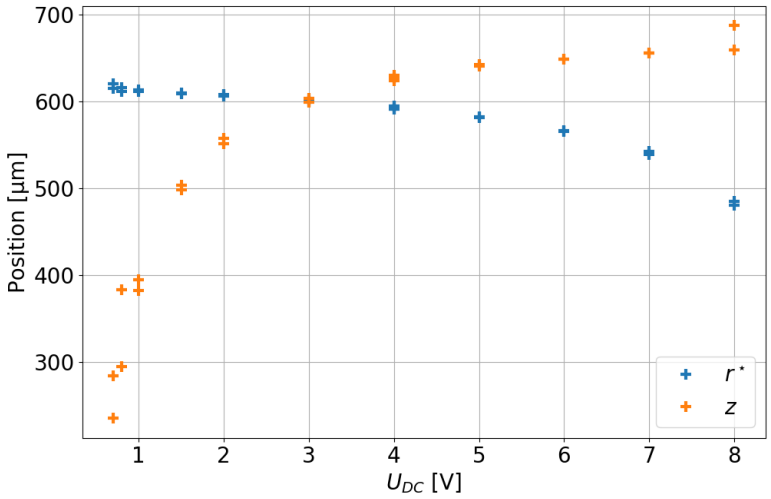

(A) Position of the cloud center relatively to the upper left corner of image, against the axial trapping potential.

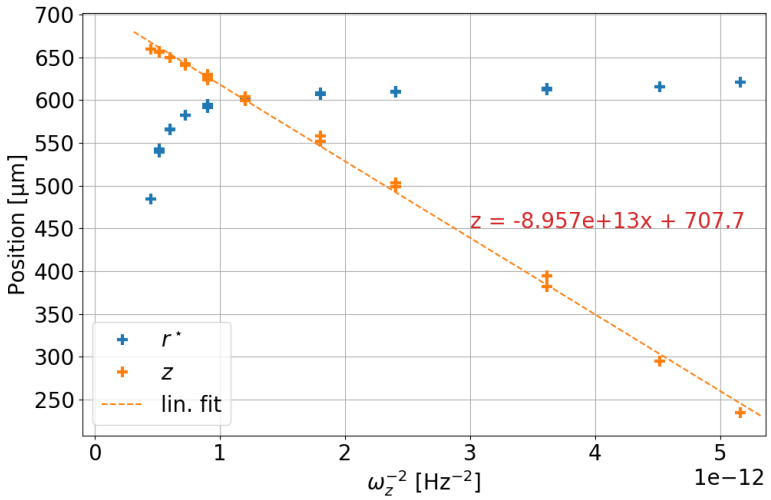

(B) Position of the cloud center relatively to the upper left corner of image, against the square inverse of angular frequency of axial potential.

FIGURE 2.6: Position of the cloud center relatively to the upper left corner of image, against axial potential in volts or angular frequencies. The radio-frequency field amplitude is set to U_{RF} = 27.625 V, with frequency $\Omega/2\pi$ = 2.044 MHz.

2.4.2 Radial contact potential

As seen above, the cloud radial position detected by the camera changes depending on the applied axial potential. It would be handy to measure the contact potential in the radial direction in the same manner as just above. In that case, it is required to vary the radio-frequency amplitude and measure the radial motion of the ion cloud. Nevertheless, the motion of the ion ensemble in a radial direction of the trap may cause a displacement in a direction not coplanar with the object plane of the detection. In that case, the apparent position of the cloud would not change significantly, given a fixed optical detection setup. Nevertheless, in case of such a motion, the image sharpness would also change, which can

be benefited. The strategy developed in Kamsap [Kam15] thesis in order to track the ion motion in a similar case consist in moving the objective in order to keep the image sharp. The ion ensemble position is then deduced from the motion of the objective. The current state of the detection setup in `GiantMol` do not allow to properly track the ions along the optical axis. Alternatively, a second camera could be placed so it observes the cloud in an axis normal to those of the first camera.

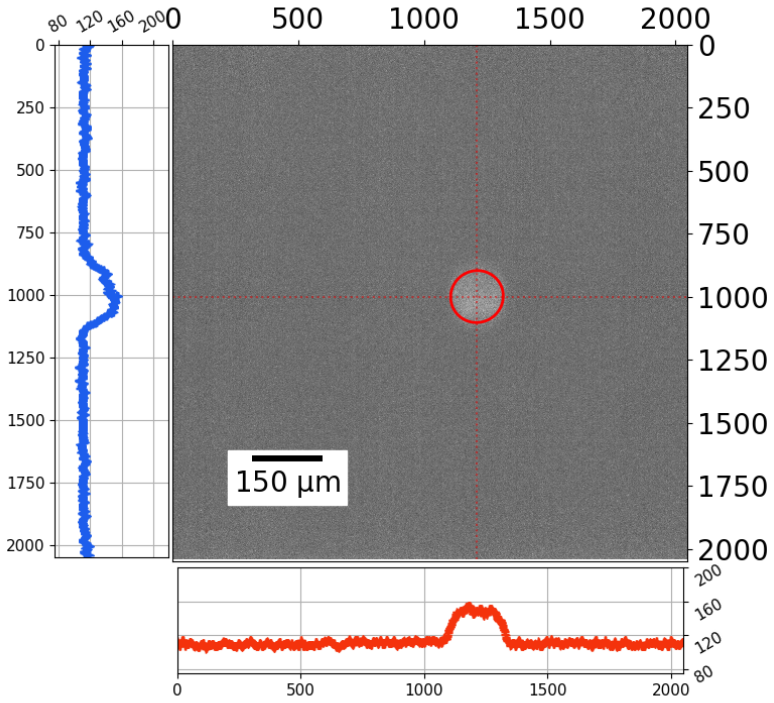

(A) Axial voltage 1/-6/1 V DC.

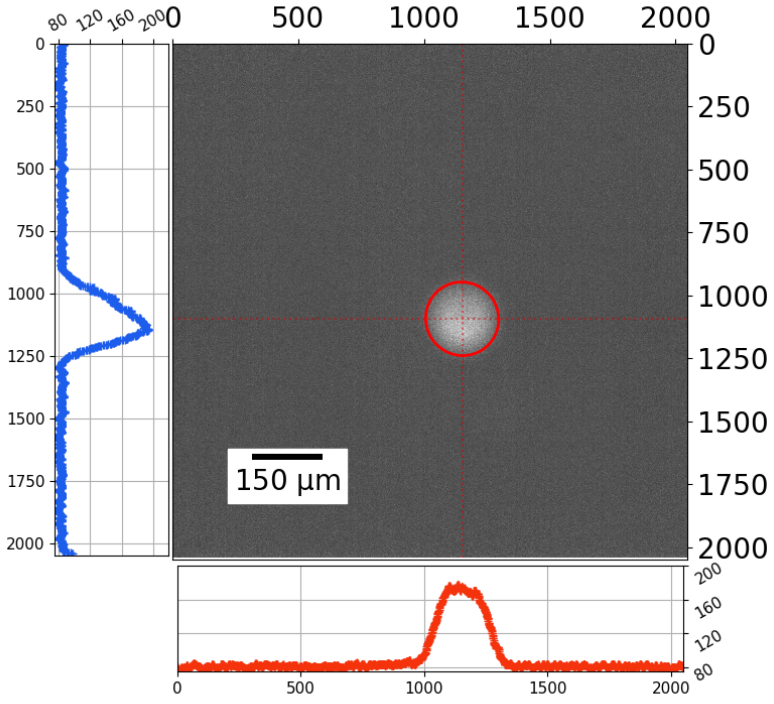

(B) Axial voltage 1/-3/1 V DC.

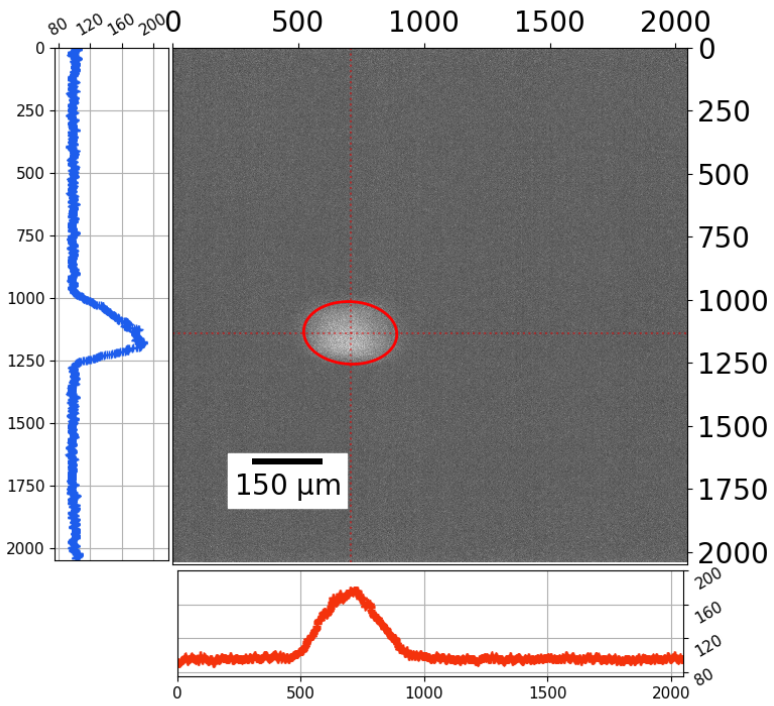

(c) Axial voltage 1/0.2/1 V DC.

FIGURE 2.7: Cloud fluorescence pictures with ellipse fit in red. Center coordinates is at intersection of dashed lines. Fluorescences profiles along dashed lines are represented in side of the picture. z-axis, which is the trap axis, through which laser are injected, is horizontal on the pictures. Measured on 2 July 2021.

Chapter 3

More than one ion

The above description of potential allows us to compute an analytical expression of the motion of a single ion. However, as soon as two or more ions are trapped together, the system defined by the set of trapped ions becomes much more complex to describe. This complexity comes from the apparition of Coulomb interaction between the trapped ions. This interaction couples the x and y directions (Eq. 1.12). Its analytical resolution becomes then much more complex, but the introduction of relative and center-of-mass (c.m.) coordinates simplify the description [Blü89].

3.1 Motion description for an ensemble of trapped ions

3.1.1 Center-of-mass motion description

Let's call $\mathbf{R_{CM}}/\mathbf{V_{CM}}$ the position and velocity of the *center of mass with respect to the trap's frame of reference*. The description of center-of-mass motion is straightforward given by the previous analysis from chapter 1.2, and the equations can be used provided the coordinates $u(t)$ are replaced by the center-of-mass coordinates $\mathbf{R_{CM}}$.

3.1.2 Relative motion description

In the trap's frame of reference, the equations of motion for the set of ions are expressed as follows

$$\begin{cases} \dfrac{d^2}{dt^2}\,\mathbf{u} + (a - 2q\cos 2\tau)\,\mathbf{u} = \dfrac{q_e^2}{4\pi\varepsilon_0 m}\displaystyle\sum_{j=1}^{N}\left(\frac{\mathbf{u_i} - \mathbf{u_j}}{\mathbf{r_{ij}^3}}\right) & \text{(3.1a)} \\ \dfrac{d^2}{dt^2}\,z + \omega_z^2\, z = \dfrac{q_e^2}{4\pi\varepsilon_0 m}\displaystyle\sum_{j=1}^{N}\left(\frac{z_i - z_j}{\mathbf{r_{ij}^3}}\right) & \text{(3.1b)} \end{cases}$$

Let's call $\mathbf{r_i} = (x_i, y_i, z_i)$ and $\mathbf{v_i}$ the motion variables of an ion relatively to the center-of-mass, then :

$$\mathbf{u_i} = \mathbf{R_{CM}} + \mathbf{r_i} \tag{3.2}$$

$$\dot{\mathbf{u_i}} = \mathbf{V_{CM}} + \mathbf{v_i} \tag{3.3}$$

with $\mathbf{u_i} = (u, z)$ the coordinates of an ion i in the trap's frame of reference.

We can decompose the motion of an ion as the sum of, the motion of cloud center-of-mass ($\mathbf{R_{CM}}$) and, its motion in the center-of-mass frame of reference ($\mathbf{r_i}$). The first uncoupled Mathieu equation determined in section 1.2 (Eq. 1.12) is still suitable for the center-of-mass coordinates, thus all the developments of section 1.2 can be applied to the ion cloud as a whole. The Coulomb coupling will only appear in the motion equations expressed in relative coordinates

$$\begin{cases} \dfrac{d^2}{dt^2}\, x_i + (\widetilde{a} - 2q\cos 2\tau)\, x_i = \dfrac{q_e^2}{4\pi\varepsilon_0 m} \displaystyle\sum_{j=1}^{N} \left(\frac{x_i - x_j}{\mathbf{r_{ij}^3}} \right) & \text{(3.4a)} \\ \dfrac{d^2}{dt^2}\, y_i + (\widetilde{a} - 2q\cos 2\tau)\, y_i = \dfrac{q_e^2}{4\pi\varepsilon_0 m} \displaystyle\sum_{j=1}^{N} \left(\frac{y_i - y_j}{\mathbf{r_{ij}^3}} \right) & \text{(3.4b)} \\ \dfrac{d^2}{dt^2}\, z_i + \omega_z^2\, z = \dfrac{q_e^2}{4\pi\varepsilon_0 m} \displaystyle\sum_{j=1}^{N} \left(\frac{z_i - z_j}{\mathbf{r_{ij}^3}} \right) & \text{(3.4c)} \end{cases}$$

The relative coordinates are particularly interesting when temperature is to be measured.

3.2 Effective temperature and energies

Thermodynamically, only physical quantities related to the internal behaviour of the cloud are interesting to consider. However the motion of the ions may exhibit a behaviour related to an external source. This motion only affects the center-of-mass, thus when computing temperature, the energy from the global movement must be removed from the energy from the internal movement. So the temperature is not given by $\frac{3}{2}k_BT = \frac{1}{2}\langle m\dot{\mathbf{u}}_\mathbf{i}'^2\rangle$ but by

$$\frac{3}{2}k_BT = \frac{1}{2}\left(\langle m\dot{\mathbf{u}}_\mathbf{i}'^2\rangle - \frac{\langle m\dot{\mathbf{u}}_\mathbf{i}'\rangle^2}{\langle m\rangle} \right) \tag{3.5}$$

which is the classical expression for temperature to which the energy of center-of-mass has been removed. Finding a replacement expression for $\langle m\dot{\mathbf{u}}_\mathbf{i}'^2\rangle$ is the goal of the following demonstration. By definition of center of mass :

$$\mathbf{V_{CM}} = \frac{\sum_i^N m\dot{\mathbf{u}}_\mathbf{i}'}{\sum_i^N m} = \frac{\langle m\dot{\mathbf{u}}_\mathbf{i}'\rangle}{\langle m\rangle} \tag{3.6}$$

we can state that :

$$\langle m\dot{\mathbf{u}}_\mathbf{i}'\rangle = \langle m\rangle\mathbf{V_{CM}}. \tag{3.7}$$

An expression for $\langle m\dot{\mathbf{u}}_\mathbf{i}'^2\rangle$ can be obtained,

$$\langle m\dot{\mathbf{u}}_\mathbf{i}'^2\rangle = \langle m\rangle\mathbf{V_{CM}^2} + \langle m\mathbf{v}_\mathbf{i}^2\rangle \tag{3.8}$$

assuming that $\langle \mathbf{V_{CM}} \mathbf{v_i} \rangle = \langle \mathbf{V_{CM}} \rangle \langle \mathbf{v_i} \rangle = \mathbf{V_{CM}} \langle \mathbf{v_i} \rangle = 0$ ($\mathbf{V_{CM}}$ and $\mathbf{v_i}$ are independent and $\mathbf{V_{CM}} = 0$), and benefiting from the fact that $\langle m\mathbf{V_{CM}} \rangle = 0$ and $\langle \mathbf{V_{CM}}^2 \rangle = \mathbf{V_{CM}}^2$ by definition of center of mass. Inserting equation 3.7 and 3.8 in equation 3.5, the temperature can be written simply

$$\boxed{\frac{3}{2} k_B T = \frac{1}{2} \langle m \mathbf{v_i}^2 \rangle .} \tag{3.9}$$

The computation above supposes that the motion in the relative frame of reference is thermal – i.e brownian. In particular when talking about effective temperature of ions, it is referred to any motion not periodic with a particular frequency, nevertheless there is at least one external periodic driving field : the radio-frequency trapping field with given frequency $\Omega = 2\pi / T_{RF}$. In order to properly remove its contribution from the relative velocities $\mathbf{v_i}$, it is possible to either "use velocities computed from displacements between times that differ by a complete rf period" [Sch00], or average the velocities over a complete radio-frequency period, which is the strategy we use in our computer program, and can be applied by using time averaged quantities, represented as

$$\boxed{\overline{\mathbf{v_i}}(t + T_{RF}) = \frac{1}{T_{RF}} \int_t^{t+T_{RF}} \mathbf{v_i}(t') dt' .} \tag{3.10}$$

Thus in order to properly compute the temperature over one radio-frequency period, the formula is

$$\boxed{\frac{3}{2} k_B T = \frac{1}{2} \left\langle m \left(\frac{1}{T_{RF}} \int_t^{t+T_{RF}} \mathbf{v_i}(t') dt' \right)^2 \right\rangle = \frac{1}{2} \left\langle m \overline{\mathbf{v_i}}^2 \right\rangle .} \tag{3.11}$$

3.3 Radio-frequency heating

3.3.1 Descriptive definition

Radio-frequency heating is an effect of capital importance in order to understand the mechanism at play during a detection event in the `GiantMol` experiment. Radio-frequency heating is a **collective effect** due to the Coulomb interaction occurring between ions immersed in the radio-frequency field. While the trajectory of a single ion is periodic and thus its energy and temperature constant over many radio-frequency period (see comments of section 1.5), the trajectories of the ions in a cloud are **perturbed** by the Coulomb interaction. Thus the ions can be perturbed from their equivalent periodic individual trajectories and displaced to non-conservative trajectories. This means the ions trajectories may not be periodical and ions may gain energy, thus **increase temperature**.

3.3.2 Origin and phenomenology

Equation 3.4 highlights this **coupling** between equations through the Coulomb repulsion term. Intuitively, radio-frequency heating intensity directly depends on two factors : first

the strength of the radio-frequency field, second the strength of the Coulomb interaction. Nevertheless, while the dependency of the Coulomb interaction to the inter-ionic distance $\mathbf{r_{ij}}$ is clearly visible, it is also the case for the strength for the radio-frequency field. Indeed, the radio-frequency field amplitude (or micromotion amplitude) exhibits quadratic dependence with respect to distance to trap axis (Eq. 1.5). A study of radio-frequency heating in function of $\mathbf{r_{ij}}$ or its average $\langle \mathbf{r_{ij}} \rangle$ is then a more complex task than it seems at first sight, but it is the path followed by Reinhold Blümel [Blü89; Nam14] since the late 80's.

3.3.3 Qualitative description – physical principle of `GiantMol`

Radio-frequency heating introduces energy in the cloud, which in turns causes a cloud increase of temperature. The heating rate H a cloud bears is defined as the temperature variation over a given period of time, so has unit of [K/s]. Globally, three regimes can be identified for radio-frequency heating (Fig. 3.1), depending on the cloud temperature. For more details on cloud state in function of the temperature, you can see below subsection 3.5. First it is important to consider how does heating rate qualitatively varies with temperature T. According to Nam, Jones, and Blümel [Nam14], the heating rate takes a maximum value for a certain temperature, and monotonously converges towards a lower value when the temperature tends towards 0 and $+\infty$ K. This behaviour translates into a lambda shape when heating rate is represented against cloud size (Fig. 3.1). The cloud size is proportional to the cloud temperature.

The physical explanation for this shape is that the chaotic behaviour introduced by radio-frequency heating is maximum for a certain average inter-ionic distance, where the ions are close enough for the coulombian interaction to perturb them significantly, but far enough for the ions to be tightly hold. Indeed, while the cloud is cold enough, the cloud is a crystal, and every ion keeps its place relatively to its neighbours, so all the ions trajectories are quasi-periodic. While the cloud is hot enough, the ions are far enough so they can be considered in individual trajectories described by Mathieu equation (as in chapter 1). In our experiment the radio-frequency heating is never negligible, so the laser cooling must be maintained, otherwise it will end up on the right part of figure 3.1, past the R point.

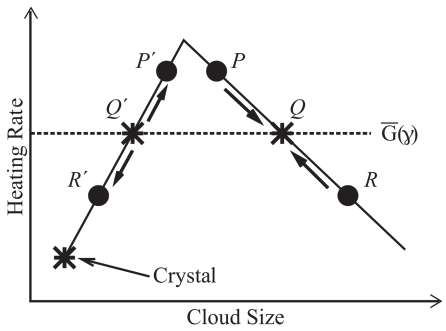

FIGURE 3.1: Dependance of heating rate, against cloud size. Taken from [Nam14].

When introducing cooling, the cloud reaches a state where the strength of laser cooling (G) equals the heating rate (H). For instance, if the cloud is initially in a state at the right of Q', the introduction of a cooling creates a point Q where a balance between heating and cooling exists. The configuration the cloud is converging to is that of Q. When trying to obtain a crystal it is thus required to have a cooling powerful enough to reach the crystal state, and an initial condition that leads to the crystal state (at the left of Q' in figure). Once

in this state, the cooling will maintain the cloud in a crystal state as long as the cooling power is maintained above the heating rate for crystal state. Note that the specific shape from figure 3.1 and the positions of points is dependant on the trapping and cooling parameters, as much as the initial conditions. Thus if there are no initial conditions that can lead to a crystal, it is experimentally possible to choose a set of parameters that facilitate the apparition of a crystal, before switching to the desired set of parameters.

For any reason, if a small amount of energy is introduced in the system so that the heating rate overcomes the cooling power, then the cloud is going to heat up to the next situation where cooling and heating balances, assuming the ions are not lost (by leaving the trap or colliding with the rods). In fact, because laser cooling becomes quickly inefficient when the temperature significantly change, the cloud will heat up to a high temperature where the heating rate becomes negligible (to the right part of curve 3.1). Work presented later in part III demonstrate that a charged projectile injected in the cloud can bring around 50 meV to a cloud initially cooled at 5 mK, and that is enough in order to produce an increase of temperature up to 3000 K.

This is the effect upon which `GiantMol` is relying. In our experiment, we propose to work with a stable crystal cloud maintained with just enough cooling so $G > H$, it is equivalent to work just below the Q' point. The giant charged projectile is then expected to bring a small amount of energy in the cloud, putting the cloud in a state above Q', where the heating overcomes the cooling $H > G$. The small amount of energy introduced would trigger a massive change in temperature due to the radio-frequency heating bringing the cloud to temperatures levels the projectile alone could not produce. The radio-frequency pattern from figure 3.1 can be compared to the numerical heating rate discussed in section 9.4, notably represented in figure 9.19.

Finally, note that this scheme suppose no latent heat from phase transition (see cloud state in subsection 3.5.2 for more details), which would be detrimental because energy transmitted from the projectile to the cloud would not be converted into temperature increase. It is observed that no significant latent heat occurs for a 1000 ions cloud, nevertheless some effects appear for one higher order of magnitude (see subsection 3.5.3).

3.3.4 Quantitative study

In order to study radio-frequency heating, it is wise to retrieve the temperature T of the ion cloud during a long period of time, with constant radio-frequency field amplitude and number of ions. Intensity of radio-frequency heating can be related to the variation of temperature in a given period of time. It is of interest to quantify the heating rate $H(t) = \Delta T/\Delta t$, defined as the rate at which temperature increases. This measurement can be done retrieving in the same time the cloud temperature. The temperature being related to kinetic energy, it is also interesting to express the heating rate in function of the kinetic energy E_{kin}. The determination of the cooling power G would ideally help a lot to pre-determine the equilibrium positions, thus the temperature upon which radio-frequency bolting will occur.

Nevertheless experimentally this task is complicated by the fact that it is hard to retrieve the temperature of the cloud instantaneously. Also many other effects may be mistakenly interpreted as radio-frequency heating while it is not, for instance excess micromotion due to trap imperfections [Ber98]. Nevertheless following the purpose of `GiantMol`, this excess micromotion could also be benefited from. Radio-frequency heating can be more easily studied through numerical simulations. Among the works, Ryjkov, Zhao, and Schuessler [Ryj05] did study radio-frequency heating in linear Paul traps. They determined that for ion temperatures between 0.1 mK and 15 K, the maximum radio-frequency heating was reached around 2 K. They also show radio-frequency heating increases with number of ions, in accordance with Nam, Jones, and Blümel [Nam14].

3.4 Aspect ratio

3.4.1 Definition

The shape of an ion cloud can be described by an ellipsoid[1], and cloud aspect ratio is one important cloud parameter essential in order to understand `GiantMol` principle, alongside with radio-frequency heating. For a given cloud with half-length L and radius[2] R, aspect ratio can be geometrically defined as

$$\alpha \overset{\text{def}}{=} \frac{R}{L}. \tag{3.12}$$

3.4.2 Measurement method

Those dimensions can be determined experimentally by fitting the fluorescence image with an ellipsoid. The mathematical model is developed in frame 3.4.1. The ellipse fitting is not directly applied to the raw camera image, this latter is first transformed according to the following method (Fig. 3.2). The camera image is first smoothed with a gaussian filter. Then a mask of equivalent dimension is generated from the smoothed image. For every image pixel, a mask pixel is set to zero or one depending if the corresponding image pixel value is below or above a defined threshold. This generates a binary image whose pixels considered within the ellipse are set to one, and the others are set to zero. The coordinates of the points situated at the frontier between the high and low state are retrieved and fitted by an ellipse. This means the points are fitted with the least-square method applied to the function developed in the frame 3.4.1. This is a method slightly different from the one used by Kamsap [Kam15] in his thesis. Kamsap [Kam15] works with the smoothed image. He locates the center and use the fluorescence profiles. I first use a Gaussian smooth to sharpen the image, then locate the cloud by identifying all the pixels above a certain threshold defined by the background light. This allows to find the edges rather than using

[1] The following description does not apply to situations where the set of ions settle in particular conformations such as ion chain, zigzag or pancake, but it is no big deal because those cases are not relevant for our application. For details on the analysis of a chain configuration, see the article from Kamsap et al. [Kam17].

[2] Radius is the radial half-length, the distance between the center of the ellipsoid and the edge, on the radial axis.

the ellipse center and fluorescence profiles. The mask is used for convenience in order to have a well defined mathematical object for the ellipse fit of the cloud edges.

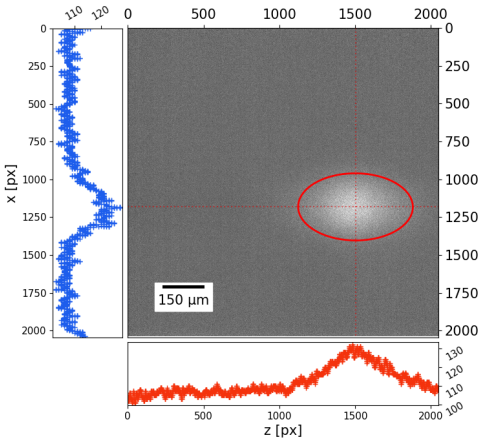

(A) A cloud image with superimposed ellipse determined from the ellipse fitting. Ellipse is in red line, ellipse axis are dashed lines. The orange and blue data on the edge of the image are pixel profile alongside the ellipse axis.

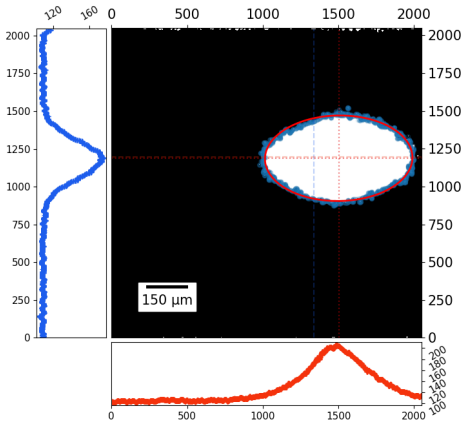

(B) Ellipse fitting method detailed. The mask is represented, alongside with the points located at its edge – blue points. the ellipse fit – red curve – and ellipse axis – dashed lines – are represented. The orange and blue data on the edge of the image are smoothed pixel profile alongside the ellipse axis.

FIGURE 3.2: Retrieving of cloud dimensions and shape through ellipse fitting.

3.4.3 Potential shape

In the framework of cold ion cloud, the cloud aspect ratio depends on the stiffness of the harmonic trapping potentials ω_u, and ω_z. A formula relates α to ω_z^2/ω_r^2 the potential aspect ratio [Hor02]. In the case where $\alpha < 1$

$$\frac{\omega_z^2}{\omega_r^2} = -2\frac{\sinh^{-1}(\alpha^{-2}-1)^{0.5} - \alpha(\alpha^{-2}-1)^{0.5}}{\sinh^{-1}(\alpha^{-2}-1)^{0.5} - \alpha^{-1}(\alpha^{-2}-1)^{0.5}}. \tag{3.13}$$

For $\alpha > 1$ proceed to the following change : sinh $\rightarrow$ sin and $(\alpha_{RL}^{-2}-1) \rightarrow (1-\alpha_{RL}^{-2})$.

Box 3.4.1: Ellipse fitting

In projective geometry, conic sections are plane curves resulting from the intersection of a cone with a plane. They are characterised by the following order two polynomial equation

$$Ax^2 + Bxy + Cy^2 + Dx + Ey + F = 0. \tag{3.14}$$

The above equation describes ellipses for any $\Delta' = B^2 - 4AC < 0$, with semi-axis Ox and Oy. With no consideration for the ellipse rotation with respect to the trap

frame of reference, the equation can be written as

$$\frac{(x-u)^2}{a^2} + \frac{(y-v)^2}{b^2} = 1 \tag{3.15}$$

with (u;v) coordinates of ellipse center, and a and b the semi-major and semi-minor axis. It is possible to retrieve the center position and axis dimensions with

$$\begin{cases} u = \dfrac{2CD - BE}{\Delta'} & (3.16) \\ v = \dfrac{2AE - BD}{\Delta'} & (3.17) \end{cases}$$

and

$$\begin{cases} a \\ b \end{cases} = -\frac{1}{\Delta'}\sqrt{2(AE^2 + CD^2 - BDE + F\Delta') \times (A + C) \pm \sqrt{(A-C)^2 + B^2}}. \tag{3.18}$$

Any numerical fit providing with coefficients A,B,C,D,E and F can thus be used to recover the ellipse parameters u,v,a and b.

3.5 Potentials, ion number, and cloud state

3.5.1 Number of ions and trapping potential

In order to estimate the total number of ions in the cloud N, it is possible to use the cloud volume V alongside with cloud density n_c, so that the total number of ions is

$$N = Vn_c. \tag{3.19}$$

For an ellipsoid, $V = \frac{4}{3}R^2L/2$, and for a cloud with homogeneous density [Kam15],

$$n_c = \frac{2m\varepsilon_0}{q_e^2}\omega_x^2. \tag{3.20}$$

Notice the use of ω_x and not ω_r. n_c, as given by Kamsap [Kam15] is the maximum density reached by a cold cloud whose temperature tends towards 0 K. For a quadrupolar field it is homogeneous along the radial direction for a crystalline or liquid cloud. It is required to provide a criterion in order to know which state the ion cloud is. A comparison of this formula with density numerically computed in our simulations is discussed in subsection 9.2.2.

3.5.2 Cloud state

In the framework of charged plasmas, it is possible to evaluate the state of the plasma with the so-called plasma parameter Γ_p. This plasma parameter is determined by the ratio of

the mean energy of the inter-ionic interactions E_{coul}, to the typical energies of the motional degrees of freedom E_{kin}.

$$E_{coul} = \frac{q_e^2}{4\pi\varepsilon_0 a_{WS}} \tag{3.21}$$

$$E_{kin} \propto k_B T \tag{3.22}$$

$$\Gamma_p = \frac{E_{coul}}{E_{kin}} = \frac{q_e^2}{4\pi\varepsilon_0 a_{WS} k_B T} \tag{3.23}$$

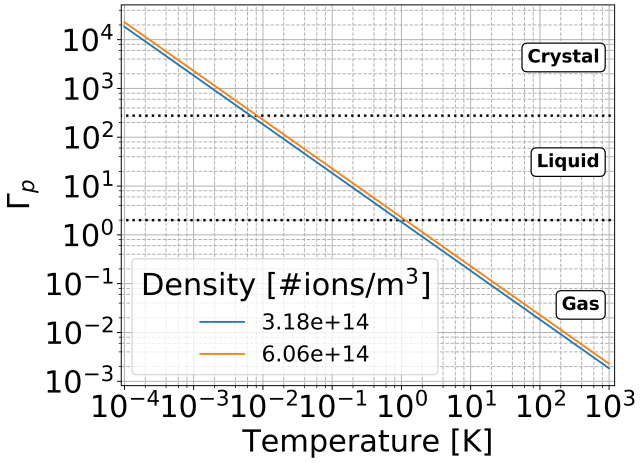

FIGURE 3.3: Plasma parameter in function of temperature, for two typical ion densities, later encountered when analysing numerical simulations. Horizontal dotted lines represent phase transitions for 1024 ions computed according to Schiffer [Sch02a].

with a_{WS} the Wigner-Seitz radius for the crystallised structure, defined as the average interparticle spacing so that the ion density is $n_0 = \frac{3}{4\pi} a_{WS}^{-3}$ [Dub96a]. This latter parameter can be assimilated to the distance between two ions of the same shell in the crystal, and sometimes to the average inter-ionic distance in the whole crystal. The higher the plasma correlation parameter Γ_p, the stronger the Coulomb interaction with respect to thermal energy. Low values of the plasma correlation parameter Γ_p are associated with a cloud in the gas state. Correlation effects will start to appear for values $\Gamma_p > 2 = \Gamma_p^{g\leftrightarrow l}$, for which the cloud is said in liquid state. Then long range order appears at $\Gamma_p \approx 100$, where the ion density displays oscillations with respect to the cloud radius. With increasing plasma parameter, concentric shells starts to form a pseudo-crystal lattice, starting with outer shells [Dub96b; Mor06; Mor07]. Figure 3.3 illustrates the values of Γ parameter against temperature, for a 1024 ions cloud. The two lines represent two configurations with extrema density meet in numerical works presented further (part III).

3.5.3 Phase transition and latent heat

In the particular case of the liquid $\leftrightarrow$ crystal phase transition, extensive numerical works since the late 60's demonstrate the specificities of finite-size plasma against infinite ones [Bru66; Far93]. It is known that the value of plasma parameter for which a liquid $\leftrightarrow$ crystal transition occurs varies inversely with the number of ions in the plasma ($\Gamma_p^{l\leftrightarrow c} \propto 1/N$).

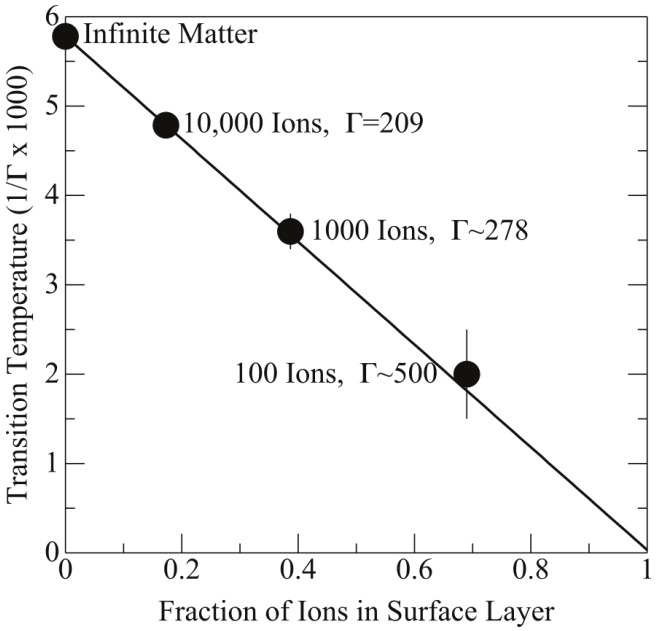

FIGURE 3.4: Transition temperature as a function of the fraction of ions in surface layers and total number of ions. Taken from Schiffer [Sch02a].

The extensive Molecular Dynamics simulations from Schiffer [Sch02a] provide a demonstration of this effect. In appendix D the fundamentals of phase transition are detailed and figure D.1, adapted from Schiffer [Sch02a], illustrates how in a Coulomb crystal, the total energy and the specific heat vary as a function of the temperature and the number of ions. From the analysis of Schiffer [Sch02a] I focus here on the results presented in figure 3.4. The increase of the transition temperature with the number of ions is clearly visible. Generally, the more the ions, the higher the transition temperature, the lower the transition Γ_p parameter. With infinite Coulomb crystals – One-component plasmas – the value for which transitions to the crystal state occurs is $\Gamma_p^{l\leftrightarrow c} = 175$, while in finite crystals this value is such that $\Gamma_p^{l\leftrightarrow c} \approx 200$ for 10000 ions, $\Gamma_p^{l\leftrightarrow c} \approx 278$ for 1000 ions and $\Gamma_p^{l\leftrightarrow c} \approx 500$ for 100 ions [Sch02a].

$\Gamma_p(1/T)$ being a function inverse of temperature, this increase of $\Gamma_p(1/T)$ with decreasing of ion number implies a diminution of the transition temperature when the ion number decreases. This variation in temperature for the liquid $\leftrightarrow$ crystal phase transition relates directly to the transition latent heat decreasing with the number of ions [Sch02b] , until there is no more apparent latent heat. Such a regime with no latent heat exists for clouds with number below a certain threshold whose value is below 10000 ions. Provided the number of ions is significantly under this threshold, any energy brought into, or removed from, the cloud at phase transition directly contributes to a variation of temperature of the cloud. This is a consideration of particular interest in the case of `GiantMol` experiment. The minimum amount of latent heat is desired as it is required the introduced giant molecule heats the ion cloud as much as possible, and too much latent heat at phase transition would have detrimental effects. The effect of phase transition over fluorescence is investigated lower, subsection 4.7.2.

Chapter 4

Laser cooling principle and demonstration

LASER Doppler-cooling is designed to slow down the trapped particles. The analytical description of laser cooling is summed up in this chapter. This description is done in the framework of a two-level system, which is sufficient to understand the main features of laser cooling. A first description of the cooling of a single atom with velocity v is provided. This description provides the typical elements used to describe the trapping of ions. Then, in order to study the fluorescence of an ensemble of ions properly, the description of laser cooling is extended to an ensemble of ions with Maxwell-Boltzmann distribution.

Also, in this chapter, the radio-frequency field driving the ion motion in the radial direction is not treated. Nevertheless this is demonstrated that the oscillation amplitude of the ions in the trap follows a thermal probability distribution derived from the Boltzmann distribution [Esc03a], which is taken into account. Also, although the radio-frequency field causes a non-thermal additional Doppler effect in the radio direction, this can be ignored by injecting the laser along the trap axis. Thus the radio-frequency field is neglected where it is identified it has no significant impact on the analysis, and its remaining effects are discussed after the presentation of the laser cooling.

4.1 Basic principle with a single two-level system

A detailed description of laser Doppler-cooling can be found in a lecture from Les Houches school from Champenois [Cha08] and in a book from Foot [Foo05a; Foo05b]. Two other references from Wineland, Drullinger, and Walls [Win78] and Cohen-Tannoudji [Coh98] deal with laser cooling in the context in which it was developed. Hereinafter, the description of laser cooling is split into two parts. First, a simple picture of laser cooling in the manner of classical mechanics, satisfying in order to get an intuitive understanding of laser cooling, but failing to account for some important effects. Then, the general details of the analytical description are given to finally highlight the important parameters.

4.1.1 Two-level system

Let us consider the case of a two-level system (Fig. 4.1), with g and e the ground and excited levels, with respective energies E_g and E_e. Given an atom of momentum $\mathbf{p} = m\mathbf{v}$, and a laser beam with wave-vector $\mathbf{k_L} = 2\pi/\lambda$, laser cooling relies on absorption then emission of photons, according to the two following phenomena :

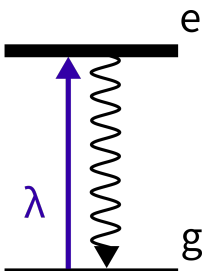

FIGURE 4.1: Two-level model for an atom.

- ➢ *Resonant* radiation pressure : when the atom absorbs a photon, its momentum is modified, so that $\mathbf{p_i} \rightarrow \mathbf{p_j} = \mathbf{p_i} + \hbar\mathbf{k_L}$ (Fig. 4.2a) ;
- ➢ Spontaneous emission : the excited atom emits a photon in a random direction over the whole 4π steradians. The time between absorption and emission is proportional to the excited level lifetime $\tau = 1/\Gamma_t$. The emission modifies the atom momentum, so that $\mathbf{p_j} \rightarrow \mathbf{p_f}$ (Fig. 4.2a).

Over a long period of time where multiple photons are absorbed, always from the same direction defined by the laser beam. The momentum transfer induced by the repeated absorptions of photons can be assimilated to a pressure effect, entailing the name of radiation pressure, specifically called resonant because it relies on a resonant absorption process. Also in average, the spontaneous emission is isotropic, thus spontaneous emission does not, in average, contribute to a net change in momentum.

With this simple picture, it now appears that it is possible to remove kinetic energy from the atom by carefully designing the resonant radiation pressure process so that $|\mathbf{p_j}| < |\mathbf{p_i}|$. Lasers are used because they can provide a radiation with low divergence and well defined wavelength. In the following, first, the conditions required by the momentum and energy conservations are developed (subsection 4.1.2). Then, second, the excitation probability of the ion by the laser, as a function of the laser and atomic parameters – among which its velocity – is then studied (section 4.2). Spontaneous emission is also taken into account. Because of spontaneous emission introducing a **Brownian motion** of the ion, atoms cannot be cooled until a null velocity is reached. Its effect on the lower temperature it is possible to reach is well known (subsection 4.2.3). Then, the description of the cooling of a single ion must be completed in order to account for the cooling of an ensemble of ions. This is done by adding the contribution of the velocity distribution to the excitation probability (subsection 4.3).

4.1.2 Laser Doppler cooling from an energetic point of view

Applying both conservation of momentum and kinetic energy it is possible to study the interaction of a photon with an atom (Fig. 4.2). Let's define $\mathbf{p_i}$ and $\mathbf{p_f}$ the initial and final momentum of the atom. The left part of the equation represents the two bodies system before absorption, the right part the one body system after absorption.

$$\mathbf{p_i} + \hbar\mathbf{k_L} = \mathbf{p_f} \tag{4.1}$$

$$\frac{\mathbf{p_i}^2}{2m} + \hbar\omega_L + E_g = \frac{\mathbf{p_f}^2}{2m} + E_e \tag{4.2}$$

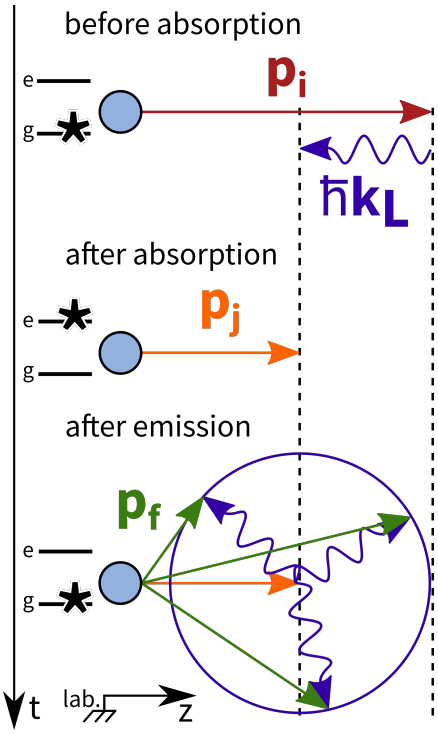

(A) In the frame of reference of the laboratory, schematic of absorption then emission of a photon by an atom (chronologically from top to bottom). The atom depicted by the blue disk, initially has a momentum $\mathbf{p_i}$. The photon, depicted by a waved arrow, initially has a momentum $\hbar\mathbf{k_L}$. When the atom absorbs the photon, the latter excites the atom. On the left side, the star represents a grounded or excited atom, depending if the star is on the below or above bar.

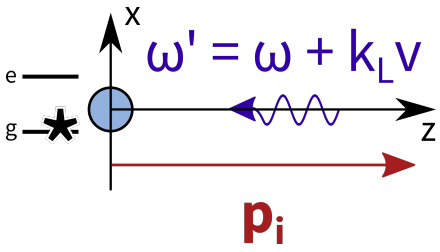

(B) Representation of the Doppler effect. A photon with frequency ω in the laboratory frame of reference is observed in the frame of reference of the atom with frequency $\omega' = \omega + k_L v$.

FIGURE 4.2: Interaction of an atom with a photon. The atom is depicted by the blue disk, the photon by the waved arrow.

with $\omega_L = \frac{c}{\lambda}$ the laser light angular frequency required to trigger atom excitation, in the laboratory frame of reference and c the speed of light. Assembling those two equations, the appropriate laser frequency to produce radiation pressure can be computed as a function of the transition frequency of the atom at rest ω_0

$$\hbar\omega_L = \underbrace{E_e - E_g}_{\hbar\omega_0} + \underbrace{\frac{\mathbf{p_i}\hbar\mathbf{k_L}}{m}}_{\text{Doppler}} + \underbrace{\frac{(\hbar\mathbf{k_L})^2}{2m}}_{\text{Recoil}}. \tag{4.3}$$

This equation shows that the laser angular frequency ω in the laboratory frame of reference is not equal to the one of the atomic transition at rest ω_0. A small shift proportional to $\mathbf{k_L} \cdot \mathbf{v_i}$ must be applied to the laser angular frequency. This shift is identified as Doppler effect[1] and highlights the necessity to consider the atom frame of reference. The last term

[1] Doppler effect implies a relationship between the photon angular frequency in the laboratory frame of reference ω and the photon angular frequency in the frame of reference of the moving atom ω'.

proportional to $\mathbf{k_L^2}$ is negligible with respect to the transition natural width. In terms of angular frequency it is thus possible to write

$$\omega_L = \omega_0 + \mathbf{k_L} \cdot \mathbf{v_i}. \tag{4.4}$$

The sign of this scalar product depends on the projection of one vector on the other, which gives rise to two cases :

- either the scalar product is $\mathbf{k_L} \cdot \mathbf{v_i} = k_L v_i > 0$. In that case, the photon and the atom are *co-propagating*, and the radiation pressure results in an increase of the atom momentum by $\Delta\mathbf{p} = \hbar\mathbf{k_L}$;
- or the scalar product is $\mathbf{k_L} \cdot \mathbf{v_i} = -k_L v_i < 0$. In that case, the photon and the atom are *contra-propagating*, and the radiation pressure results in an decrease of the atom momentum by $\Delta\mathbf{p} = \hbar\mathbf{k_L}$.

Thus in order to provide laser cooling through radiation pressure, it is required to favour the second case where the momentum decreases. To do so it is sufficient to illuminate the ions with a smaller frequency than the transition frequency, i.e with a negative laser detuning $\delta \overset{\text{def}}{=} \omega_L - \omega_0$. The condition for an atom to be excited by a photon is as follows

$$\boxed{v_i = \frac{\omega_0 - \omega_L}{k_L}.} \tag{4.5}$$

Indeed, in the atom's frame of reference, the photon wavelength $\omega_L' = \omega_L + k_L v_i$, and in order to excite the transition it is required that $\omega_L' = \omega_0$ thus $\omega_L = \omega_0 - k_L v_i$, in the laboratory frame of reference. The photons will then preferentially interact with the contra-propagating atoms, i.e the atoms whose momentum $\mathbf{p_i}$ have a negative projection on the wave-vector $\mathbf{k_L}$.

4.2 Doppler cooling in the narrow velocity distribution approximation

4.2.1 Brief exhibition of quantum formalism applied to two-level system

Because of spontaneous emission, the analytical description of the atom cannot be done using time-dependent Schrödinger's equation. Using the **density operator** ρ is the right approach for this problem. For a given vectorial basis with two vectors $|\psi_e\rangle$ and $|\psi_g\rangle$, representing the excited and grounded states e and g, the density operator $\rho(t)$ is able to render **all possible realisations** that our two-level system can achieve. It is defined as

$$\rho(t) = \sum_k P_k \, |\psi_k\rangle \, \langle\psi_k| \tag{4.6}$$

with $k = e, g$. The density operator can be represented as a square matrix, in which each element represents the probability of realisation of a state, computed as

$$\rho_{ij} \overset{\text{def}}{=} \langle \psi_i | \, \rho(t) \, | \psi_j \rangle \tag{4.7}$$

The **density matrix** for a two-level system can thus be written as

$$\rho(t) = \begin{pmatrix} \rho_{gg} & \rho_{ge} \\ \rho_{eg} & \rho_{ee} \end{pmatrix}. \tag{4.8}$$

The diagonal terms of the density matrix represent the probabilities to find the quantum system in a state corresponding to the chosen basis, so that $P_e = \rho_{ee}$ the probability to find the system in the excited state, and $P_g = \rho_{gg}$ the probability to find the system in the grounded state. The off-diagonal elements represent the coherences and describe the degree of superposition of the system. It is of highest interest to find an expression for those terms, particularly the coherence term ρ_{ge}, in order to know more about the two-level system.

4.2.2 Probability of excitation and fluorescence

The above description exhibits the cyclic absorption and emission of photons. The solution of the Optical Bloch Equations provides the probability of excitation of an ion as

$$\boxed{\rho_{ee} = \frac{1}{2} \frac{\Omega_R^2}{\Omega_R^2 + 2\Delta_\star^2 + \Gamma_t^2/2} = \frac{A/2}{A + B + \Delta_\star^2}} \tag{4.9}$$

with $\Delta_\star \overset{\text{def}}{=} \omega_L - \omega_0 - \mathbf{k_L} \cdot \mathbf{v_i}$ the detuning between the actual laser frequency and the required transition frequency of the atom accounted for Doppler effect, $\Omega_R = \mathbf{d} \cdot \mathbf{E}/\hbar$ the Rabi frequency defined as the product of the electric dipole $\mathbf{d}$ and the electric field $\mathbf{E}$. It can be written as a function of the laser parameters and level lifetime

$$\Omega_R^2 = \frac{3\lambda^3 \Gamma_t}{4\pi^2 \hbar c} I = \frac{3\lambda^3 \Gamma_t}{4\pi^2 \hbar c} \left(\frac{P_L}{\pi w^2} \right). \tag{4.10}$$

with P_L the laser power, w the laser waist radius and $I = P_L/(\pi w^2)$ the laser beam intensity. It is very convenient to define a saturation parameter s so that

$$s \overset{\text{def}}{=} \frac{\Omega_R^2}{\Gamma_t^2/2 + 2\Delta_\star^2} = s_0 \frac{1}{1 + (2\Delta_\star/\Gamma_t)^2} \tag{4.11}$$

$$s_0 \overset{\text{def}}{=} \frac{2\Omega_R^2}{\Gamma_t^2} = \frac{I}{I_{sat}}. \tag{4.12}$$

so finally

$$\rho_{ee} = \frac{1}{2} \frac{s}{1+s}. \tag{4.13}$$

Also, for convenience in the computation and later numerical simulations, it is possible to define ρ_{ee} as a function of $A = {}^1\!/_2\Omega_R^2$, $B = {}^1\!/_4\Gamma_t^2$.

Related to an ensemble of ions submitted to a common environment, this quantity ρ_{ee} is the probability of occupation of the excited state. The following section focuses on the study of fluorescence of a single ion, while the case of a population is treated after (section 4.3). The emitted fluorescence F is proportional to the spontaneous scattering rate of the atom and the probability of excitation

$$\boxed{F = \Gamma_t \rho_{ee}.} \tag{4.14}$$

4.2.3 Doppler cooling limit temperature

In the case where the transition line is wide, i.e the linewidth is much more important than the recoil energy, $\Gamma \gg \frac{(\hbar \mathbf{k_L})^2}{2m}$ and $|\mathbf{k_L} \cdot \mathbf{v_i}| \ll |\omega_L - \omega_0|$. In this case, it is demonstrated the laser detuning for which the lower temperature is minimal is $\Delta_\star = -\Gamma/2$ [Let77]. In the case of a low intensity, the lower limit temperature it is possible to reach is

$$T_{lim} = \frac{\hbar \Gamma_t}{2k_B} \tag{4.15}$$

if no other source of heating than the stimulated emission intervene. In the two-level Ca^+ system when only considering the cooling transition $S_{1/2} \rightarrow P_{1/2}$, $T_{lim} = 0.55$ mK.

4.2.4 Fluorescence behaviour

Equation 4.9 can be conveniently used to analytically determine the excitation probability of the ion against its velocity (Fig. 4.3). This is particularly interesting in the context of `GiantMol` because the detection relies on the observation of a fluorescence modification, that directly depends on how does ρ_{ee} varies. For a single ion temperature is not a relevant quantity, nevertheless in order to facilitate the comparison of this situation with the case where there are multiple ions, the velocity of the single ion is converted into an equivalent temperature by the formula $T = \frac{1}{2} m v^2 / k_B$, when needed. Figure 4.3 shows ρ_{ee} against the equivalent temperature of the single ion, for several detunings. The dotted line is computed for a $\delta = -\Gamma/2$ detuning which is the detuning with the lowest Doppler limit, and the red line stands for a $\delta = -\Gamma$ detuning as used later in numerical simulations (Part III). This figure 4.3 shows that for negative detunings, the temperature of highest fluorescence is higher that the lowest possible temperature.

The analytical derivation of ρ_{ee} with respect to the velocity can be written as

$$\frac{\mathrm{d}}{\mathrm{d}v}\rho_{ee} = \frac{A}{2} \frac{2(\omega_L - \omega_0 - \mathbf{k_L} \cdot \mathbf{v_i})}{(A + B + (\omega_L - \omega_0 - \mathbf{k_L} \cdot \mathbf{v_i})^2)^2} \tag{4.16}$$

$$\frac{\mathrm{d}^2}{\mathrm{d}v^2}\rho_{ee} = \frac{f}{g} = \big[-2(A + B + (\delta - \mathbf{k_L} \cdot \mathbf{v_i})^2)^2 \tag{4.17}$$

$$+8(\delta - \mathbf{k_L} \cdot \mathbf{v_i})^2 (A + B + (\delta - \mathbf{k_L} \cdot \mathbf{v_i})^2)\big] \frac{A}{2(\dots)^4}. \tag{4.18}$$

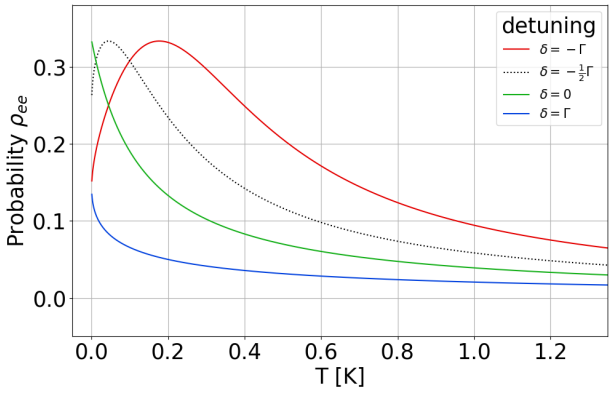

FIGURE 4.3: The excitation probability of a single ion as a function of the equivalent temperature. Four different detuning settings are compared, all with $\Omega_R = \Gamma_t$. The black dotted line shows ρ_{ee} for $\delta = -\Gamma_t/2$ detuning, the red line ρ_{ee} for $\delta = -\Gamma_t$, the green line ρ_{ee} for a $\delta = 0$ and the blue line ρ_{ee} for $\delta = \Gamma_t$.

By equalizing each of the above equation with 0, this allows to find the equivalent temperature for which the excitation probability is maximum, and when the variation of excitation probability is maximum. In the conditions of the simulations where $\Delta\omega = -\Gamma$ and $\Omega_R = \Gamma$

$$\frac{\mathrm{d}}{\mathrm{d}v}\rho_{ee} = 0 \rightarrow T = 171\mathrm{mK} \tag{4.19}$$

$$\frac{\mathrm{d}^2}{\mathrm{d}v^2}\rho_{ee} = 0 \Leftrightarrow \Delta_\star = \pm\sqrt{\frac{A+B}{3}} \rightarrow T = \frac{m\Delta_\star^2}{2k_B}\frac{1}{k^2} \rightarrow T = 44\mathrm{mK} \text{ or } T = 398\mathrm{mK}. \tag{4.20}$$

This description suits very well for the case of a single ion trapped or in case of a population with a very narrow velocity distribution, i.e when the velocity distribution is negligible compared to the width of ρ_{ee} at the same temperature. The fluorescence will increase with the temperature up to 171 mK, before decreasing. It decays below its initial level after approximately 600 mK. This means that in order to produce a measurable fluorescence difference the temperature must be raised over this 600 mK value at least. The thorough considerations on the fluorescence difference, accounting for the velocity distribution of ions and the noise in the signal, is to come in section 4.3.

4.3 Doppler cooling of a thermal ion cloud with a velocity distribution

4.3.1 Fluorescence behaviour

An ensemble of ions may exhibit a velocity distribution not negligible with respect to the excitation probability. This may be the case if the ensemble of trapped particles behaves as a gas accordingly to the Maxwell-Boltzmann distribution $MB_T(v)$. Then the excited population is related to the following quantity

$$\boxed{F = N \times P_e = N\Gamma \int \rho_{ee}(v) \times MB_T(v)\,\mathrm{d}v} \tag{4.21}$$

which is also related to the fluorescence F. Figure 4.4 shows ρ_{ee} and $MB_T(v)$ for a given temperature $T = 1$ mK, $\delta = -\Gamma$ detuning and $\Omega_R = \Gamma$. The blue curve is the velocity distribution, orange curve the excitation probability against the velocity of an ion for a given laser direction. The green curve is the symmetric of the orange curve and represent the excitation probability of an ion in a laser coming in the opposite direction of the previous. In the single laser case, the fluorescence is the purple coloured area which also represents the integral F (Eq. 4.21). With a temperature this low, the effect of the velocity distribution may be minimal and equation 4.21 can be well approximated by equation 4.14. Nevertheless, especially in the case of `GiantMol` where the ion ensemble is planned to heat several order of magnitude, the carefull study of the flluorescence must account for the velocity distribution. Indeed when the ensemble heats, the velocity distribution broadens, and because it is asymetric and so is the excitation probability ρ_{ee} within its boundaries, the effect of the velocity distribution cannot be neglected anymore. Figure 4.5 compares the fluorescence of a single ion (Eq. 4.14) with that of a collection of 1024 ions with a Maxwell-Boltzmann distribution (Eq. 4.21). The broadening effect of the velocity distribution is visible due to the fact that the fluorescence evolution is slower for a given temperature variation.

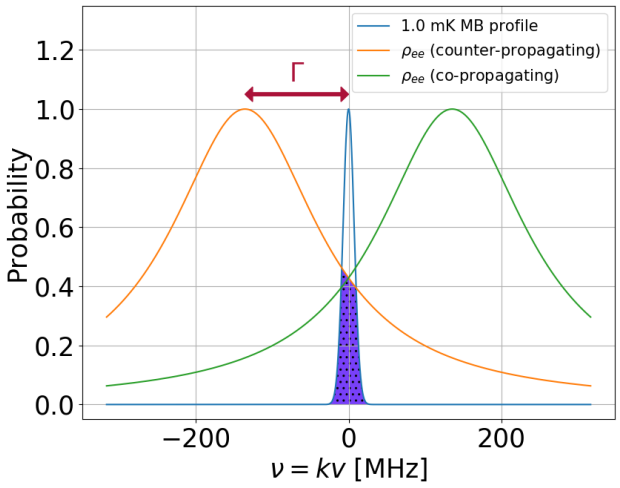

FIGURE 4.4: The excitation probability as a function of the ion velocity v expressed as $\nu = kv$. The blue curve is the Maxwell-Boltzmann velocity distribution for a 1 mK gas, and the orange and green curves are Doppler profile for detuning $\delta = -\Gamma_t$ and $\delta = \Gamma_t$ respectively. Both curve represent a laser beam coming in opposite directions. The saturation is $\Omega_R = \Gamma$.

The analysis of the fluorescence as a function of the temperature can be carried out numerically. In that case, figure 4.6 shows the fluorescence of 1024 ions in the same settings as before ($\Omega_R = \Gamma_t$) for four detunings.

With $\delta = -\Gamma_t$, $\Omega_R = \Gamma$, the numerical analysis provides a maximum fluorescence for $T = 171$ mK, and a maximum fluorescence variation for $T = 26$ mK, which is close to the above mentioned values in the case of a narrow velocity distribution. This indicates that the narrow distribution approximation holds well for temperatures in the range around 100 mK.

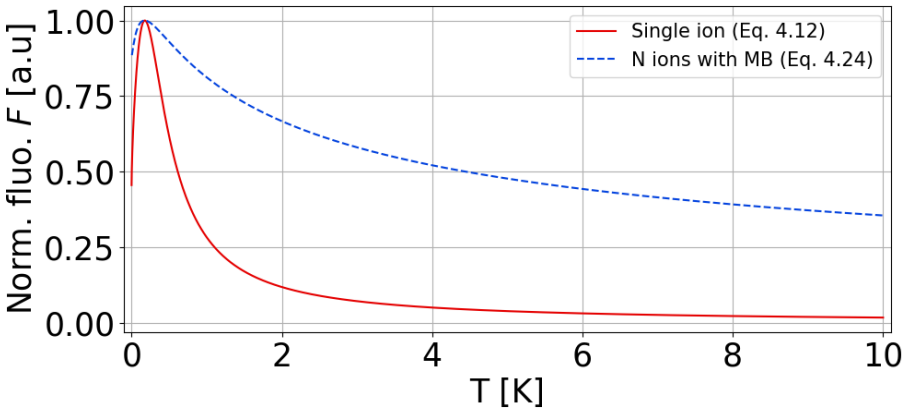

FIGURE 4.5: Fluorescence signals computed from equations 4.14 and 4.21 for, respectively, a single ion, and a collection of 1024 ions with a Maxwell-Boltzmann distribution.

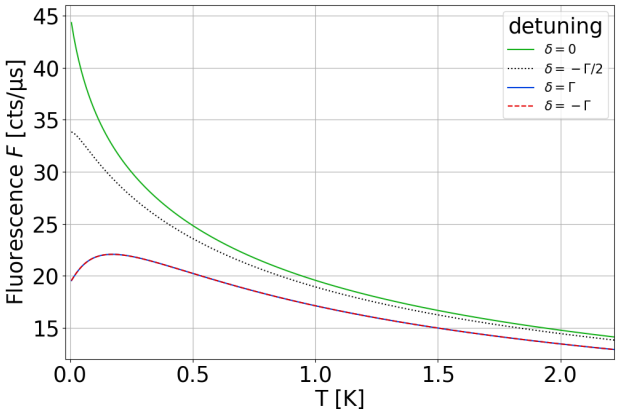

FIGURE 4.6: The fluorescence of an ensemble of 1024 ions in four different detuning settings, for detuning $\delta = -\Gamma_t$, $\Omega_R = \Gamma_t$.

4.3.2 Minimum temperature difference for detection

In order to measure an observable fluorescence signal, the fluorescence variation induced by the change in temperature must differentiate from the noise in the signal. Considering a Poisson noise, the fluorescence level $F(t_1)$ after the change must be so that it is the former fluorescence level $F(t_0)$, more or less the Poisson noise σF. This condition is written as $F(t_1) = F(t_0) \pm \sigma F$. Equation 4.21 allow to compute such temperature value, and figure 4.5 allows to visualise the problem for cases with a single ion or a collection of ions with a velocity distribution. The temperature to overcome for the fluorescence difference to be observable, when starting from the Doppler cooling limit, is $T = 600$ mK. This result underestimate the temperature observed in the simulations by a factor ten (Fig. 9.1). This is probably due to the fact that the Maxwell-Boltzmann distribution may be inappropriate to describe the thermal state of the cloud in a quick evolution induced by the passing of a projectile in less than 10 µs. Nevertheless this provides a first interesting approximation.

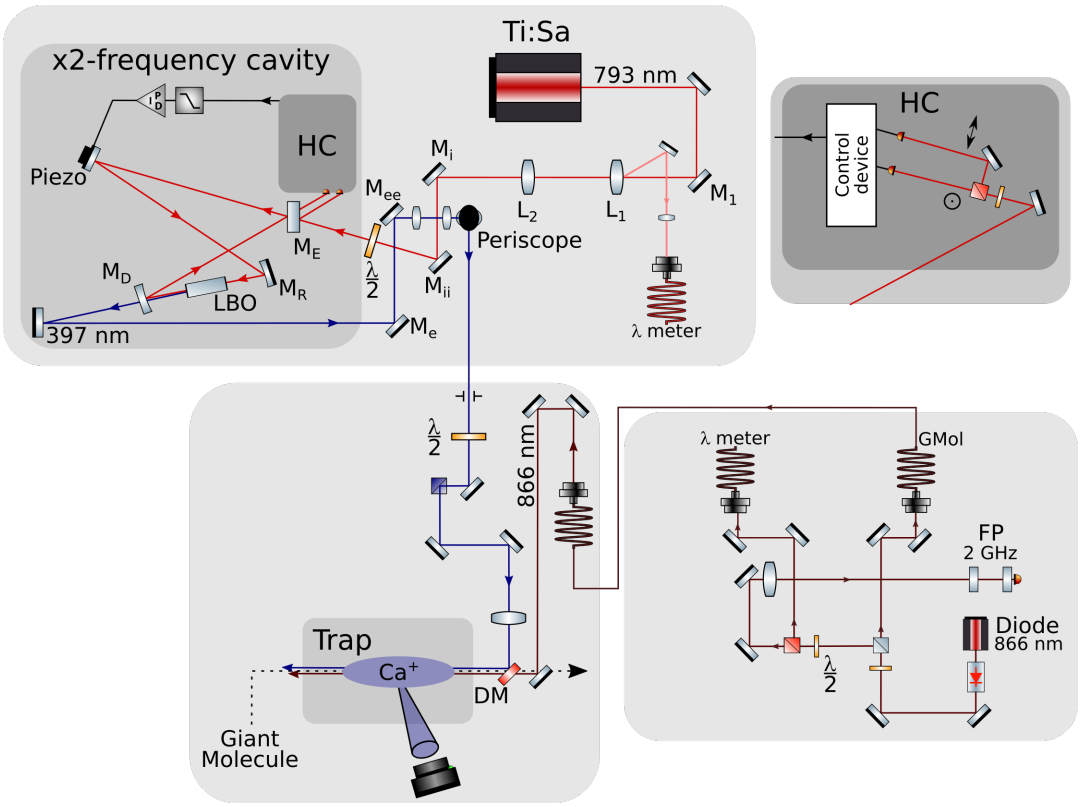

FIGURE 4.7: Schematics of the optical part of the experiment. M is for mirror, L for lens, DM for dichroic mirror, $\lambda/2$ and yellow rectangles are for half-wave plates. HC is for Hänsch-Couillaud, λ meter for the wavelength measuring device. FP is for Fabry-Pérot interferometer with 2 GHz FSR. ComponentLibrary by Alexander Franzen is licensed under a Creative Commons Attribution-NonCommercial 3.0 Unported License.

4.4 Laser setup

4.4.1 Apparatus

The whole laser apparatus is presented in figure 4.7. The 397 nm laser beam is produced through laser doubling of a 793 nm beam in a Lithium Triobate – LBO : LiB_3O_5 – crystal, mounted in a lab-made enhancing cavity. The 793 nm laser beam is produced with a Coherent® Titanium:Sapphire Ring laser model 899-21. The Titanium:Sapphire laser is pumped with a 532 nm 10 W beam produced by a Spectra-Physics® Neodymium:YVO_4 laser. The re-pumper 866 nm laser beam is produced with a Moglabs® Cateye External Cavity Diode laser model CEL002. Laser wavelengths are measured with a multichannel HighFinesse® wavelength meter model WS7 through fiber pickup in a convenient place. The refractive index used by the wavelength meter are given in table 4.1. The 397 nm wavelength is determined by doubling the 793 nm wavelength. Although in this document wavelength is often referred to characterise light, frequency offers the advantage to be independent of the refractive index. In order to be able to convert wavelengths into frequencies (et vice versa) through the formula $\lambda = c/(fn(\lambda))$, I provide the value of air refractive index given by our wavelength meter :

TABLE 4.1: Refractive index of air given by our wavelength meter for two laser wavelengths and frequencies, with temperature 22.8°C and pressure 1007 mbar. Measured on September 2021.

λ [nm]	f [THz]	n
793.69966	377.61139	1.0002750
866.21444	345.99995	1.0002746

4.4.2 Frequency-doubling

Frequency doubling in Second Harmonic Generation – SHG – is used to produce the cooling 397 nm beam. The Ti:Sa 793 nm beam with approximately 800 mW is injected in a LBO crystal. The low birefringence angle of LiB_3O_5 and its non hygroscopic nature are two key arguments justifying its choice. Nonetheless, the reader is warned that LiB_3O_5 remains slightly sensitive to water and can form a solution when directly exposed to water – properties which is named *deliquescence*. Thus crystal surfaces should not be directly exposed to water at risk of damaging the surface state [Li75]. The length of the crystal is chosen to be 14 mm to optimise doubling efficiency according to Boyd and Kleinman [Boy68] theory. This length is the optimum compromise between a high focalisation limited by diffraction and a constant width beam. The 793 nm beam mode adaptation is designed so that the waist is located in the LBO with an approximate size of 25 µm. In order to maximise the blue 397 nm intensity the crystal is located in a bow-tie cavity where the 793 nm beam achieves multiple passing in the crystal. The maximum output recorded for 397 nm beam was approximately 20 mW, with an average power output between 10 and 15 mW [Poi18].

4.4.3 Frequency lock – Hänsch-Couillaud

Principle

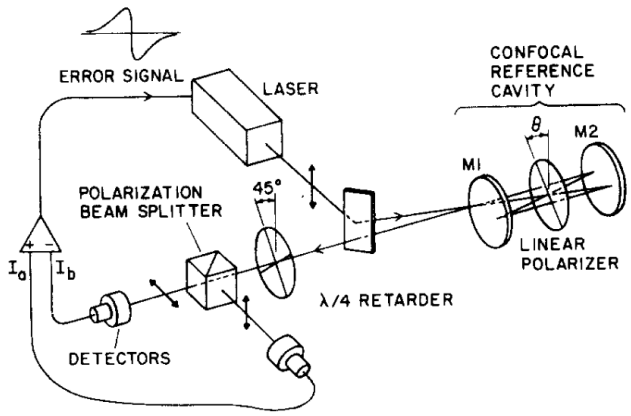

FIGURE 4.8: Principle of the Hänsch-Couillaud lock device as presented in the original article [Hän80]. Contrary to this schematics, in our experiment the error signal does not act on the laser wavelength but on the cavity length via a piezoelectric element upon which a mirror is mounted.

The 397 nm wavelength stability is ensured via a Hänsch-Couillaud lock device (see Fig. 4.8 and HC in Fig. 4.7) [Hän80]. The principle relies on **polarisation spectroscopy**. Two servo beams are extracted from the Ti:Sa laser : a reflection of the incident beam on

the entrance mirror of the doubling cavity M_E, and a reflection of the beam that rotates inside the cavity and leaves the cavity through the same mirror M_E. In the first case only the perpendicular polarisation component is reflected, while the parallel polarisation component is introduced in the cavity and will be captured by the second photodiode. The two reflections are mixed and pass through a $\lambda/4$ retarder and a polarisation beam splitter. Two photodiodes measure the output of the polarisation beam splitter. In the case the cavity is resonant with the laser, there is no phase shift between the two reflections and the photodiodes see the same signal. When the laser frequency changes, or the cavity length, a phase shift is introduced and the signals after the polarisation beam splitter are unbalanced. Electronics compare both photodiode signals and produce an error signal, sent to a piezoelectric element via a cascade of amplifiers.

Stability

The piezo bandwidth is in the range of [0; 3000] Hz, while the electronics guarantees similar characteristics. Laser intensities were acquired with photodiodes observing small leaked signals from optical elements. Figure 4.9 is about the laser beam intensities. The red and blue curves are related to the 793 and 397 nm laser beams. The yellow curve is the electronic signal from the Hänsch-Couillaud output. The 793 nm laser beam intensity varies up to 25% over a period of time of 30 ms. In the signal from the blue 397 nm laser the intensity variation is up to 40%. This is an important variation. The signal from the Hänsch-Couillaud is displaying many oscillations between its working range [-10;10] V.

A Power Spectral Density (Fig. 4.10) analysis shows that the Hänsch-Couillaud signal is working with negligible oscillations below 400 Hz, and starts to display characteristic frequencies around 500, 800, 1050, 1075 and 3900 Hz. Those frequencies can be significantly found in the signal from laser beam intensities (for the three first indicated frequencies).

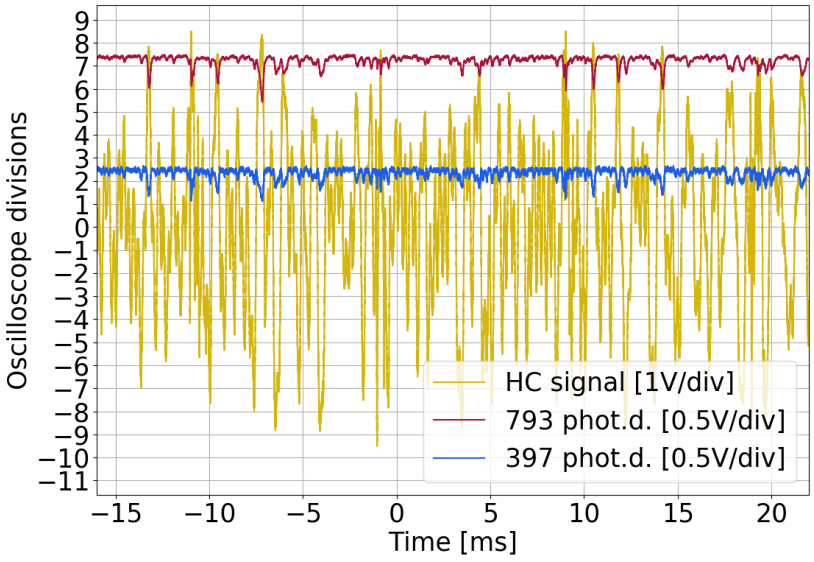

FIGURE 4.9: The yellow curve is the output of the Hänsch-Couillaud, which is the error signal. The red curve is signal from a photodiode observing a Ti:Sa leak behind a mirror in the cavity. The blue curve is signal from a photodiode observing the 397 laser outside the cavity.

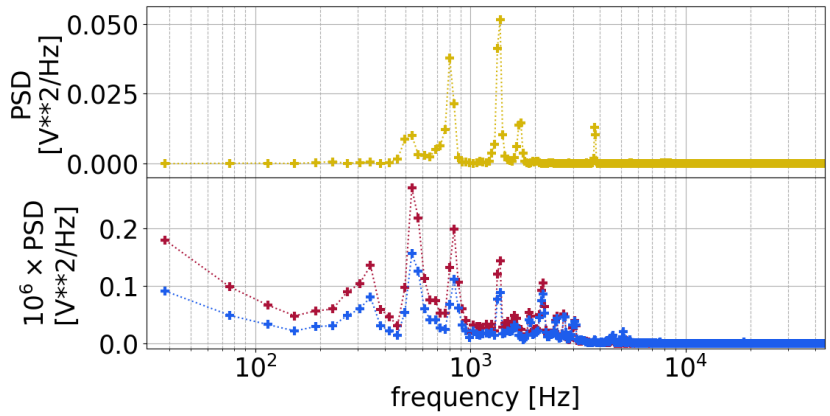

FIGURE 4.10: Power spectral density of the three signals from error signal and laser photodiodes.

4.4.4 Injection in the trap

The two laser beams are injected in the trap along its axis. The 397 nm beam is guided to a vacuum viewport separating the trap in vacuum condition from the atmosphere through several optical elements exhibited in the figure 4.7. The 397 nm beam is superimposed to the 866 nm re-pumper with a dichroic mirror just before the vacuum viewport. The 866 nm re-pumper is transported via optical fiber to the vicinity of the porthole. A half-wave plate allows to change the linear polarisation of the re-pumper. The aperture is radially limited to 5mm of diameter by the electrodes. Mode adapting is set to shape beams so they fit through the limited aperture over the approximately 50cm long path through electrodes in the vacuum chamber.

4.5 Production of $^{40}Ca^{+}$

4.5.1 Neutral calcium beam

Neutral calcium is initially stored in the oven placed below the trap, in the form of 99% pure calcium nuggets provided by Sigma Aldrich®. If required, a description of the atomic beam produced by the oven can be found in subsection 5.3. The calcium beam is produced by resistively heating the oven. Temperatures above 360°C are required in order to provide a beam, corresponding to an oven current of 0.8A. The temperature curve as a function of the oven current is shown in figure 4.11. Equation 4.25, modelling the heating device as a black body, is used to fit the data with a function of the form

$$T = \left(aI^2 + b^4\right)^{1/4} \tag{4.22}$$

with $a = R/Dh\sigma_{SB}\epsilon = 2.6 \cdot 10^{11}$ and $b = T_a \approx 295$ K. With an oven resistance at room temperature of $R = 3.8\Omega$, the product Dh can be computed as $Dh = 2.59 \cdot 10^{-4}$ m^2, or a $h = 12.9$ cm long wire with given radius $D = 2$ mm.

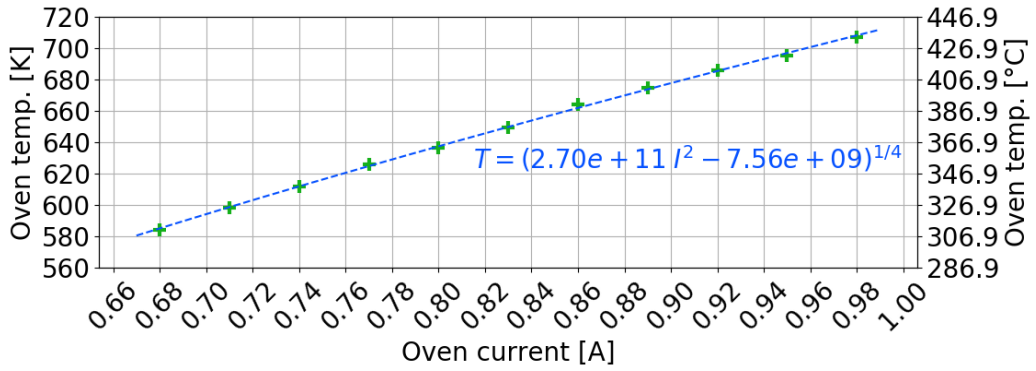

FIGURE 4.11: Oven temperature as a function of oven current, with steps of about 15 minutes at each temperature. Error bars are smaller than the points. The thermocouple is located between the resistive wire and the small copper pot containing the Calcium nuggets.

4.5.2 Ionisation by electron bombardment

The calcium atoms are ionised by electron bombardment. The electron gun providing the electrons is split into two parts, the filament emitting the electrons, and a Wehnelt anode surrounding the filament (Fig. 4.12). The electron current emitted by the filament is an ascending function of the current I_{e-gun} supplied to the filament, and the energy of the electrons is proportional to the acceleration voltage applied to the filament V_{acc}. The electron gun filament is a tungsten wire model W557512 provided by Advent® with diameter of 0.125 mm. Its work function is estimated to 4.5 eV [Höl79]. Its resistance is 0.3 Ω at room temperature, but as it varies a lot with temperature, the following table 4.2 provides the resistance at several filament currents. It is important to notice that the electron gun, when

TABLE 4.2: Voltage and resistance of the electron gun filament depending on the applied current.

I_{e^-gun} [A]	1.60	1.66	1.72	1.77
V_{e^-gun} [V]	1.4	1.5	1.6	1.7
Resistance R [Ohm]	0.875	0.904	0.930	0.960

TABLE 4.3: Ionisation energies data for the first calcium species from A. Kramida et al. [A K20]. Ionisation energy of Ca atom is 6.11315547 eV.

Sp. Name	Ion charge	Ionisation energy [eV]	Ground shells
Ca I	0	6.11315547	[Ar]$4s^2$
Ca II	+1	11.871719	[Ar]$4s$
Ca III	+2	50.91316	[Ne]$3s^2 3p^6$

turned on, perturbs the ion cloud. It may be due to two effects : the influence of the potential applied to the Venhelt, which is in the vicinity of the ions, and the influence of the emitted electrons perturbing the ions and depolarizing the trapping electrodes. It is conceivable to move the cloud along the trap z-axis from few millimetres with an axial voltage during the process in order to minimise the electron induced perturbation.

As presented in the table 4.3, the ionisation energies (Tab. 4.3) of Ca and Ca^+ are respectively 6.11 eV and 11.87 eV, which is commonly accessible via an electron gun. The presence of Ca^{2+} and higher charge ions in the trap can be limited by using low acceleration voltages below 11.87 V. Also it is possible to eject the hypothetical higher charge ions by increasing the trapping parameters so only the singly-charged Ca^+ ions are stable in the trap. This can be done by increasing the radio-frequency voltage up to 200 V. Doing so, no significant difference between a first cloud kept at low parameters and another cloud pushed up to high parameters, was observed, even though the highest -250 V potential was used to accelerate electrons. As a result of this experiment, we claim that nor Ca^{2+} is produced, neither higher charge state Ca ions.

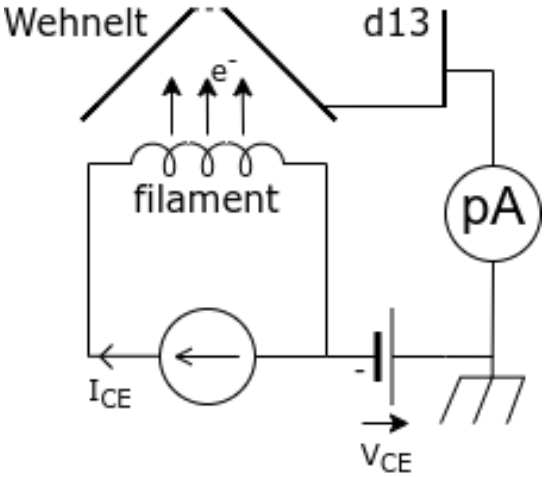

FIGURE 4.12: Electrical layout of the electron gun, and position of the picoAmperemeter during the characterisation of the electron gun. The Wehnelt is a conical shaped electrode with an aperture along its main axis for the accelerated electrons to go through. d13 refers to an electrode according to the layout presented in part II, it is connected to the Wehnelt.

A short experiment done on 13 April 2021 with the electron gun allows to determine the appropriate currents and voltages to use. Indeed it is possible to use the anode as an electron collector in order to measure the electron current I_{d13} depending on the applied

filament current I_{e^-gun} (Fig. 4.13). For the tungsten filament of the electron gun, with fusion temperature T_f = 3422K and R = 0.930 Ω @ 1.72 A, an estimate emittance ϵ = 0.5, the estimated maximum current for the filament is I_f = 4.05A. Nevertheless, because many parameters are approximated it is reasonable to take some margin. Indeed the resistance increases with temperature, the effective length of the filament is only being estimated to h = 1mm, and the emittance is estimated. I would propose to divide the maximum current by two. I_f = 2A is perfectly satisfying as the measured currents are already satisfying for currents below this limit (Fig. 4.13). The highest current ever injected in the filament was 1.75 A.

Also, because the influence of the acceleration over the electron current is negligible with respect to that of filament current (Fig. 4.13), the acceleration voltage is kept as low as possible in order to produce Ca^+ ions without other ions.

In the left part of the figure 4.13, temperature in function of the current are an estimate. The temperatures are computed using formula 4.25, but are considered reasonably close to what is expected. Indeed in this context the filaments are expected to emit electrons in significant quantities for temperatures slightly above 2000 K.

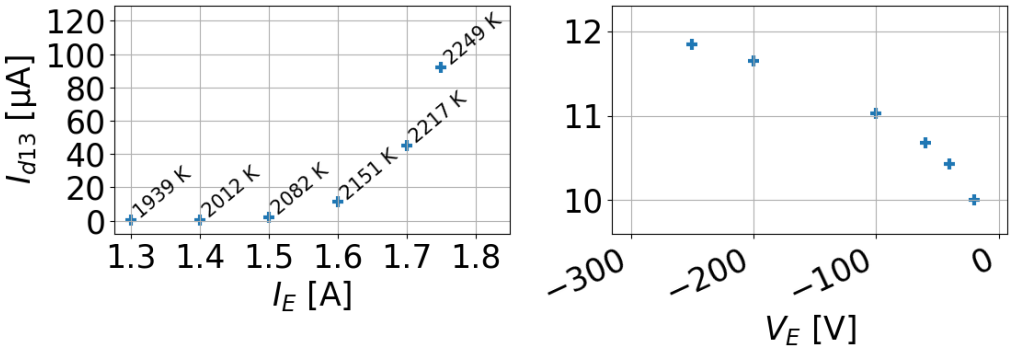

FIGURE 4.13: Collected electron current by the anode d13, (left) depending on the current applied to the filament with estimated filament temperatures indicated, (right) depending on the acceleration voltage. Vertical axis is current in µA. Error bars are smaller than the points.

Box 4.5.1: Thermodynamics of filaments

Thermodynamic considerations In order to understand the thermodynamic of a heating filament or wire supplied by direct current, the black body radiation model gives satisfying results. The electrical power P_{DC} introduced in the filament is usually a well known quantity, that can be related to the power of a black-body radiation P_{BBR}. This approach taken by Halas and Durakiewicz [Hal98] brings interesting considerations when studying the behaviour of filaments such as in electron guns or thermocoaxial wires in ovens. For a given filament with resistance R, cross-section S, perimeter D, with current I flowing through it, the appropriate equations are

$$P_{BBR} = P_{DC} \tag{4.23}$$

$$Dh\epsilon\sigma_{SB}(T_m^4 - T_a^4) = RI^2 \tag{4.24}$$

$$T_m = \left(\frac{R}{Dh\sigma\epsilon}I^2 + T_a^4\right)^{\frac{1}{4}} \tag{4.25}$$

with $\sigma_{SB} = 5.67 \cdot 10^{-8}$ the Stefan-Boltzmann constant, T_a the ambient temperature, ϵ the emittance of the black-body. The curve seems to approach the data with good precision.

Thermionic considerations When heating a material, especially a metal, emission of electrons can occur when the temperature is high enough. A very simple equation (Richardson-Dushman) provides a formula for the current density j of electrons emitted by a heated material. The current density $J_{e^-} = I_{e^-}/Dh$ of electrons emitted by the filament is given as

$$J_{e^-} = \frac{I_{e^-}}{Dh} = A_G(T)T^2 e^{-\frac{W(T)}{k_B T}} \tag{4.26}$$

with $A_G(T) = (1 - \bar{r}(T))\epsilon A_0$ a temperature dependent factor expressed as a function of the reflection coefficient $\bar{r}(T)$ and a constant $A_0 = 1.2017310^6$, $W(T)$ the material work function. Because of all the parameters depending on temperature, it is required to proceed to many experiments in order to individually determine the parameters. Halas and Durakiewicz [Hal98] propose an iterative method in order to solve this problem. This is beyond the scope of this present work but this article provides a method to determine such current. Reader is advised that, even so it could be tempting to use equation 4.25 to replace temperature in Richardson-Dushman (Eq. 4.26), it could be a bad decision. Indeed many parameters are temperature dependent and it is not possible to find an analytical value for electron current as a function of the filament current. I tried to fit the data from figure 4.13 with such equation, but cannot find a satisfying value, and in fact literature frequently warns the reader that it is a frequent mistake to try to compare this formula to electron currents experimentally measured [Her49; Not56].

4.6 Measuring the saturation of the transition

Saturation occurs for laser intensities above a certain value I_{sat}. When the transition is saturated, the fluorescence do not vary linearly with the laser intensity. This is due to the fact that the transition rate Γ_t limits the amount of transitions that are possible to achieve for a given period of time. Saturation intensity is defined as

$$I_{sat} \overset{\text{def}}{=} \frac{\pi}{3}\frac{hc}{\lambda^3}\Gamma_t. \tag{4.27}$$

For our two-level Ca^+ system, $I_{sat} = 7.179 \cdot 10^{-2}$ mW/mm^2.

Saturation can be estimated experimentally in order to choose an appropriate laser intensity. The principle is to measure the fluorescence of the ions as a function of laser intensity, in order to identify how the fluorescence evolves. The measurement of the fluorescence in function of laser intensity is carried out, for the 397 nm laser (Fig. 4.14) and the 866 nm laser (Fig. 4.15). The laser dimensions were as follows : $S_{397} = \pi/4 \times r_x \times r_y = \pi/4 \times 826.6 \times 99.63\ \mu m^2 = 0.065\ mm^2$ and $S_{866} = \pi/4 \times 616.2 \times 649.4\ \mu m^2 = 0.31\ mm^2$, the first dimension being the horizontal diameter, the second the vertical diameter. For each laser intensity, a fluorescence signal is retrieved according to the following procedure : the laser is applied during five seconds to ions, during which the laser is briefly interrupted in order to evaluate the background light. The effective fluorescence signal is the difference between background and maximum signal value, each of it being computed over 31 averaged points (155 ms). In the highest fluorescence levels (2617 counts over 5 ms) standard deviation of the fluorescence signal has been verified similar to those estimated in the case of a Poissonian distribution, thus error bars have been computed according to Poissonian noise. It turns out error bars are never bigger than the points in figures 4.14 and 4.15, thus they are only represented in the first figure 4.14 as black lines[2]. For a fluorescence signal of 2600 counts per 5 ms, the standard deviation is 51, which is 2% of relative error.

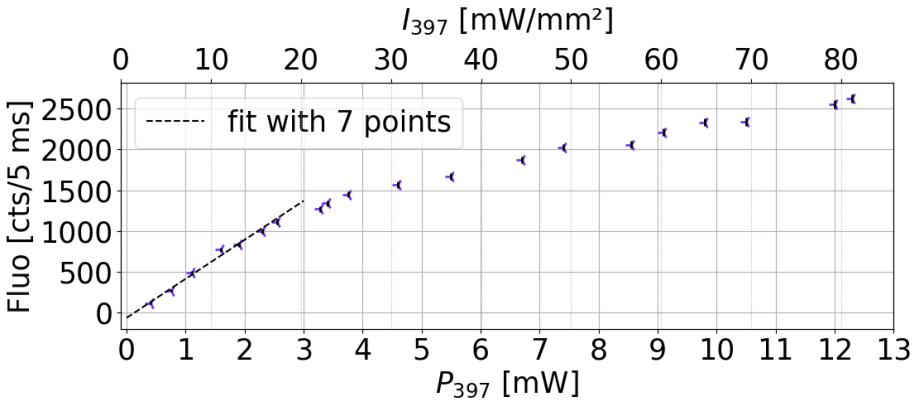

FIGURE 4.14: Fluorescence of an ion cloud against 397 nm cooling laser power, error bars in black. The 866 nm laser power is $P_{866} = 1$ mW. A linear fit is done with the first seven points satisfying a linear variation at sight, before saturation sets in.

4.7 Temperature of ions and laser injection

4.7.1 Ion cloud temperature measurement

Measuring the ion cloud temperature is not an easy task and implies some approximations. One method leans on the velocity distribution width dependency as a function of temperature. By scanning a laser and measuring the ion cloud fluorescence, it is indeed possible to reflect the velocity distribution of ions by the intermediary of the Doppler effect. Indeed, a hot cloud means a large velocity distribution, and thus means a wider range of

[2] Excessively zooming on the figure allows to see the error bars are smaller than the points.

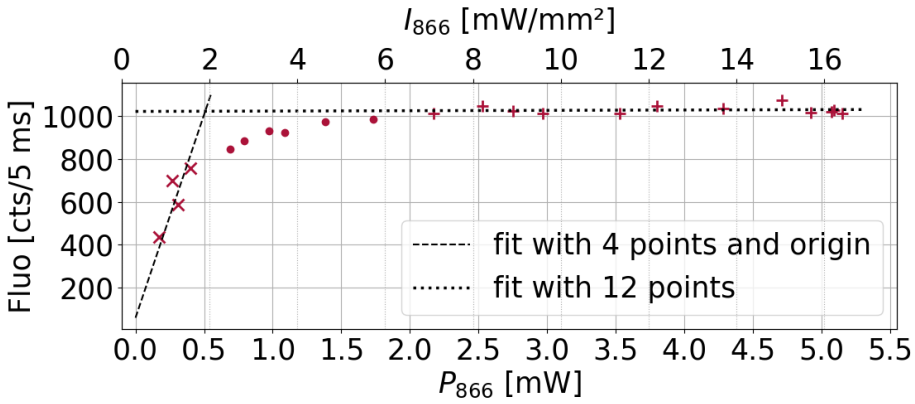

FIGURE 4.15: Fluorescence of an ion cloud against 866 nm cooling laser power, error bars smaller than the points. The fluorescence given for each power originates from a temporal averaging of the fluorescence signal over 100 points. The 397 nm laser power is P_{397} = 2 mW. A linear fit is done with the first four points satisfying a linear variation at sight, with the origin added. Another linear fit is done at high laser power when the fluorescence is obviously constant.

frequencies must be swept in order to reach the whole distribution. By scanning the blue cooling laser (Fig. 4.17) the cooling itself varies. Thus scanning the blue to determine the temperature can only provide an estimate of the temperature, always higher than the real ions temperature for a given laser setting. The other drawback of scanning the blue laser is that when the frequency reaches the value where only co-propagating ions are in resonance, the cloud suddenly heats and fluorescence is lost, so only half of the distribution can be explored. Nevertheless such a method provides satisfying result for "hot" clouds ($T > 1K$). In contrary, keeping the cooling laser constant and scanning the red repumper laser (Fig. 4.16) can ensure a more constant laser cooling, nevertheless the existence of a dark state in which ions are not sensitive any more to cooling must not be neglected. Under the assumption the frequency fluorescence during a laser scan with central frequency ω_0 has a Gaussian profile, it is possible to link its full width at half maximum (FWHM) $\Delta\omega_D$ to the temperature T.

$$\frac{\Delta\omega_D}{\omega_0} = \frac{2\sqrt{\ln 2}}{c} \times 2230\text{ms}^{-1}\sqrt{\frac{T}{300\text{K}}\frac{1\text{a.m.u}}{M}} \tag{4.28}$$

with c the speed of light, T the temperature in Kelvin, M the mass in atomic mass units. Thus the temperature is

$$T = 300M\left(\frac{\Delta\omega_D}{\omega_0} \times \frac{c}{2230 \times 2\sqrt{\ln 2}}\right)^2. \tag{4.29}$$

4.7.2 Fluorescence signals and their specificities

At first approximation, it is obvious that the scanning of a laser should give a Gaussian fluorescence signal. This statement is based on the fact that the probability of excitation

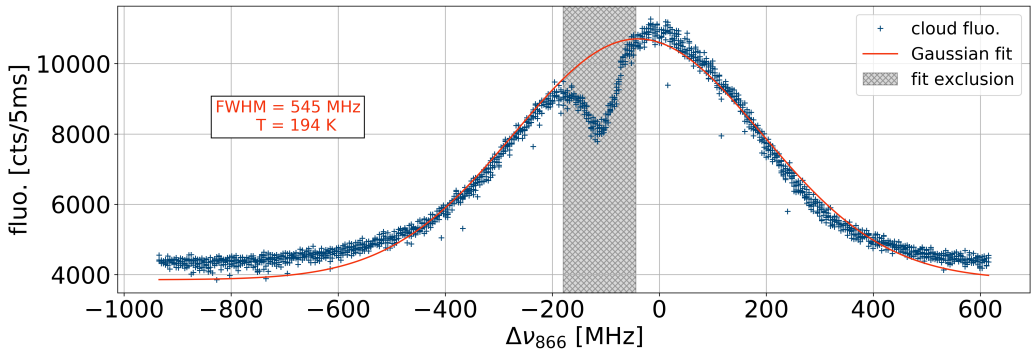

FIGURE 4.16: Fluorescence of a cloud during a repumper laser scan. P_{397} = 14.6 mW, P_{866} = 3.85 mW, λ_{397} = 793.70013 nm, U_{RF} = 41.43 V, U_{DC} = 2.5 V. Recorded on 3 July, 2019.

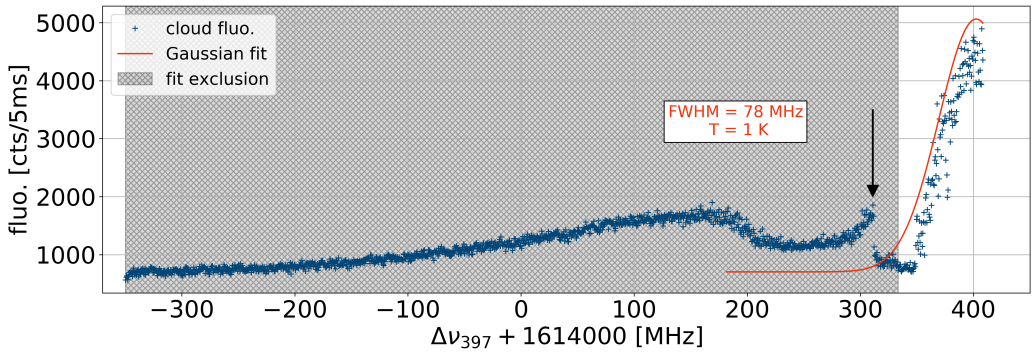

FIGURE 4.17: Fluorescence of a cloud during a cooling laser scan. P_{397} = 2.4 mW, P_{866} = 8.1 mW, λ_{866} = 866.21386 nm, U_{RF} = 24.25 V, U_{DC} = 0.6 V. The black arrows indicate the timing of liquid to crystal phase transition. Recorded on 16 April, 2021.

varies as a Gaussian curve as a function of the detuning $\Delta\omega = \omega_0 - \omega$. Nevertheless, many phenomena modify the fluorescence profile from its expected Gaussian behaviour.

First, phase transitions in the cloud produce fluorescence variations looking like sudden drops and jumps. The physical details of those phase transitions have already been discussed page 58 (see also appendix D). The fluorescence variation indicated by an arrow in figure 4.17 is representative of what is happening at phase transition. Diedrich et al. [Die87] tells us, "the jumps in the spectra are caused by a phase transition [...] between a state of uncorrelated motion [...], where the radio-frequency heating is important, and an ordered state characterised by a sharper spectral structure", this sharper spectral structure reflects a narrower velocity distribution of the ions. Moreover, in that case cooling can become quickly much more (or less) efficient, making hard to correlate the fluorescence signal to the cloud state. About the significance of the fluorescence dip, Hornekær and Drewsen [Hor02] comment that "the fluorescence dip, in general, is not an indication of a transition into a shell structure, or fully crystalline, regime. Our observations indicate that the fluorescence dip marks the transition into a liquidlike state, and that the formation of shell-structure ordering evolves as a continuous process from that point." This continuous process is also visible in their own numerical simulation with finite plasmas.

Second, dark states appear for certain detuning values, in which some atoms fall, lowering the fluorescence compared to the simple Gaussian. Those dark states are seen when a particular relation between both detunings is reached. The fluorescence lowering induced by the dark state is less pronounced than when a phase transition occurs, and is much broader. A dark state is visible in figure 4.16 in the hatched area (around -100 MHz). It is also visible in figure 4.17 before the arrow (from 200 to 300 MHz approximately). More details on this phenomena are given in Collombon [Col19a] thesis.

4.7.3 Effect of laser angle of injection

Initially, the lasers were introduced in the trap with a 30° angle with respect to trap z-axis. This was done with the intent to address all components of ion velocities through the non-null projection of laser wave-vectors **k** on the three axis. It turns out laser cooling is much less efficient this way, compared to the later layout where lasers are introduced along the trap z-axis. The main reason for that is Doppler effect being increasingly preponderant with laser angle due to the radial velocities of ions. Indeed, when introduced along the axis, the laser wavelength is unmodified regarding radial velocities, and the transition efficiency is only sensitive to axial distribution of velocities. It would be no problem if the cloud was a pure real gas in Maxwell-Boltzmann equilibrium, nevertheless due to the different kind of trapping field confining the ions, radial and axial velocity profiles are not the same. While radially the ions are literally shaken by the radio-frequency field, only a weak static potential is confining axially. The Doppler effect expresses as a scalar product between the ion velocity and the wave-vector (Eq. 4.4), thus, if the laser is introduced along the z-axis it is along a direction normal to the direction of radial velocity, the scalar product is null, thus no significant Doppler effect can be introduced whatever the speed of ions along the radial direction. The greater the angle with which the lasers are introduced with respect to the trap axis, the higher the Doppler effect due to radio-frequency motion – micromotion. Indeed, because the ions are oscillating back and forth in the radial direction, and laser has a projection over this direction, the scalar product $\mathbf{k} \cdot \mathbf{v} \neq 0$. For the atoms the laser frequencies appear shifted : increased when the atoms go towards the laser and decreased when the atoms go in the same direction as the laser. In order to properly cool the ions it is required to address the atomic transition in both cases where the shifts are of opposite signs. This renders the lasers less efficient in cooling, especially if the shifted frequencies are so far from each other that it is not possible to address both with one laser.

Going from the laser introduced from the side with 30° angle to laser introduced along the trap axis increased the cooling so the temperature reached could be at least decreased by 2 orders of magnitudes. No crystalline structure could be observed before the lasers were introduced along the trap z-axis.

First temperature measurements were carried out scanning the repumper laser. Initially, the temperature of the ions was around 2000 Kelvin. With wavelength $\lambda_{397} = 396.85034\text{nm}$[3] the repumper had to be scanned over the range $\lambda_{866} = [866.22055, 866.20545]$ ($\Delta\nu_{866} =$

[3] The Ti:Sa laser wavelength twice this number because of the frequency-doubling process occurring in the meantime.

6.03GHz). The fluorescence scan showed a frequency width at half maximum of $\approx$ 1.75GHz. Later, as shown in figure 4.16, temperatures of the order of 100 K could be reached, still with laser with 30° incidence. Only when the lasers were introduced longitudinally temperatures of 1 K and below could be reached. In that case the appropriate cooling wavelength was around λ_{397} = 396.84988 nm. The figure 4.17 shows a fluorescence profile with a fit only for the last part of the curve where the cloud is crystalline. While the Gaussian curve seems a bit off the measurements, it provides an estimate of the temperature of T = 1 K., which is an upper estimate for the real value.

Conclusion of part I

The basics of ion trapping and laser cooling have been explained in this chapter, alongside with the more advanced concepts required to match the specificities of `GiantMol` applications. In particular, the `GiantMol` experiment being the framework for a detector for heavy molecules, its purpose is not only to stabilise and cool trapped ions as much as possible, but keep them in a state sensitive enough to be significantly perturbed by a charged particle. This sensitivity translates into a tendency for ions to heat to temperatures above room temperature, which is radically different from the usual applications of trapped ions. The extensive study of the typical linear Paul trap geometry have been carried out. The trap from `GiantMol` has been investigated and characterised and the necessity for improvement in domains such as trap defects and laser cooling stability are to be made for the experiment. The understanding of more complex concepts related to ensembles of ions, such as radio-frequency heating, are important in order to properly manoeuvre the apparatus as a detector for charged molecules. Thus a more quantitative analytical formulation of radio-frequency heating should be seek for. Those analytical elements will reappear later when dealing with the numerical simulations, in part dedicated to compensate the lack of formalism able to render radio-frequency heating in a satisfying, predictable, way. The study of trapped ions in the framework of dynamical systems can be useful because it provides another tool to discuss the behaviour of the ions and their stability. In particular this is adapted to discuss the non-linearities. Using dynamical systems approach, Brewer et al. [Bre90] show that "the route to chaos is due solely to ion-ion collisions". For them this is the nonlinear Coulomb interaction occurring when ions collide that cause transient instabilities. In return, those instabilities can be interpreted as the reason why the ions leave their stable trajectories in the trap, and considering radio-frequency field, why they gain energy. A careful analytical study of such system may help relate the trapping regime with the intensity of the heating. An idea to circumvent the solicitation of a complex analytical model for radio-frequency can be found in a recent article from Kalincev et al. [Kal21], “Motional heating of spatially extended ion crystals”, highlights another mechanism than that of radio-frequency heating in order to bring heat into the cloud. This method relies on the displacement of the ions away from the radio-frequency nodal lines, which in turns brings excess micromotion and radio-frequency noise to the center-of-mass motion [Ber98].

Part II

THE MOLECULAR SOURCE

Introduction

"Ne t'attarde pas à l'ornière des résultats."

– René Char *in* Fureur & Mystère

In the previous part, the description of the trapped ions, constituting the detector part of `GiantMol` has been carried out. It included the presentation of the trapping method, the cooling of the ions and the multiple effects relevant in the context of `GiantMol`. The `GiantMol` experiment requires a molecular source in order to be able to fully test the working principle. The source should create molecules as heavy as possible with as low a charge state as possible.

The goal of this part is to explicitly describe the apparatus generating and manipulating the charged molecules. This part is cut into three chapters. Chapter 5 is devoted to the thorough description of the molecular source. The molecular source includes the electrospray responsible for the generation of the charged molecules in a gas state, along with the first vacuum elements accommodating the inlet flow to low pressures. Then chapter 6 is dedicated to the description of the guiding of charged particles following the step mentioned before. In both chapters above mentioned, the fundamental and analytical considerations upon which the related apparatuses are based on is thoroughly carried out. The intent is to provide an intuitive understanding of what is happening in such apparatus. Also this serves as a base in order to operate `GiantMol` and propose improvements. A careful attention is paid to the recent state of the art developments achieved after the prototype was designed, before my arrival in the team. Then chapter 7 is dedicated to the description of the detection with test measurements of small molecules in `GiantMol` explained.

In our prototype, the `GiantMol` Ion Cloud Detector (GICD) based on the quadrupole ion trap above mentioned in part I is inserted in a vacuum chamber with pressure in the range of 10^{-9} mbar, maintained by an ion pump (see section 2.2). The figure II.1 sums up the apparatuses devoted to molecule guiding surrounding the GICD. Its longitudinal axis is combined with the axis common to a set of electrodes devoted to the guiding of the molecular ion. The molecular source is an ElectroSpray Ionisation source (ESI) [Fen89; Fen90] at atmospheric conditions, leading to a series of chambers separated by small apertures so they can be differentially pumped to the lowest pressure. Through a capillary duct, the ESI atmospheric beam is injected in a first chamber pumped to 10^{0} mbar. Then this beam is brought through a small skimmer aperture to a second chamber pumped to 10^{-3} mbar, where an octupole guides it to its next destination. Through a third aperture electrically driven with pulses, the molecules are extracted from the octupole and driven into a third chamber brought at 10^{-6} mbar. In there a quadrupole beam bender orientates the molecules to the next and last chamber where the GICD is located. Control MCP are located in

the bender and GICD chambers. Electrodes operated following the principle of ion optics are located along the molecular ion trajectory. In this chapter, the variables associated with their respective physical quantities are summed up in the table 5.1, with additionnal details on frame 5.2.1.

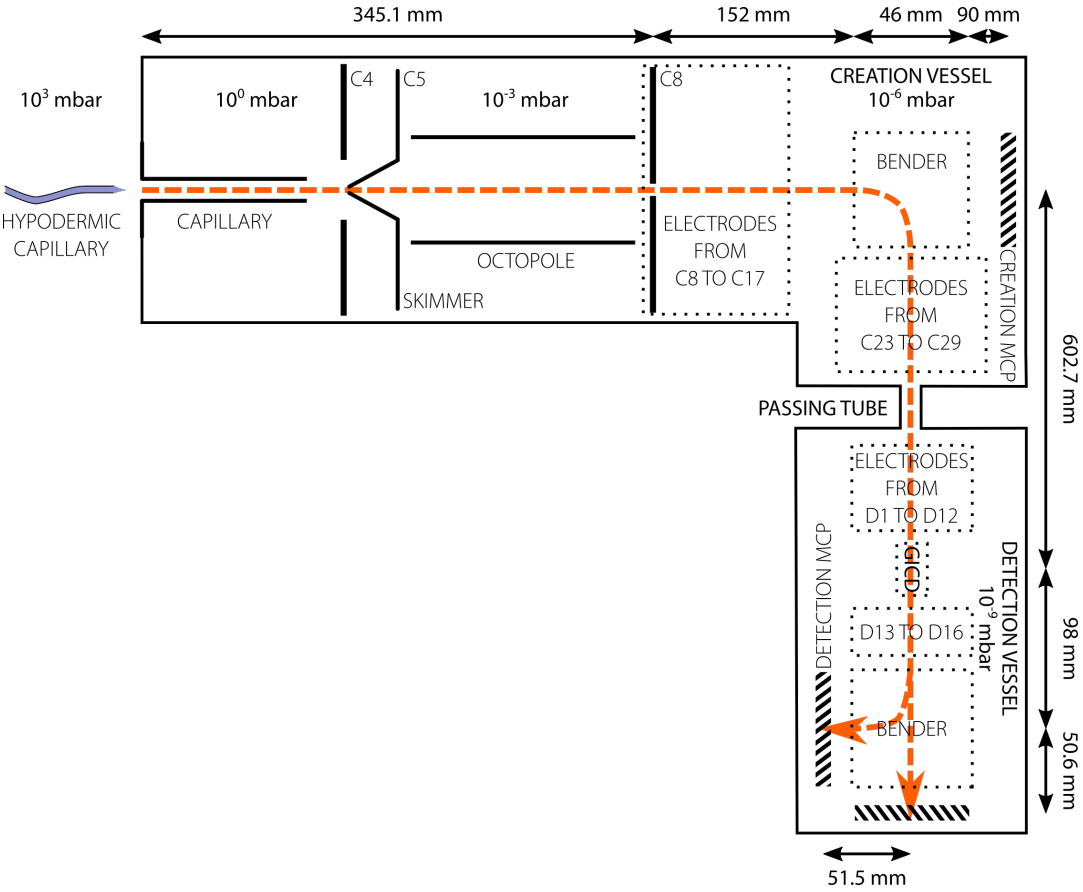

FIGURE II.1: Electrical layout of guiding elements from the electrospray to the GICD and MCP beyond. The distances refer to the dimensions in the plan. The orange dashed arrow indicate the trajectory of the molecular ions (M^+).

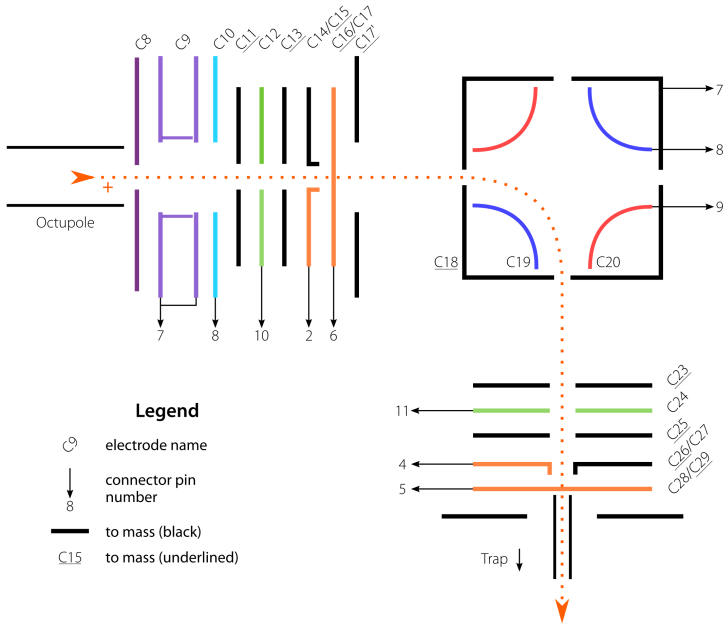

FIGURE II.2: Electrical layout of guiding elements from the exit of octopole until the tube separating the creation chamber at 10^{-6} mbar to the GICD vessel at 10^{-9} mbar.

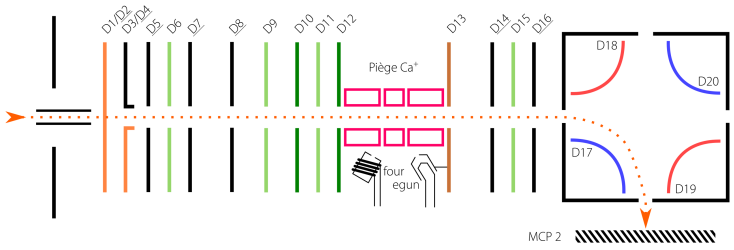

FIGURE II.3: Electrical layout of guiding elements in the detection chamber at 10^{-9} mbar.

Chapter 5

Molecular source

The molecular source, designates the part of the apparatus producing charged molecules and guiding them to the detection trap. The first component is the electrospray source [Fen90] producing the charged molecules in a manipulable state, which are then controlled by other elements mainly for the purpose of guiding them to their destination. Because the settings of the second part depend on the charge-to-mass ratio, the operation of the electrospray source must be very stable and reproducible.

5.1 Electrospray Ionisation Source

5.1.1 General principle

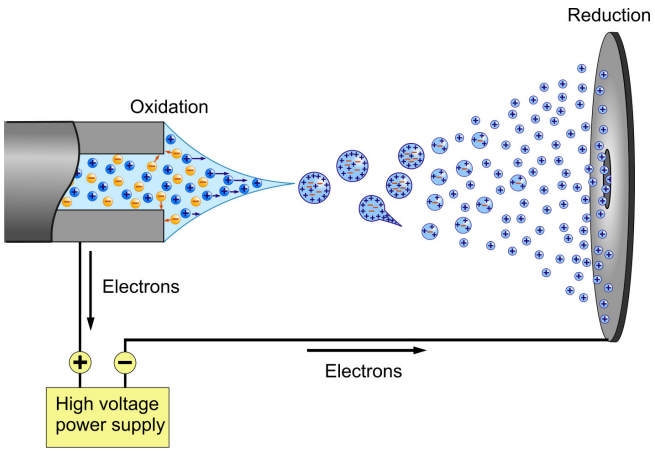

FIGURE 5.1: Diagram of electrospray ionization in positive mode: under high voltage, the Taylor cone emits a jet of liquid drops. The solvent from the droplets progressively evaporates, leaving the remaining droplets more and more charged. When the charge exceeds the Rayleigh limit the droplet explosively dissociates, leaving a stream of charged (positive) ions.

An electrospray source (Fig. 5.1) is a device able to produce a beam of charged molecules from a solution. The electrospray source is a combination of a capillary – in our case a hypodermic needle – in which the molecule in solution flows at a set throughput, and an inlet capillary at ground constituting the entrance of the vacuum chamber. A high voltage ($\approx 2-3$ kV) is applied to the solution capillary exit and the inlet capillary is heated ($\approx 100^{\circ}$C) and pumped. At the exit of the solution capillary, due to the high voltage difference with respect to the inlet capillary at ground, a Taylor cone is building up. From there, droplets form and are ejected towards the inlet capillary. Two mechanisms are often highlighted for the production of the charged molecules from the droplets :

TABLE 5.1: List of hydrodynamic parameters used in chapter 5.

a_0 [m]	Droplet radius.
A_c [m^2]	Capillary cross-section.
$B = 2\pi R_c$ [m]	Wet perimeter in capillary.
c [$m\,s^{-1}$]	Sound velocity in gas (depends on local conditions).
$d_{air} = 0.364$ [nm]	Kinetic diameter of nitrogen (N_2).
$D_c = 2R_c$ [m or cm]	Capillary diameter.
f_i	Velocity distribution of a molecular beam.
Kn	Knudsen number.
L_c [m or cm]	Capillary length.
$M_{air} = 28.9647 \cdot 10^{-3}$ [$kg\,mol^{-1}$]	Dry air molar mass at standard conditions.
Ma	Mach number.
$N_A = 6.022141 \cdot 10^{23}$ [mol^{-1}]	Avogadro number.
$P_{in} = P_{atm}$ [Pa or mbar]	Atmospheric pressure at capillary entrance.
$P_1 = P_\infty$ [Pa or mbar]	Pressure in the vessel downstream the capillary.
Q_v [$m^3\,s^{-1}$ or $L\,s^{-1}$]	Volumetric flow.
$R = 8.134$ [$J\,K^{-1}\,mol^{-1}$]	Molar gas constant.
R_c [m or cm]	Capillary radius.
Re	Reynolds number.
T [K]	Temperature.
u [$m\,s^{-1}$]	Flow velocity.
z_C [m]	Distance from capillary nozzle to end of continuum flow.
z_M [m]	Distance from capillary nozzle to Mach disk along capillary axis.
z_S [m]	Distance from capillary nozzle to skimmer aperture.
α [$m\,s^{-1}$]	Thermal velocity of gas.
γ	Gas specific heat ratio.
η [Pa s]	Dynamic viscosity.
λ [m]	Mean free path.
ν_{HS} [s^{-1}]	Collision rate for any molecule in the gas. Number of collision per second.
σ_D [$J\,m^{-2}$]	Surface tension.
σf_i	Full-Width at Half-Maximum of function f.
0	As an index, indicate the physical quantity is taken in stagnation conditions, i.e where the flow velocity is null upstream the capillary.
∞	As an index, indicate the physical quantity is taken asymptotically.

- **Charge Residue Model** proposed by Pierre Dole [Dol68], is the intuitive description where charged molecules are isolated after the droplets containing charges successively evaporate and divide until the sole charged molecule remains. The division process is due to surface tension inability to compensate for Coulomb repulsion intensifying when droplet radii decreases (see Box 5.1.1). ;
- **Ion Evaporation Model** proposed by Iribarne and Thomson [Iri76], is a more sophisticated description where the charged molecule is ejected from the droplet by the Coulomb interaction. When gradually the solvent vaporises, droplets radius decrease and charge density among the droplets increases. When the size of the droplet is small enough, typically around 10 nm, the charge density in the droplet is high enough to provoke ejection of the molecule.

The efficiency of the production of charged molecules depends on a combination of chemical and physical parameters developed later, such as the surface tension of solvent, its pH, the temperature of the capillary, the distance travelled by the droplets in the atmosphere and the voltage applied.

Box 5.1.1: Rayleigh instability

The stability condition of a droplet with charge Q_D, radius a_0, surface tension σ_D, is given by the following formula :

$$Q_D^2 < 16\pi a_0^3 \sigma_D \tag{5.1}$$

Originally calculated by Rayleigh [Ray82] in 1879 this formula has been verified by Dawson [Daw70] in 1970. The recommended size for a droplet in order there is only one macromolecule in the droplet is approximately 0.1 µm [Dol68]. This article also states that the "electric field at the tip of the liquid orifice should be of the order of magnitude of 40 kV cm^{-1} and the liquid should have an electrical conductivity in the range $10^{-9} - 10^{-8}$ Ω^{-1} cm^{-1}" [Dol68]. The electrical potential V can be expressed as $V = Q_D/a_0$. Equation 5.1 can then be rewritten as

$$V < \frac{Q_D}{a_0} = \frac{\sqrt{16\pi a_0^3 \sigma_D}}{a_0} = \sqrt{16\pi a_0 \sigma_D} \quad \text{statV (CGS-ESU)}^1 \tag{5.2}$$

$$V < c_{cgs} \cdot 10^{-8} \sqrt{16\pi a_0 \cdot 10^2 \sigma_D \cdot 10^3} \quad \text{V (ISU)} \tag{5.3}$$

This in turn provides us with a formula for the limit radius of a droplet submitted to a voltage V :

$$a_0 > \left(\frac{V}{c_{cgs} \cdot 10^{-9}} \frac{1}{\sqrt{16\pi\sigma_D \cdot 10^3}} \right)^2 \text{m.} \tag{5.4}$$

With an estimated surface tension of 34.685 mNm^{-1} for a 50:50 methanol:water mix [Vaz95], a voltage of $V = 2700$ V, the minimum radius of a droplet produced by the electrospray is 465 µm.

[a] CGS-ESU units : 1 statV = $c_{cgs} \cdot 10^{-8}$ V, $c_{cgs} = 29.9792458 \cdot 10^{9}$ cm/s, σ_D erg/cm^2 = 10^{-3} N/m or J/m^{2}ŝ.

5.1.2 Operation of the electrospray ionisation source

In the case of the `GiantMol` experiment, the electrospray source is operated with a positive voltage of 2700 V applied to the needle, while the entrance capillary is surrounded by a counter-electrode set to ground. The needle is kept between 4 and 5 millimetres from the entrance capillary. The throughput is controlled by a laboratory SyringePump®model NE-300, and is typically set to 10 µL/min but can be set to 15.

The molecule under investigation is dissolved in a mixture of water and methanol in equal volume (50v:50). Considering methanol (CH_3OH) with density 791 kg/m^{-3} @ 25 °C, the 50v:50 mix above mentioned is in terms of mass proportion equivalent to 44m:56. A few droplets of acetic acid can be added to the solution in order to lower the pH and facilitate the protonation of molecules. Notably, methanol can be replaced by acetonitrile (C_2H_3N) with density 776 kg/m^{-3} @ 25 °C. Surface tensions for methanol:water mix can be obtained in Vazquez, Alvarez, and Navaza [Vaz95]. In the above mentioned conditions, the surface tension of the methanol:water mix solution is σ_D^0 = 34.685 mN/m @ 25 °C.

The pressure between the needle and the entrance capillary is that of the atmosphere, while the pressure at the exit of the capillary is 1 mbar. It faces a conical shaped skimmer with aperture 1 mm beyond which pressure is 10^{-3} mbar. The exit of the capillary is slightly offset with respect to skimmer aperture, in order to filter out the core part of the flux that contains condensed solvent droplets detrimental for the detectors. The distance between the capillary output and the skimmer can be set within range of few millimetres to centimetres.

5.2 Capillary physics

Because it is required to have molecules go from the electrospray needle in atmospheric pressure, to the detector in the vacuum chamber ($<$ 1 mbar), a device is needed that ensures the proper reduction of the pressure at the entrance of the vacuum chamber. It is demonstrated that a capillary is the most efficient device to handle the inlet flow [Cam84] and in modern commercial analytic instruments, inlet capillaries are still the privileged choice [Wiß16]. Basically it is a pipe small enough to guarantee the entering flow of gas is not substantially degrading the vacuum, also used to vaporise the remaining solvent by heating the gas. The stability and reproducibility of the detection signal relies on the stability of the flow in the capillary. In this respect, because of reproducibility issues regarding the detection signal of molecules in our experiment, the behaviour of the flow in the capillary was investigated. It turns out that this field is still controversial and a current debate animates the community on what is happening in this situation. Nevertheless an

overview of this debate allowed to highlight the important elements that help understand how does the flow is behaviouring in the capillary and beyond.

To model the flow, the throughput and its turbulence, several analytical models are identified but they all have flaws. Mostly, in the best case the throughput can be estimated with a relative error of 20% with respect to experiments, which is good enough to design the experiment. An extensive review from Wißdorf et al. [Wiß16] compares those models to experiments. In the following I will be presenting the Hagen-Poiseuille laminar model that is usually referred to in the domain of mass spectrometry when it comes to capillaries. I will also present the turbulent model from Wutz, Adam, and Walcher [Wut92], referred as Wutz/Adam turbulent model in Wißdorf et al. [Wiß16]. Then I will discuss the limits to this models, summarize the controversies on this domain and point out the references experimentally and numerically studying the problem of capillary flow. The modelling of the flow in the capillary can be done with several models, either laminar or turbulent. While in the field of mass spectrometry the flow is considered laminar in the inlet capillaries, there is currently a controversy on this topic, with several works highlighting at least turbulent transitions in the capillaries. The need for a model better than that of Hagen-Poiseuille is identified. The inlet capillary used in `GiantMol` is a metallic pipe L_c = 114 mm long with a diameter of D_c = 400 µm.

Box 5.2.1: Flow characteristic numbers

Here are exhibited the definition of important dimensionless numbers. Those numbers characterising the hydrodynamic fluids are important in order to determine whose are the dominant effects to consider and thus which approximations can be done in order to simplify the computations. Many more details can be found from Rapp [Rap17].

Reynolds number

A flow in a pipe can be laminar, turbulent or in an intermediate state. Depending on the situation the determined values for the flow can be quite different and an estimate for the flow state must be provided. The Reynolds number Re is the parameter of choice in order to determine in which case the fluid situates. It is a dimensionless parameter defined as the ratio of internal forces to viscous forces within the fluid.

$$\mathrm{Re} \overset{\text{def}}{=} \frac{\overline{v} D_c \rho}{\eta} = \frac{4 M_{molar} Q_v P}{R T_0 B \eta} \tag{5.5}$$

with $\overline{v}$ the mean velocity of the fluid, D_c the capillary diameter, η the dynamic viscosity, $B = \pi D_c$ the capillary perimeter. For $\mathrm{Re} < 2000$ a flow will be considered laminar, for $\mathrm{Re} > 4000$ turbulent, and in between the flow exhibits instabilities that can lead to turbulent transitions.

Mach number

The velocity of a fluid can be characterised relatively to the speed of the sound in the fluid c, given the actual conditions. This leads us to describe the Mach number as

$$\mathrm{Ma} \overset{\text{def}}{=} \frac{\overline{v}}{c} \tag{5.6}$$

$$c = \sqrt{\gamma \frac{P}{\rho}} \tag{5.7}$$

with γ the ratio of the specific heats, $\gamma = 1.4$ in the case of an ideal diatomic gas at room temperature. For Mach numbers $M < 0.8$ the regime is said sub-sonic, for $0.8 < M < 1.2$ the regime is said trans-sonic, and above the regime is said supersonic $M > 1.2$, or hypersonic $M > 5$.

Knudsen number

The mechanics to which a flow is submitted depends on the ratio of the molecular mean free path length λ to some representative physical length scale L. Knudsen number is that ratio so that

$$\mathrm{Kn} \overset{\text{def}}{=} \frac{\lambda}{L} = \frac{\eta}{P}\sqrt{\frac{\pi k_B T}{2m}} \times \frac{1}{L}. \tag{5.8}$$

It is representing the rarefaction of a flow. For $\mathrm{Kn} < 0.01$ it is said continuum flow, for $\mathrm{Kn} > 10$ it is said free-molecular flow, and for values in between it is said slip/-transitional flow. The characteristic length can be, the diameter of a duct, the cross-section of a flow, the size of an object in the flow (wing blade for example).

5.2.1 Basic laminar flow model

The simple **Hagen-Poiseuille equation** , under the assumption that the flow is laminar and the capillary is "long enough", provides the pressure difference ΔP between the capillary ends as function of the volumetric flow rate Q_v,

$$\Delta P = P_{in} - P_{out} = P_{in} - P_{\infty} = \frac{8\pi\eta L_c}{A^2} Q_v, \tag{5.9}$$

with η the dynamic viscosity, L_c the length of the pipe, $A = \pi R_c^2$ its cross section. The ∞ symbol signifies that the value is taken far enough from the nozzle, and that it is the value to which it tends asymptotically. This equation is also only valid when the pipe is long enough so that $L_c/R_c > \mathrm{Re}/48$. This equation leads to a very odd situation because at this point the Reynolds number can only be an estimate because the flow is not known. Typical values found in the literature for capillaries similar to that of `GiantMol` can reach values as high as 4000 [Wiß16], which is the sign for a turbulent flow, contradicting the

fundamental assumption in Hagen-Poiseuille equation. The problem comes from the fact that in Hagen-Poiseuille the Reynolds number is considered constant along the capillary which is false. Nevertheless, using $\mathrm{Re} = 4000$, it is possible to compute $\mathrm{Re}/48 = 83.3$, which is much smaller than $L/R_c = 287.5$. Hypothetically, this means that the capillary is long enough. **Hagen-Poiseuille equation** can be written as

$$\boxed{Q_{v-HP} = \frac{A^2}{8\pi\eta L}\Delta P.} \tag{5.10}$$

This allows for the determination of the following values (see Box 5.2.1)

$$Q_{v-HP} = 2.65 \cdot 10^{-5}\mathrm{m}^3/\mathrm{s} \tag{5.11}$$

$$= 1.59\ \mathrm{L}/\mathrm{min} \tag{5.12}$$

$$v_{HP} = 210\ \mathrm{m}/\mathrm{s} \tag{5.13}$$

$$\mathrm{Re}_{HP} = 505 \tag{5.14}$$

$$\mathrm{Ma}_{HP} = 17.8. \tag{5.15}$$

Those values are close from the one retrieved in the literature, but with some refinements it is possible to find better formulas for the capillary flow. Indeed in Wißdorf et al. [Wiß16] other models are compared and found in better agreement with experiment (Fig. 5.2). The main problem with Hagen-Poiseuille is that the values provided by this equation do not correspond to the measured flows in the typical mass spectrometry capillaries. For instance, Gimelshein et al. [Gim14] indicate that the mass flow computed with Hagen-Poiseuille is "more than four times larger than the expected mass flow rate based on the CFD predictions". Also this Hagen-Poiseuille equation does not account for turbulences that are observed and provide unrealistically high velocities, above $\mathrm{Ma} = 1$, which is in contradiction with experiment and simulations (Fig. 5.3). The next models are more advanced and show a more realistic behaviour, with saturation of the flow around a pressure difference of 800hPa, which is the case in numerical simulations Gimelshein et al. [Gim14] and Skoblin et al. [Sko17].

5.2.2 Wutz/Adam flow model

As reported in Wißdorf et al. [Wiß16], the agreement with experiment of three models are compared, for several capillary arrangements and materials. Two models from Wutz, Adam, and Walcher [Wut92] called laminar and turbulent Wutz/Adam model, and one from Livesey [Liv04], are tested. The latter, implying an iterative process in order to solve the flow, is not described here for simplicity and because the model from Wutz, Adam, and Walcher [Wut92] already provides a satisfying result. The two **Wutz/Adam equations** for flow are

$$Q^{lam}_{v-W/A} = \frac{\pi}{128\eta}\frac{D_c^4}{L_c}\frac{p_{in}^2 - p_{out}^2}{2}\frac{1}{p_{in}}\frac{60}{10}\ \mathrm{L/min} \tag{5.16a}$$

$$Q^{turb}_{v-W/A} = D_c\left(\frac{20\pi^2}{16\cdot 3.2}\frac{D_c^3(p_{in}^2 - p_{out}^2)}{2L_c}\right)^{4/7}\left(\frac{RT_0}{M_{molar}}\right)^{3/7}\left(\frac{4}{\pi\eta}\right)^{1/7}\frac{1}{p_{in}}\frac{60}{10}\ \mathrm{L/min} \tag{5.16b}$$

with lengths in cm, pressures in mbar, and constants in ISU. The $^{60}/_{10}$ coefficient is here to ensure unit consistency[1]. Both flows are compared to flow obtained with Hagen-Poiseuille equation and Bernoulli's principle (Fig. 5.2).

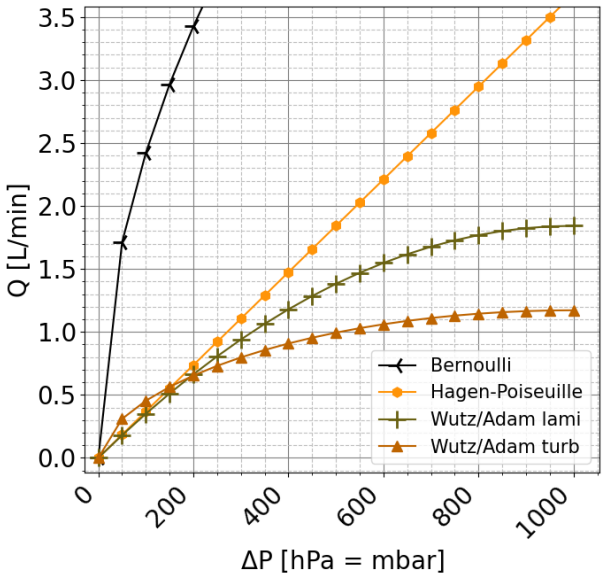

FIGURE 5.2: Comparison of flow deduced from Bernoulli equation, Hagen-Poiseuille equation and the two Wutz/Adam equations. The capillary characteristics are those of `GiantMol` experiment. Bernoulli equation is an upper limit and quickly grows out of the displayed area. Laminar W/A model converge asymptotically towards Hagen-Poiseuille for small ΔP.

5.2.3 Detailed controversy

It turns out, the recent article from Wißdorf et al. [Wiß16] initiated the controversy on the turbulence of the flow in capillaries. They claim that "there is currently no investigation on the gas flow of common inlet capillaries that clearly verifies the generally assumed laminar flow conditions" and in fact there is only few studies comming after them, not systematically agreeing. Skoblin et al. [Sko17] investigated the problem using their own numerical simulations and experiments both from them and Wißdorf et al. [Wiß16]. Using the laminar Wutz/Adam model they suggest that "the detailed numerical laminar model of the flow describes the dependence of the volume flow rate on the pressure difference between the atmospheric and forevacuum volumes of the interface very well". While they do not reject that turbulent transitions can occur, especially in the high pressure part of the duct, they emphasie that "at the low pressure end of our simulations the flow must be laminar", with Reynolds numbers below 2000. In Skoblin et al. [Sko17] the assumptions of Wißdorf et al. [Wiß16] and Livesey [Liv04] are also criticised. Numerical works from Gimelshein et al.

[1] While this detail may seem trivial, the units are not explicit in the works referred. Especially, this factor $^{60}/_{10}$ is not appearing explicitely while it is required, this is why I explicitely emphasises it.

[Gim14] and Bernier et al. [Ber18] also are ambiguous. Notably, Bernier et al. [Ber18] compares Wißdorf et al. [Wiß16] and Skoblin et al. [Sko17] and highlights that the discrepancy "underlines the need for a profound understanding of the involved processes for the development of ion sources of improved performance". According to Bernier et al. [Ber18], one of the major issue is that "the injection of the charged particles into the capillary is crucial for the transmission efficiency and that the heating does not only affect droplet desolvation but also has a crucial effect on the turbulent transition and thus can be significant for the overall losses". Evidences that desolvation is not complete after a typical ESI process involving a capillary are provided by Markert et al. [Mar21]. In this article it is shown that droplets are still present in the flow after capillary and skimmer.

The work from Gimelshein et al. [Gim14] provides numerical simulations of velocity, pressure and other flow parameters in the case of a capillary. They confirm that "the supersonic flow is observed noticeably upstream of the capillary exit" (Fig. 5.3). The Mach number only grows to significantly super-sonic values outside of the capillary when the gas can expand. They also state that the position of the Ma = 1 isoline depends on whether turbulences are accounted for, or not. Nevertheless the influence of turbulences on the expanding plume is negligible. The Mach number significantly grows only when outside the capillary, downstream. The pressure in the capillary is still one third of the atmospheric pressure near its exit. This study is important because it provides an argument to the detriment of Hagen-Poiseuille model. It also emphasises on the need for numerical simulations if precise values are required.

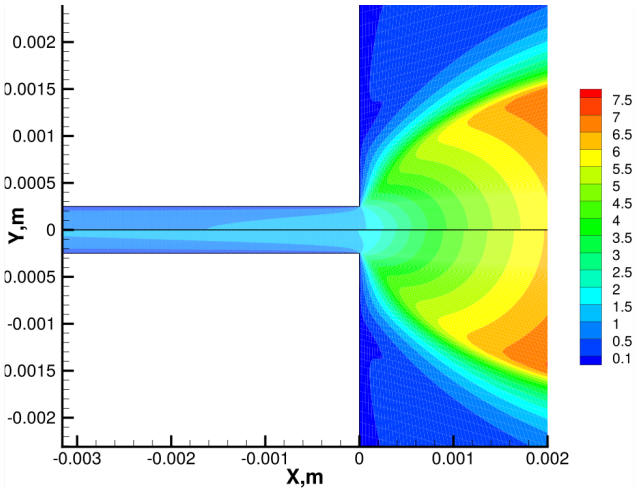

FIGURE 5.3: Numerical simulation of carrier Mach number in a free jet downstream a capillary similar to that of `GiantMol`. Capillary dimensions here are length 100 mm, diameter 0.5 mm, and is heated to 227 °C. The colour indicates the Mach number of the gas carrier. From Gimelshein et al. [Gim14].

Notably, one change that could be done is installing a slowly converging funnel inlet to optimise the laminar flow at the beginning. Basic considerations on fluidics are summed up in the frame 5.2.1 while the analytic description of the flow with the equations is discussed below.

5.3 Free jet, molecular beams and skimmer

The above description allows to determine a realistic flow in the capillary, nevertheless the behaviour of the super-sonic flow at the output of capillary forces to use another formalism to describe it. In a space of few millimetres the flow goes from the capillary nozzle to the skimmer, a conical shaped part designed to sample the molecular flow from its super-sonic state (Fig. 5.4). By moving to a volume where the pressure is three orders of magnitude lower, the carrier gas will expand and thus cool to lower temperatures. In our case it is not recommended to sample the molecular ions in a super-sonic state, because under this cool state condensation and molecular combinations under the form of addition [Dol68] – adduct ions[2] – can occur thus leading to the opposite of what a molecular source is designed for, desolving molecular ions. The role of the skimmer is to get rid of the adduct ions. The physics of the flow from the capillary to the skimmer is explained below.

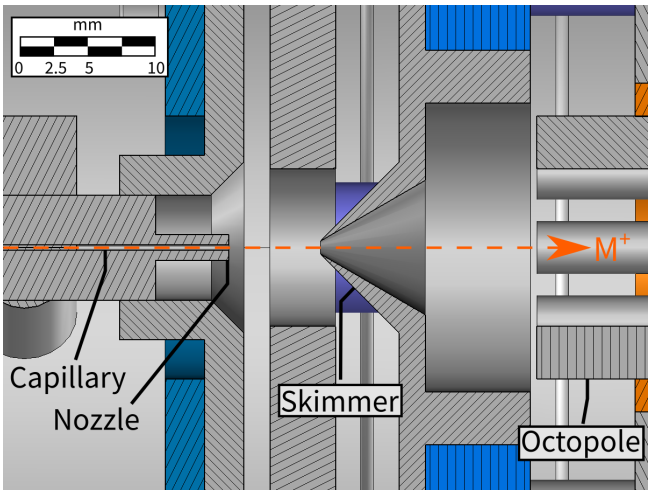

FIGURE 5.4: Sectional view of the capillary nozzle and skimmer assembly. A planar electrode is located between the capillary nozzle and the conical skimmer. The orange dashed arrow indicate the trajectory of the molecular ions (M^+).

5.3.1 Supersonic free jet expansion after the capillary

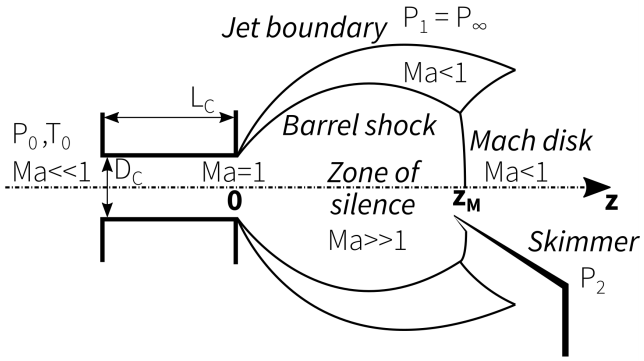

FIGURE 5.5: Super-sonic free jet flow characteristics in the capillary nozzle – skimmer space.

[2] In mass spectrometry an adduct ion is "an ion formed by interaction of two species, usually an ion and a molecule, and often within the ion source, to form an ion containing all the constituent atoms of one species as well as an additional atom or atoms."[IUP97b]

TABLE 5.2: Values of jet properties in `GiantMol` for an inlet gas at 373.15 K.

λ_0 [nm]	Kn_0	z_M [mm]	$(z_S)_{max}$ [mm]
67.3	$1.68 \cdot 10^{-4}$	8.47	9.06

After the end of the capillary the flow can expand into a super-sonic flow. Close to the capillary exit, up to a certain distance z_C, the flow is still considered continuous and collisions among the flow are important. Then beyond this distance the flow is considered frozen, collisions are negligible and the velocity distribution is mainly orientated towards the axial direction. The flow in this state is called a "supersonic, free jet, expansion" because its cross-section is not defined by a nozzle, and it expands in a lower pressure volume at supersonic velocities . There is a definite volume after the capillary nozzle where the gas is in this super-sonic state (Fig. 5.3), and the frontier downstream is the Mach disk, separated from the nozzle by the distance z_M (Fig. 5.5, top part). It is beneficial to catch up the flow in this zone where it has an excellent directivity. For this, a simple planar electrode is not sufficient because it would trigger turbulences under the form of a bow shock, due to the super-sonic state of the flow. The proper element designed to sample the molecules without perturbing it is the skimmer (Fig. 5.5, bottom part). Its shape accommodates the Mach disk and samples a small portion of the flow so the molecules have the similar momentum. According to Campargue [Cam84], an angle close to 50° maximises the beam intensity – 45° internal, 55° external. He also establishes two characteristic lengths as follows

$$z_M = 0.67 D_c \sqrt{\frac{P_0}{P_\infty}} \tag{5.17}$$

$$z_C \approx \frac{1}{10} z_M. \tag{5.18}$$

Furthermore, the distance between nozzle and skimmer z_S optimizing the beam intensity is defined as

$$(z_S)_{max} = 0.125 D_c \sqrt[3]{\frac{1}{Kn_0}\frac{P_0}{P_\infty}}, \tag{5.19}$$

with $Kn_0 = \lambda_0 / D_c$ the nozzle Knudsen number, λ_0 the stagnation mean free path. Typical values for `GiantMol` are given in table 5.2.

The optimum distance is greater than the distance between nozzle and Mach disk. Ideally if one desires to sample the super-sonic beam, it would be necessary to put the skimmer as close as possible to the Mach disk. A way to improve the optimal position and make it happen upstream Mach disk would be to decrease the pressure in the chamber. Notice that in chamber asymptotic conditions, the values are $\lambda_\infty = 6.73$ µm and $Kn_\infty = 0.168$. However, as the beam is required to be sampled in sub-sonic conditions, the skimmer must be placed downstream the Mach disk. Down there, the temperature of the gas will increase, which facilitates the dislocation of adduct ions into their respective components.

5.3.2 Collisions in the beam

A Knudsen number close to unity suggests that the continuum hypothesis may or may not be valid. This is due to the fact that Knudsen compares the mean-free path of the particle to the physical dimensions of the problem, in a ratio. Here, asymptotically where the mean-free path is highest, $\mathrm{Kn}_\infty < 2$. Computing Knudsen number in realistic conditions at nozzle, $\mathrm{Kn}_\infty < 3 \cdot 10^{-3}$ @ 373 K, 100 mbar. This indicates the mean-free path is small compared to physical dimensions of the problem. The collisions between molecules in carrier gas are thus a major component to determine the gas properties, this clearly validates the continuum hypothesis. It is possible to compute the rate of collisions of molecules in the carrier gas. As the molecular ions under investigation are highly diluted in the carrier gas, computing the collision rate of the carrier gas alone already provides a very good estimate of the collision rate for the molecular ions. This hypothesis is furthermore supported by the fact that the latter is intended to be significantly heavier (and bigger) than the carrier gas mainly composed of nitrogen (N_2) and can thus be considered at rest with respect to the carrier gas flow. The collision rate in the case of nitrogen molecules considered as hard spheres is

$$\nu_{HS} = \frac{\overline{v}}{\lambda} = \sqrt{\frac{8RT}{\pi M_{air}}} \times \frac{PN_A d_{air}^2 \pi \sqrt{2}}{RT} \tag{5.20}$$

$$= \frac{4PN_A d_{air}^2 \sqrt{\pi}}{\sqrt{M_{air} RT}} \tag{5.21}$$

with $\overline{v}$ the average velocity of molecules in the ideal gas in kinetic gas theory, P the pressure. In the case of the nozzle, the collision rate is $\nu_{HS}^{noz} = 1.21 \cdot 10^9$ collisions per second.

5.3.3 Thermodynamic properties of an isentropic flow

As shown in figure 5.3, the flow inside the end tip of a capillary is trans-sonic (with Mach number $\mathrm{Ma} < 1.1$), and goes super-sonic only when the gas can expand in a broader chamber. Thus, even though the above equations 5.16 have proven relevant to compute the inlet flow, it is not possible to deduce the velocity from it as the flow cross-section evolves in an unknown manner. A better method consists of using the properties of a one-dimensional isentropic flow[3]. For this assumption to hold, the gas must be considered ideal and expanding freely in a vessel where the external pressure is small enough in order to neglect its effect on the expanding jet. In such a case, it is possible to express the pressure P, density ρ, and temperature T of the gas flow, as a function of stagnation parameters and Mach number [Oos13, p. 69; Hab85; Dol68].

[3] An isentropic and reversible process is adiabatic. In literature the flow is indifferently referred as isentropic or adiabatic.

TABLE 5.3: Values of thermodynamic properties of the free jet in `GiantMol` for an inlet gas at 298.15 K and a downstream pressure of 100 Pa.

γ	Ma_∞	T_∞ [K]	u_∞ [m/s]	α_∞ [m/s]
1.67	6.687	18.66	632.29	103.5
1.4	5.566	41.43	718.09	154.19

$$\frac{p_0}{p} = \left[1 + \frac{\gamma^\star}{2}\mathrm{Ma}^2\right]^{\frac{\gamma}{\gamma^\star}} \tag{5.22a}$$

$$\frac{\rho_0}{\rho} = \left[1 + \frac{\gamma^\star}{2}\mathrm{Ma}^2\right]^{\frac{1}{\gamma^\star}} \tag{5.22b}$$

$$\frac{T_0}{T} = \left[1 + \frac{\gamma^\star}{2}\mathrm{Ma}^2\right] \tag{5.22c}$$

with $\gamma^\star = \gamma - 1$. In the case of a gas acting as a monoatomic medium, the specific heat ratio can be taken as $\gamma = 1.67$, while in the case of a gas acting as a diatomic medium, it must be taken as $\gamma = 1.4$. Literature is ambiguous on this topic, but as Cassanova and Stephenson [Cas67] point out with similar conditions, "as the expansion progresses, the collision rate drops, and equilibration of the rotational mode ceases to be important. The gas then acts like a monatomic (sic) medium with $\gamma = 1.67$ rather than 1.4". The above formulas 5.22 can be reworked to provide the thermodynamic values at given distance from the capillary exit, providing the Mach number is known. The particular asymptotic case where the flow pressure p is that of the chamber $p = p_\infty = p_{out}$ is interesting because it can be computed easily. The asymptotic Mach number Ma_∞ can be retrieved from the equation 5.22a

$$\mathrm{Ma}_\infty = \sqrt{\frac{2}{\gamma^\star}\left[\left(\frac{p_0}{p_\infty}\right)^{\frac{\gamma^\star}{\gamma}} - 1\right]}. \tag{5.23}$$

This is the Mach number at chamber pressure once the expansion is entirely done. The typical asymptotic values expected with `GiantMol` geometry and settings are given in table 5.3.

Those results from table 5.3, and from Dole et al. [Dol68], are in accordance with numerical simulations from Gimelshein et al. [Gim14]. This temperature must be interpreted as translational. The article from Dole et al. [Dol68] describes the transport of 51000 Da and 411000 Da macromolecular ions in a similar system.

5.3.4 Molecular beam

The collimated super-sonic molecular beam in itself can be described from the temperature and the Mach number. Its velocity distribution $f_n(v)$ and flow velocity u can be computed as [Hab85]

$$f_n(v) = N_n v^n \exp\left[-\frac{(v-u)^2}{\alpha^2}\right] \tag{5.24}$$

$$u = \mathrm{Ma}\sqrt{\gamma\frac{kT}{m}} \tag{5.25}$$

$$\alpha = \sqrt{\frac{2k_BT}{m}} \tag{5.26}$$

with N_n a normalisation constant, $n = 2$ for the velocity distribution and $n = 3$ for the flux density distribution. The Full-Width at Half-Maximum of the transverse velocity distribution is

$$\sigma f_2(v) = 2\alpha\sqrt{\ln 2}. \tag{5.27}$$

Notice that this description, just like this whole subsection on free jets, applies to the output of the calcium oven detail in section 2.1.1.

5.3.5 Skimmer effect

Placing the skimmer downstream the Mach disk where the flow is sub-sonic allows to sample unsolvated, unadducted molecules. It is also the way to retrieve molecules with smaller energy so they can be introduced in the octupole and thermalize with the ambient gas. While the pressure in the octupole vessel is 10^{-3} mbar, the collision rate of any carrier gas incoming is $\nu_{HS}^{8pole} = 6.68 \cdot 10^6 \mathrm{s}^{-1}$. This means a collision occurs every 0.15 µs, which is enough to thermalise any incoming molecular ion trapped in the octupole. In practice, at the octupole exit, we notice no molecular ion with kinetic energy different from the one we set at the octupole exit pulse.

5.4 Octupole guiding and bunch generation

5.4.1 General layout

Beyond the skimmer is located a guiding octupole driven with radio-frequency fields. It is operated in the same fashion as a quadrupole trap and the reader is referred to section 1.1 – Multipole expansion – for more details on the generated potential. The octupole is 21 cm long, made of eight 4 mm diameter rods, with 16 mm entraxe between opposed rods. The internal radius of octopole is thus $r_0 = 6$ mm. Its purpose is to guide charged molecules downstream. Two alternating voltages in phase opposition are applied to the rods so half of the rods are supplied with one voltage, and the other half with the other, in an interlaced pattern. Given each rod is supplied with a voltage with amplitude V_8[4], the

[4] This way the voltage amplitude between two rods in phase opposition is $2V_8$, and the peak-peak amplitude is $4V_8$.

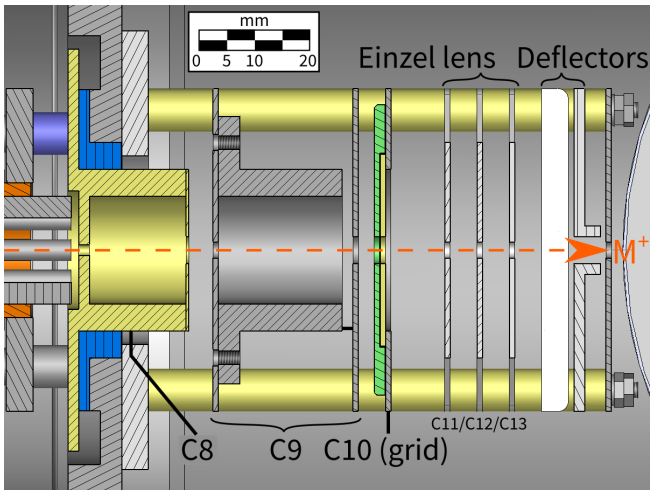

FIGURE 5.6: Sectional view of the octupole exit area. Downstream end of the octupole is on the left part of the figure. The yellow (C8) and grey (C9) cylindrical electrodes are both pulsed with timed pulses. A thin grid is located between the green and yellow planar electrodes. Einzel lenses and deflectors close the walk. The orange dashed arrow indicate the trajectory of the molecular ions (M^+).

electric pseudo-potential generated by the octopole is Ψ_8

$$\Psi_8 = 4\frac{q_e^2 V_8^2}{M r_0^2 \Omega^2}\left(\frac{r}{r_0}\right)^6. \tag{5.28}$$

This octupole leads to a system of electrically pulsed planar electrodes described hereafter.

5.4.2 Bunch generation and particle guiding efficiency

In the first place, the pulsed electrode system serves the purpose of controlling the ejection of the molecular ions from the octupole. The current electrode layout used to this purpose is illustrated with the figure 5.6. The principle is to apply a voltage of same charge as the molecular ions in order to block them, and apply an opposite voltage in order to attract the molecular ions and let them pass through eventually. But it turns out the electrode system can be used in order to narrow the velocity distribution of the extracted molecular ions, which increase the quality of the beam and thus the quality of the detection. I am going to describe an extraction system made of a single electrode then highlight the main disadvantages of such system, compared to a dual electrode system.

Single electrode layout for extraction

With a single electrode (C8) it is possible to extract the molecular ions, nevertheless this induces mainly two detrimental effects. First, because the electric field is symmetric with respect to the single electrode plane, any molecule accelerated in the upstream part of the device will be then slowed once it passes the electrode. Second, because of the velocity and spatial distribution of the molecular ions in the octupole upstream, the potential generated by the electrode will induce a range of various initial conditions, depending on the initial distributions. Thus the several molecular ions in several initial conditions are submitted to as many accelerations values and durations as there are initial conditions. This way it is not possible to consider the molecular ions have a single initial condition, initial

energy, but rather a distribution. As we will see later in chapter 6, the guiding of charged particles using the principles of charged particle optics, is dependent on the initial energy of the guided particles, and all parameters such as electrode focal length or beam divergence depend on the initial conditions. So as the beam divergence is proportional to the range of initial conditions, it is of great interest to reduce it as much as possible. A detection of light molecules with this single electrode layout is showed and discussed in section 7.2.

Double electrode layout for extraction

In our experiment, this velocity distribution problem is reduced with the help of a strategy involving a double electrode layout for molecule extractions. After the first extraction electrode C8, another electrode C9 is used (Fig. 5.6). This second C9 electrode is supplied in order to slow the early ions and synchronise them with the late ions. This is done by applying a voltage of similar amplitude but with a slight delay so the ions passing through C8 see a slowing potential during a relatively small period of time. This last step where the axial velocity and spatial distributions of the molecular ions are reduced is what is called **bunch generation**. Section 7.2 also discusses the effect of the double electrode strategy.

Quantitative informations about the double electrode layout

The electrode layout downstream the octupole is presented in figure 5.6. The pulse timing is represented in figure 5.7. Both electrodes are powered with independent pulse generators able to provide positive and negative voltages up to 250 V. As we are generating and guiding positively charged molecular ions, the potential will be set to negative values for the acceleration of the particles. Small positive values ($\approx$ +10 V) can be used to ensure the stream is blocked when desired. The pulses are generated in periodical sequences with a period of $T_P \approx 150$ ms. During two durations T_8^- and T_9^-, negative pulses with amplitude V_8^- and V_8^- are sent to electrode C8 and C9, respectively (Table 5.4). The delay between each pulse Δt_r can be tuned, as much as the delay with the end of the negative pulse Δt_f (Table 5.5).

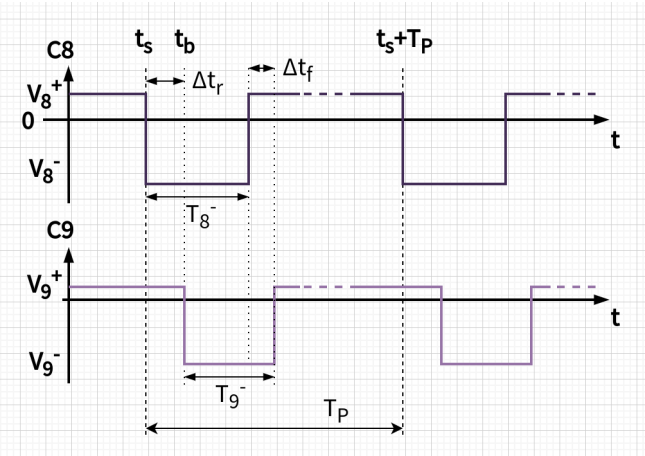

FIGURE 5.7: Timing diagram for the pulsed electrodes at the octopole output. C8 is the first planar electrode serving as octopole endcap. C9 is the Gaussian tube apparatus downstream C8. The negative pulses are applied with period T_P, they are triggered with a short delay Δt_r and reset to positive value with delay Δt_f. The positive and negative values are indicated with indices $^+$ and $^-$.

The pressure in octupole chamber is 10^{-3} mbar and beyond the exit electrodes is 10^{-6} mbar. The electrical pulses on the electrodes ensure that a trigger signal is available in sync with ejection of charged molecules. This facilitates the understanding of the measurements carried out later. Nevertheless it is also possible to let the molecules freely flow from the source to beyond the octupole with only static potentials, provided the gradient is favourable to such behaviour. But doing so there is no trigger information available which makes the setting of the downstream devices an unreliable task and the interpretation of the detection signal a convoluted task.

TABLE 5.4: Typical values for C8/C9 electrode pulse powering in `GiantMol`

Electrode (i)	T_i^- [µs]	V_i^- [V]	V_i^+ [V]
C8	10	-250	10
C9	5	-200	0

TABLE 5.5: Typical values for C8/C9 electrode pulse timing in `GiantMol`

T_P [ms]	Δt_r [µs]	Δt_f [µs]
$100 \rightarrow 1000$	$\sim 0 \rightarrow 5$	$1 \rightarrow 2$

Chapter 6

Electronic lenses and other particle guiding

Beyond the octupole exit the charged molecules are guided by a set of electrodes whose design and operation are in the domain of **charged particle optics**. This *ambiguous* choice of name is justified by the analogy with the guiding and shaping of photon beams. It is of use when designing devices such as cathode ray tubes or electron guns, but also more complex devices such as (old) oscilloscopes, particle accelerators and eventually mass spectrometers. Charged particle optics relies on electrodes fed with direct or alternating current to deviate and shape beams of charged particles. The electrodes can be stacked in pairs or triplets and be in the form of plates or cylinders, but more complex designs such as quadripole can be used.

6.1 Overview of charged particle optics

6.1.1 To determine particle trajectories and operate devices

In the short introduction of its report, Hinterberger [Hin06] points out that "the theory of electrostatic lenses has been developed in the time 1930-1955". During those early years, the study of the particle trajectories in various basic situations was dependent on the determination of the potential generated by the electrodes through which the charged particles travelled. Using Lorentz force and potential it is indeed always possible to determine the trajectory of a charged particle, but it requires an analytic method. Then around 1950, a formalism derived from Gaussian paraxial optics was developed by several authors, allowing to emancipate from the computation of exact potentials, provided some approximations such as paraxial rays were made. This Gaussian optic formalism provided the properties of various electrode layout through matrix forms, and concepts such as lens, focal length and refractive index were transposed from optics to charged particle optics. Nevertheless, a warning is addressed to the reader regarding the exactitude of this formalism in charged particle optics. Because of the specificities of electromagnetic fields, and especially its inhomogeneities that have no equivalent in optics, the analogy with optics is more uncertain than most of the bibliography suggests. Furthermore, the massive character of the guided particles, makes it even more distant from optics, especially when

relativity gets involved. When designing and operating such electrostatic systems, it is advised to use modern numerical methods. In our case the reference has been the professional software SIMION®[1] , a powerful tool dedicated to ion optics. Very recently in order to complete the capabilities of SIMION, another tool has proven interesting for its versatility, ease of use, the free of charge and multi platform AgrosSuite[2] [Kar13]. Those programs are based on a finite difference, or finite element method, respectively, in order to determine the fields and then particle trajectories. Still, the formalism remains essential in order to develop an intuition for the design and operation of electrostatic lenses.

6.1.2 Informations and critical points

As an introduction to the field, the article from Harb et al. [Har10], describes the physics and the formalism of the basic elements used in charged particle optics. It is suited to describe most of the electrodes used in the `GiantMol` experiment, when it comes to guide molecular ions. In particular, it highlights very well how the electrode potentials are referenced with respect to the molecular ion source potential. This speaks in favour of a source with the best possible energy definition. Also this article introduces the important limitations in the use of the approximations and formalism mentioned above. Notably, by comparing the formalism with experiments, Harb et al. state that using the actual potential rather than simply the voltages applied to the electrodes improve the agreement of analytically computed parameters with experimentally measured parameters. Without this substitution " [...] the predicted f_{VMI} values would be about three times larger than those reported [...]", with f_{VMI} being the focal value of their Velocity-Mapping-Imaging spectrometer, constituted of one einzel lens and two single electrodes, only. Chapter six from El-Kareh and El-Kareh [El-70] is pointed out as a reference to compute the potential in charged optics devices. A recent book from Liebl [Lie08] sums up quite well the formalism but lacks some important precisions that can be found in the two other references. A general review compatible with relativistic particles is given by Wollnik [Wol87]. Another difficulty introduced in that case is that the guided particles have a velocity-dependent mass. Fortunately, in our case it is very reasonable to estimate the encountered velocities v smaller than the speed of light c by 5 orders of magnitude. These references highlight very well how the trajectories of charged particles do not depend on their rest mass but only on their kinetic energy, in the non-relativistic limit. Another major complication could originate from the use of magnetic fields, which we do not use in `GiantMol`.

[1] https://simion.com/
[2] http://www.agros2d.org/

6.2 Analytical developments

Charged particle optics fundamentally relies on the integration of the motion of charged particles in the fields generated by the elements (**E** and **B**). The relevant equation to describe the motion of a particle with mass M, charge $Q = Z_e q_e$ with $Z_e \in \mathbb{N}$ is

$$q_e(\mathbf{E} + \mathbf{v_M} \times \mathbf{B}) = M\mathbf{a_M}, \tag{6.1}$$

with $\mathbf{v_M}$ and $\mathbf{a_M}$ the velocity and acceleration of the charged particle. The trajectory of charged particles is always solvable using this equation. From this equation, Louis de Broglie [Bro50] deduces that "particles with identical origin of potential describe trajectories of identical forms that do not depend on Q/M. Later the author states that "with the help of an electrical centred apparatus, it is impossible to separate different masses originating from the same source". Also, applying an identical α factor to all the voltages involved in the guiding of the charged particle lead to the same trajectory. In particular, if the voltages vary accordingly to the source, a variation of the source potential do not induce any change in the behaviour of the system[3]. Nevertheless the combination of the above fundamental equation with other principles inspired from optics (such as Fermat's principle, refractive index and focal lengths) allows for the description of charged particle beams in terms similar to that of optics. At last, using paraxial approximation allows for the use of matrix formalism.

6.2.1 Matrix formalism for elementary charged particle optics devices

A set of electrodes represented by the matrix **M** will act on the beam coordinates r and θ as

$$\begin{pmatrix} r' \\ \theta' \end{pmatrix} = \mathbf{M} \begin{pmatrix} r \\ \theta \end{pmatrix}. \tag{6.2}$$

For example, in the case of the **drift space**, the particle is not submitted to any field, thus drifts. The matrix **D** describes a drift space with length D

$$\mathbf{D} = \begin{pmatrix} 1 & D \\ 0 & 1 \end{pmatrix}. \tag{6.3}$$

When dealing with the propagation of a particle **in the presence of an electric field**, for instance between two electrodes E and G, at voltages V_E and V_G, separated by a distance l, the proper matrix **H** devoted to account for the motion is defined as

$$\mathbf{H} = \begin{pmatrix} 1 & h_1 \\ 0 & h_2 \end{pmatrix} \tag{6.4}$$

[3] This is not strictly true when magnetic fields are involved, or in case special relativity applies.

with

$$h_1 = \frac{2l}{1+\sqrt{\delta_\star}} \tag{6.5}$$

$$h_2 = \sqrt{\delta_\star^{-1}} \tag{6.6}$$

$$\text{so that } \delta_\star = \frac{U_G - U_S}{U_E - U_S}. \tag{6.7}$$

U_E and U_G represent the actual axial values of the potential in the E and G electrode planes, with U_S representing the actual source potential. The reason I am discussing the above case is because I want to highlight how the effect of the field depends on the potential of the source U_S, or equivalently the source energy qU_S. For every device in charged particle optics, it is important to consider the difference between the axial voltage in the device and the axial voltage of the source. This is why later in the document, the electrode voltages may be referenced directly with respect to the source because those are the values to enter in most of the computations. Such voltages/potentials values are represented as $\Delta V = V_S - V_E$.

Also, by using axial voltage, I mean the real potential along the electrode axis which is smaller than the voltage applied to the electrode or device. Indeed, let be V_E the voltage applied to an electrode with a centro-symetric hole, U_E the actual potential in the center of the hole, the latter is smaller than the former $U_E < V_E$. Harb et al. [Har10] compare measured focal lengths with computed ones, for simple electrode layouts, and report an error of a factor of three with respect to experiments, if the simple electrode voltage V is used in analytical computations rather than U. In support for this praxis, it is noticed [Lie08] that "the first-order optical properties of a system are completely determined by the axial potential distribution. This is a consequence of the Laplace equation [...]". Only electrical fields are considered from now on.

6.2.2 Single planar electrode

The simplest possible electrode layout is a planar electrode with circular aperture. Its effect on a charged particle can be represented by the matrix **E** so that

$$\mathbf{E} = \begin{pmatrix} 1 & 0 \\ -\frac{1}{f_E} & 1 \end{pmatrix} \tag{6.8}$$

$$\text{with } f_E = -\frac{1}{Q}\frac{4\varepsilon_E}{E_E^+ - E_E^-} = -\frac{4(U_E - U_S)}{E_E^+ - E_E^-} = -\frac{4\Delta U_E}{E_E^+ - E_E^-} \tag{6.9}$$

with ε_E the particle energy. E_E^- represents the field value before the electrode E, E_E^+ the field downstream the electrode. If the field is considered homogeneous, it is possible to define $E_E^- = (V_R - V_E)/l$ with $V_R - V_E$ the potential difference between the previous electrode R and the current electrode E, l the distance between those electrodes. E_E^+ is computed in the same fashion. Harb et al. [Har10] also propose to compute $E_E^+ = 0.5(V_E + U_E)$ as an average. For a source potential of $U_G = -200$ V, the focal length of the single planar electrode is represented in figure 6.1 as a function of the potential in the axis of the central electrode.

6.2.3 Immersion and emission lenses electrode

The above considerations help understand the way immersion and emission lenses work. A similar matrix description for those devices can be found in the book from Liebl [Lie08]. Immersion lenses are a combination of two electrodes with null fields in their outer parts. The situation is analogous to optical immersion lenses with focal lengths f_1 and f_2 on each side. The immersion lenses make the transition between two media with refractive indices n_1 and n_2. In that case $f_2/f_1 = n_2/n_1$. Charged particle optics tells us that the refractive indices can be defined as square root of the potential the particle is going through : $n_i = \sqrt{U_i}$.

The presentation of immersion lenses is also the opportunity to present two modes of operation for a set of electrodes. It is possible to set the electrodes either as a converging-diverging ($\Delta U_1 < \Delta U_2$) set or a diverging-converging ($\Delta U_1 > \Delta U_2$) set. Those modes are also mentioned as decel-accel or accel-decel, depending on which electrode decelerates or accelerates the particles. Their respective advantages and disadvantages are discussed below when describing the einzel lenses.

Emission lenses are used to shape beams of particles emitted from a surface with a given distance with respect to the lens. This principle is interesting in order to understand imaging in charged particle optics. Indeed an emission lens is able to produce the image of the surface. Let be a the object distance, b the image distance, f_1 and f_2 the upstream and downstream focal lengths, the following formula analogous to Newton's imaging equation writes as

$$(a - f_1)(b - f_2) = f_1 f_2. \tag{6.10}$$

This formula can be used with any device.

6.2.4 Einzel lens electrode

Einzel (or unipotential) lens (Fig. 6.2) are particularly interesting, because with such device it is possible to focus a beam of particles and control its exit energy independently. Its effect on charged particles is the combination of three planar electrodes separated by two uniform fields. The relevant matrix is the product of the corresponding matrices

$$\mathbf{M_L} = \mathbf{E_3 H_2 E_2 H_1 E_1}. \tag{6.11}$$

Often, the Einzel lens is used with symmetrical voltages, which is the only configuration ensuring focusing without energy change. Furthermore the external electrodes are also often set to ground. The matrix can then be written as

$$\mathbf{M_L} = \mathbf{O H_2 I H_1 O} = \begin{pmatrix} m_{11} & m_{12} \\ -\frac{1}{f_L} & m_{22} \end{pmatrix} \tag{6.12}$$

with **O** for the external electrodes, and **I** for the central one raised to voltage $\Delta V_L = V_S - V_L$. f_L is the focal length of the whole einzel lens. In this configuration, with a symmetrical environment and a source potential of $U_G = -200$ V, the focal length of the einzel lens is represented in figure 6.1 as a function of the potential in the axis of the central electrode. The computation uses the same approximations as in the article from Harb et al. [Har10]. This provides an idea on how does the focal length of an einzel lens evolves with this potential.

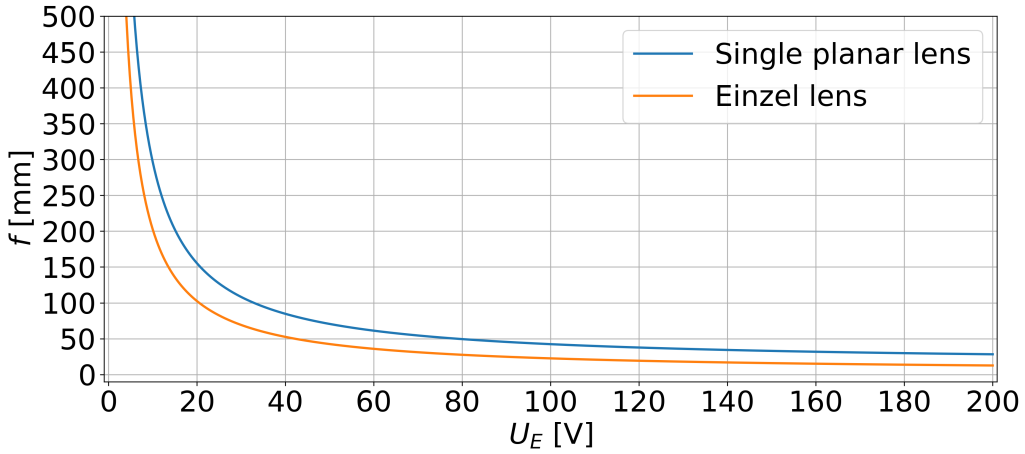

FIGURE 6.1: Focal lengths of a single planar electrode and an Einzel lens as a function of the central potential in the central electrode.

Again, depending on the voltage scheme the Einzel can be in decel-accel ($\Delta V_L < V_S$ or $V_L/V_S > 0$) mode or accel-decel ($\Delta V_L > V_S$ or $V_L/V_S < 0$) mode. V_S is the source potential such as the beam energy is $q_e V_S$. The decel-accel mode is advantageous for two reasons, first it uses grounded external electrodes and a central electrode raised to voltage with same polarity than that of the source, second because a high refractive index is possible using a central voltage similar to that of the source, which brings particles closer to the optical axis, allows for best focusing, shorter focal length. However, while the accel-decel mode requires higher negative voltage to ensure the same focusing power, it is more convenient as it bears lower spherical and chromatic aberrations. Indeed in accel-decel mode the energy spread in the beam in minimised. So if not too small focal lengths are required, accel-decel mode is to be privileged. In decel-accel mode, a careful design of the lenses allows to stand at higher focusing power for exactly $\Delta V_L/\Delta V_B = 1$ which is convenient because both the source and the lens can be fed with the same supply. This way it is possible to turn off the beam by increasing the central voltage until the saddle point has higher potential than the beam energy.

Liebl [Lie08] provides many other comments useful to design such devices. One last comment about construction is that the most critical parts are ensuring a good electrode concentricity and insulation for voltage stability. "Distances and contours are less critical as long as everything is rotationally symmetric."

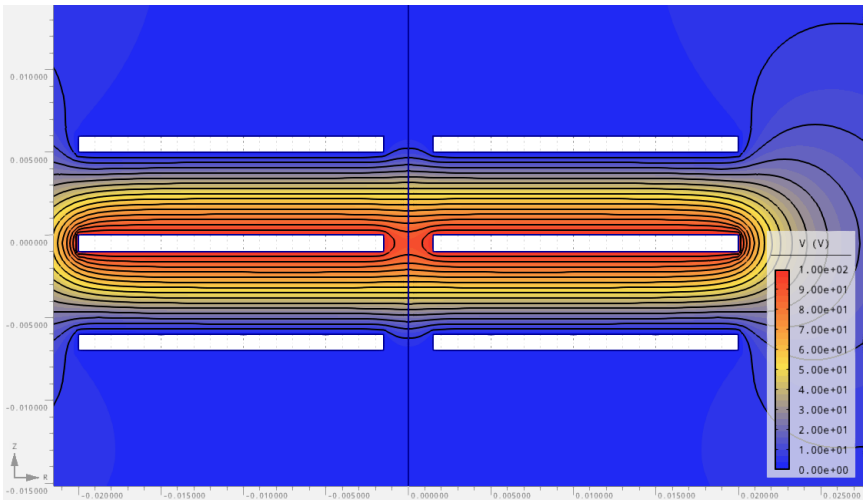

(A) Einzel lenses layout at the octupole exit. The aperture radius is 1.5 mm. The closest distance between electrode faces is 5 mm. Electrode have 1 mm thickness.

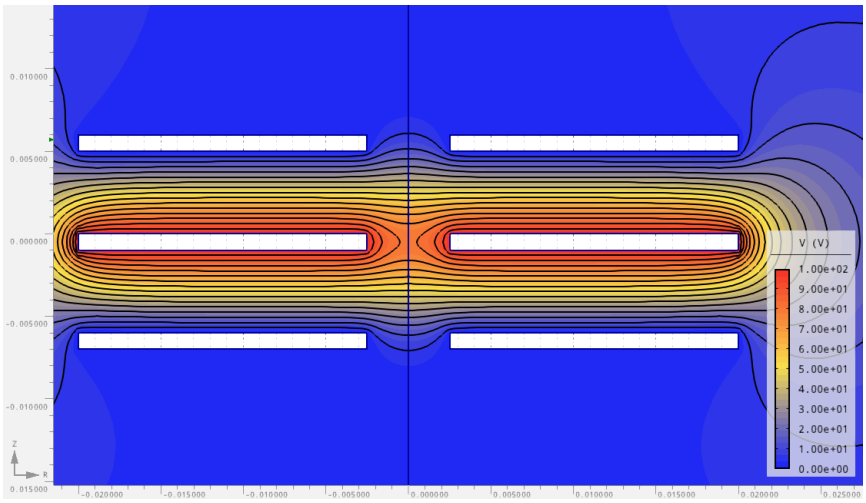

(B) Einzel lenses layout downstream the bender, before the passing tube. The aperture radius is 2.5 mm. The closest distance between electrode faces is 5 mm. Electrode have 1 mm thickness.

FIGURE 6.2: The potential generated by two Einzel lens layout with central electrode supplied with V_L = 100 V and outer electrode at ground. Potential simulated with Agros2D [Kar13].

The scalar electric potential of two Einzel lens layouts is presented in figure 6.2. Figure 6.2a reproduces the lens geometry downstream the octupole exit, with 1.5 mm aperture radius and 5 mm distance between 1 mm thick electrodes (for a total of 13 mm overall length). Figure 6.2b reproduces the lens geometry downstream the bender, with 2.5 mm aperture radius and identical electrode dimensions. Here the central electrode voltage is taken as 100 V. In those figures, the color represents the scalar electric potential ranging from 100 V (red) to 0 V (blue). The 15 black lines represent iso-potentials. It is possible to see that the narrower the aperture, the flatter the iso-potential lines in the apertures. The paraxial approximation upon which lies the matrix formalism is all the more valid as the iso-potential lines are parallel. Thus the geometry of figure 6.2a is better that the geometry of figure 6.2b when considering the paraxial approximation. Nevertheless the greater the

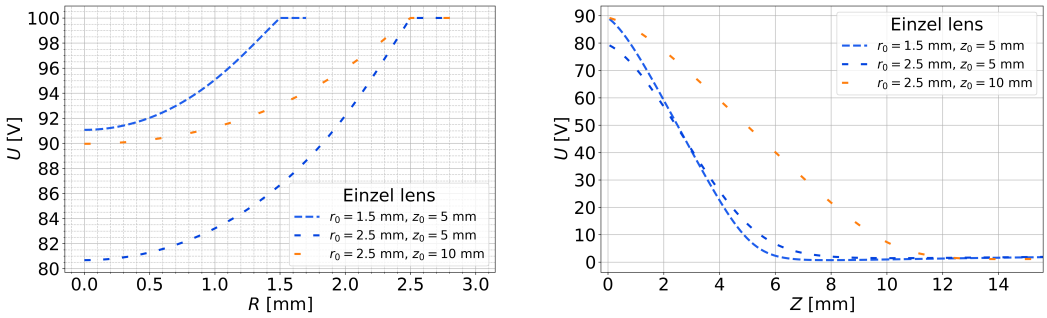

(A) Radial potential in the plane of the central electrode of einzel triplet.

(B) Longitudinal potential across the central axis of the Einzel triplet.

FIGURE 6.3: Radial and longitudinal potential in three Einzel lens layouts. In the Einzel layouts the electrode apertures are centred on the same axis (z-axis) with identical radius r_0. The electrodes are separated by distance z_0 between the closest faces. The blue lines represent geometry with $z_0 = 5$ mm of spacing between electrodes along the z-axis. The orange line is a geometry with $z_0 = 10$ mm. Potential simulated with Agros2D [Kar13].

aperture the more molecules can go through. There is a trade-off between iso-potential flatness and molecular flux. Figure 6.2 also demonstrates how the potential along the axis deviates from the potential applied to the electrode. In the narrower geometry (Fig. 6.2a), the axial potential in the central aperture is 91 V, while it is 80 V in the wider geometry (Fig. 6.2b). In terms of focusing the properties of those layouts are substantially different. For an incoming collimated beam of 100 Da particles with 200 eV initial energy, the focal distances of those layouts are 49 mm and 69 mm for, respectively, the narrower and the broader aperture.

Figure 6.3a depicts the potential value in the radial plane of the central electrode. The two above geometries are represented with blue lines. A supplementary geometry, corresponding to the Einzel lens upstream the GICD, is represented with the orange line. It is possible to see that for a constant electrode spacing z_0, the axial potential gets closer to the potential of the electrode for smaller aperture. Also, for a constant aperture radius, the axial potential gets closer to the potential of the central electrode for higher electrode spacing z_0. Figure 6.3b depicts the potential along the axis for the three same layouts.

6.2.5 Parallel plate deflectors

In order to adjust the direction of a beam of charged particles by a few degrees around an optical axis, small electrostatic deflectors can be used under the form of parallel plate condensers, as in cathode ray tubes. In our case the deflectors are intended to be used with small angles, without changing the optical axis of the system. Let's consider the beam of particles is near the optical axis and reaches the deflector with an angle ϕ_0 small enough so that $\tan \phi_0 \approx \phi_0$. The deflector applies a deflection force $q_e E = m\ddot{y}$ to the beam in a direction perpendicular to the optical axis. The beam escapes the deflector with a new direction, at an angle ϕ to the optical axis. For an incident particle with energy $q_e V_0$, moving along the z-axis, with the electrical field E applied over the y-axis, the integration of the

equation of motion leads to the following deviation distance and angle

$$y = n_q \frac{EL^2}{4V_0} \tag{6.13}$$

$$\tan\phi \approx \phi = n_q \frac{EL}{2V_0} \tag{6.14}$$

with n_q the number of charges the particle bears. $x_d = 0.5L$ is the virtual center of deviation, halfway through the deflector. After its passage through the condenser the particle energy drops back to $q_e V_0$.

6.2.6 Electrostatic quadrupole bender

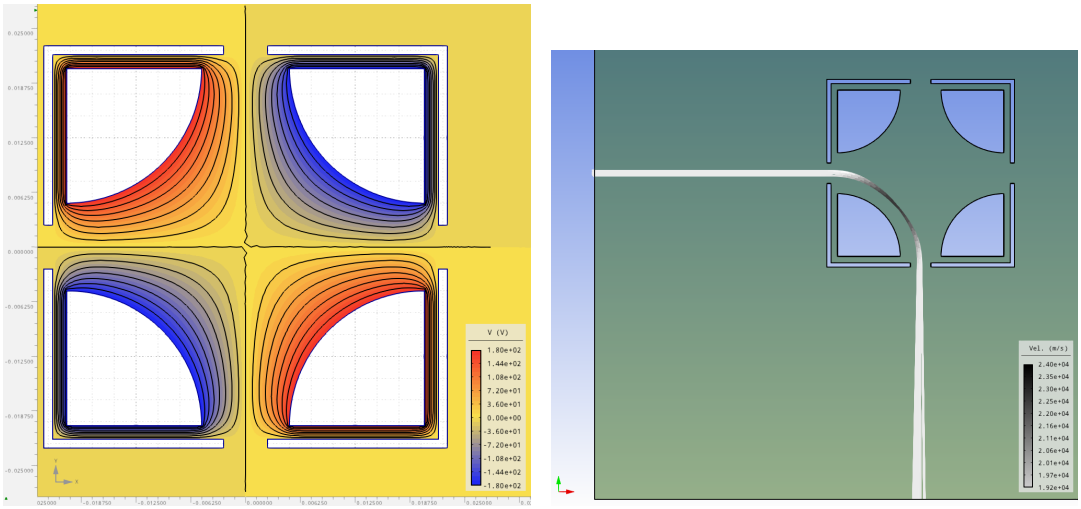

(A) Bender potential with electrodes raised at ±180 V. The color scale is so that blue is −180 V, red is 180 V and yellow is 0 V. In this picture, any positively charged particle entering the bender turns towards the closest negatively charged electrode.

(B) 30 particles trajectories with mass 100 Da, a single charge, 200 eV of initial energy. The color represent the velocity so the scale from slow to fast is white to black.

FIGURE 6.4: Potential and particle trajectories simulated with Agros2D [Kar13], for a bender raised at ±180 V as in the experiment.

When it is required to orientate the particle beam in a specific direction with a new optical axis, bigger electrostatic deflectors must be used. Some can be used under the form of electrostatic or magnetic sectors, made of a toroidal electrode. Another layout used here is the quadrupolar electrostatic bender. Similar in construction to the linear quadrupole ion trap (see section 1.2), it is fed with a set of two opposite sign electrostatic voltages, and the charged particles are introduced in the radial direction rather than the axial direction. Figure 6.4a illustrates the bender geometry used in `GiantMol`, the color representing the electric field. Figure 6.4b illustrate the trajectories of 30 charged particles in this bender. 30 particles with 200 eV initial energy, mass 100 Da and a single charge are used for this illustration. The applied field causes the charged particles to turn so that they follow the nearest electrode of opposite sign to their charge. Entering the bender, positively charged

particles will follow the negatively charged electrode in a curve nearly parallel to the electrode surface. The transfer matrix of the quadrupolar electrostatic bender is as follows [Rei08, pp. 98-103]

$$\mathbf{M_B} = \left(\begin{array}{c|c} \underline{M_B^x} & \mathbf{0} \\ \hline \mathbf{0} & \underline{M_B^y} \end{array}\right) \tag{6.15}$$

with

$$\underline{M_B^x} = \begin{pmatrix} \cos(z\sqrt{\kappa}) & \frac{1}{\sqrt{\kappa}}\sin(z\sqrt{\kappa}) \\ -\sqrt{\kappa}\sin(z\sqrt{\kappa}) & \cos(z\sqrt{\kappa}) \end{pmatrix} \tag{6.16}$$

$$\underline{M_B^y} = \begin{pmatrix} \cosh(z\sqrt{\kappa}) & \frac{1}{\sqrt{\kappa}}\sinh(z\sqrt{\kappa}) \\ -\sqrt{\kappa}\sinh(z\sqrt{\kappa}) & \cosh(z\sqrt{\kappa}) \end{pmatrix} \tag{6.17}$$

$$\text{and } \kappa = \frac{QE_0}{r_B M v^2} = \frac{V_0}{V_S r_B^2} \tag{6.18}$$

$$E_0 = \frac{2V_0}{r_B}. \tag{6.19}$$

The matrices $\underline{M_B^x}$ and $\underline{M_B^y}$ are each built upon the same vector space as introduced above. By carefully choosing one of the possible equations generated with this matrix, the voltage V_0 to apply to the electrode in order to leave the bender with the right position and angle can be retrieved. By using the second line of the $\underline{M_B^x}$ matrix

$$\begin{pmatrix} x \\ x' \end{pmatrix} = \underline{M_B^x} \begin{pmatrix} x_0 \\ x_0' \end{pmatrix} \tag{6.20}$$

$$x' = -x_0\sqrt{\kappa}\sin(z\sqrt{\kappa}) + x_0'\cos(z\sqrt{\kappa}). \tag{6.21}$$

Setting the origin of z axis at the beginning of the rotation, with initial conditions $x_0 = 0$ and $x_0' = \pi/2$, and after the bend ends at $z = L$ where L is the total travelled distance, the equation gives

$$\boxed{L\sqrt{\kappa} = \frac{\pi}{2}} \tag{6.22}$$

$$\boxed{V_0 = V_S r_B^2 \left(\frac{\pi}{2L}\right)^2.} \tag{6.23}$$

In the above computation, a first approximation of the voltage can be computed considering the path length as an arc of radius r_B over a quarter turn. Nevertheless doing so the computed voltage to apply is smaller than the experimental one. This is due to the fact that the path length is smaller than the arc of radius. Numerical simulations of the trajectories demonstrate that two effects are relevant. First the path taken by the charged particle is not an arc of circle, but is a shorter path. Indeed the radius of curvature evolves along the curve and reduce during the first half of the turn before returning to its original value when the particles leave the bender. Second, refractive index $n = \sqrt{V}$ along the trajectory must be taken into account. When the particle turn, they do not follow an iso-potential line (V = cte), thus the path length is not just the geometrical length but is represented by

a more complex expression integrating the refractive index along the path. This consideration that we have not introduced before is related to the Fermat's principle and implies that the real path length is proportional to the refractive index integrated over the trajectory. This can only be determined precisely with a numerical integration which has not been done. Nevertheless it turns out that in the case of our experiment, applying a correction factor of 0.9 to the path length L allows to compute a reasonably accurate value for the voltage to apply. Also, it is interesting to notice that in practice the voltage V_0 to apply is similar to the source voltage V_S.

Chapter 7

Detection

7.1 Micro-channel plates control detection

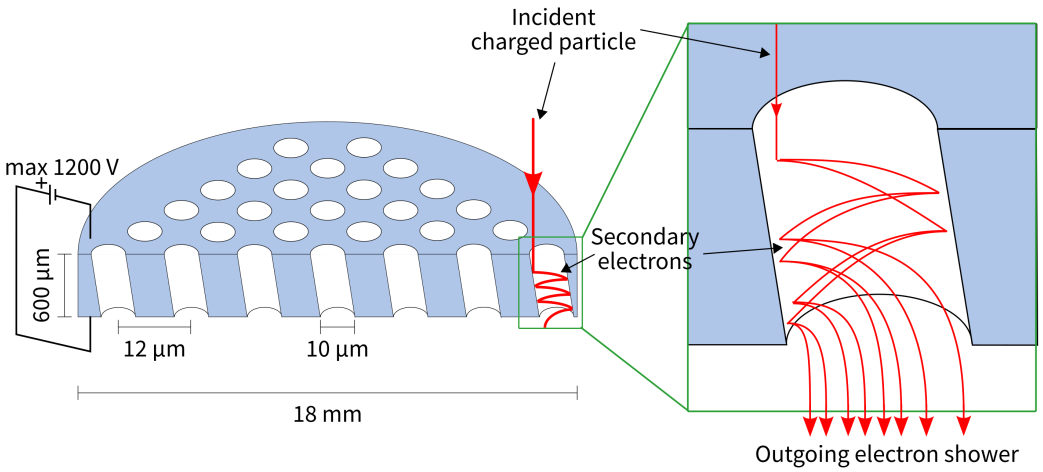

FIGURE 7.1: A single micro-channel plate with magnification of a triple cascade on the right side. The incoming charged particle in red hits the anode in a micro channel which triggers an electron cascade if it comes with sufficient velocity.

7.1.1 Micro-channel plates principle

Micro-channel plates (MCP) are detectors working according to the principle of secondary electron emission. When the molecular ion under investigation is sent towards the MCPs, the relative ion signal increases with the ion velocity [Twe06]. As a consequence, there is an incoming velocity below which no measurable detection signal can be measured. This is due to the fact that MCPs relies on the emission of a primary electron when the ion collides with the MCP surface (Fig. 7.1). The minimum threshold velocity required is related to the surface ionisation work function of the material used in the MCP. A consequence of this fact is that above a certain mass, no detection is possible due to the fact that it is not possible to accelerate the mass above the velocity threshold. The acceleration is due to the MCPs being submitted to an important voltage that cannot be excessively high. Usually it is in the range 1-3 kV.

The Micro-channel plates used in the `GiantMol` experiment are provided by Photonis®. The specific model is APD 2 MA 18/12/10/5 D 60:1 [1]. APD stands for MCP detector assemblies, 2 stands for the number of MCP stacked together in this assembly and MA stands for Metal anode. The following sequence 18/12/10/5 can be tracked in figure 7.1. 5 stands for the bias angle [°], 60:1 for the aspect ratio (thickness:channel diameter). The maximum voltage is 1200 volts per MCP which allows for 2400 volts in total but it is not useful to go higher than 2000 volts as the efficacy saturates. The nominal gain is said $G > 10^7$.

Two MCP are located in the prototype, each of it used accordingly to the principles described just below. The first MCP is located in the creation vessel, and usually referred as the creation MCP. It is located 28 cm from the extraction electrode, and is reachable only if the first bender is set to mass. Its signal is read on an oscilloscope. The second MCP is located downstream the GICD and is referred to as detection MCP. It is intended to be used in combination with the electronic devices described below for particle counting. Before December 2020, the detection MCP was located on the GICD axis, at a distance from the extraction electrode of 914 mm. Then after this date it has be moved on another axis normal to the former one and its distance from the extraction electrode is 906 mm.

7.1.2 Detection electrical scheme

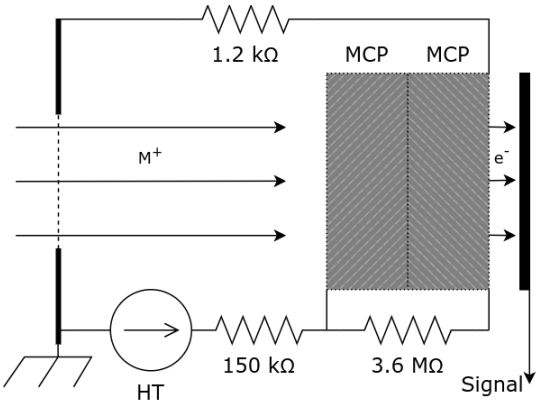

FIGURE 7.2: Electrical layout of the creation vessel MCP. The HT is the high voltage supply for the MCP, the H+ represents the direction from which charged molecule comes, the e^- are the electrons from the output shower, collected by an electrode. The first electrode on the left is at ground, its aperture is covered by a grid (dashed line).

Simple oscilloscope with impedance

It is possible to read the signal from an MCP by simply collecting the electron current with an anode (Signal in Fig. 7.2). Converting this current into a voltage is a common procedure in order to read a signal on an oscilloscope. In that case, the higher the output impedance, the higher the voltage for a given current, and the longer the decay time after the excitation. The MCP in the creation vessel is mounted with a 1MΩ impedance. The line is sent to an oscilloscope channel to which a knobbed variable resistor is mounted in parallel, in the range [0;10] kΩ if needed. This impedance lowering allows for sharper peaks in the signal,

[1] https://scilab.co.jp/product/vacuum/download/photonis_detector.pdf, and https://www.sii.co.jp/jp/segg/files/2013/04/file_IMAGE_FILE_5260_IMAGE02.pdf

with smaller amplitude, in the case of a continous flow of particles where the signals probably overlap. This is a convenient way to measure MCP signals. It is the way the creation MCP is wired and used.

Signal counting

Another way to retrieve signal a from the MCP is by counting impulsions. Similar to the previous case, the MCP is mounted with a given impedance, and the output voltage is sent to a series of instruments counting signals (Fig. 7.3). This is how the detection MCP is wired and used. After the MCP, a pre-amplifier is used to raise the voltage in the range of 1-100 mV approximately. A amplifier discriminator is used to produce NIM-standard gates for every input signal crossing a set threshold. A NIM-TTL converter is used to produce countable TTL signals. The TTL signals can be either read on an oscilloscope (Fig. 7.6 and 7.7) or counted with any appropriate setup (Fig. 7.3). The filtering of noise counts can be achieved with the careful selection of trigger thresholds and gains. Also, windowing of detection periods in sync with the extraction pulse can be of great advantage. Few dark counts are expected for every period of 100 µs and the measured signals can be quite small around ten counts per 100 µs. The above detection chain can be embedded in a single device, such as the RoentDek®LET1+ timing discriminator, including a pre-amplifier, amplifier-discriminator and outputs in both NIM and TTL standards.

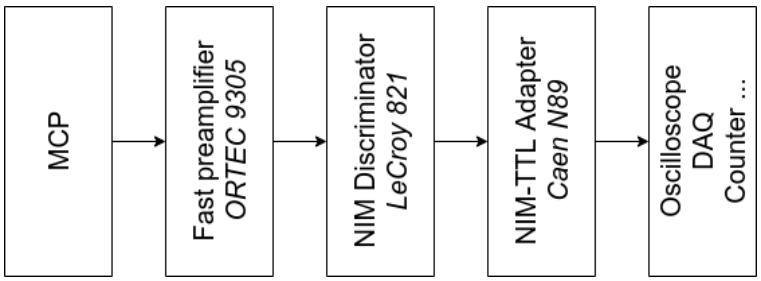

FIGURE 7.3: Diagram of detection signal chain for the detection MCP. The signal starts from the left and is sent to the devices at the right. DAQ is for Digital AcQuisition, that can be achieved using a computer acquisition system.

7.2 Comparing two extraction schemes

7.2.1 Molecules used

In our experiment, three molecules were manipulated and injected in the experiment. Their name, mass and formula are summed up in the table 7.1. The lighter molecule, pyridine (PYR), was used first to test the apparatus and observe the first detection signals. Because it is a lightweight and small molecule, this is the most convenient molecule to manipulate. Indeed, its basic heterocyclic structure guarantees a low fragmentation susceptibility, and its small size guarantees a limited number of charges can settle on the molecule. Those arguments allows for a less ambiguous detection signal than the other molecules. Tryptophan (TRP) is an amino-acid. It is 2.58 times heavier than PYR and is built upon two

TABLE 7.1: Physical properties of the molecules.

Molecule	Nickname	Molar mass [g/mol]	Chemical formula
Pyridine	PYR	79.102	C_5H_5N
Tryptophan	TRP	204.229	$C_{11}H_{12}N_2O_2$
Dibenzo-18-crown-6	DBCE	360.406	$C_{20}H_{24}O_6$

heterocyclic structures bond together (indole) with a chain group. It is much more susceptible to fragmentation. Dibenzo-18-crown-6 is 4.56 times heavier than PYR and much bigger. It is one of the most popular crown ethers, explaining why it is later referred as DiBenzo-Crown-Ether (DBCE). This cyclic structure can be fragmented in many ways and also allow for forming adduct ion with many other compounds such as water or methanol.

7.2.2 Single beam pulse

As explained in subsection 5.4.2 the prototype was first equipped with a single extraction electrode to siphon the molecular ions from the octupole and accelerate them towards the detectors. The effect of the extraction pulse duration over the signal measured by the creation MCP is illustrated by the figure 7.4. Those measurements are carried out with TRP pulsed at -250 V, MCP voltage of 1880 V and impedance of 5000 Ω. In the figure 7.4 the traces are provides for five pulse durations. The early pairs of sharp peaks visible on the top left part of the figure 7.4 are synchronous with the beginning and the end of the pulse. There are two positive peaks for each curve, and the curves are synchronised with respect to the first peak. This peak is in sync with the beginning of the extraction which is set at $t = 0.9$ µs. The other sharp peaks happening at $t > 0$ correspond to the end of the pulse. Their location depends on the pulse duration and the important timings are indicated in framed numbers.

Figure 7.4 demonstrates that the pulse duration has a significant effect on the signal shape. In particular, the signal broadness is dependent on the pulse duration. In some case this renders the detection signal hard to interpret. For instance the signals from pulse durations greater than 35 µs show a long lasting signal with many local minima ; even though only one molecular species is extracted, several misleading time-of-flights are measured. Still, the cleaner signals from shorter pulse durations are quite broad compared to the following strategy involving a double pulse scheme. This is due to the drawbacks already developed in subsection 5.4.2.

As an example of the bad precision such device offers, I propose to compute the equivalent acceleration voltage from the time-of-flight and mass of the molecular ion. With a distance-of-flight between the extraction electrode and the MCP of $d_{of} = 28$ mm, and time-of-flight taken at signal extrema, the efficient voltage is $V_{eff} = 47$ V @ $T_8^- = 5$ µs pulse and $V_{eff} = 36.7 \pm 1.17$ V @ $T_8^- \geq 10$ µs, which is far from the real 250 V applied (see 5.7 for timing diagram) to the electrode. Furthermore, signal is increasing over time ranges of 10-15 µs, so if computing the efficient voltage for early signals, it is possible to evaluate values as high as 450 V which is incompatible with the real value applied. This problem highlight an

ill-defined initial condition for the molecular ions. In particular the range of conditions at extraction time is so that the equivalent potential ranges from 50 to 450 V, which is nearly one order of magnitude. Nevertheless, as we have seen chapter 6, the guiding electrodes are set for a given initial energy of the molecular ions. Here it is hard to accommodate all the molecular ions with a single configuration. This explains why it is hard to observe molecular ions with the detection MCP downstream the trap, and is the reason why another strategy is developed to extract molecular ions from the octupole.

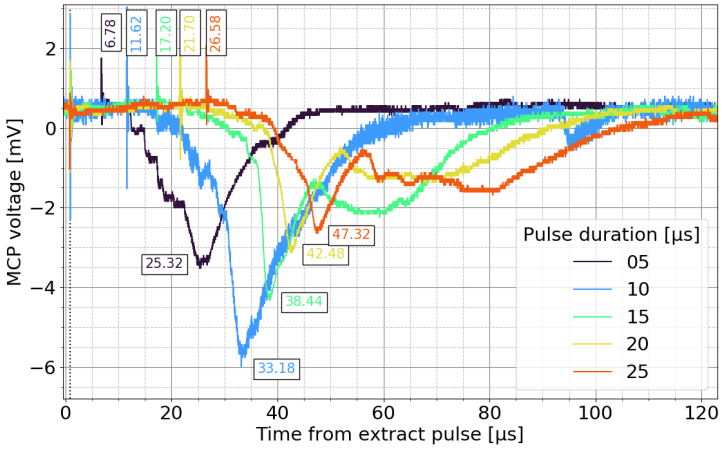

FIGURE 7.4: MCP signal for several extraction pulse durations. The framed numbers indicate the time for specific points. The pulses are triggered 0.9 µs after time origin. The molecular ion is TRP.

7.2.3 Double beam pulse

By the end of June 2019, the extraction scheme is modified by the installation of a more complete electrode layout, with the intent to enhance the molecular extraction and facilitate the detection of molecules in the downstream MCP. The molecular beam is pulsed at the octupole exit by a set of two electrodes (C8/C9). The effect of the double extraction pulse duration on the signal measured by the MCP is illustrated by the figure 7.5. Those measurements are carried out with a mix of PYR and DBCE pulsed at $V_8^- = -250$ V first and $V_9^- = -200$ V then, MCP voltage of 1880 V and impedance of 3925Ω (see 5.7 for timing diagram). The power supply for the C8 and C9 electrodes have a rise time of, respectively, 150 ns and 50 ns. In the figure 7.5, similarly to previously, the sharp peaks in the MCP signals due to C9 pulse interferences are present. The first pulse is displayed as a chronogram in the bottom left part of the graph (see the step function).

In the case of the double extraction pulse, I have chosen to illustrate my demonstration of the improvement by choosing to discuss two pulse durations that previously gave rise to complex detection signals on MCP. Indeed with pulse durations of 15 and 25 µs, the signals from single pulse (Fig. 7.4) were convoluted and showed extended broad peaks. In the case of the double extraction pulse, the measured signals looks cleaner. Indeed only two main peaks are visible, corresponding to each molecular ion species with masses 200 Da and 448 Da.

As for the time-of-flight, it provides a better result in estimating the applied voltage, while it is still far from the measured energy by a 15% error. Indeed, considering the end of

the first pulse as the time to which reference time-of-flight, the estimated efficient voltage is $V_{eff} = 161 \pm 1.5$ V for both duration tested. The estimated extraction energy is evaluated by applying a voltage to a downstream grid until the signal vanishes. The estimated extraction potential is 180 V. While a small uncertainty remains on the time origin the error is acceptable considering the level of precision we are demanding. Indeed to demand more precision would require to carefully calibrate the apparatus and anyway the improvement on the signal introduced by the double pulse are enough for the purpose of this work.

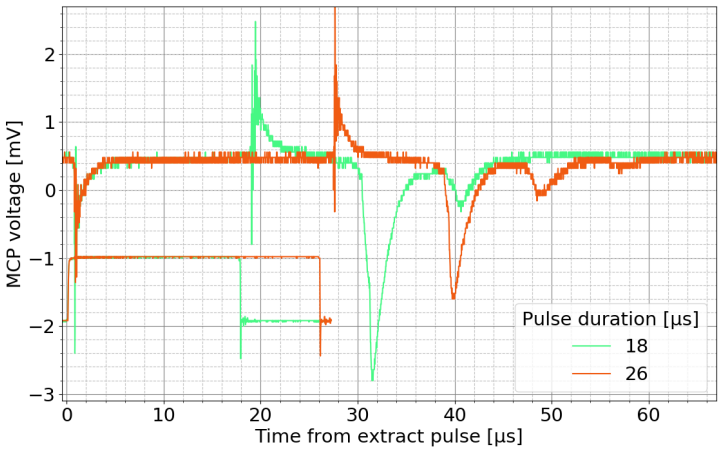

FIGURE 7.5: MCP signal for two extraction pulse durations. The first extraction pulse for electrode C8 is displayed as a step function in the lower left corner. The duration of the second extraction pulse is equal to the time between the two short lived narrow pulses visible in the beginning of the MCP traces. The positive short lived pulse is induced by a parasitic potential originating from the pulse. The molecular ions are PYR and DBCE.

Box 7.2.1: Time-of-flight

The time-of-flight is defined as the time a particle spend between two specific moments. Usually, it is representing the time between a trigger letting the particle free and a detection. In the case all the potential energy is converted to kinetic energy and the initial particle velocity is negligible compared to the velocity after acceleration, it is possible to write

$$QV_s = \frac{1}{2}Mv^2. \tag{7.1}$$

From there it is either possible to compute the velocity expected provided the extraction voltage V_s is known, or compute the equivalent effective voltage provided the distance d_{of} and time of flight t_{of} are known. In the first case, the velocity can be expressed as

$$v_{of} = \sqrt{\frac{2Q}{u_{amu}[\text{kg Da}^{-1}]}}\sqrt{\frac{V_s}{M[\text{Da}]}}\ \text{m s}^{-1} \tag{7.2}$$

$$= 1.384 \cdot 10^4 \sqrt{\frac{Z_e V_s}{M}}\ \text{m s}^{-1} \tag{7.3}$$

$$= 1.384\sqrt{\frac{Z_e V_s}{M}}\ \text{cm µs}^{-1}, \tag{7.4}$$

in the second case, simply,

$$V_s = \frac{1}{2Q} M v^2. \tag{7.5}$$

7.3 Guiding molecule to the GiantMol ion cloud detector

7.3.1 Description of a detection

With the help of the electrode layout presented in figures II.1, II.2 and II.3 it was possible to guide small molecular ions (PYR) towards the MCP beyond the trap. An extensive numerical simulation through SIMION was previously carried out to obtain an electrode setting to start from. It turned out to be in good agreement with experimental values providing detection of molecules by the MCP beyond the GICD.

The figure 7.6 is an example of detection of PYR. The MCP signal is here transformed by the signal chain from figure 7.3. Thus, each excitation on the MCP is transformed into a TTL signal. This signal is then sent to an oscilloscope and can be read as the blue curve. The purple step curve is indicating the timing of the second extraction pulse C9. All curves are synchronised with the pulse onset defined as $t = 0$. In figure 7.6 two bunches of TTL signals can be considered as originating from MCP excitation. A first TTL around 30 µs and another set of between 45 and 50 µs. The two pikes on the MCP signal before 10 µs accompany the onset and offset of the pulse and must be discarded as irrelevant signal. The PYR signal is related to the later group of gates around 45 µs delay. The earlier gates around 30 µs are rather due to parasitic molecular ions generated from the octupole atmosphere by the pressure gauge. Indeed when the octupole gauge is shut down the signal around 30 µs vanishes. A typical signal with neither molecular ions nor electrospray and the gauge activated can be seen in figure 7.7. In this later figure the TTL around 30 µs are visible and representative of a signal originating from the pressure gauge rather than molecular source.

7.3.2 Parameters

The voltage values used in order to guide the molecular ions towards the detection MCP are indicated in the table 7.2. Additionally, the voltages for other apparatuses are as follows. Electrospray needle : 2700 V. Capillary : 0 V, 107 °C. MCP voltage 1780 V. Pulse repetition period : $T_P = 70$ ms. C8 pulse : $0/-250$ V, $T_8^- = 5.92$ µs. C9 pulse : $0/-200$ V, $T_9^- = 6.47$ µs. As a control measure, the creation MCP was used regularly to check the source was operating correctly. The creation MCP was set to 1880 V and could be reached by setting the bender electrodes to 0 V.

The molecule is PYR. It was conditioned in a solution of water:methanol with volumetric proportions 50:v50, and concentration $2.4 \cdot 10^{-4}$ [M = mol/L]. No acetic acid was used.

The pressures in the vessels were accordingly to the table 7.3.

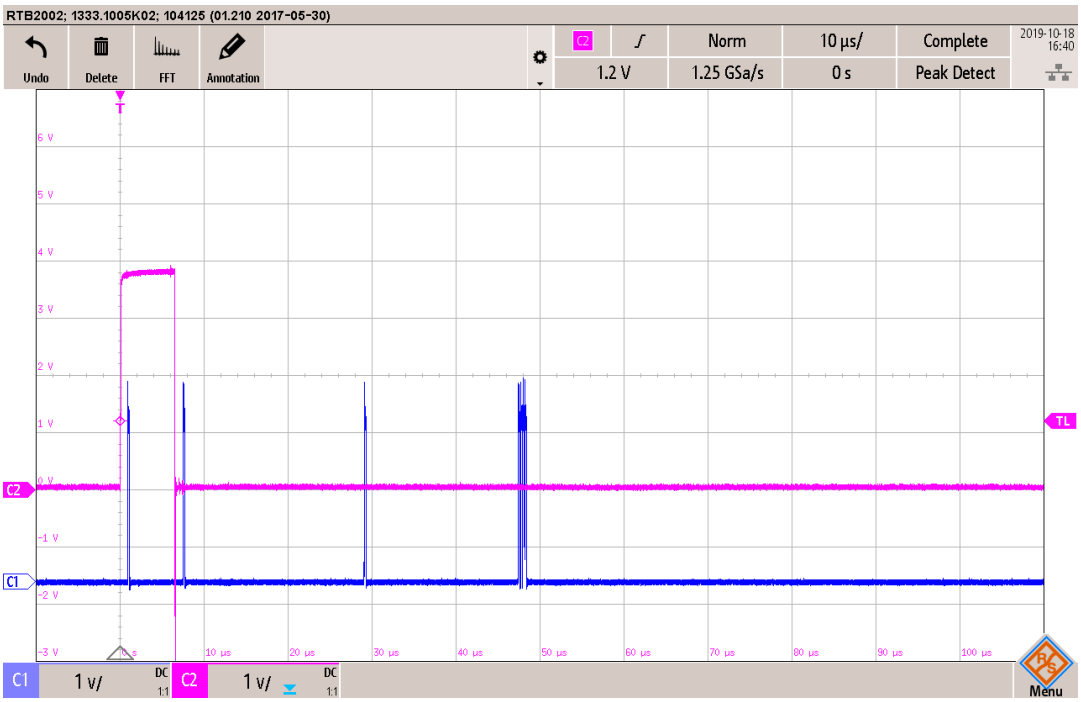

FIGURE 7.6: Signal measured at the output of the detection MCP through the detection chain from figure 7.3. The TTL gates around 45-50 µs are detection signal of PYR from detection MCP. Oscilloscope settings are 1V/div and 10µs/div.

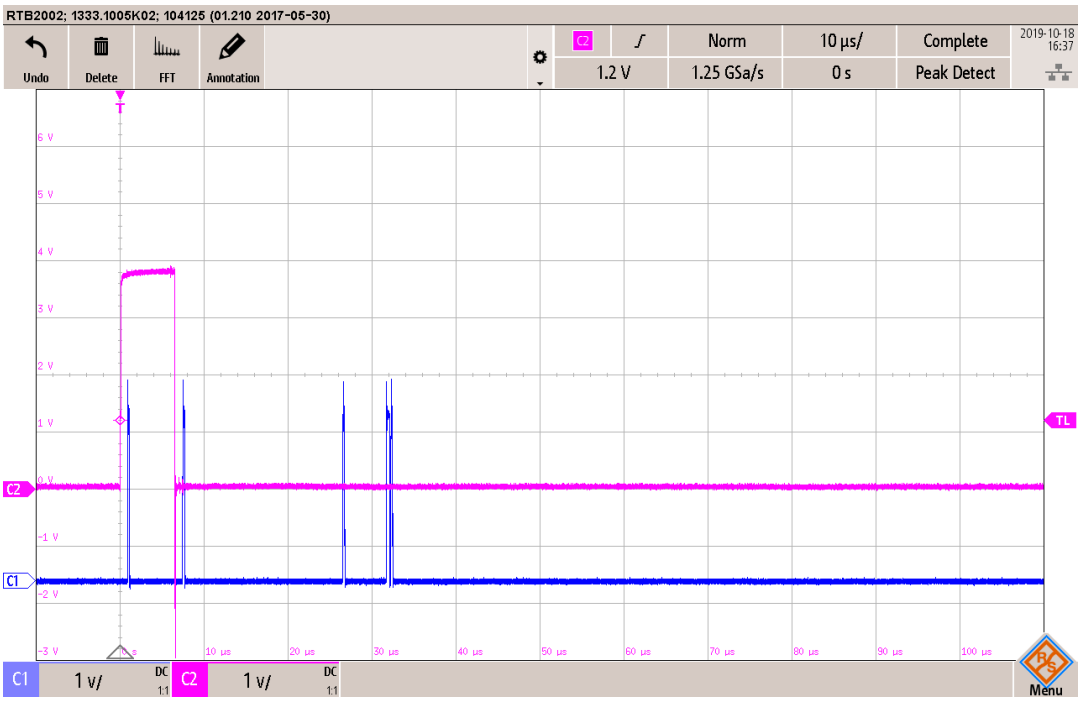

FIGURE 7.7: Signal measured at the output of the detection MCP through the detection chain from figure 7.3. The TTL around 30 µs are detection signal of gauge ions from detection MCP.

TABLE 7.2: Typical values for the electrodes in the guiding of PYR towards th detection MCP.

C4	C5	$C8^+$	$C8^-$	20	18	0	-250
C10	C12	C14	C17	0	85	0	0
C20	C19			180	-180		
C24	C27	C28		62	0	0	
D1	D3	D6		3	-3	50	
D9	D10	D11	D12	106	0	20	0
D13	D15			0	2		
D18	D17			0	0		

TABLE 7.3: Typical pressures inside GiantMol vessels, in mbar.

P_1	P_8	P_B	P_P
$2.9 \cdot 10^0$	$2.0 \cdot 10^{-3}$	$2.0 \cdot 10^{-6}$	$2.0 \cdot 10^{-8}$

Conclusion of part II

The molecular source is intended to produce molecular ions in the gaseous phase and then guide them to the `GiantMol` Ion Cloud Detector. It is composed of an Electrospray Ionisation Source, several parts such as a capillary, a skimmer, a guiding octopole, and a large set of electrodes and other electric devices intended to manipulate the molecular ions. Its operation relies on the combination of principles emanating from several disciplines and requires to accommodate electrostatics with fluidics. The fundamentals and practical considerations inherent to such system are presented in this part. The current controversies, also presented in this part, highlight the fragility of any attempt to analytically predict and design such device. While the analytical considerations allow to design the experiment and develop an intuitive understanding of the devices, the technological choices must be enlightened by a systematic study of the apparatus. Numerical simulations have also proven to be of help since few years in order to reduce the range of parameters around which research the best working point. In the bibliography, the emphasis is put on numerical models allowing to reproduce experiments and find the best configuration, that can be tested and explored in the experiment. While some numerical predictions could be carried out for the guiding of the particles and successfully brought to the experiment, the lack of reproducibility of the experiment is the main challenge we are facing now about the molecular source. Many developments have been pointed out, such as improving the capillary and skimmer assembly, improving the electrospray source, and also carrying out numerical simulations including fluidics and thermics in the capillary/skimmer assembly. While the signal intensity on the test creation MCP have been observed to vary to more than one order of magnitude (voltage in range from -2 mV to -40 mV), a similar experiment in another lab team (H2M) shows that it is possible to stabilise the signal with a mV precision over long period of time. The first experimental results of molecular ion guiding of relatively small ions ($M < 500$ Da) are encouraging and prove that the essential elements to guide molecular ions are present. The next step in guiding would be to increase the mass of the detected molecules, which is not possible now due to the limitations dealt with above.

Part III

DETECTOR BEHAVIOUR AND PROOF-OF-CONCEPT BY MOLECULAR DYNAMICS SIMULATIONS

Introduction

"Never send a human to do a machine's job."

– The agent Smith *in* Matrix

Purpose of numerical simulations

COMPUTER simulations are **mathematical modelling performed on a computer** in order to **generate representative scenarios** for a model, in our case of a **physical problem**. The first purpose of such computer simulations is to **predict** the behaviour of real systems. In this case, computer simulations are a **complement** to experiments or analytical predictions, as they can provide informations by far unavailable experimentally or by analytical derivation. Computer simulations are thus a wonderful tool to investigate real system and offer an element of comparison to experiments and/or theory when they are available. The other side of the coin is that numerical simulation outcomes are only a result from the model built for the specific application and computer. Put simply, a simulation is a manifestation of a model, and it can only render certain aspects of a situation. Thus it is of utmost importance to ensure the consistency of the computer model with the physical problem. This concern is addressed in all numerical projects and has become lately a field of research on its own. Nowadays in return, numerical simulations can also be used to verify the accuracy of mathematical models. A very interesting demonstration of the impact of numerical simulations as much as their issues and the controversies that it can raise can be found in the bibliographical memoir from Palmer [Pal09] about Edward Norton Lorentz, who established seminal principles in the domain of chaotic system, thanks to numerical simulations.

In the `GiantMol` context, computer programs are designed to simulate the behaviour of trapped ions submitted to various forces. This specific problem is part of **direct N-Body** problems [Ped21], a subset of **molecular dynamics** problems where the reciprocal interaction between particles are computed over the whole set. In our case, the computer simulations are mainly used, to prove that the concept of the experiment is practicable and, to study the behaviour of the system in order to better understand the mechanisms at play. The physical considerations regarding ion trapping and cooling are presented in part I. In this chapter 8, the mathematical model of ion trapping and cooling will be presented, along with the interaction model between the ions and the molecular ion via Coulomb interaction. Then chapter 9 is dedicated to the presentation of the results obtained with the code presented before. In this ultimate chapter, the simulation of a successful detection, demonstrating the `GiantMol` detection effect, will be thoroughly presented. Later,

statistics carried out to cover a large set of parameters will be presented. This will be useful to provide a range of settings providing detection. Also those statistics will be useful to study the mechanisms at play in the `GiantMol` principle. This will also serve the purpose of searching for tendencies, systematic effects and to investigate the detection mechanism in order to find a detection criterion. A detection criterion is a principle that distinguishes settings leading to a working detector and a non-working detector. Ideally, a detection criterion is a clear, unambiguous, rule based on experimental parameters and that allow for the determination of the detection efficiency in advance. It is for example an analytical law, or a threshold, that defines if the detector will provide a detection or not. Investigating the huge amount of parameters allowed to search for such detection criterion which is still ongoing.

Physics for the numerical model

Numerical simulations are designed to reproduce the `GiantMol` experiment in which a giant molecule is injected in a trapped and laser cooled ion set. The extensive physical description of those topics has been carried out in the former parts : laser cooling of trapped ions in part I, production of a molecular ion and its guiding in part II. The numerical model used for computer simulations is based on this physics, with a strong focus on the trapped ions and the interaction of a charged projectile with the set of trapped ions. In our model, the Ca^+ ions are trapped in a linear quadrupole with a set of alternating potentials $\Phi(x,y,t)$ (introduced in Eq. 1.5). A static potential $\Phi^\star_{DC}(z)$ (introduced in Eq. 1.34) is added in order to confine in 3D. The expressions are recalled below

$$\Phi_{Rad}(x,y,t) = \frac{U_{st} + U_{RF}\cos\Omega t}{2r_0^2}(x^2 - y^2) \tag{7.6}$$

$$\Phi^\star_{DC}(z) = U_{DC} m\omega_z^2 L^2 \left(1 - \exp\left(-\frac{z^2}{2L^2}\right)\right). \tag{7.7}$$

In the model, the trap dimensions are similar to that of `GiantMol` and presented in figure 1.7. The difference is that the rods are considered as a single segment of infinite length to which only radio-frequency field is applied. The axial potential is superimposed to the potential created by the radio-frequency field and its center is defined as the center of coordinate system.

The Ca^+ ions are modellised as two-level systems (see section 4.1) with only the cooling transition at 397 nm considered. In this model, only one laser is required in order to provide Doppler laser-cooling. Absorption, spontaneous and stimulated emissions are integrated in the model. The excitation probability is computed according to the von Neumann's equation applied to a two-level system. This computation is developed in section 4.2 and leads to the following excitation probability (introduced in Eq. 4.9)

$$\rho_{ee} = \frac{1}{2}\frac{\Omega_R^2}{\Omega_R^2 + 2\Delta_\star^2 + \Gamma_t^2/2} = \frac{A/2}{A + B + \Delta_\star^2} \tag{7.8}$$

with $\Delta_\star \stackrel{\text{def}}{=} \omega - \omega_{eg} = \Delta\omega - \mathbf{k_L} \cdot \mathbf{v_i}$ the detuning between the actual laser frequency and the required transition frequency of the atom accounted for Doppler effect. $A = {}^1\!/_2\Omega_R^2$, $B = {}^1\!/_4\Gamma^2$.

The giant molecule is injected in the trap with a given kinetic energy and position. Nothing in the numerical simulation reproduces any of the experimental devices used to produce, guide or detect the projectile. It is simply a charged particle added to the numerical simulation. In our experiment, the charged projectile is sent to go through the trapped ions. It is expected the projectile interacts with cloud via Coulomb interaction during few micro seconds. During the interaction, and after, the fluorescence emitted by the ions is carefully monitored. The detection is considered successful if a permanent fluorescence variation is observable.

Chapter 8

Computer programs for direct N-body simulations

8.1 N-body Molecular dynamics computer program

In the context of trapped ions in radio-frequency fields, important results were first introduced using either **Monte-Carlo method** with energy minimizing algorithms or molecular dynamics. While Monte-Carlo method could only account for "the ion dynamics within an ordered structure and not the dynamics of the formation of an ordered structure" [Cas88], the **molecular dynamics** method could account for the whole dynamics, but at the cost of a prohibitive simulation time in clouds with more than few ions with late 80's computer capacity. One technique to circumvent this limitation was to use periodic edge conditions, in an effective static potential and infinite space [Rah86; Win87; Sch88]. Nevertheless effects due to finite size and non-linear dynamics could not be neglected regarding dynamics and thermodynamics (see for instance subsections 3.4 and 3.5). The increase in processing unit power, and the development of parallel computing, allowed to overcome those limitations by including a bigger finite number of ions, in a truly alternating field. While molecular dynamics with reasonably resolved micro-motion was only possible for few ions in the 80's while, it is now possible to compute several thousands of ions with a much smaller time-step, for longer periods of time.

When studying the dynamics of atoms or ions, laser cooling can be introduced in two different ways. First by modelling cooling by a friction force, which is quite simple and time effective but incompatible with our need for a fluorescence diagnostics. This way of modelling cooling is also not compatible with integration algorithm such as **velocity-Verlet method**. Second by modelling cooling by a corpuscular light-matter interaction. In this approach the interaction modifies the momentum of atoms by a mechanism of absorption-emission of photons. A random number generation compared to probabilities periodically triggers the interaction if required. This allows to monitor an emitted fluorescence.

The cooling of trapped ions with a single laser is already numerically studied by Marciante et al. [Mar10]. Independently, in the context of the `GiantMol` experiment, a projectile charged particle can be introduced in the system to study injection of a giant molecule. The interaction between the charged projectile and the trapped ion is purely done through

TABLE 8.1: List of numerical parameters used in this section.

i	Time step variable (index) in computer program.
j	Other ion index variable in loops in computer program.
$k_C = 1/(4\pi\varepsilon_0) = 8.9875 \cdot 10^9$ [Nm^2/C^2]	Coulomb factor constant.
$m = 6.6551079 \cdot 10^{-26}$ [kg]	$^{40}Ca^+$ trapped ion mass
$M = M^{GMol} = 1.6605389 \cdot 10^{-21}$ [kg]	Giant molecule projectile mass.
N	Total number of ions.
n	Ion index variable in computer program.
$Q = Q^{GMol} = Z_e q_e$ [C]	Giant molecule charge.
U_{RF} [V]	Radio-frequency voltage amplitude.
U_{DC} [V]	Axial confining static voltage.
r_0 [mm]	Trap internal radius.
γ [kg/s]	Friction parameter in the computer program.
δi	Time interval between two time steps in computer program.
τ_{RF} [s]	Radio-frequency voltage period in computer program.
$\overline{\cdot}$	Notation for temporal average.
$\langle \cdot \rangle$	Notation for population mean.

Coulomb interaction of point charges. In the context of `GiantMol` experiment, the useful detection signal is seek for in the fluorescence. This quantity can be monitored as long as laser cooling is present.

8.2 Structure of the simulations

N°	PROGRAM INTERACTION	Laser	Giant Mol.	Int. algo.
1	INITIALISATION	0	0	Lan
2	RF TUNING	1	0	V-V
3	THERMALISATION	1	0	V-V
4	INJECTION	1	1	V-V
5	POST-INJECTION	1	0	V-V

PROGRAM RF HEATING	Laser	Giant Mol.	Int. algo.
INITIALISATION	0	0	Lan
RF RELAX	0	0	V-V

0 : off
1 : on
Int. algo. : Integration algorithm
Lan : Langevin
V-V : Velocity-Verlet

FIGURE 8.1: The two main molecular dynamics programs used during this thesis. Each program is reduced to a set of steps computed chronologically in order from top to bottom. The presence of laser and giant molecule in the simulation is indicated by a *0* (no) or a *1* (yes). The integration algorithm used is indicated with the label ***Lan*** (Langevin algorithm) or ***V-V*** (Velocity-Verlet algorithm).

The molecular dynamics code is written in ForTran 90 with OpenMP single-node parallelization. It integrates the trajectory of each ion considering all forces applied to the ions (See frame 8.4.1) in a step-by-step process supported by integration algorithms described below. Several versions of the computer program have been used during this thesis, but only the two programs whose results are presented later are presented here (Fig. 8.1). A first program called `INTERACTION` is dedicated to the study of the interaction of a charged projectile with a laser cooled set of ion. Its development was initiated before I joined the

group. A second program called RF HEATING is dedicated to the study of the behaviour of the ion set in a radio-frequency field alone, and was developed during my PhD from the first code. In figure 8.1, each code is presented in a box whose first line is the code title. Each of the program steps are presented in their order of execution from top to bottom, and are separated from the other by dashed lines. Also are indicated the presence of the laser, giant molecule and the type of integration algorithm for each step. During the execution of the program, the desired parameters are saved at different rates, and in particular at the end of each step in order to be passed to the next step. The acquisition scheme for critical parameters such as the temperature is specified below.

8.2.1 INTERACTION program

INTERACTION was the first complete program used and this is the program which generated the data for the article "Non-destructive detection of large molecules without mass limitation" [Poi21]. It is executed in five steps. The first INITIALISATION step is dedicated to the establishment of the numerical environment, in which the radio-frequency amplitude is set to a low value of 10 V. Ions are initialised at null velocity with random positions, with the only condition to respect a spatial Gaussian random distribution. While the ions are set in motion by the trapping potential, a numerical process reproducing friction, Brownian motion and a thermal bath acts on the ion velocities which leads the ion set to a defined temperature. The integration algorithm used during this first part of the simulation is the **Langevin algorithm**. Then after a predefined number of numerical time steps, the program switches to the following steps, where the cooling laser is always activated and **Velocity-Verlet** is used as integration algorithm. Also, the fluorescence of the ions is computed at a rate identical to the radio-frequency period τ_{RF}. The second step is RF TUNING, a step where the radio-frequency voltage amplitude is increased to the desired value using a hyperbolic tangent function [Ped15]. Then in a third step, the THERMALISATION step is dedicated to the thermalisation of the ions. This step is in fact simulating the dynamics of trapped ions with laser cooling, and its duration is also predetermined. The INJECTION step is no more different from the former step, except a charged projectile is introduced in the simulation and set to collide with the ions with a specified kinetic energy. The charged projectile is initialised and removed far enough from the cloud not to perturb the ion set. The duration of this fourth step depends on the time-of-flight of the projectile. Then the fifth step, POST-INJECTION, is again identical to the THERMALISATION step, except it is called differently because the charged projectile interacted with the ions and ion temperature and fluorescence are closely monitored to search for changes. This last step is run long enough for a change in the ion dynamics to have time to appear.

8.2.2 RF HEATING program

RF HEATING program is dedicated to the study of the dynamics of the ion cloud solely stored in a trapping field, without laser cooling and without molecule injection. Its name

comes from the fact that it was developed for the purpose to study radio-frequency heating. It uses the advances in code developed for the `INTERACTION v2`, and notably shares in common two of its core steps `INITIALISATION` and `RF TUNING`. The last step is developed especially for this program. It is called `RF RELAX` and is dedicated to the computation of the dynamics of the ions in the trapping-field once the right settings have been established by the previous steps. Numerically, the two last steps are identical, excepted the radio-frequency voltage amplitude is variable in `RF TUNING` and fixed in `RF RELAX`. No fluorescence is collected in this program, and the analysis mainly relies on the observation of the dynamical parameters (position, velocities and accelerations), as much as other ion set parameters such as thermodynamic ones (temperature) or energetic ones.

8.3 Computer and program performance

During my PhD I have had access to three computers solely dedicated to the execution of the numerical project. Those computers will be refereed with respective nicknames : Simu1, Simu2 and Mesocentre[1]. The two first computers are classical desktop computers hosted in the lab, while Mesocentre is not strictly speaking a computer, but is in fact the name of the whole AMU computing facility. In particular Mesocentre makes available 158 rackmount computers equipped with 32 computer cores, available upon request, all at the same time if desired. Hobitton was the first computer used in my numerical works, and proved sufficient when few simulations were programmed. However, concerns about execution time appeared when hundreds of simulations were required to run for statistical purposes. The use of Simu2 and Mesocentre proved to be unavoidable when a large amount of simulations were necessary to carry out the systematic and statistical study. In Poindron et al. [Poi21], the data set represents a total of 2800 individual runs of `INTERACTION` program. The main characteristics, and a performance comparison, are available in the table 8.2.

8.3.1 Comparative computer performances

Given fixed simulation parameters (number of time steps, time step interval ...), the wall-clock duration[2] of the simulation mainly depends on the number of interactions (ions) and the machine computing power. To compare the performance of each computer, the average wall-clock execution time of `INTERACTION` with fixed simulation parameters, is measured. The data from Poindron et al. [Poi21] are used as they have been produced with the three machines. In particular, the simulation is done for $N = 1024$ ions, simulating a 10.53 ms molecular dynamics.

[1] https://mesocentre.univ-amu.fr/ressources/

[2] Wall-clock time, or elapsed real time, is the actual time taken from the start of a computer program to the end. It is different from CPU time, or process time, which is the amount of time for which a CPU processed instruction of a computer program. In the case of a single-core CPU wall-clock time and CPU time are usually similar, but in the case of a multiple-core CPU, the CPU time is bigger than wall-clock time. The rule is to add the CPU time for each core. Generally, computing center allocate users a certain amount of CPU time.

TABLE 8.2: Computer characteristics and performances of the ForTran computer code INTERACTION. Mesocentre is only one SkyLake node.

Computer	CPU	RAM	Exec. time [min/run]
Simu1	Xeon W3690 | 6 cores @ 3.47 GHz	12 Go	48.3
Simu2	Xeon W2155 | 10 cores @ 3.30 GHz	32 Go	8.0
Mesocentre	Xeon Gold 6142 | 32 cores @ 2.60 GHz	192 Go	6.7

Simu2 and Mesocentre have similar performances. In terms of FLOPS [3], which is an indicator of how much operations a computer carries out per second, both computers provide around 10 GFLOPS in the context of the program INTERACTION described above. Simu1 is approximately seven time slower than the two other computers. In Poindron et al. [Poi21], the wall-clock execution time by Simu1 would have been 93 days. By combining both Simu2 and one Mesocentre node, it was possible to reduce the computation time to a dozen of days. In practice, the data were produced over a month, as data analysis was carried out periodically, as simulations went along.

8.3.2 Execution speed optimisation

In the process of reducing the execution time, programming the code in C language allowed for a dramatic reduction of execution time by at least one order of magnitude [Ped21] ! Indeed a thorough investigation of the ForTran program performances highlighted that some of the optimisations expected were not triggered by the usual options. To get around this problem required to explicitly refers to the optimisations in the computer program which is not possible in ForTran. A C language computer program was developed especially because this language allows for the explicit call of instructions related to hardware functions. By doing so, notably, it was possible to explicitly call the AVX-512 processor instructions and use the built-in hardware for the inverse square root ($1/\sqrt{x}$) unit in the Xeon CPU. As $1/\sqrt{x}$ is a particularly used function in codes involving Coulomb forces, it allowed to dramatically reduce the execution time. In single-core execution, the computation speed has been reported to increase by 340% [Ped21], with excellent scalability with the number of cores. The use of explicit optimisations in C language allowed for Simu2 to reach $\approx$ 500 GFLOPS, which represents $\approx$ 75% of its theoretical maximum performance. The use of a C language version of the computer program for later numerical simulations is thus expected.

8.4 Integration algorithms

8.4.1 Ion initialisation – Langevin algorithm

The first preliminary steps in the molecular dynamics code are the initialisation and the thermalisation to a predetermined temperature. With the Langevin algorithm, an integer number N of ions are created with a null velocity and a position randomly chosen in a

[3] FLoating-point Operations Per Seconds

Gaussian distribution, within the trap boundaries. They will evolve with a fixed time step, in a radio-frequency trapping field and a static potential for confinement. Coulomb repulsion is considered between each pair of ions. The thermalisation is induced by a Langevin process involving a friction term. A random walk at a specific bath temperature is implemented. The following set of equations describes the dynamics of the ion n with coordinates $\mathbf{r_n} = (x_n, y_n, z_n)$. It is based on forces described in the frame 8.4.1.

$$m\partial_{ii}x_n = q_e^2 k_C \sum_{\substack{j=1 \\ j\neq n}}^{N} \left(\frac{x_n - x_j}{|\mathbf{r_n} - \mathbf{r_j}|^3} \right) - \frac{2q_e U_{RF} \cos\Omega i}{r_0^2} x_n - \gamma \partial_i x_n + \sqrt{2\gamma m k_B T_b}\Theta_{x_n} \tag{8.1}$$

$$m\partial_{ii}y_n = q_e^2 k_C \sum_{\substack{j=1 \\ j\neq n}}^{N} \left(\frac{y_n - y_j}{|\mathbf{r_n} - \mathbf{r_j}|^3} \right) + \frac{2q_e U_{RF} \cos\Omega i}{r_0^2} y_n - \gamma \partial_i y_n + \sqrt{2\gamma m k_B T_b}\Theta_{y_n} \tag{8.2}$$

$$m\partial_{ii}z_n = q_e^2 k_C \sum_{\substack{j=1 \\ j\neq n}}^{N} \left(\frac{z_n - z_j}{|\mathbf{r_n} - \mathbf{r_j}|^3} \right) - \left. \frac{\mathrm{d}\Phi_{DC}^{\star}(z)}{\mathrm{d}z} \right|_{z_n} - \gamma \partial_i z_n + \sqrt{2\gamma m k_B T_b}\Theta_{z_n} \tag{8.3}$$

The resolution of the ion dynamics is numerically done using vGB82 algorithm from Gunsteren and Berendsen [Gun82]. Once the initialisation is finished the thermal bath and the friction are not applied anymore and the Langevin algorithm is replaced by velocity-Verlet algorithm for dynamics integration.

8.4.2 Velocity-Verlet algorithm

The velocity-Verlet algorithm is relevant when no velocity-dependent forces are present in the dynamics. In that case, the algorithm is working as follows.

The new set of equations describing the dynamics of the ions only consider electrical forces – Coulomb repulsion and trapping potentials :

$$m\partial_{ii}x_n = q^2 k_C \sum_{\substack{j=1 \\ j\neq n}}^{N} \left(\frac{x_n - x_j}{|\mathbf{r_n} - \mathbf{r_j}|^3} \right) - \frac{2qU_{RF} \cos\Omega t}{r_0^2} x_n \tag{8.4}$$

$$m\partial_{ii}y_n = q^2 k_C \sum_{\substack{j=1 \\ j\neq n}}^{N} \left(\frac{y_n - y_j}{|\mathbf{r_n} - \mathbf{r_j}|^3} \right) + \frac{2qU_{RF} \cos\Omega t}{r_0^2} y_n \tag{8.5}$$

$$m\partial_{ii}z_n = q^2 k_C \sum_{\substack{j=1 \\ j\neq n}}^{N} \left(\frac{z_n - z_j}{|\mathbf{r_n} - \mathbf{r_j}|^3} \right) - \left. \frac{\mathrm{d}\Phi_{DC}^{\star}(z)}{\mathrm{d}z} \right|_{z_n} . \tag{8.6}$$

Knowing the position $\mathbf{r_n}(i)$ and velocity $\mathbf{v_n}(i)$ of an ion n at a given time step i, those equations allow the determination of the acceleration at this time step $\mathbf{a_n}(i)$. Then the dynamics at the next time step $i + \delta i$ is determined with the velocity-Verlet algorithm : first

the new position is determined, then the new velocity, so that :

$$\mathbf{r_n}(i+\delta i) = \mathbf{r_n}(i) + \mathbf{v_n}(i)\delta i + \frac{1}{2}\mathbf{a_n}(i)(\delta i)^2 \tag{8.7}$$

$$\mathbf{v_n}(i+\delta i) = \mathbf{v_n}(i) + \frac{1}{2}\mathbf{a_n}(i)\delta i. \tag{8.8}$$

Using the set of three equations above with those new parameters allows to compute the acceleration at time step $i + \delta i$, and it is then possible to compute the dynamics of the following time step using the same principle.

This is what I call the **core algorithm** because it is the minimal application to describe the dynamics of the trapped ions : equations of motion and velocity-Verlet algorithm. This is sufficient when it comes to studying the dynamics of trapped ions only. Nonetheless many other functionalities may be required. The functionalities in the program that go beyond the code algorithm presented above are described below as **supplementary functionalities**. Their use depends on the scientific purpose of the program execution.

Box 8.4.1: Forces

The force an ion n is subject to is the sum of the forces it undergoes. The following describes all the forces an ion can undergo in our simulations.

Coulomb repulsion between ions The total Coulomb repulsion that an ion n is subject to, is the sum of all the Coulomb forces applied by each of the other ions j of the cloud.

$$F_n^{u/Coul} = q_e^2 k_C \sum_{\substack{j=1 \\ j\neq n}}^{N} \left(\frac{u_n - u_j}{|\mathbf{r_n} - \mathbf{r_j}|^3} \right), \text{ with } u = x, y, z \tag{8.9}$$

and q_e the ion charge in Coulomb, $k_C = 1/(4\pi\varepsilon_0)$.

Trapping forces Two electric fields are applied to the ions in order to confine them in the trap : a radio-frequency field and a static field. The forces are expressed as follows :

$$F_n^{u/RF} = \frac{2q_e U_{RF}\cos\Omega t}{r_0^2} u_i, \text{ with } u = x, y \tag{8.10}$$

$$F_n^{z/DC} = -\left.\frac{\mathrm{d}U_G(z)}{\mathrm{d}z}\right|_{z_i}. \tag{8.11}$$

with $\Phi^\star_{DC}$ the axial static potential obtained by fitting the current trap geometry with SIMION. The fit analytically expresses as

$$\Phi^\star_{DC} = U_{DC} m\omega_z^2 L^2 \left(1 - \exp\left(-\frac{z^2}{2L^2}\right)\right) \tag{8.12}$$

with $L = 2.45$ mm a characteristic length given by the fit. This potential acts as a harmonic potential at its center with characteristic frequency $\omega_z = 90.8$ kHz for $U_{DC} = 1$ V. The frequency is deduced from the fit (Fig. 1.6).

Friction and Brownian motion for Langevin dynamics Additional forces can be added to reproduce a viscous friction and a Brownian motion, expressed as follows :

$$F_n^{u/Fric} = \gamma \partial_t u_i, \text{ with } u = x, y, z \tag{8.13}$$

$$F_n^{u/BM} = \sqrt{2\gamma m k_B T_b}\Theta_{u_i}. \tag{8.14}$$

with $\partial_t = \frac{\partial}{\partial t}$, γ a friction coefficient, k_B Boltzmann's constant, T_b the temperature of the thermal bath, θ a collection of independent standard Wiener processes modelling Brownian motion through Markov chain Monte-Carlo method [Ske02]. Those two forces are only used in the initialisation part of the code.

8.5 Supplementary functionalities

8.5.1 Variable time step with distance of closest approach

By carefully choosing a sufficiently small time step it would be reasonable to run this algorithm with a constant time step. Without a charged projectile, choosing a tiny time step adapted to the highest temperature may produce extremely long simulations with no substantial benefits at lower temperatures. Conversely choosing a time step relevant for cold ions may be inappropriate to higher temperatures. As we are mainly interested in the dynamics of the cold ions it could be justified to choose a time step relevant up to a certain temperature (< 1 K) and tolerate some error at the highest temperatures (typically up to 10^3 K). The first choice has been to choose a time step small enough to fill one radio-frequency period with one hundred time steps. This leads to the first definition of time step as $\delta i = \tau_{RF}/100 = 2\pi/(100\Omega_{RF})$.

Nonetheless, when a charged projectile is inserted in the simulation, it can be wise to have a variable time step decided in order not to miss collisions. To select an appropriate simulation time step rendering all collisions properly, it is wise to compute the distance of closest approach of particles. Knowing the positions and velocities of ions, it is possible to compute the distance of closest approach of two ions, i.e the smallest distance two ions will interact, by comparing their kinetic and Coulomb energies. By doing so to each pair of particles at every time step, the smallest closest approach distance in the cloud can be retrieved and used to determine the appropriate time step. But a variable time step may also be time consuming, so it is mostly reserved to the `INJECTION` step.

Thermodynamic distance of closest approach

Considering two ions colliding, with velocities $\mathbf{v_1} = -\mathbf{v_2}$ separated by distance r, in the frame of reference of their center of mass, the distance of closest approach is :

$$r_c = \frac{2Z_e^2 k_C}{m v_1^2}. \tag{8.15}$$

Replacing the ion velocity v_1^2 by the population mean value $\langle v^2 \rangle = kT$ of Maxwell-Boltzmann distribution at temperature T, we have :

$$\boxed{r_c = \frac{2Z_e^2 k_C}{k_B T}.} \tag{8.16}$$

This typical result arises from the equalisation of kinetic energy with Coulomb energy is the two particle system. The computation assumes conservative forces and energy conservation. The knowledge of this distance of closest approach is essential in order to properly render the collisions with an appropriate time step. Indeed the time step δi must be small enough in order to resolve the particle trajectories with a spatial resolution lower than this distance of closest approach r_c. The criterion for the time step is that "in a time step the ions should move much less than their minimum approach distance" [Sil16]. If not, the particle may step over another particle it would have otherwise collided with if the time step was smaller. This condition mathematically translates into

$$\delta i \ll r_c \tag{8.17}$$

or more precisely (8.18)

$$\delta i = \alpha r_c \tag{8.19}$$

introducing α as a constant.

It is then possible to run test simulations in order to evaluate the optimum value α so it is small enough to render the collisions physical but not too small in order to reduce the computation time as much as possible. Because the time step is compared to the distance of closest approach which is constant for a given temperature, it is possible to choose a time step fitting all the possible situations in a trapped ion experiment by choosing an arbitrarily low temperature, such as the Doppler limit.

Variable time step

Nevertheless the above computation would make the time step unreasonably small if the temperature increases by several order of magnitudes as it is the case in `GiantMol`. Thus during the simulation it may be relevant to evaluate the optimal time step at every step, so the time step is variable. In `GiantMol` numerical simulations, this is done only when the charged projectile is introduced or when the precise dynamics of the trapped ions is investigated.

To implement the variable time step, it is done by comparing the time step δi with the actual closest distance between ions $\min r_{nj}$ rather than with the general distance of closest approach [Sil16]. With equation 8.16 and some other considerations that can be found in the article [Sil16], the variable time step is defined as follows

$$\boxed{\delta i = \min_{\substack{n,j=1\ldots N \\ j\neq n}} \frac{-v_{nj} + \sqrt{v_{nj}^2 + a_{nj} \times r_{nj} \times \alpha}}{a_{nj}}} \tag{8.20}$$

with $a_{nj} = \|\mathbf{a_n} - \mathbf{a_j}\|$,$v_{nj} = \|\mathbf{v_n} - \mathbf{v_j}\|$ and $r_{nj} = \|\mathbf{r_n} - \mathbf{r_j}\|$, the accelerations, velocities and distances in the frame of reference of each pair of ions (n,j), $\alpha = 10^{-1}$. The author notice that "$v_{nj}\delta i$ wasn't sufficient to describe a Coulomb interaction because as the ions approach their minimal approach distance and as the velocity v_{nj} vanishes the second term $0.5a_{nj}(\delta i)^2$ [...] can no longer be neglected."

8.5.2 Radio-frequency ramp

The tuning of the radio-frequency is a step whose goal is to smoothly change the radio-frequency voltage amplitude. This is required to bring a cold cloud with temperatures below 1 K to some of the highest values of radio-frequency voltage amplitude that have been tried. For instance, it is not possible to bring hot initialised ions to sub-Kelvin temperatures with a radio-frequency voltage amplitude such as $U_{RF} = 70$ V. Also, simply starting from a low radio-frequency voltage amplitude such as $U_{RF} = 23$ V and switching later to the desired value is detrimental to the ion cloud stability. The tuning from a low radio-frequency amplitude U_{RF}^{start} to a high amplitude U_{RF}^{end} is thus a step on its own. During this RF tuning step, the radio-frequency voltage amplitude is controlled by a hyperbolic tangent function according to Pedregosa-Gutierrez et al. [Ped15, eq. 6], so that at simulation time step i the radio-frequency amplitude is

$$U_{RF}(i) = \frac{2Q}{Mr_0^2}\left(U_{RF}^{start} + \frac{U_{RF}^{start} - U_{RF}^{end}}{2}\mathrm{d}U_{rf}\right) \tag{8.21}$$

$$\mathrm{d}U_{rf} = 1 + \frac{\tanh\left(2N_H i^\star - N_H\right)}{\tanh N_H} \tag{8.22}$$

$$i^\star = \frac{(i - j_{start})}{j_{end} - 1}, i \in [\![j_{start}, j_{end}]\!]. \tag{8.23}$$

For $N_H = 1$, $U_{RF}(i)$ is a linear function, while for $N_H \to \infty$, $U_{RF}(i)$ becomes a step function. In our case $N_H = 4$. $\mathrm{d}U_{rf}$ ranges from 0 to 2. j_{start} and j_{end}, both integers defining the time step index at the start and end of the `RF TUNING` step, are defined so that the total number of numerical time steps are $j_{end} - j_{start}$.

8.5.3 Laser cooling implementation

To each atom is associated a state variable representing if the atom is in the ground state or in the excited state. At fixed interval of time of same radio-frequency phase in the simulation, the probability of excitation and de-excitation of every atom is compared to a random number generation (RNG). If the drawing is favourable to either excitation or de-excitation, the state of the atom is changed and an instantaneous change in velocity is applied to the atom.

In case of absorption, the probability of excitation of an atom with velocity $\mathbf{v_n}$, in a time interval δi, at steady-state, is [Mar11] :

$$P_e(\mathbf{v_n}, di) = \Gamma_0 \rho_{ee}(\mathbf{v_n})\delta i \tag{8.24}$$

with Γ_0 the natural width of the transition, ρ_{ee} the occupation probability of the excited state (see Eq. 4.9). In the results presented here, saturation parameter is chosen as $s = 1$ and detuning as $\Delta^\star = -\Gamma_0$.

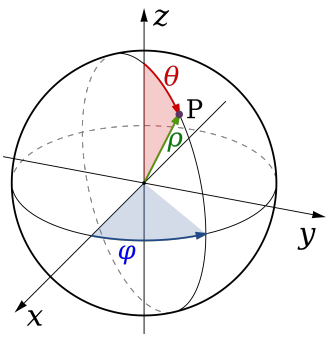

FIGURE 8.2: Spherical coordinates. z-axis is trap axis, along which lasers are injected.

Every time a RNG is generated, if $\texttt{rng} > P_e(\mathbf{v_n})$ the atom is excited and its velocity is modified so that $\mathbf{v_n}(i + \delta i) = \mathbf{v_n}(i) + \hbar\mathbf{k_L}/m$ with $\mathbf{k_L}$ laser wave-vector. In spherical coordinates (Fig. 8.2), one can write :

$$\boxed{\mathbf{v_n}(i + \delta i) = \mathbf{v_n}(i) + \frac{h}{m\lambda}\begin{bmatrix}\cos\phi\sin\theta\\ \sin\phi\sin\theta\\ \cos\theta\end{bmatrix}.} \tag{8.25}$$

The trap axis is z-axis and is also the axis along which the lasers are injected in the experiment. When so, $\theta = 0.01$ and $\phi = \pi/4$. The small non-null θ value is set to break symmetry with respect to trapping potential so ions do not rotate around the z-axis at unrealistic velocities [Mar10]. By substituting the cos and sin function by their small-angle approximations, it is easy to see that the laser contribution is mostly on the z-axis. Also in our simulations the lasers are fixed to a specific direction, dimension, wavelength and power.

Now if the atom is already in the excited state, the probability of de-excitation $P_g(\mathbf{v_n}, \delta i)$ is to be considered. Spontaneous emission and stimulated emission are accounted for. In time the probability follows a decreasing exponential law and if $\texttt{rng} > P_g(\mathbf{v_n})$ the atom de-excites and its velocity is modified according to Eq. 8.25, generating a photon in a random direction – thus ϕ and θ are randomised [Mar11].

8.5.4 Giant molecule injection

A giant molecule with mass M^{GMol} and charge Q^{GMol} can be injected in the cloud in order to reproduce the prototype experiment purpose. At a specified time, the giant molecule is generated at position $(0; 0; -z_0)$ on the z-axis with an initial velocity $v_0^{GMol} = (0; 0; v_{z0}^{GMol})$ in direction of the ion cloud. The initial velocity is computed so that the giant molecule will

pass through the center of coordinates of the frame of reference with a specified energy E^{GMol}. Because of the axial static potential being null in the origin and higher in the vicinity, the potential energy U_0^{GMol} due to the axial static potential at $-z_0$ is subtracted from the initial giant molecule energy. So the giant molecule is injected with initial energy :

$$E_0^{GMol} = E^{GMol} - U_0^{GMol} \tag{8.26}$$
$$= E^{GMol} - U_G(-z_0) \tag{8.27}$$
$$= E^{GMol} - U_{DC} Q^{GMol} M \omega_z^2 L^2 \left(1 - \exp\left(-\frac{(-z_0)^2}{2L^2}\right)\right) \tag{8.28}$$
$$v_{z0} = \sqrt{\frac{2E_0^{GMol}}{M^{GMol}}} \tag{8.29}$$

8.6 Motion, temperature and energy

8.6.1 Effective temperature

As said in chapter 3, the motion of the ions can be separated into two part : the motion of the center-of-mass in the laboratory frame of reference, and the motion of the particles relatively to the center-of-mass. The temperature of the ion population is understood as the temperature related to the particle velocity relatively to the center-of-mass. Indeed this is the motion comparable to Brownian motion, i.e thermal motion.

Let us call the velocity of an ion n at any time step i, $\mathbf{v_n}(i) = [v_n^x; v_n^y; v_n^z]$, and its thermal speed $\overline{\mathbf{v_n}}(i + \tau_{RF}/2) = [\overline{v_n^x}; \overline{v_n^y}; \overline{v_n^z}]$, the velocity computed from the average over one radio-frequency period. Let us use $\langle \cdot \rangle$ as the notation for the mean of the population. The simulation time step δt_i is variable for each time step i. Those quantities write as follows :

$$\overline{\mathbf{v_n}}(i + \tau_{RF}/2) = \sum_u \overline{v_i^u}\, \mathbf{e_u} \text{ , with } u = x, y, z \tag{8.30}$$
$$\langle \overline{\mathbf{v_n}} \rangle = 1/N \sum^N \overline{\mathbf{v_n}} \tag{8.31}$$
$$\text{with } \overline{v_n^u} = \frac{1}{\tau_{RF}} \sum_{k=i}^{i+\tau_{RF}} v_n^u(t) \delta t_k. \tag{8.32}$$

At thermal equilibrium, using the Maxwell-Boltzmann description, we can define the temperature of the ion cloud as follows :

$$\frac{3}{2} k_B T = E_{kin} \tag{8.33}$$
$$\frac{3}{2} k_B T = \frac{1}{2} m \langle \overline{\mathbf{v_n}}^2 \rangle \tag{8.34}$$
$$\boxed{T = \frac{m \langle \overline{\mathbf{v_n}}^2 \rangle}{3 k_B}.} \tag{8.35}$$

Furthermore it is possible to decompose the temperature for every axis. Doing so we can show that $T = \frac{1}{3}(T_x + T_y + T_z)$. For that we decompose the mean velocities.

$$\langle \overline{\mathbf{v_n}}^2 \rangle = \langle \overline{\mathbf{v_n^x}}^2 \rangle + \langle \overline{\mathbf{v_n^y}}^2 \rangle + \langle \overline{\mathbf{v_n^z}}^2 \rangle \tag{8.36}$$

$$\frac{3k_BT}{m} = \frac{k_BT_x}{m} + \frac{k_BT_y}{m} + \frac{k_BT_z}{m} \tag{8.37}$$

$$T = \frac{1}{3}(T_x + T_y + T_z) \tag{8.38}$$

Computing the temperature from the velocities, it is important to respect the following order of operations :

$$\mathbf{v_i} \xrightarrow[\tau_{RF}]{\text{time avg}} \overline{\mathbf{v_i}} \xrightarrow{\text{square}} \overline{\mathbf{v_i}}^2 \xrightarrow[\text{N ions}]{\text{pop mean}} \langle \overline{\mathbf{v_i}}^2 \rangle \tag{8.39}$$

8.6.2 Cloud energy

Effective temperature can be interpreted as a marker related to the internal kinetic energy of the ion cloud. Indeed, because the effective temperature is based on a velocity averaged over the radio-frequency motion ($\langle \overline{\mathbf{v_i}}^2 \rangle$), it only accounts for motion that is not related to radio-frequency, i.e to external periodical forces. So the effective temperature is based on the velocity reflecting the internal state of the cloud, and so we can compute an effective temperature and a **total kinetic energy** (E_{kin}) from this radio-frequency averaged velocity $\langle \overline{\mathbf{v_i}}^2 \rangle$.

Nevertheless the trapping fields still explicitly intervene as a **potential energy** (E_{pot}) of the cloud. For each ion, its potential energy must be computed as a function of its position and the local value of both the radio-frequency field and the static field. The total potential energy of the ion cloud is the sum of the potential energy of each ion.

The computation of the total cloud energy would be incomplete without considering **Coulomb energy** (E_{coul}). The same way the external trapping field is a source of potential energy, the Coulomb repulsion between ions is producing a field and the energy under Coulomb form increases as the inter-ionic distance decreases.

The total energy of the cloud is thus

$$\overline{E_{tot}} = \overline{E_{kin} + E_{pot} + E_{coul}} \tag{8.40}$$

The bars above energies are here to signify the averages over a radio-frequency period. The energy variation over time is thus

$$\frac{\mathrm{d}}{\mathrm{d}i}\overline{E_{tot}} \tag{8.41}$$

Box 8.6.1: Energies

Refering to the set of equations 8.4, 8.5 and 8.6, the formulas for kinetic, potential and Coulomb energies of the whole cloud are as follows.

$$\overline{E_{kin}} = \frac{m}{2}\sum_{n=1}^{N}\left(\overline{\mathbf{v_n}}^2\right) \tag{8.42}$$

$$\overline{E_{pot}} = \overline{\frac{m\omega_z^2}{2}\sum_{n}^{N} z_n^2} \tag{8.43}$$

$$+\overline{\left(-\frac{q_e U_{RF}}{r_0^2}\cos\Omega t - \frac{m\omega_z^2}{4}\right)\sum_{n}^{N} x_n^2} \tag{8.44}$$

$$+\overline{\left(+\frac{q_e U_{RF}}{r_0^2}\cos\Omega t - \frac{m\omega_z^2}{4}\right)\sum_{n}^{N} y_n^2} \tag{8.45}$$

$$\overline{E_{coul}} = \frac{k_C q_e^2}{2}\sum_{\substack{n,j=1\\ j\neq n}}^{N}\frac{1}{\overline{r_{nj}}} \tag{8.46}$$

Chapter 9

Numerical proof-of-concept and main results

The results from numerical simulations carried out in this work are split into two parts. First a numerical proof-of-concept of the detection principle is demonstrated. A typical simulation result is exhibited and serves the purpose to highlight the important parameters observed in the simulation. In particular, the detection is explained and the method to determine whether or not detection occurred is presented here. Second, the analysis of the behaviour of the trapped ions in several trapping conditions is carried out. The computer program was run to provide significant statistics and the behaviour of the system is studied in terms of experimental parameters, with physically relevant parameters with respect to trapping.

9.1 Numerical proof-of-concept

9.1.1 Detailed description of the interaction simulation

The numerical simulations done in order to validate the `GiantMol` detection principle, and their analysis, gave birth to a publication in the *Journal of Chemical Physics* in 2021, under the name "Non-destructive detection of large molecules without mass limitation" [Poi21]. The data were generated over a few weeks, but are gathered in files to date `20200903`. In order to test the detection principle, the strategy is to reproduce the physical conditions of the interaction of a charged heavy projectile with a laser cooled trapped ion cloud, in a systematic way with a statistical approach. The program `INTERACTION` is run systematically for several trapping conditions in order to identify the working range of such a detector. To ensure each of the 28 conditions is tested robustly, 100 runs were generated for each of them. The detection efficiency of each condition is then determined according to the proportion of detection cases with respect to the total number of simulations per condition.

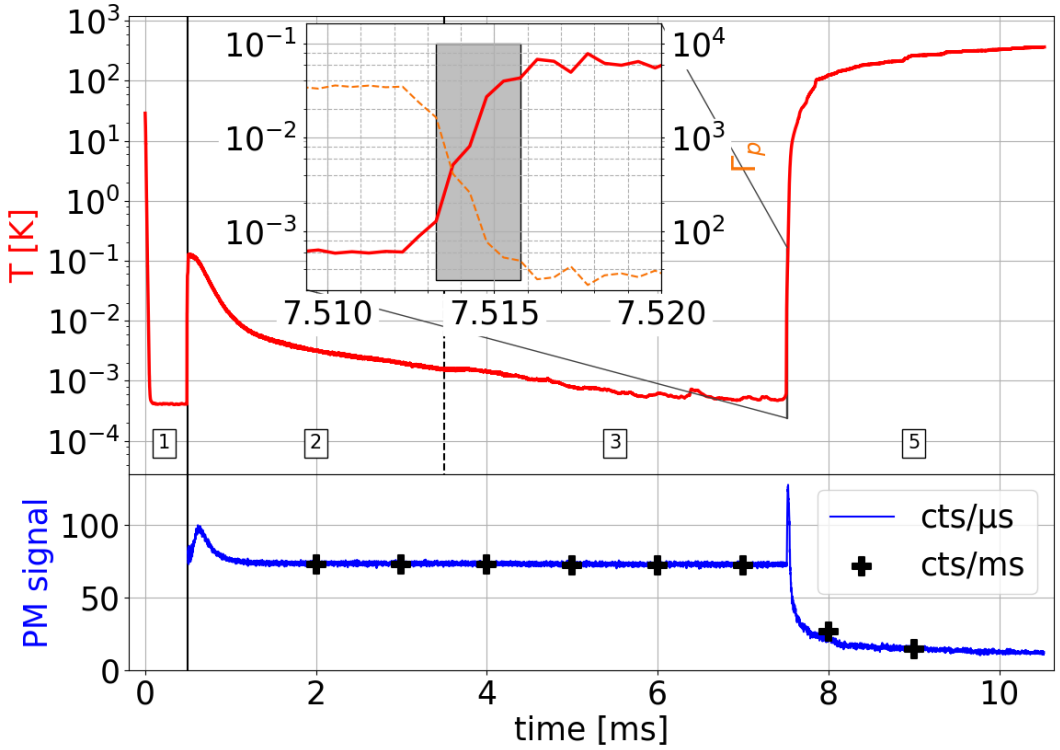

FIGURE 9.1: Ion cloud temperature and fluorescence during a run of computer program `INTERACTION`. Top : red curve is the temperature of the ion cloud. The inset is magnification of the injection step. The orange curve is the plasma parameter. The grey rectangle represents the actual period of time when the projectile is within the ion cloud, according to cloud boundaries determined at the time when the projectile is injected in the simulation. The framed numbers indicate which program step is executed. The step 2 and 3 are separated by a dashed line, the step 4 is very brief and mostly covers the inset. Bottom : blue curve is the measured fluorescence of the ion cloud with a 1 µs integration time. The black crosses are the same information integrated over a 1 ms time and accounting for a realistic detection efficiency of 10^{-3}.

Description of successful detection

In order to introduce the statistical results, here is described one successful detection. This result (Fig. 9.1) is provided by the computer program `INTERACTION`. The trapping parameters are U_{RF} = 64.61 V and U_{DC} = 3 V (condition 10 in Fig. 9.5). The ion collection is composed of N = 1024 Ca^+ ions, which results in an ellipsoidal cloud of approximately total length L = 469.2 µm and radius R = 46.8 µm (Fig. 9.2a). The giant molecule projectile is injected so its kinetic energy in the trap center – which is the coordinate origin – is E^{GMol} = 50 eV, its charge $Q^{GMol} = 1q_e$, its mass $M^{GMol} = 10^6$ Da.

The top part of the figure 9.1 shows the temperature and plasma parameter, of the cloud, and the bottom part the fluorescence. In the bottom part, two integration times are represented for the fluorescence. The temperature is sampled once per radio-frequency period, just as the fluorescence. The blue curve represents the fluorescence with a 1 µs resolution, which is twice the radio-frequency period τ_{RF}. The black crosses represent the fluorescence signal as it would be observable in realistic conditions, with a 1 ms integration time and a detection efficiency of 10^{-3}, typical for experimental conditions.

The figure 9.1 illustrates the organisation of the code into five steps, numbered with

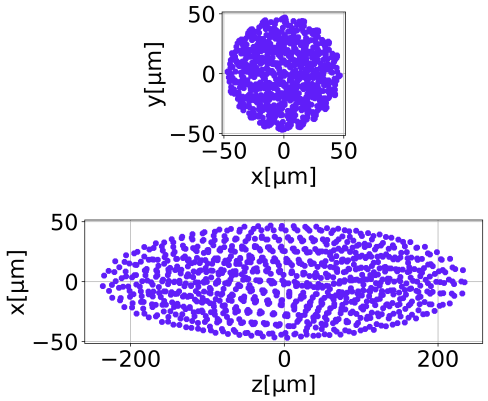

(A) Ion structure at the end of thermalisation (3), before injection (4), for the simulation from Fig. 9.1. The cloud is in a crystal state ($\Gamma_p \approx 4000$).

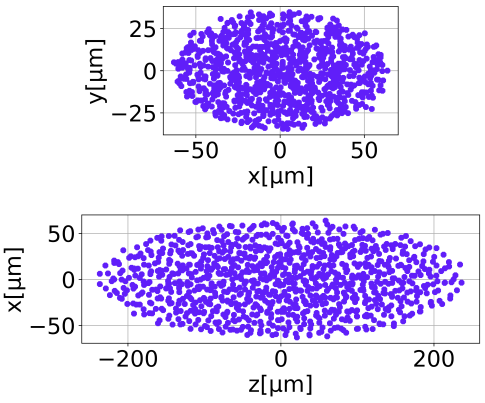

(B) Ion structure at the end of injection (4), before post-injection (5), for the simulation from Fig. 9.1. The cloud is in a crystal state ($\Gamma_p \approx 40$), but due to the collision with the charged projectile, some ions are not on their periodic stable trajectory.

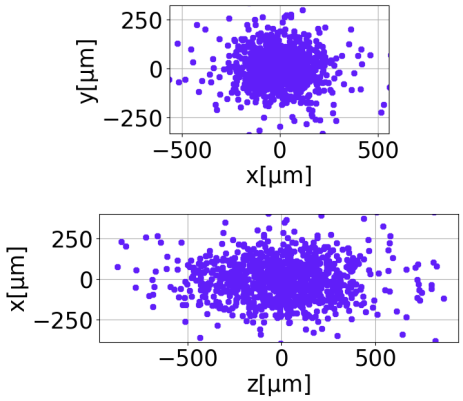

(C) Ion structure at the end of the simulation, after post-injection (5), for the simulation from Fig. 9.1. The cloud is in a gas state ($\Gamma_p < 2$).

FIGURE 9.2: Ion cloud structure at three times in the simulation illustrated with Fig. 9.1. U_{RF} = 64.61 V, q_x = 0.6, U_{DC} = 3 V. 1024 ions.

the framed number in accordance with figure 8.1. First the ions are initialised without laser and their temperature is brought to a lower limit of $5 \cdot 10^{-4}$ K with the Langevin algorithm. Then the laser is triggered while the integration algorithm is changed to velocity-Verlet. The simulation starts with a low radio-frequency amplitude of U_{RF} = 10.77 V (q_x = 0.1) and during the second phase the amplitude is risen to U_{RF} = 64.61 V with hyperbolic tangent function. Then the simulation is carried out until a satisfying cold temperature is reached, below mK, representative of temperatures in experiments. At the end of the third step, the giant molecule projectile is injected and is in the simulation throughout the fourth step where it collides with the cloud of trapped ions. Then the final fifth step is dedicated to dynamics of the trapped ions without the charged projectile.

In the case of the figure 9.1 the detection is successful. A durable, observable, fluorescence variation related to the passing of the projectile is identifiable. Notice the short lived

fluorescence increase during the passing of the molecule is not experimentally observable and thus cannot be considered as detection signal.

The detection signal is determined by comparing two fluorescence level sampled before and after the passing of the projectile. The fluorescence is averaged over the 100 last data points of thermalisation step (3) (F_3), and over the 100 last data points of the simulation (5) (F_5). The difference of fluorescence $\Delta F = |F_3 - F_5|$ is then compared to the signal noise σ_F. During the thermalisation step, when the temperature is below 10 mK, the fluorescence level is 73 ± 1 counts/µs. During the injection, the fluorescence evolution is characterised first by an increase up to 126 ± 1 counts/µs @ 400 mK, before a decrease down to 11 ± 1 counts/µs. During the decrease, the fluorescence crosses its original level @ 4 K. In this case the signal is $\Delta F = 62 \pm 1$ counts/µs. In order to compute a signal-to-noise ratio, this value is compared to a Poissonian noise $\sigma_F = \sqrt{F_M}$ at the highest of the two fluorescence levels $F_M = \max(F_3, F_5)$, so that

$$\boxed{SNR = \frac{\Delta F}{\sigma_F} = 5.0.} \tag{9.1}$$

Description of the temperature and fluorescence evolution during crossing

Once the projectile enters in the simulation, the temperature evolution in figure 9.1 is split into two parts. A first increase in temperature about 40 mK is noticeable during the passing of the projectile inside the ion cloud (see Fig. 9.1 inset). This increase from the reference level starts 11 µs after the projectile introduction, 1.5 µs before the projectile enters the cloud, when the projectile is located approximately 185 µm from the cloud boundary. However this increase in temperature is only few mK and is much less significant than the increase happening when the projectile is within cloud boundaries. The time spent by the projectile crossing of the cloud is 2.0 µs. The temperature increases to 20 mK, then still increasing during 3 to 4 µs after the projectile left the cloud boundaries, and reaches about 40 mK, 18 µs after the projectile injection. Then a second increase of temperature up to several hundreds of kelvin occurs over a larger period of time. 1 K is reached 55 µs after the projectile introduction. While the first increase in temperature is attributed to Coulomb interaction between the projectile and ions in cloud, the second increase in temperature is attributed to the **radio-frequency heating** (see subsection 3.3) . Also, in that last moments when the temperature grows beyond 1 K of several order of magnitude, the laser cooling efficiency greatly decreases.

9.1.2 Projectile behaviour during the interaction

Projectile trajectory

During its travel, the energy lost by the projectile is $\Delta E = 11.42$ meV. Entirely converted to kinetic energy in this 1024 ion cloud, this is equivalent to an increase in temperature of 86 mK (Eq. 8.33). Considering that laser cooling remains efficient during a non-negligible part of the interaction, and that a part of the energy is also converted in Coulomb energy,

it can be considered that the projectile energy variation is a good first approximation for the temperature increase.

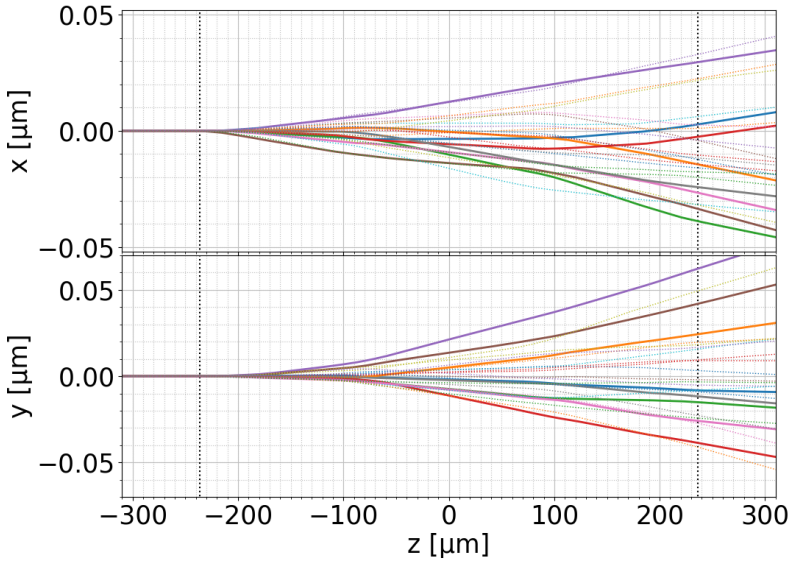

(A) Projectile trajectories in x-z and y-z planes in similar conditions as in Fig. 9.1. Single trajectories from 25 simulations are illustrated, with 8 trajectories specifically highlighted.

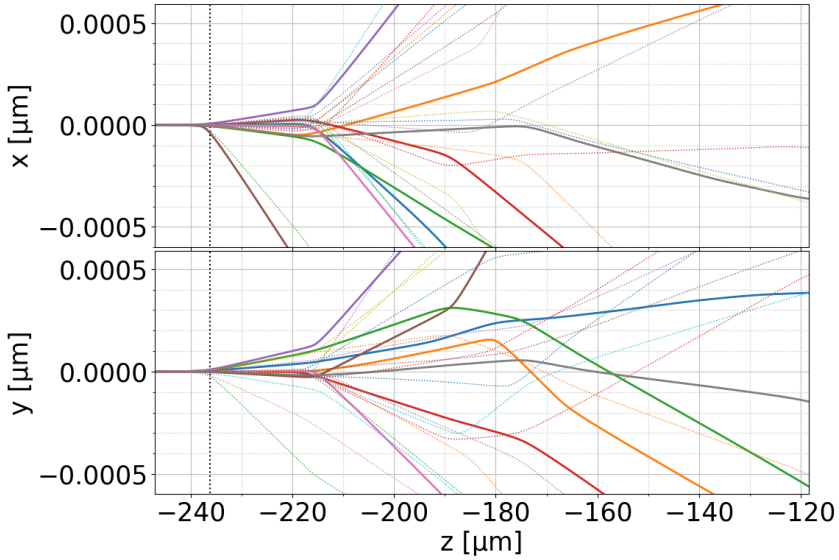

(B) Same as Fig. 9.3a, with a zoom on the cloud entrance position.

FIGURE 9.3: Projectile trajectories in x-z and y-z planes in similar conditions as in Fig. 9.1. Eached coloured line is one trajectory for one molecular ion injected in one simulation. Some of those trajectories are in bold line for clarity.

Not only the kinetic energy of the projectile is known, but also all its trajectory, with sampling rate as low as the simulation time resolution. A first observation of projectile trajectories in the same condition as before (Fig. 9.1) allows us to say that the projectile remains near the z-axis along which it is propagating. While collisions between projectile and ions make the projectile trajectory non-linear, the radial deviation of the projectile

from z-axis at the cloud exit is less than one thousandth ($< 1/1000$) in terms of cloud radius. The trajectory of 25 projectiles, projected over x-z and y-z planes, is illustrated by figure 9.3.

Projectile kinetic energy

Another observation of the projectile kinetic energy is illustrated by figure 9.4, for only eight projectiles, whose trajectories are highlighted in the previous figure 9.3a. Ions are initialised with a kinetic energy so that only velocity along the z-axis is non-null. Once the projectiles are at less than 50 µm ($\approx L/8$), their kinetic energy tend to differentiate from the quadratic reference induced by the potential. The main reason for such behaviour is that Coulomb interaction of the projectile with the Ca^+ ions becomes significant. Two kind of Coulomb interaction can be identified. First binary collisions, characterised by quicker change in projectile energy than caused by the second source of interaction, mean field interaction. In that last case the energy variation is expected to be smooth and with a constant weaker slope. For instance, following the brown lower curve in figure 9.4, the step-like behaviour occurring around $z = -80$ µm exhibits an energy variation of approximately 6 µeV, and is characteristic of a binary collision. Then the projectile leaves the cloud and reaches the position where it is removed from the simulation. The energy difference ΔE between the initialisation and the removal of the projectile is recorded. Notice that in figure 9.4 it seems that the collisions with the highest energy exchange are happening around specific positions. For instance in figure 9.4, around -100 µm or -200 µm, the energy exchanges are recognisable by the sudden energy variation of the projectile. This distribution of positions seems symmetrical with respect to the center of the trap ($z = 0$). Nevertheless the energy exchange intensity does not seem symmetrical, i.e the energy loss is not divided into two equal quantities on each side of the trap. In the case where the energy variation is the highest at collision, the particle loses 7 µeV, which happens mainly around ± 100 µm. Smaller energy exchanges in the range $1 - 5$ µeV are more frequent. This structured repartition of energy exchange could be explained by the structured atomic distribution in the crystallised cloud, which exhibits a shell structure with layers separated from each other by a given distance, rather than a random homogeneous distribution. Nevertheless this explanation is not sufficient to justify the grouped localisation of energy exchanges because the inter-shell space does not correspond to the distance between the energy exchange areas in figure 9.4. In the cloud a dozen of layers are identifiable, which leads to an inter-shell distance of approximately 40 µm, a number 2 to 5 times smaller than what is observed in figure 9.4 between the areas with the highest energy exchanges.

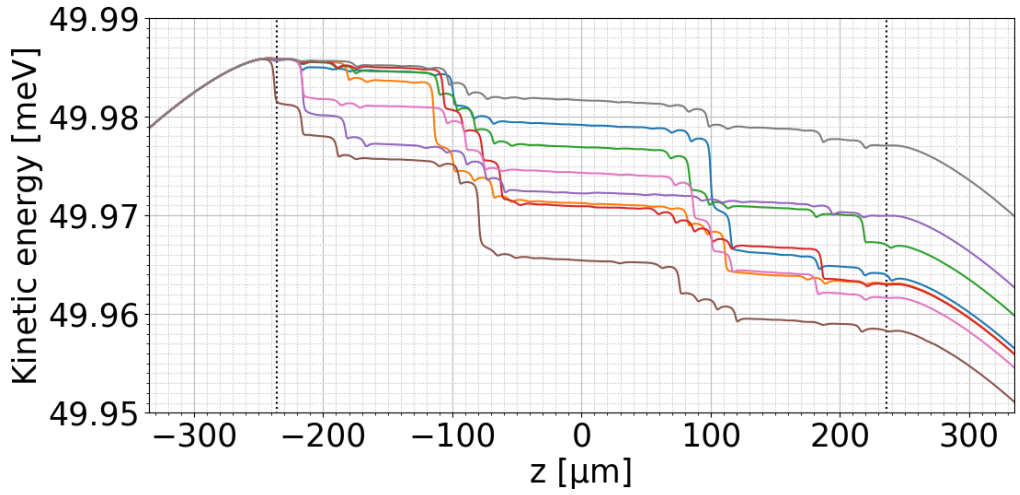

FIGURE 9.4: Projectile kinetic energies in similar conditions as in Fig. 9.1. The curves are associated with each of the 8 trajectories specifically highlighted in Fig. 9.3a. The dashed vertical lines are indicating the cloud boundaries.

9.1.3 Statistics and detection rate

Presentation of the detection efficiency

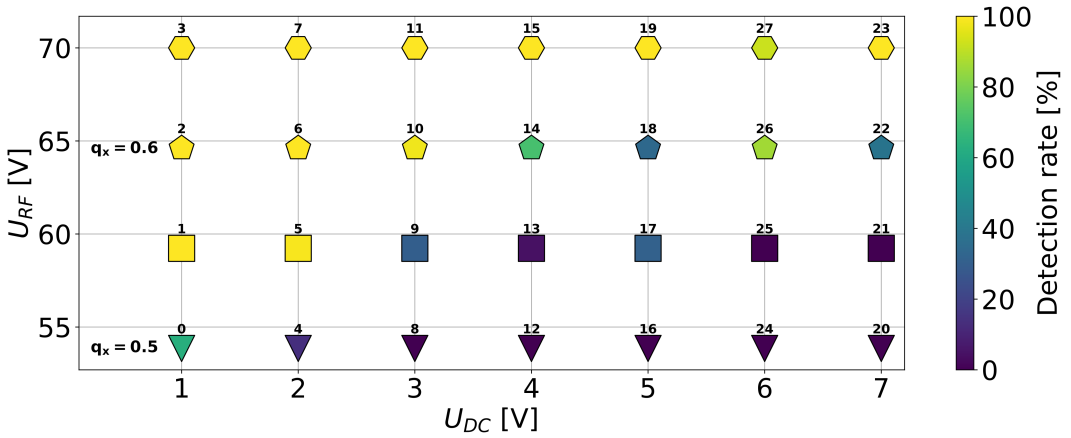

FIGURE 9.5: Detection rate as a function of the radio-frequency amplitude U_{RF} and axial confinement voltage U_{DC}, for E0=50 eV. qx is the Mathieu parameter associated to the radio-frequency trapping. See the color chart that codes the detection rate. The radio-frequency amplitude is also coded with the marker shape, which is also used later in other figures.

According to the process developed above, the fluorescence difference ΔF and SNR are determined for 28 trapping conditions, each simulated 100 times. In every case where the signal-to-noise ratio overcomes unity a detection is claimed to have happened. The detection rate $\%D$ for one condition is the ratio of the number of the simulations indicating a detection $\#D$ by the total number of simulations $\#S = \#D + \#\overline{D}$ for that given condition

$$\%D = \frac{\#D}{\#D + \#\overline{D}}. \tag{9.2}$$

This detection rate $\%D$ has been computed for each trapping condition (Fig. 9.5). The fluorescence variation ΔF is either 0 or $\Delta F/F_M \approx 0.8$, which leads to signal-to-noise ratios either 0 or 5.0. Axial potentials from $U_{DC} = 1$ V to $U_{DC} = 7$ V have been tested, in combination with four radio-frequency amplitudes in the following set : $U_{RF} = 53.85$ V, $U_{RF} = 59.23$ V, $U_{RF} = 64.61$ V and $U_{RF} = 70.00$ V, equivalent to Mathieu parameters $q_x = 0.5$,$q_x = 0.55$,$q_x = 0.6$ and $q_x = 0.65$. This range of values is tested because it exhibits a variety of different behaviours that can be explored in order to investigate the detection mechanism. Also, this is an interesting range because it provides several set of similar conditions with different behaviours, for instance a range of data with identical radio-frequency amplitude, but with a detection efficiency varying with the axial potential. Selecting a too high or to low radio-frequency field would provide less informations as it would essentially provide never working or always working detectors.

The results from those statistics can be interpreted as follows. First, the detection rate is 100% for every condition with the highest radio-frequency amplitude tested, except for $U_{DC} = 6$ V where the efficiency is 92% which remains excellent. In contrary, below $U_{RF} = 55$ V the detection efficiency remains poor, it is 0% except with the condition with lower voltages that offers a detection efficiency of 63%. In between, the detection efficiency increases with the radio-frequency amplitude. Also globally the detection efficiency increases when the axial confining potential decreases. About the tendency concerning radio-frequency amplitude, the observed dependency of detection rate with amplitude can be related to the radio-frequency having more and more effect on the cloud stability when its amplitude increases. Notably, radio-frequency heating will be stronger with higher radio-frequency amplitude. It is clear that higher axial potential voltages imply shorter clouds (Fig. 9.7), thus less interaction between the projectile and the cloud. Also increasing U_{RF} may also lengthen clouds. This also increase the cloud density (Fig. 9.9). Increasing the axial potential U_{DC} also slightly increases the ion density.

Non-detection scenario

The successful detection case (Fig. 9.1) is a good representative example of what happens when detection occurs. A radically different example comes from non-detecting cases (Fig. 9.6) with $SNR < 1$. In the non-detecting scenarii, the temperature evolution is much more simple. The first temperature increase due to Coulomb interaction is still visible, nevertheless there is no second increase as the temperature returns to its initial value. Thus the fluorescence also returns to its initial value and the signal-to-noise ratio approaches unity. With no means to actually observe the short-lived fluorescence peak, those scenarii do not provide detection. This emphasizes the need to trigger radio-frequency heating in order to provoke a long-lasting fluorescence difference.

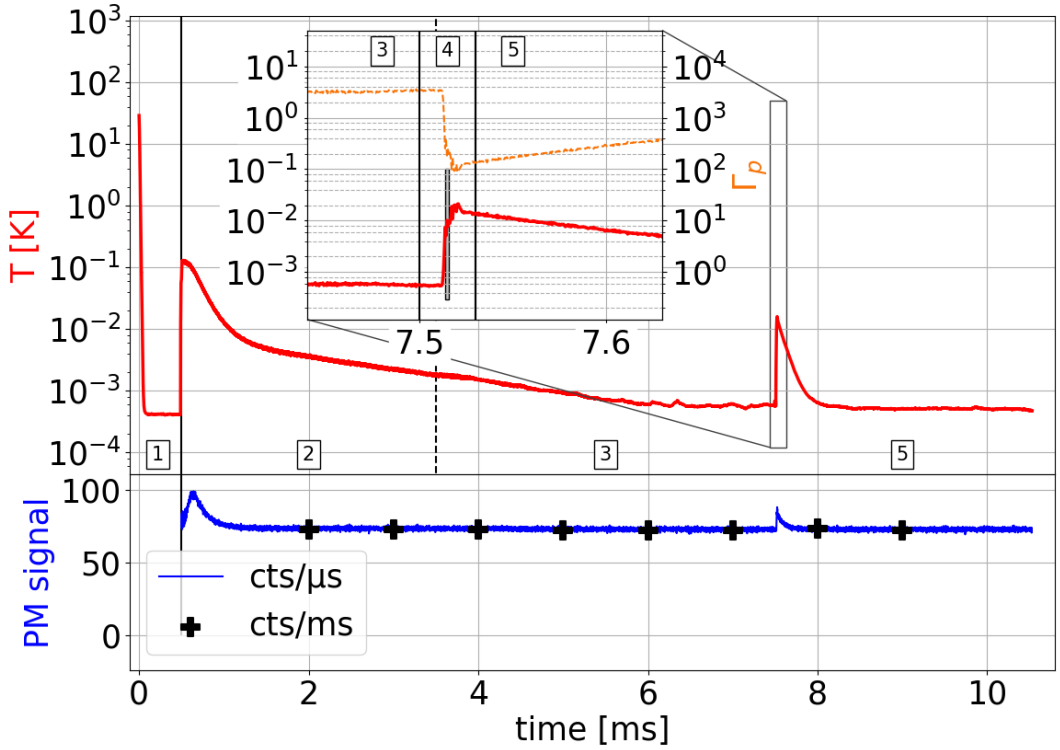

FIGURE 9.6: Ion cloud temperature and fluorescence during a run of computer program `INTERACTION v2`, with U_{RF} = 53 V, U_{DC} = 3 V. Top : red curve is the temperature of the ion cloud. The inset is a zoom in the same information. The grey rectangle represents the actual period of time when the projectile is within the ion cloud. The framed numbers indicate which program step is executed. Bottom : blue curve is the measured fluorescence of the ion cloud with a 1 µs integration time. The black crosses are the same information integrated over a 1 ms time and accounting for a realistic detection efficiency of 10^{-3}.

9.2 Physical quantities at play

In order to study the interaction mechanism it is more relevant to think in terms of physical relevant quantities rather than trapping voltages. Such quantities are cloud dimensions, secular frequencies, plasma parameters, cloud density, and also the projectile energy loss. Some of those parameters are much more convenient when it comes to comparing several experimental setups. The following informations are provided with the same set of data introduced above. Some of the informations are rearranged, but some other such as the projectile energy loss, or the secular frequencies, are introduced in this part. Among the discussed physical quantities, there is no discussion about the laser. Indeed, it is possible to act on the trapped ensemble by changing the cooling conditions, set by the laser cooling. Nevertheless this ability to modify this laser setting is limited by the constraint on the detection : indeed changing the laser condition changes the fluorescence and requires to work in conditions less advantageous in terms of fluorescence.

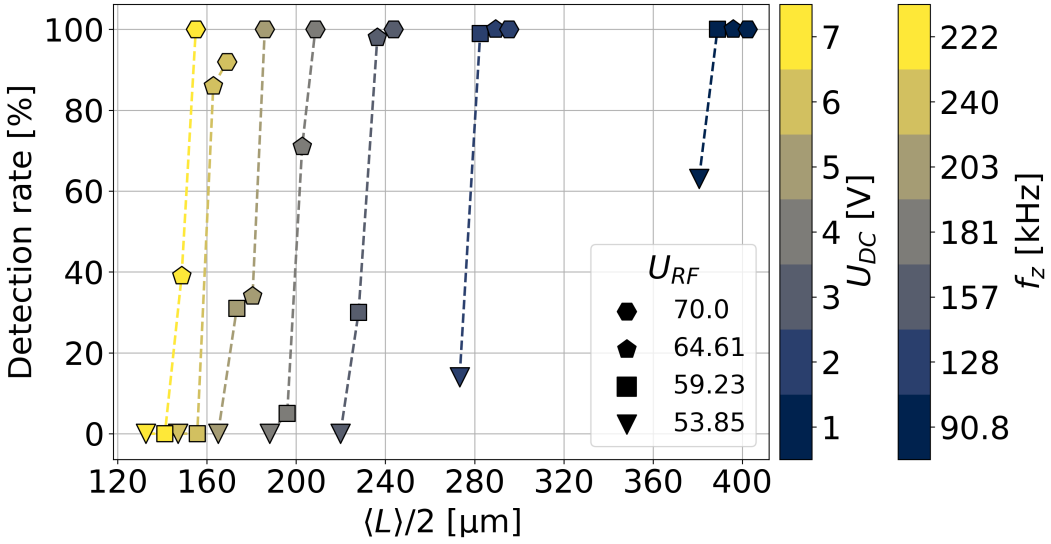

FIGURE 9.7: Detection rate as a function of the average cloud half-length $\langle L \rangle$. The marker shape indicates the radio-frequency amplitude U_{RF}, and the color codes for the axial confining potential U_{DC}, or axial secular frequencies f_z. The dashed lines are linking the points with same U_{DC}.

9.2.1 Cloud length

While the first statistical results (Fig. 9.5) demonstrate the relevance of the radial and axial potentials in the detection mechanism, the following results illustrates the role of the cloud length. Figure 9.7 shows the detection rate (vertical axis) as a function of the average cloud half-length $\langle L \rangle/2$ (horizontal axis), the axial potential (color) and the radial potential amplitude (marker shape).

Figure 9.7 shows that in order to increase the detection rate, it is required to lengthen the cloud, and increase the radio-frequency amplitude. The longer the cloud, the smaller is the required radio-frequency voltage to reach a given detection rate. For a given cloud length (let's say around 160 µm), a smaller radio-frequency (59.23 V, square mark) provides 0% detection rate, while increasing the radio-frequency to 64.61 V (pentagon mark) then 70 V (hexagon mark) provides a detection efficiency of nearly 90% then 100%.

Nevertheless notice how the non-linearity for the axial potential around 5 V seen before affect this statement. Indeed for radio-frequency at 59.23 V (q_x = 0.55), the detection efficiency is very bad (< 10%) for U_{DC} = 7, 6 and 4 V of axial potential, but substantially better ($\approx$ 30%) for U_{DC} = 5 V of axial potential. Looking carefully at the cloud densities for those voltages, they are all comparable. Similarly, looking at the secular frequencies, no argument can be found for such behaviour. The argument may be laying in the cloud configuration, the layer position and ions within layers. This point for 5 V is already visible on the main statistics figure 9.5 : observing each line with constant radio-frequency, it seems that some non-linearities in the detection rate appear around 5 V. The same comment can be done for 6 V. Refining the simulations around this voltage may provide new arguments in order to understand what is happening. Nevertheless, from the already done simulations, it seems the argument is neither in terms of secular frequencies, cloud length or projectile energy variation.

The detection rate as a function of the radial secular frequency and cloud half-length is visible in figure 9.8. The secular frequencies are useful in order to compare with other experiments. Figure 9.8 also illustrates how the detection rate increase when the cloud length increases, for all parameters constant.

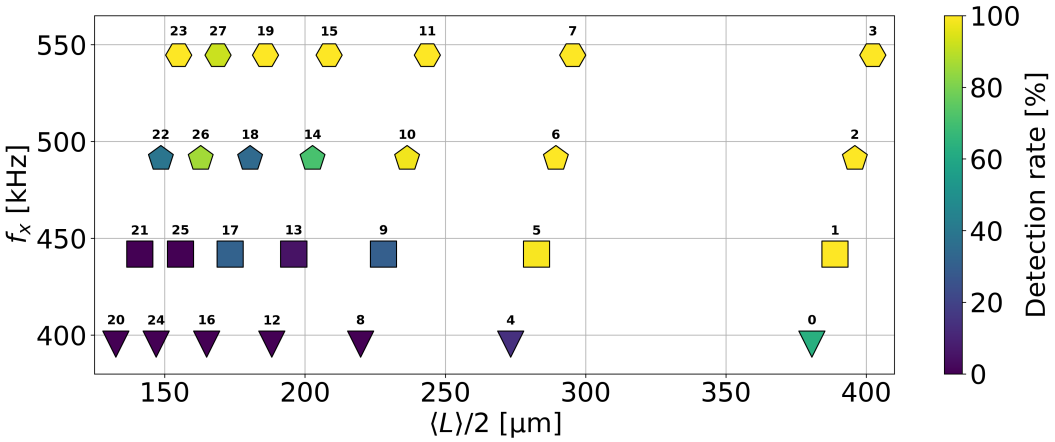

FIGURE 9.8: Radial secular frequency against the cloud length for all the tested conditions. The color indicates the detection rate %D. The symbol shapes are defined in figure 9.7.

9.2.2 Density

Another physical quantity relevant to study the dependence of detection rate with, is the cloud density (Fig. 9.9). Numerically, the cloud density n_0 is computed using the number of ions N divided by the volume V of the ion cloud considered as an ellipsoid, so that

$$n_0 = \frac{N}{V} = \frac{N}{\frac{4}{3}\pi R^2 L/2}. \tag{9.3}$$

Figure 9.9 shows that the density mainly increases with radio-frequency amplitude. Remarkably, for a given radio-frequency field, the cloud density increases when the axial potential decreases. The detection rate is represented by the vertical axis. For the most dense clouds, the detection efficiency is very good, whatever the axial potential (thus the length). Nonetheless, once the density (or radio-frequency amplitude) diminishes, longest clouds (or lowest axial potentials) are required, which is coherent in terms of both projectile interaction with the cloud and cloud density increasing when the axial potential decreases.

This density computed from numerical simulations is compared to the theoretical maximum density given by equation 3.20. Computed numerical densities appear to be always higher than the expected densities given by equation 3.20. The difference is up to 20% in the worst cases, corresponding to the weakest radio-frequency field. This difference decreases when the radio-frequency amplitude rises and is up to 10% for the highest radio-frequency.

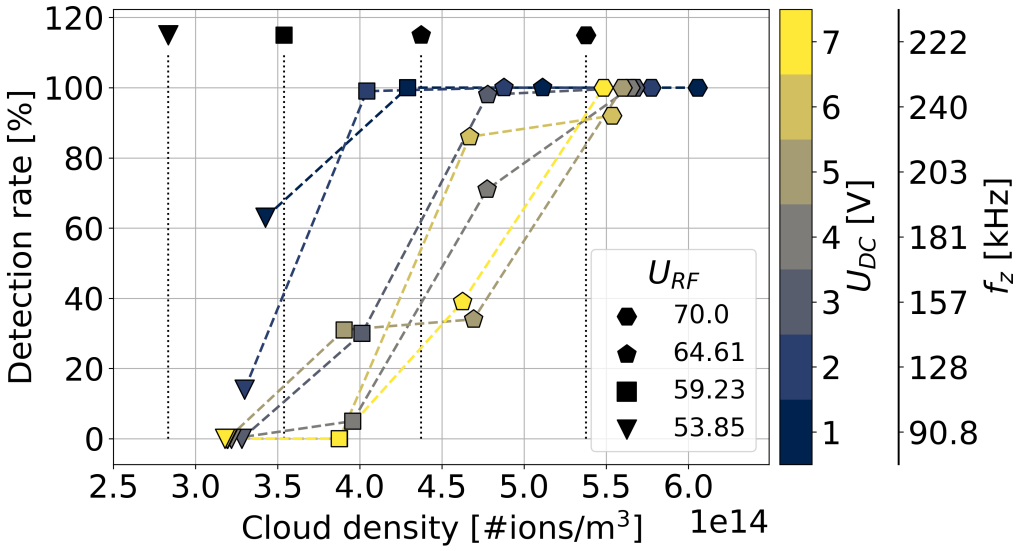

FIGURE 9.9: Detection rate as a function of the cloud density n_0. The marker shape indicates the radio-frequency amplitude U_{RF}, and the color codes for the axial confining potential U_{DC}, or axial secular frequencies f_z. The dashed lines are linking the points with same U_{DC}. The horizontal lines indicate the theoretical densities for the U_{RF} amplitudes associated with the shape above the line. They are computed using equations 3.20 and 1.20 with no adiabatic approximation.

9.2.3 Secular frequencies

The detection efficiency was also plotted on a graph versus the secular frequencies (Fig. 9.10) or the projectile energy loss ΔE (Fig. 9.12). The first graph is quite similar to figure 9.5 because frequencies and trapping voltages are related by a proportionality constant. The conclusions are thus the same, higher frequencies favor higher detection rate, and high axial secular frequencies f_z are compensated by high radial frequencies f_x. In the second graph, the projectile energy loss is displayed in the purple colormap. It is not possible to strongly correlate the cases with high detection rate with cases with high energy loss. Globally, the lower the axial secular frequency, the higher the energy loss, which is explained by the increasing length of the cloud when the axial secular frequency decreases. The points number 3,5 and 11 are the most favourable in terms of energy exchange between the projectile and the ion cloud. The average energy loss $\Delta E < -30$ meV is more important than the other cases where the energy loss remains smaller $\Delta E > -20$ meV. In the right part of figure 9.12, the energy losses are similar, but the detection rate is better on the top part where the radial secular frequency is higher f_x. This supports the idea that both the Coulomb interaction and the radio-frequency heating are required to provide a measurable fluorescence modification ; the initial energy brought by the projectile perturbs the ion cloud, and the higher radio-frequency field amplifies this perturbation.

Replacing the axial secular frequency by the cloud length, it is also possible to do the same comment on the impossibility to find a relevant strong correlation between the energy exchange and the cloud length. This is an indication that not only the cloud length counts as an important parameter. But as said, there is still some trend showing that, the longer the cloud, the bigger the interaction, the bigger the energy loss.

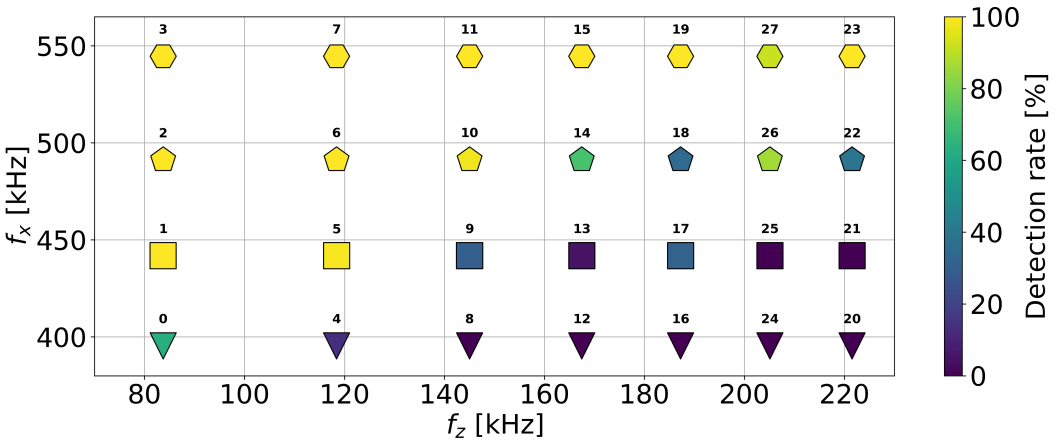

FIGURE 9.10: Radial secular frequency against the axial secular frequency for all the tested conditions. The color indicates the detection rate %D. The symbol shapes are defined in figure 9.7.

9.3 Analysis of the projectile energy

9.3.1 Stopping power

Stopping power of a plasma is defined as the rate of energy loss per unit distance travelled by a charged particle [Hay20]. Knowing the initial energy of the particle, and the distance travelled, it is easy to link the stopping power to the energy lost by a projectile during its travel. The attempt to correlate this projectile energy loss ΔE and detection efficiency is not clear enough to claim anything reproducible in the current simulation. A careful study of the energy loss distribution for each condition does not allow to observe a correlation between detection and energy loss. For a given condition, in terms of projectile energy loss ΔE, there is no clear distinction between the cases that provide detection, and those that do not.

If it was possible to make the energy exchange bigger, i.e increase the energy loss, probably the behaviour would be less ambiguous. Indeed the energy exchange is in the range of -50 meV, which is enough to destabilise the ion cloud, but not enough to overcome laser cooling : indeed a significant part from this amount of energy is dissipated by laser cooling. To verify this assumption it is required to look at the initial comments from subsection 9.1.1 where the energy exchange and its effect on thermal energy are looked at. This previous study reveals that if all the energy from the projectile is converted into thermal energy, the temperature increase expected is about 86 mK, while it is only 40 mK. If more energy is transferable to the cloud the detection would be easier to trigger. Nevertheless a study of the plasma stopping power determined that the configuration is already that with the highest projectile energy loss (Fig. 9.13). It is also visible that the energy lost by the projectile increase when the axial potential decreases. Considering that clouds are longer for smaller axial potential, this confirms that the longer the cloud, the greater is the energy loss thus the interaction of the projectile with the ion cloud. Nevertheless, the average projectile energy loss is hard to correlate with the average cloud length and the secular frequency. This is visible on figures 9.11 and 9.12, which are a presentation of the

same data from the aforementioned statistical runs, but with energy loss rather than detection rate. Maybe 100 run for each condition is not enough to observe a significant effect on the average, maybe there are still too much dispersion in terms of projectile energy loss. For a given condition, the energy loss dispersion is visible in figure 9.13. The dispersion is represented by the vertical lines, and indeed for a majority of conditions, the dispersion represents more than 20 % of the average value, and in some case the dispersion is even 200 % . This means that for a single condition, the projectile energy loss usually is around the average value at more or less this dispersion.

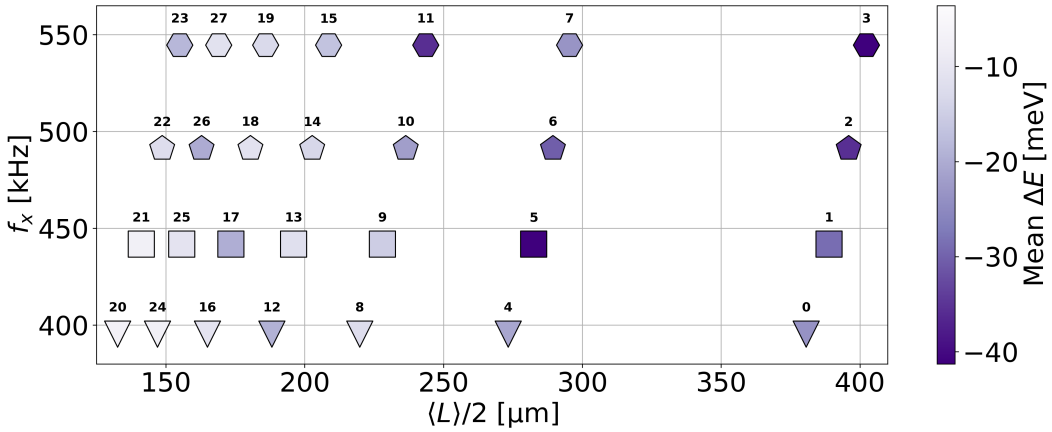

FIGURE 9.11: Radial secular frequency against the cloud length for all tested conditions. The color indicates the mean projectile energy loss ΔE. The symbol shapes are defined in figure 9.7.

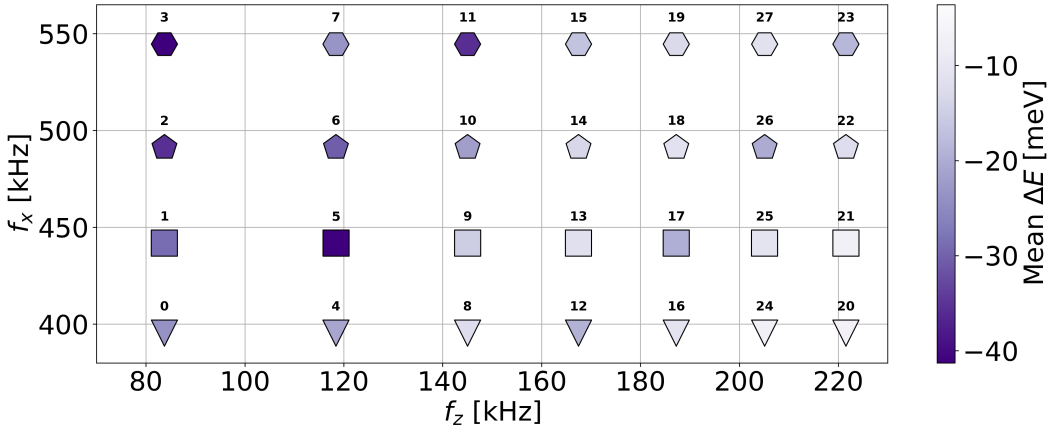

FIGURE 9.12: Radial secular frequency against the axial secular frequency for all tested conditions. The color indicates the projectile energy loss ΔE. The symbol shapes are defined in figure 9.7.

9.3.2 Stopping power as a function of the projectile initial energy

One important parameter in the detection that has been obliterated until now is the incident energy of the particle. In the domain of plasmas, it is a well known fact that the energy lost by a particle injected in a plasma depends on its incident energy [Zwi99, section 4.2.1]. The effect of the plasma on the energy lost by the particle is called stopping

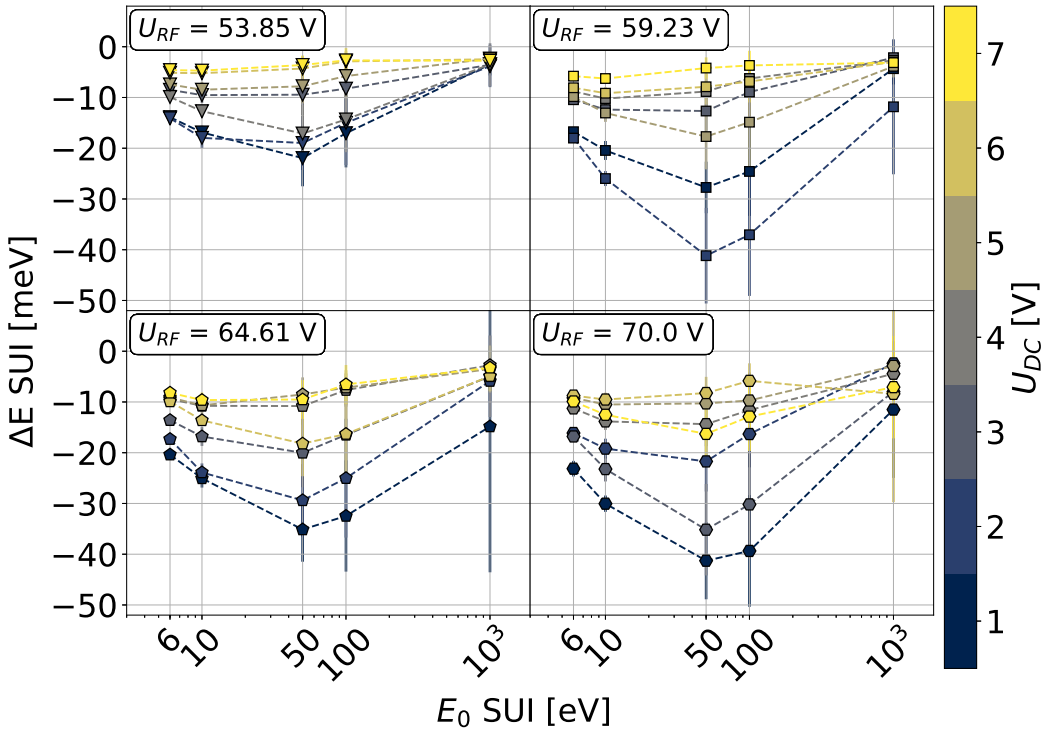

FIGURE 9.13: Energy loss by the projectile ΔE, versus the projectile kinetic energy E^{GMol} at the center of the trap. 28 different sets of voltages (U_{RF},U_{DC}) are tested by 20 independent simulations. The average value is plotted with its error bar standing for ± 1 standard deviation vertical lines). Each of the four subplots stands for one U_{RF}, and the colour code translate the values of U_{DC} (see the color chart on the right side of the figure). The dashed lines are linking the points with same U_{DC}. SUI is the projectile molecule.

power. This very energy lost by the projectile ΔE has been mentioned lately and is also an important parameter.

In order to maximise the amount of energy transferred from the projectile to the GICD, it is advisable to optimise the energy of the injected projectile and set it at a level where the cloud stopping power is maximum. In the context of `GiantMol`, numerical simulations were carried out in order to study the stopping power of the cloud in function of the incident projectile energy. Other factors such as radio-frequency amplitude and axial potential were systematically tested. The stopping power, i.e the projectile energy variation ΔE during its voyage, in function of those parameters is illustrated by the figure 9.13.

It appears that it any case, among the tested incident energies, an optimum is identified at $E^{GMol} = 50$ eV. As identified in the bibliography, the stopping power as a function of incident energy shows only one extremum, so if someone desires to study more thouroughly the stopping power, it is advised to search a better configuration around $E^{GMol} = 50$ eV. Nonetheless it is not a priority to furnish a more precise value for the optimum energy as experimentally controlling the projectile energy with a sub eV precision is extremely challenging and no need for that is yet identified.

9.4 Radio-frequency heating study

The radio-frequency heating is a key factor in the detection mechanism of `GiantMol`, we therefore investigated it more thoroughly through specific simulations. From this study, the possibility for a general rule allowing to predict a detection simply by considering the trapping conditions may arise.

9.4.1 Principle

Thermal evolution

Numerical simulations of the trapping of ions alone, without laser-cooling and without projectile injection are discussed in this section. This simulations are done using the code `RF HEATING` (Fig. 8.1). Those simulations study, first the temperature evolution, and second, the energy variation within the ion ensemble.

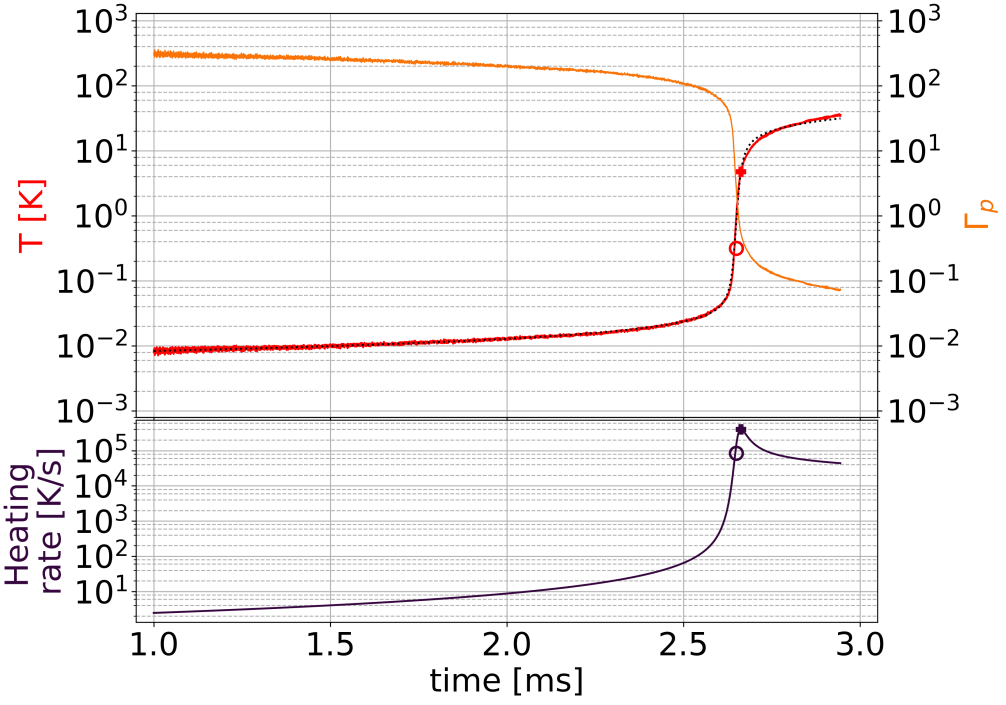

FIGURE 9.14: Top : Semilog-y representation of the cloud temperature T (red) and the plasma parameter Γ_p (orange) during a run of computer program `RF HEATING`, with U_{RF} = 64 V, U_{DC} = 7 V, 1024 ions. The dashed line is a fit of the temperature used to compute a heating rate (see equation 9.4). Bottom : Semilog-y representation of the heating rate H computed from the first order derivative of the above fit. The circle indicate when $t = t_0$ and the cross when the derivate of the analytical fit is maximum.

A typical computer simulation of an ion cloud in a radio-frequency and electrostatic field is shown in figure 9.14. Only the velocity-Verlet part of the simulation is represented, during which the cloud evolves from a cold situation (T = 5 mK) to a hot one ($T > 50$ K). In that case, a collection of 1024 Ca^+ ions is confined with a set of voltages with amplitudes

U_{RF} = 64 V, U_{DC} = 7 V, with neither laser nor injected projectile. In the top part of figure 9.14, the temperature T of the ion cloud is in red and the dashed line represent a fit according to a function described below (Eq. 9.4). The heating rate as a function of time is represented by the purple curve in the bottom part of the figure 9.14 and is computed by deriving the fitted temperature versus time.

It appears that the temperature first slowly increases from 10 mK to approximately 40 mK in approximately 2.6 ms which represents 90% of the simulation duration. Then the temperature grows by three orders of magnitude and reaches 10 K in approximately 0.1 ms, then reaches 40 K during the next 0.2 ms. In terms of average heating rate, the respective values during those three phases are 10 K/s, then 10^5 K/s and $1.5 \cdot 10^5$ K/s.

Thermal runaway and critical timing

With this average perspective, I propose to discuss the thermal evolution as follows : first the temperature of the cloud is low and grows minimally, then the temperature increases much more quickly with the heating rate increasing by several orders of magnitude in a short period of time ($<$ 0.1 ms). Let us call the phenomenon to which is submitted the cloud and that is the cause of this thermal evolution the "thermal runaway". As we will see later, the thermal runaway is related to the radio-frequency heating. According to the average perspective proposed, this thermal runaway is characterised by a **critical timing** where the heating rate itself suddenly grows. This critical timing can be understood as "the time required since the beginning of the experiment for the cloud temperature to suddenly raise", relatively to a cloud initially cooled to a cold temperature in the crystalline phase. This critical timing, and the temperature associated with this, is of interest in order to characterise the prevalence of thermal runaway, to understand how important it is for a given condition. A shorter critical timing means a stronger thermal runaway. A criterion to localise temporally this critical timing is developed below. Because the temperature computed in the simulations showed quick oscillations it was not possible to interpret the time derivative of this signal and link it with a heating rate with a physical meaning. The frequencies characterising the oscillations in the temperature could not be related to characteristic frequencies related to trapping. The use of time averages, as presented in subsection 8.6.1, do not improve the analysis. In order to bypass this problem caused by the oscillations, the temperature is fitted with an analytical expression. This allows to then proceed to a time derivative on this analytical signal, which provides a good estimate of the heating rate. The function used to fit the temperature is as follows

$$\log_{10} T = A\frac{t - t_0}{(C + (t - t_0)^2)^D} + B. \tag{9.4}$$

In the case of figure 9.14, the coefficients are the following

$$A = 3.90, B = -0.125, C = 2.33 \cdot 10^{-10} \tag{9.5}$$

$$D = 0.446, t_0 = 2.649. \tag{9.6}$$

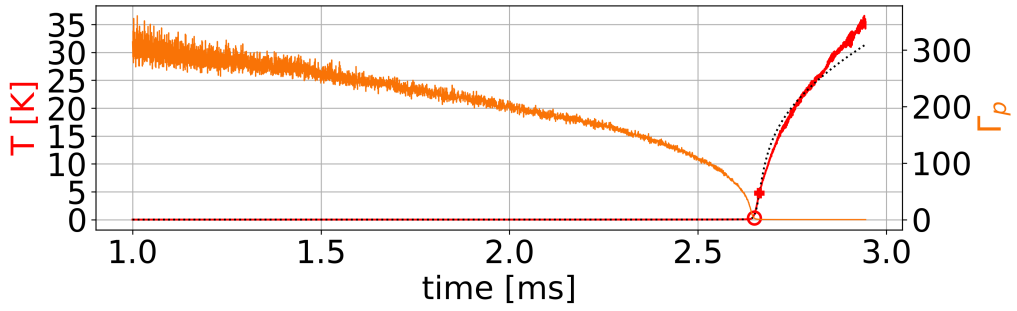

FIGURE 9.15: Linear representation of the ion cloud temperature T (red) and the plasma parameter Γ_p (orange) during a run of computer program `RF HEATING`, with U_{RF} = 64 V, U_{DC} = 3 V, 1024 ions. The dashed line is a fit of the temperature according to equation 9.4. The circle indicate when $t = t_0$ and the cross when the derivate of the analytical fit is maximum.

t_0 is the critical timing and 10^B is the temperature at $t = t_0$ for which the critical timing is happening. The circle in figure 9.14 indicates the critical timing (t_0,10^B). As the logarithmic representation of figure 9.14 may be luring, the same data are represented in linear scale in figure 9.15. The above numerical definition of the critical timing seems to represent with a satisfying precision the moment where the temperature suddenly increases, due to the dominance of radio-frequency heating. The maximum of heating rate is represented with the cross. It is happening at t_{max} = 2.663 ms. During the first heating phase where the temperature is below 40 mK, the cloud goes from crystal to liquid ($\Gamma_p < 278$) and no dramatic effect from this transition is visible in the temperature evolution. Between t_0 and t_{max}, the cloud is vaporising in the gas state ($\Gamma_p < 2$), and again no dramatic effect is visible on the temperature evolution.

9.4.2 Systematic study

The above mentioned protocol was carried out over a set of 17 conditions, ran once, in order to search for systematic effects. The critical timing and temperature are discussed below, then a discussion on the heating rate is carried out.

Study of critical timing and temperature

A dependence of t_0 and B against the radio-frequency amplitude could be established. In the discussion below, numerical simulation are carried out with N = 1024 ions, U_{DC} = 7 V, and a varying radio-frequency field in the range 60 − 68 V. Figure 9.16 shows the critical timing t_0 as a function of the radio-frequency amplitude U_{RF}. A rendition of the same data with $1/\sqrt{t_0}$ as a function of U_{RF} allows for the establishment of the following linear dependency :

$$\frac{1}{\sqrt{t_0}} = 6.66 \cdot 10^{-2} U_{RF} - 3.74. \tag{9.7}$$

This analysis of the critical timing as a function of the radio-frequency amplitude shows that, the stronger the radio-frequency amplitude, the sooner is the critical timing. The

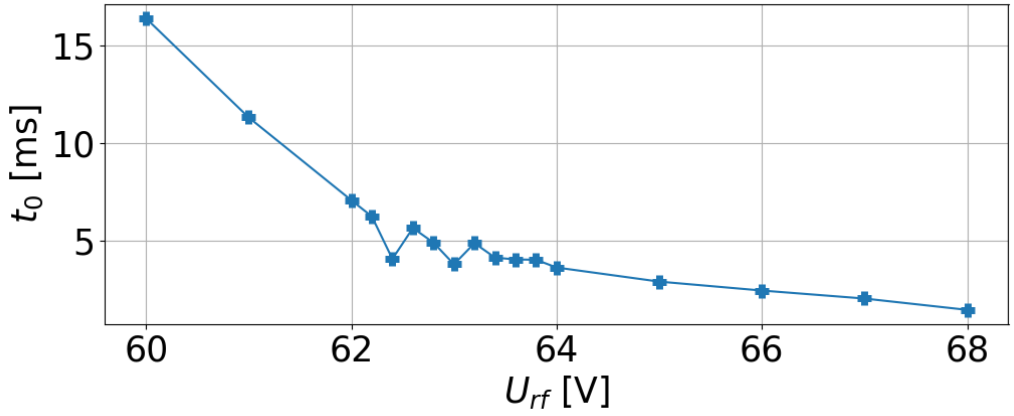

FIGURE 9.16: Critical timing t_0 deduced from the fit, as a function of U_{RF} for 17 conditions, using computer program `RF HEATING`, U_{DC} = 7 V, 1024 ions. The blue line only links the neighbour data points.

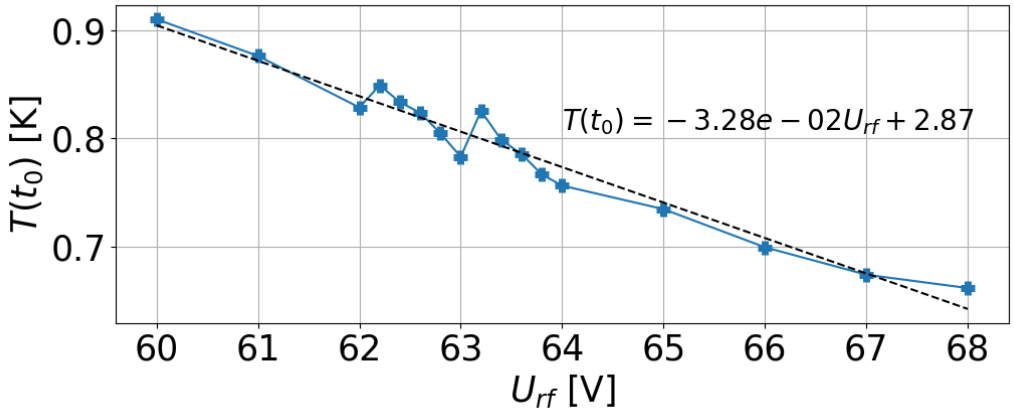

FIGURE 9.17: Cloud temperature at critical timing t_0 deduced from the fit, as a function of U_{RF} for 17 conditions, using computer program `RF HEATING`, U_{DC} = 7 V, 1024 ions. The dashed line is a linear fit whose equation is written in black. The blue line only links the neighbour data points.

cloud is quickly brought to high temperatures by a higher radio-frequency field. An analysis of the $B = T(t_0)$ parameter versus U_{RF} is illustrated by figure 9.17, in which a linear fit is represented by the dashed line, with equation

$$T(t_0) = -3.28 \cdot 10^{-2} U_{RF} + 2.87. \tag{9.8}$$

This information is really interesting because it provides the temperature which is required to trigger the high heating rate phase of the thermal runaway. In the context of `GiantMol`, if the giant projectile is able to transfer enough energy so the cloud temperature reaches this value $T(t_0)$, then the radio-frequency heating is able to bring the ion cloud to high temperatures where the fluorescence is significantly different from its initial level (subsection 4.2.4). In order to trigger a significant and observable fluorescence change the cloud must be heated beyond 600 mK (subsection 4.2.4) and the Coulomb interaction alone is

reported to heat the cloud to approximately 100 mK solely (Fig. 9.1).

In the RF heating simulation presented here, the laser cooling is not taken into account, but as previous numerical simulations demonstrated it, it is expected that approximately half the energy loss by the projectile is converted into thermal energy. Using such assumption it is possible to estimate the amount of energy it is required to transfer from the projectile to the cloud. It is possible to imagine a protocol in order to predict the conditions that ensure favourable detection. This would require to know the critical timing temperature $B = T(t_0)$ (Fig. 9.16) and the energy loss by the projectile ΔE (Fig. 9.13) during the collision with a cloud trapped with given conditions. A systematic study of such a protocol with laser cooling is still to be made for a broader set of parameters. Also a careful study of the energy transferred from the projectile to the cloud as a function of trapping and cooling parameters is probably beneficial.

Heating rate

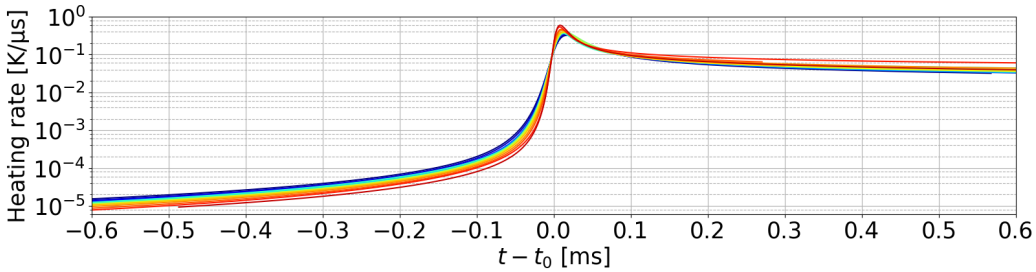

FIGURE 9.18: Heating rate H deduced from the fit, as a function of U_{RF} for 17 conditions, using computer program `RF HEATING`, U_{DC} = 7 V, 1024 ions. Each coloured line stands for one specific U_{RF}, going from lower U_{RF} (blue) to higher U_{RF} (red).

For the same conditions, the heating rate is studied separately. All the heating rates H versus time are represented in figure 9.18. The relative heating rate, defined as H/T is plotted against time in 9.19. Figure 9.20 is a close-up of figure 9.19 centred on $t-t_0 = 0$. In those figures, the curves are all synchronised with the critical timing t_0 so that the horizontal axis is $t - t_0$. It turns out the heating rate curves are superimposing with a relatively good accuracy, displaying a kind of universal behaviour. The function underlying the temperature evolution look identical for all curves, excepted only the t_0 value varies when varying U_{RF}, thus an analytical expression must include this t_0 parameter or any other parameter that can account for this specificity. 0.6 ms before the critical timing, the heating rate curves are bounded by two curves different from each other by a factor 2, the heating rate from the low radio-frequency amplitude having the highest heating rate. Around $t - t_0 = 0$ the factor between the highest and lowest heating rate is also a factor 2, but with relative position reverted : the highest heating rate is thus of the highest radio-frequency amplitude, with peak value of 0.6 K/µs. Also, the heating rate for the highest radio-frequency amplitude peaks approximately 8 µs after t_0, while the heating rate for the lowest radio-frequency amplitude peaks approximately 18 µs after t_0. This is related to the fact that the heating

rate H itself grows faster for higher radio-frequency amplitudes ($\mathrm{d}H/\mathrm{d}T$ higher when U_{RF} is higher.). Comparing the relative heating rates H/T, the curves look closer at first. Indeed at $t - t_0 = -0.6$ ms, the curves are bounded by two curves with factor $1/3$. Nevertheless at $t - t_0 = 0$ the difference between the curves goes up to factor 3. Also, the maximum for each curve is localised at $t - t_0 = 0$. In this case, the higher the curve at $t - t_0 = 0$, the higher U_{RF}.

The heating rate curves for all conditions are comparable to the pattern in figure 3.1 provided by Nam, Jones, and Blümel [Nam14]. Indeed it is possible to see that the heating rate, as a function of the temperature, displays a global maximum with two monotonous slopes surrounding it. Among the differences between our computed heating rate and the pattern proposed by Nam, Jones, and Blümel [Nam14] is that the slopes are non-linear in our simulations and that the heating rate is highly asymmetric, with much higher values on the right part of the curve where the temperature is above the temperature for which the heating rate is maximum.

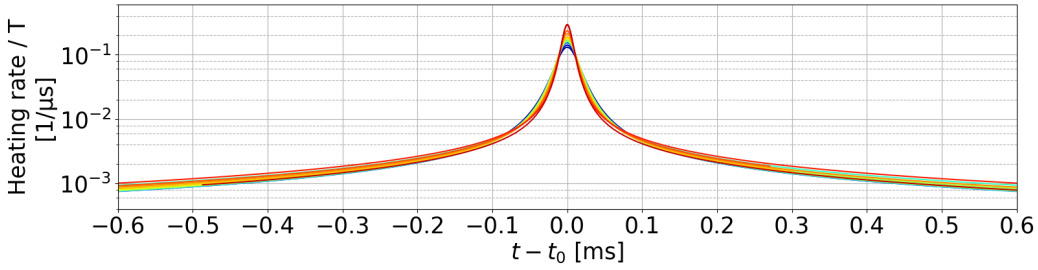

FIGURE 9.19: Heating rate H deduced from the fit, as a function of time for 17 conditions, using computer program `RF HEATING`, $U_{DC} = 7$ V, 1024 ions. Each coloured line stands for one specific U_{RF}, going from lower U_{RF} (blue) to higher U_{RF} (red).

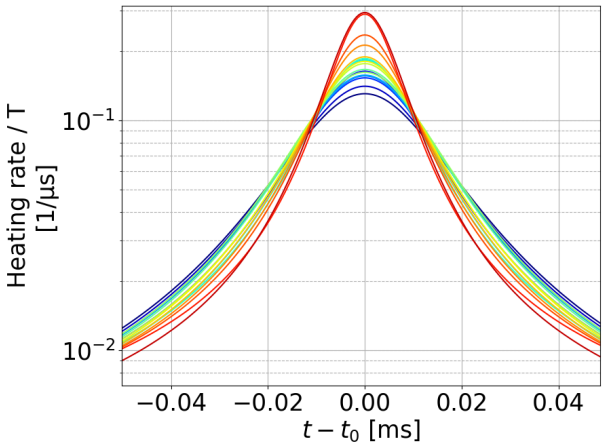

FIGURE 9.20: Relative heating rate H/T deduced from the fit, as a function of time for 17 conditions, using computer program `RF HEATING`, $U_{DC} = 7$ V, 1024 ions. Each coloured line stands for one specific U_{RF}, going from lower U_{RF} (blue) to higher U_{RF} (red).

Conclusion of part III

NUMERICAL simulations are an essential part of the `GiantMol` project. They reproduce the interaction of a singly-charged individual molecular ion with an ensemble of trapped and laser cooled Ca^+ ions. They also provide a platform for the study of the behaviour of the ion ensemble in the trapping alone. They also may be used for other purposes.

In this work, the numerical simulations have demonstrated the detection principle proposed in `GiantMol` is achievable. In principle, the detection signal is an observable variation of the ion fluorescence. The numerical simulations demonstrate that the detection signal is induced by the two following effects : first, the Coulomb interaction occurring during the interaction of the molecular ion with the ion cloud is the source of an energy transfer from the projectile to the cloud, inducing a heating of $\approx$ 50 mK, second, when the detection is successful, the temperature of the cloud increases by several order of magnitude due to the radio-frequency heating dominating. The conditions under which a detection signal can be observed are presented. Detection is successfully achieved for the highest radio-frequency voltage (U_{RF} = 70 V) or for lower voltages down to U_{RF} = 59 V if the axial potential is small enough ($U_{DC} \leq 2$). The numerical simulations highlight that the probability of detection increases when the radio-frequency amplitude increases, and when the axial potential decreases. The axial potential is inversely correlated with the cloud length. The detection efficiency can be related to the length of the cloud and the cloud density.

The stopping power of the ion ensemble is also a key parameter because it has a direct effect on the amount of energy the projectile can initially transfer to the cloud via the Coulomb interaction, which has a great influence on whether or not a detection will occur. The more initial energy transferred, the higher the detection efficiency. So a careful study of stopping power is of great interest. The knowledge of the parameters influencing the deposited energy in the cloud, the determination of the quantity deposited itself, completes the informations obtained in the study of radio-frequency heating that provide threshold temperatures for the radio-frequency heating to dominate (through $B = T(t_0)$ parameter). The radio-frequency heating can be more thoroughly investigated and our result compared to the bibliography, notably the extensive work from Blümel et al. [Blü89] and Nam, Jones, and Blümel [Nam14].

Part IV

CONCLUSION

"We demand rigidly defined areas of doubt and uncertainty!"

– Douglas Adams *in* The Hitchhiker's Guide to the Galaxy

10.5 Summary

THE work achieved in this thesis is intended to propose a new non-destructive detection solution for giant molecules. Currently giant molecules with masses above 10^6 Da, such as viruses, are only detectable under restricted conditions due to the limitations of the detection solutions. In particular, their detection requires either fragmentation or a high charge state, which in both cases puts the molecule in a state far from its state in biological systems. The present work discusses the non-destructive detection of a singly-charged individual molecular ion of mass 10^6 Da or higher. The detector is an ensemble of trapped and laser cooled Ca^+ ions. The detection signal is searched for in the fluorescence of this ion ensemble. The principle relies on the perturbation of the fluorescence induced by the interaction of the molecular ion with the ion ensemble. In order to demonstrate a detection according to this principle, an experimental prototype and numerical simulations are developed in parallel.

In this work, this principle is demonstrated through numerical simulations. We also demonstrate that the detection effect is due to a combination of two effects. First, energy is transferred from the charged molecule to the ion via the Coulomb interaction which leads to a small increase in temperature ($\approx$ 100 mK). Second, a mechanism known as radio-frequency heating becomes dominant and causes a quick heating of the cloud by several orders of magnitude. Both effects increase the temperature of the ion ensemble which ultimately leads to a significant observable diminution of the fluorescence.

This work presents the trapping and laser cooling of an ensemble of ions, and discusses the important elements in order to understand the detection principle (part I). It also discusses a molecular source and a system to guide molecular ions towards the detector (part II). The numerical simulations are used in order to reproduce the interaction of the giant molecule with the set of ions (part III). The specific conditions under which the detector is able to provide a detection signal are specified from the numerical results. For radio-frequency voltages of U_{RF} = 70 V, equivalent to a radial parameter of q_x = 0.65, the detection efficiency is 100% for any of the seven axial potential tested $1 \leq U_{DC} \leq 7$. When the axial potential becomes lower ($U_{DC} \leq 2$ or $f_z \leq 128$ kHz), the detection efficacy is also maximum for radio-frequencies down to U_{RF} = 59 V, equivalent to q_x = 0.55. Those numerical results allow for a comparison with the aforementioned fundamental aspects of trapping and laser cooling inherent to the detector principle. The numerical simulations also propose a discussion of the radio-frequency heating effect which is at the heart of the detection mechanism. A great part of this numerical work is dedicated to study of

the radio-frequency heating and how it can be used to increase the heating rate and produce a visible signal. For us radio-frequency heating can be seen as an amplifier for the initial energy input provided by the crossing of the charged molecule, which is used at our benefits. Nevertheless, for some other applications, radio-frequency heating is a negative effect that must be minimised. Ultimately, the principles and arguments presented in this work in order to favour the radio-frequency heating can be used in order to control the heating rate and minimise it when the situation requires to do so. The tools presented in this numerical part can be adapted and used in order to study how to minimise the heating rate, rather than trying to maximise it.

10.6 Challenges and outlook

10.6.1 Molecular source

The challenges to overcome in order to experimentally provide a detection of a heavy molecule are numerous. Indeed, currently in `GiantMol` the guiding and detection on a classical MCP is only demonstrated for pyridine (79 Da) and tryptophan (205 Da), some relatively low weight molecules. The guiding and detection of more heavyweight candidates, and ultimately the providing of an experimental demonstration of the `GiantMol` principle applied to mega-Dalton molecules, is mainly subject to three points :

- first, the improvement in stability and reproducibility of the molecular source ;
- second, the improvement of the capillary/skimmer assembly, according to the considerations of chapter 5 ;
- third, a thorough work on the electrospray source.

Candidate molecules for further testing of the source are identified in a range of several orders of magnitude : Dibenzo-18-crown-6 (360 Da), Gramicidin (1 882 Da) and Bovine serum albumin (66.5 kDa).

Several challenges not thoroughly discussed in this manuscript also await us. Among them, the most important are as follows :

- The careful control of the collision energy of the molecular ion with the ion cloud must be mastered. An experiment dedicated to the interaction of a molecule (CH_3F) with a trapped Ca^+ ion cloud already demonstrated the ability to produce a collision with a translational energy in the Kelvin range (1 K $\approx$ 0.1 meV) [Wil08], using a quadrupole guide velocity selector (which is essentially a quadrupole with a 90 degree turn.) ;
- How does the interaction depend on the number of charges of the molecular ion, or the number of molecular ions in the incoming bunch ? From what has been said in this thesis, the more charges or particles are interacting the cloud, the easier will be the detection to happen. The experimental filtering of the molecular ions with

respect to their charge number is possible with the quadrupolar bender embedded in the prototype (Eq. 6.18). Nevertheless controlling the number of molecular ions in a bunch send to the ion trap remains a challenge. A numerical study of such scenario can be developed in the future in order to characterise the effect over the ion cloud of a collection of projectiles, depending the number of elements in the bunch. Notably, the investigation on the stopping power can be beneficial. Indeed, questions such as the effect on a plasma of the number of charges of the projectile are discussed by Zwicknagel, Toepffer, and Reinhard [Zwi99], as much as the effect of the incident energy of the particle.

I want to point out that the advances in optical tweezers nowadays allow for the careful manipulation of a very broad range of objects from proteins to microorganisms. Such optical tweezers technique can be an alternative to the current solution for guiding we and others proposed, based on charged particle optics and guiding multipoles. In a review from Gieseler et al. [Gie21], the possibility to make optical tweezers compatible with ultra-high vacuum applications is discussed (section 5 from the review). Because in vacuum there is no viscous damping force, it is much more complex to capture a moving particle in the optical trap of the optical tweezers. Optical tweezers have a low damping γ_0 and can only capture particles that already have a small velocity below $\lambda\gamma_0$, with λ the optical tweezers wavelength. Gieseler et al. [Gie21] highlight the need for a molecular source able to produce a beam of particles compatible with such a condition. For particle loading, the nebulizer is presented as a plausible solution, whose principle and experiment is presented in Ricci [Ric19] thesis. The review also presents the work of Bykov et al. [Byk19] that proposed a dry solution for particle loading allowing to bypass many of the inconvenients generated by the solvent required by the nebulizer. The use of optical tweezers may also be of great advantage in order to solve another challenge, which is the careful control of the position and direction to which the molecule collides with the ion ensemble. This crucial parameter must be controlled so that the position is located around the cloud axis during the whole interaction, with a high precision compared to the cloud size. It is essential to guide the molecular ion as close as possible to the centre of the cloud so that it travels along the longitudinal axis and interacts as much as possible with the cloud, in particular without being deviated too early. Nevertheless, while optical tweezers are demonstrated for neutral molecules, it remains a challenge for charged particles.

10.6.2 Ion trapping and laser cooling

Also, the success of the experiment depends on the ability to cool the ion cloud to a low crystal temperature ($\approx$ 5 mK). Nevertheless, the high radio-frequency voltages ($>$ 50 V, $q_x > 0.5$) required in our experiment are the source of an important heating to which it is unusual to work and that challenges the laser cooling. Because of the higher susceptibility of the cloud to perturbations this high radio-frequency amplitude implies, it also demands a careful control of the ion ensemble environment, and especially a careful control of the trap defects and other unbalances. Indeed, although small imperfections may be tolerable

when trapping with small radio-frequency amplitude, they become too important when the applied field reaches such high amplitudes.

10.6.3 Numerical works

Finally the numerical work also provides some challenges. Especially, the study of the radio-frequency heating is demanding a specific framework in order to exploit the data with a reasonable consistency. Indeed, because of the oscillating behaviour of the numerical variables such as the temperature, it is impossible to benefit from a simple time derivative of the signals. While some have used a complex analytical model in order to study radio-frequency heating within limited conditions [Nam14], we tried to provide a more general and universal understanding of radio-frequency heating. Especially, we do not want to limit our study to an average effect, or a limited range of hot temperatures [Nam14], but consider it along the evolution of the temperature, which is in fact more challenging than expected. This allows us to analyse the heating rate in cold conditions where it was ppreviously reported no heating rate was measureable [Ryj05]. This required to transform the temperature in an analytical form via a fit (Eq. 9.4) in order to study it. Nevertheless, a less analytical approach may be developed in order to represent the data with more accuracy.

10.6.4 Scientific purpose

While the topic covered in this thesis manuscript mainly focuses on the detection of a molecule in a context related to analytical chemistry, this `GiantMol` experiment also relates to many other similar setups orientated towards other problematics. Reviews from Willitsch [Wil12] and Meerakker et al. [Mee12] highlight the applications orientated towards chemistry and physics, among which cold-ion chemistry which is dedicated to the study of chemical reactions at very low temperatures ($T \leq 1$ K), including for neutral molecules or other collision experiments, in order to study beam scattering. Also, the apparatus operated in `GiantMol` experiment (as in a lot of mass spectrometers), in order to carry out the confinement and the guiding of charged particles is not devoid of similarities with apparatus operated in particle physics experiments. Indeed the similarities in the fundamental prerequisites and the technologies required in `GiantMol` and experiments such as GBAR are impossible to deny [Hus18]. My point is that, experiments built with similar scales as `GiantMol` can provide an interesting platform for problematics that are in the field of particle physics : for instance a method proposed in order to accomplish sympathetic cooling of anti-hydrogen in the GBAR experiment [Hil14] is not out of the range accessible by our kind of experiment. Having access to antimatter is the real arduous problem.

On the other hand, the use of trapped ions only for frequency metrology and spectroscopy is also a fruitful application that `GiantMol` would be compatible with. Nevertheless our team already benefits from another experiment already dedicated to this goal.

The applications mentioned above could be investigated in numerical simulations. Also other relevant problematics include the stopping power. In the context of `GiantMol`, its unraveling may bring an important piece to the understanding of the detection mechanisms, with a great step towards quantitative informations.

APPENDIX

Appendix A

Radial ideal quadrupole potential computation

In the following, an expression for the ideal trapping field is going to be developed considering the simple hypothesis done above. It is a justification on why it is required a quadrupole trap to produce a trapping field satisfying the simple hypothesis above. A more general case is treated just after, where a multipole expansion of the potential produced by the linear quadrupolar geometry is done.

Considering only one coordinate direction u, in order to be able to trap an ion, it is required that the applied force expresses as $F_u \propto u$. Generalising to all directions of space, it is convenient that the total force applied to the ion is just the sum of three independent forces over each direction. From the expression of the force, it is wise to obtain an expression of the potential $\Phi(x, y, z)$ in order to solve the Laplace equation. This will provide a general expression for the potential and lead to an expression for the voltages to apply to electrodes. Later the motion equation of a trapped ion will be retrieved from this potential.

$$F_u = q_e E_u = -q_e \frac{\partial \Phi(x, y, z)}{\partial u} = -q_e \frac{\partial \Phi(u)}{\partial u}. \tag{A.1}$$

This leads to the following expression for the field

$$\Phi(u) = \alpha u^2, \text{ with } \alpha = \text{cte} \tag{A.2}$$

Finally, summing all the contributions reveals the general expression for the field

$$\Phi(x, y, z) = \alpha x^2 + \beta y^2 + \gamma z^2, \text{ with } \alpha, \beta, \gamma = \text{cte}. \tag{A.3}$$

Because this is a linear quadrupole trap with symmetry axis z, no alternating potential is applied over this direction. We will see later a static voltage applied over the z axis is sufficient to guarantee ion trapping. As for the **radial component** of the trapping field, we then have

$$\Phi_{Rad}(x, y, z) = \alpha x^2 + \beta y^2, \text{ with } \alpha, \beta = \text{cte}. \tag{A.4}$$

This gives us an expression for the potential that we can introduce in the Laplace equation to obtain restrains on the constants values

$$\Delta\Phi_{Rad}(x,y) = 2\alpha + 2\beta = 0. \tag{A.5}$$

This requires $\alpha = -\beta$. Using **field boundary conditions**, it is possible to determine that, at $x = r_0$ and $y = 0$ the field is $\Phi_{Rad}(r_0, 0) = \Phi_0 = \alpha r_0^2$, and similarly inverting x and y, $\Phi(0, r_0) = -\beta r_0^2$. This leads to

$$\alpha = -\beta = \frac{\Phi_0}{r_0^2} \tag{A.6}$$

$$\Phi_{Rad}(x,y) = \Phi_0(t)\frac{x^2 - y^2}{r_0^2}. \tag{A.7}$$

Rejecting the trivial solution where $\alpha = \beta = 0$ (no trapping), it is required to apply alternating voltages to the electrodes in order to confine in long time scales. The voltage applied to the rods can be written as $\Phi_0(t) = U_{st} + U_{RF}\cos\Omega t$, with U_{RF} the amplitude of the alternating field applied to a rod, and U_{st} a possible offset, Ω the frequency of the alternating field. This ends to

$$\boxed{\Phi_{Rad}(x,y,t) = \frac{U_{st} + U_{RF}\cos\Omega t}{2r_0^2\mathcal{L}}(x^2 - y^2)} \tag{A.8}$$

the potential created by the trap. It is created by applying two alternating voltages with amplitude U_{RF} to each pair of rods, the pairs being in phase opposition. It is remarkable that there are no coupling between x and y. A geometric constant $0 < \mathcal{L} < 1$ is added to the expression in order to account for trap's imperfections [Ped10] responsible for the introduction of higher order potentials, thus lowering the proportion of quadrupolar field in the total field. A multipolar expression can be obtained by truly integrating Laplace equations.

Appendix B

Resolution of Mathieu equation

The Mathieu equation, describing the motion of trapped ions in quadrupole traps, can be written as

$$\boxed{\frac{d^2}{dt^2}\,u + (a_u - 2q_u \cos 2\tau)\,u = 0.} \tag{B.1}$$

The range within the solutions of Mathieu equation are stable is computable and showed in figure 1.4. The Mathieu equation is a particular case of a linear type of second order equation with periodic coefficients.

The solution of Mathieu equations u takes different forms depending on the values of a_u and q_u. McLachlan comments that "in the membranal problem, the displacement from the equilibrium position is a periodic function of one of the coordinates", which is also the case in the trapped ion problem. So hereinafter, only solutions with period π or 2π in τ will be considered. This leads to the two following important considerations : first, the solutions of Mathieu equations will be reduced to cos and sin functions, second, parameters a_u and q_u are interrelated so that

$$a_u = f(q_u), \tag{B.2}$$

$f(q_u)$ being a polynomial function of q_u, possibly containing a constant term (q_u-independent) (see Eq. B.10). Most of this description is inspired from the thorough work from McLachlan [McL47], and textbooks from [Maj05; Kno16] where a synthetic summary can be found. Keep in mind that this is only about the description of a single ion in an alternating potential.

2.1 Integer order – stability range

Using both considerations above, along with edge conditions, it is possible to find solutions to Mathieu equation in the case of functions of integer order m. Then the relationship between a_u and q_u can be fully determined, under the form of a Maclaurin series[1], which is of great interest because it allows to establish the range of parameters (a_u, q_u) for which the trapped ion is stable, and thus the range of experimental parameters it is possible to explore. This range is visible on the stability diagram (Fig. 1.4a) and is bounded by the

[1] A specific case of power series expansion where the constant term is null.

curves (a_m, b_{m+1}), also refereed to as (ce_m, se_{m+1})[2], and defined so that

$$u(\tau, q_u) = ce_m(\tau, q_u) = \sum_{n=m}^{\infty} f_m(q_u) \cos n\tau \text{ with } \begin{cases} \text{n even if m is even} \\ \text{n odd if m is odd} \end{cases} \tag{B.3}$$

or

$$u(\tau, q_u) = se_m(\tau, q_u) = \sum_{n=m}^{\infty} f_m(q_u) \sin n\tau \text{ with } \begin{cases} \text{n even if m is even} \\ \text{n odd if m is odd} \end{cases} \tag{B.4}$$

2.2 Fractional order

In the general case, the parameters (a_u, q_u) can be chosen between the stability boundaries (a_m, b_{m+1}). The motion of an ion is then described by a Mathieu function of fractional order $\nu = m + \beta$, with $0 < \beta < 1$, $\beta \in \mathbb{R}$. The actual solution to Mathieu equation is then a combination of the integer order solutions bounding the actual solution, so that the solution is an infinite sum of sinus and cosinus [McL47, p. 20]

$$u(\tau, q) = \alpha ce_\nu(\tau, q) + \alpha' se_{\nu+1}(\tau, q) \tag{B.5}$$

$$\text{with } \alpha, \alpha', \in \mathbb{R}. \tag{B.6}$$

Following the same principle as before, a Maclaurin series in function of parameter q_u allows to develop characteristic values a_u for a given order ν. In return, knowing the values for trapping parameters (a_u, q_u) allows to determine the real order ν and above all β. β is an important parameter to determine in order to compute the secular frequencies and some other derived parameters such as cloud density. A relationship between β and (a_u, q_u) under the form of a generalised continued fraction [McL47, p. 106; Maj05, p. 21; Kno16, p. 38] can be used to determine the unknown parameter.

$$\beta^2 = a_u + f(\beta, a_u, q_u) + f(-\beta, a_u, q_u) \tag{B.7}$$

with

$$f(\beta, a_u, q_u) = \cfrac{q_u^2}{(\beta+2)^2 - a_u - \cfrac{q_u^2}{(\beta+4)^2 - a_u - \cfrac{q_u^2}{(\beta+6)^2 - a_u - \ddots}}} \tag{B.8}$$

$$f(-\beta, a_u, q_u) = \cfrac{q_u^2}{(\beta-2)^2 - a_u - \cfrac{q_u^2}{(\beta-4)^2 - a_u - \cfrac{q_u^2}{(\beta-6)^2 - a_u - \ddots}}}. \tag{B.9}$$

[2] *ce* and *se* stand for cosine-elliptic and sine-elliptic.

Solving this problem requires to proceed iteratively. A first trial value for β must be chosen then both side of equation B.7 must be evaluated and if the difference is above a given value, a new β value must be inserted in the equation. Usually a dozen of steps provides a satisfying result in accordance with other computation methods given by McLachlan [McL47].

2.3 Stability diagram

The limit of the stability domain (Fig. 1.4a) used in trapping experiments are given by the following set of functions, resulting from the power series expansion of characteristic values $a_m(q_u)$ [McL47, p. 106]

$$\begin{cases} a_0(q_u) = -\dfrac{q_u^2}{2} + \dfrac{7q_u^4}{128} - \dfrac{29q_u^6}{2304} + \dfrac{68687q_u^8}{18874368} + \ldots & \text{(B.10a)} \\ b_1(q_u) = 1 - q_u - \dfrac{q_u^2}{8} + \dfrac{q_u^3}{64} - \dfrac{q_u^4}{1536} - \dfrac{11q_u^5}{36864} & \text{(B.10b)} \\ \qquad + \dfrac{49q_u^6}{589824} - \dfrac{55q_u^7}{9437184} - \dfrac{83q_u^8}{35389440} + \ldots & \\ -a_0(q_u) & \text{(B.10c)} \\ -b_1(q_u). & \text{(B.10d)} \end{cases}$$

Stating $b_1(q_u) = -b_1(q_u) = 0$, this allows to compute the highest q_u for which the trap is stable : $q_{max} = 0.908$. The highlighting of such stability domain and the definition of the stability parameters in function of the experimentally accessible parameters U_{RF}, U_{DC}, ω and r_0 allows us to properly design the experiment.

For a given order ν it is also possible to compute all the characteristic values a_u in function of q_u. For any (a_u, q_u) set of parameters the continued fraction is to favour, nevertheless under the condition that $|a| \ll |q_u^2/2(\nu^2 - 1)|$, the characteristic values can be computed using the Maclaurin series form, so that

$$\nu^2 = a_u - q_u^2 \frac{1}{2(\nu^2 - 1)} - q_u^4 \frac{5\nu^2 + 7}{32(\nu^2 - 1)^3(\nu^2 - 4)} \tag{B.11}$$

$$- q_u^6 \frac{9\nu^4 + 58\nu^2 + 29}{64(\nu^2 - 1)^5(\nu^2 - 4)(\nu^2 - 9)} + \mathcal{O}(q_u^8). \tag{B.12}$$

Appendix C

Pseudo-potential and adiabatic approximation

The above considerations on ion dynamics highlights the existence of a secular motion. Furthermore, because of the presence of the driving alternating field, it is hard to neglect it. In fact it is tempting to search for a model where the ion motion is split into two independent contributions. The first contribution would originate from the trapping field, analogous to an excitation field, in first order driving the ion motion at its oscillating fast frequency $\Omega/2\pi$. The consequent motion $\boldsymbol{\mu}(t)$ would be fast with small amplitude and thus called **micromotion**. The second contribution would originate from the resolution of the Mathieu equation, analogous to a natural frequency of ion in the potential. It would give birth to a slower motion $\mathbf{R_0}(t)$ with frequency related to the secular frequency $\omega/2\pi$, with higher amplitude and called **macromotion**. In fact, this model is not science fiction at all and ever has a name : the **pseudo-potential approximation**.

3.1 Pseudo-potential derivation

Provided the adiabatic approximation is valid, the proper definition for the motion of an ion *i* in this framework starts with resolving it in two contributions, one so slow it could be considered invariant during a period of the second contribution, and it can be written as

$$\mathbf{u}(t) = \mathbf{R_0}(t) + \mu(t) \tag{C.1}$$

$$\mathbf{u}(t) = \mathbf{R_0}(t) - \varepsilon(t)\sin\Omega t \tag{C.2}$$

with $\varepsilon(t) = \frac{q_e}{m\Omega^2}\mathbf{E}(t)$. Immersed in a non uniform and alternating field, the charged particle would behave accordingly to the Newton's equation so that

$$m\frac{d^2}{dt^2}\mathbf{u}(t) = q_e\mathbf{E}(\mathbf{r}(\mathbf{t}))\sin\Omega t = m\varepsilon\sin\Omega t. \tag{C.3}$$

The idea is now to derivate twice the equation C.2, in order to combine it with equation C.3. The following derivation uses the adiabatic approximation. It is expressed in 1D and the reader must be conscious that extending in 3D, it remains valid for electric field but not necessarily for magnetic fields.

$$\text{first derivation}\begin{cases}\frac{d}{dt}\mathbf{u}(t) = \frac{d}{dt}\mathbf{R_0}(t) - \frac{q_e}{m\Omega^2}\left(\cos\Omega t\frac{d}{dt}\mathbf{E}(t) - \mathbf{E}(t)\frac{d}{dt}\sin\Omega t\right) & \text{(C.4)}\\ \approx \frac{d}{dt}\mathbf{R_0}(t) - \mathbf{E}(t)\frac{q_e}{m\Omega^2}\cos\Omega t & \text{(C.5)}\\ \approx \frac{d}{dt}\mathbf{R_0}(t) - \varepsilon(t)\Omega\cos\Omega t. & \text{(C.6)}\end{cases}$$

Using the same arguments, we can derivate equation C.6

$$\text{second derivation}\begin{cases}\frac{d^2}{dt^2}\mathbf{u}(t) \approx \frac{d^2}{dt^2}\mathbf{R_0}(t) + \frac{q_e}{m\Omega}\Omega^2\sin\Omega t\times\mathbf{E}(t) & \text{(C.7)}\\ \approx \frac{d^2}{dt^2}\mathbf{R_0}(t) + \varepsilon(t)\Omega^2\sin\Omega t & \text{(C.8)}\end{cases}$$

Substituting equation C.7 in equation C.3

$$m\frac{d^2}{dt^2}\mathbf{R_0}(t) + m\varepsilon(t)\Omega^2\sin\Omega t = q_e\underbrace{\mathbf{E}(\mathbf{R_0}(t) - \varepsilon(t)\sin\Omega t)}_{\substack{\text{first order power series dev.}\\ \text{of }\varepsilon\mathbf{E}\text{ in }\mathbf{R_0}}}\sin\Omega t. \tag{C.9}$$

$$m\frac{d^2}{dt^2}\mathbf{R_0}(t) + q_e\mathbf{E_0}(\mathbf{R_0})\sin\Omega t = q_e\mathbf{E_0}(\mathbf{R_0})\sin\Omega t - \frac{q_e^2}{2m\Omega}\nabla\mathbf{E_0}(\mathbf{R_0})^2\times\sin^2\Omega t \tag{C.10}$$

$$m\frac{d^2}{dt^2}\mathbf{R_0}(t) = -\frac{q_e^2}{2m\Omega^2}\sin^2\Omega t\nabla\mathbf{E_0}(\mathbf{R_0})^2. \tag{C.11}$$

Averaging equation C.11 over time, it is possible to write

$$\boxed{m\frac{d^2}{dt^2}\mathbf{R_0} = -\nabla\frac{q_e^2}{4m\Omega^2}\mathbf{E_0}(\mathbf{R_0})^2 = -\nabla\Psi^*} \tag{C.12}$$

with $\Psi^* = \frac{q_e^2}{4m\Omega^2}\mathbf{E_0}(\mathbf{R_0})^2$ the pseudo-potential.

In the pseudo-potential approximation, everything is happening as if the slow macromotion, was governed by this static pseudo-potential Ψ^*. The expression for the pseudo-potential is equivalent to the average micromotion kinetic energy over a trapping field period, so that

$$\overline{E_{kin}} = \overline{\Psi^*} = \frac{1}{2}m\overline{(\Omega\varepsilon\cos\Omega t)^2}. \tag{C.13}$$

3.2 Motion in the pseudo-potential

Inserting the basic decomposition (Eq. C.1) into the Mathieu equation (Eq. 1.12), it is possible to determine a motion equation for a trapped ion in the pseudo-potential (using Eq. C.19).

$$\frac{d^2}{dt^2}\mu_u(t) + (U_{st} - U_{RF}\cos\Omega t)\frac{2q_e}{mr_0^2}R_{0\,u}(t) = 0. \tag{C.14}$$

In the framework of the adiabatic approximation, it is considered for each trapping field period that the ion oscillates around an average position $R_{0\,u}$ at the micromotion frequency.

It is as if $R_{0\,u}$ is constant during a period and it is possible to integrate the above equation and retrieve an expression for $\mu_u(t)$

$$\mu_u(t) = -\frac{1}{2} U_{RF} \cos \Omega t \frac{2q_e}{mr_0^2} R_{0\,u} = 0. \tag{C.15}$$

The equation C.14 can be rewritten solely in function of $R_{0\,u}(t)$ and solved to provide us with an expression for $R_{0\,u}(t)$

$$R_{0\,u}(t) = A_u \cos(\omega_u t + \phi_u) \tag{C.16}$$

with A_u and ϕ_u arbitrary amplitude and phase depending on initial ion condition. Then the motion of an ion in the pseudo-potential is given by

$$\boxed{u(t) = A_u \cos(\omega_u t + \phi_u) \left(1 - \frac{q_u}{2} \cos \Omega t\right)} \tag{C.17}$$

with $\omega_u = \beta_u \Omega / 2$.

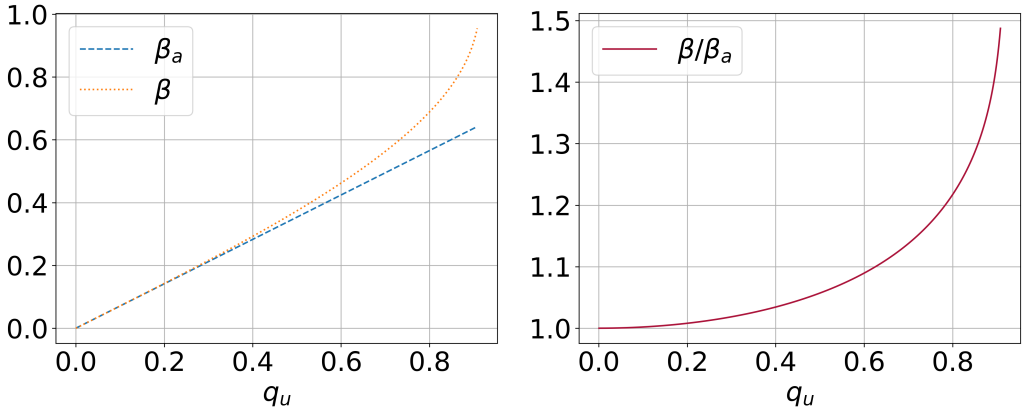

FIGURE C.1: Comparison of two computations of β parameters, in the general case, and the adiabatic case.

3.3 Mathematical aspects of the adiabatic approximation

Definition The adiabatic approximation can be understood as a synonymous of gradual perturbation approximation. To have a clear idea of how this translates for a trapped ion, I could not find a better illustration than that of Griffiths [Gri18], introducing the concept by the following explanation

> Imagine a perfect pendulum, with no friction or air resistance, oscillating back and forth in a vertical plane. If I grab the support and shake it in a jerky manner, the bob will swing around in a wild chaotic fashion. But if I *very gently and steadily* move the support, the pendulum will continue to swing in a nice,

smooth way, in the same plane (or one parallel to it) with the same amplitude. This *gradual change in the external conditions* characterises an adiabatic process.

The emphasis on the gradual change is mathematically precised in terms of frequencies. If T_i is the "internal" period representing the motion of the system in motion, and T_e the "external" time "over which the parameters of the system change appreciably" then an adiabatic process is characterised by the following relationship between the two frequencies : $T_e \gg T_i$.

Effect on dynamics Let's call the slow motion due to internal ion period macromotion, and the fast motion due to external perturbation micromotion. From the point of view of the ion motion, the definition of adiabatic approximation is equivalent to say that the macromotion is oscillating very slowly compared to the micromotion. Adiabatic approximation is valid as long as the micromotion is negligible compared to the macromotion, during a macromotion period. This can be written as

$$\overline{\frac{d^2}{dt^2}\mathbf{R_0}} = \frac{d^2}{dt^2}\mathbf{R_0} \tag{C.18}$$

with $\overline{\frac{d^2}{dt^2}\mathbf{R_0}}$ the time average over a micromotion period. It translates into the following set of mathematical constrains

$$\left|\frac{d^2}{dt^2}\mu_u\right| \ll \left|\frac{d^2}{dt^2}R_{0\,u}\right| \tag{C.19a}$$

$$|a_u R_{0\,u}| \ll \left|\frac{d^2}{dt^2}\mu_u\right| \tag{C.19b}$$

Other formulations *In terms of stability parameters*, the adiabatic approximation is considered valid for $q_u \ll 0.4$, $a_u \ll q_u$ and $\beta_u^2 \ll 1$. *In terms of ion dynamics*, this can be translated into the following set of relationships

$$\left\|\frac{d}{dt}\mathbf{E}(\mathbf{r}(\mathbf{t}))\right\| \ll \|\mathbf{E}(\mathbf{r}(\mathbf{t}))\|\,\frac{1}{T_{Omega}}\text{ , with } T_{Omega} = \frac{2\pi}{\Omega} \tag{C.20a}$$

$$\left\|\frac{d}{dt}\mathbf{E}(\mathbf{r}(\mathbf{t}))\right\| \ll \left\|\frac{d}{dt}\mathbf{R_0}(\mathbf{t})\right\| \tag{C.20b}$$

$$\left\|\frac{d}{dt}\mathbf{E}(\mathbf{r}(\mathbf{t}))\right\| \ll \left\|\frac{d^2}{dt^2}\mathbf{R_0}(\mathbf{t})\right\| \tag{C.20c}$$

Appendix D

Thermodynamics for phase transition

In thermodynamics, the absolute total internal energy of a gas confined in a harmonic potential with force $F \propto Kq_e r_i$ is

$$U(T,P,V) \stackrel{\text{def}}{=} \frac{1}{NkT}\sum_i \frac{1}{2}Kq_e r_i^2 + \sum_{i\neq j}\frac{q_e^2}{r_{ij}} - U_0 \tag{D.1}$$

is defined up to a constant U_0, but its variation can be related to the net flow of energy entering and leaving the gas. Thus it is possible to write infinitesimal quantities as

$$\mathrm{d}U = \mathrm{d}Q + \mathrm{d}W \tag{D.2}$$

$$= \mathrm{d}Q - P\mathrm{d}V. \tag{D.3}$$

Furthermore, at constant volume during the introduction of heat amount $\mathrm{d}Q$ generating a temperature variation $\mathrm{d}T$

$$\frac{\mathrm{d}U}{\mathrm{d}T} = \frac{\mathrm{d}Q}{\mathrm{d}T}. \tag{D.4}$$

By the definition of specific heat, $C \stackrel{\text{def}}{=} \mathrm{d}Q/\mathrm{d}T$, it is possible to write

$$\boxed{\frac{\mathrm{d}U}{\mathrm{d}T} = C.} \tag{D.5}$$

Latent heat L_m corresponds to the leap in total energy $U(T)$ of the gas at transition, while the specific heat $C(T)$ is proportional to the first order derivate of total energy (Fig. D.1). In the case of infinite coulombic matter, when latent heat is non-null, the temperature is constant during phase transition until enough energy is introduced into, or removed from, the cloud so the leap in total energy is achieved. The related discontinuity in total energy makes the specific heat tend to infinite value at phase transition. Nevertheless, for finite coulombic matter, the total energy leap tend to 0 as the number of atoms diminishes. For coulombic matters small enough, with less than 10 000 ions, no latent heat can be identified but there is a doubling of the specific heat at transition. Below 1000 ions the specific heat is modified up to 10% at phase transition, and there is no leap in potential energy.

Thus the temperature can vary continuously during phase transition.

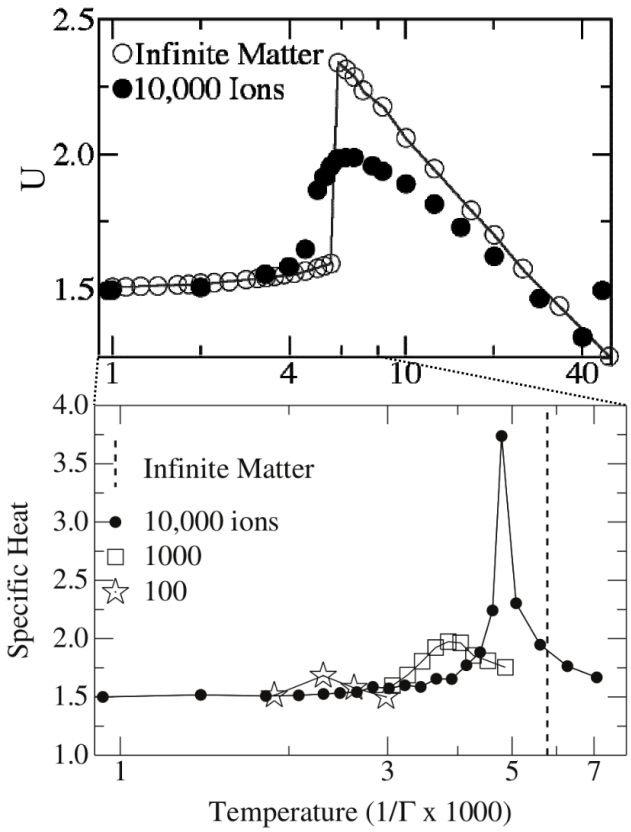

FIGURE D.1: (Top) Total energy of a Coulomb matter shown for two quantities. (Bottom) Related specific heat. Adapted from Schiffer [Sch02a].

Bibliography

[A K20] A. Kramida et al. NIST Atomic Spectra Database (ver. 5.8), [Online]. Available: [2021, September 21]. National Institute of Standards and Technology, Gaithersburg, MD. 2020 (return page 73).

[And15] Hans Harhoff Andersen. "Cooling and manipulating ions in traps with integrated optical cavities". Aug. 2015 (return page xxv).

[Ant20] Rodolphe Antoine. "Weighing synthetic polymers of ultra-high molar mass and polymeric nanomaterials: What can we learn from charge detection mass spectrometry?" *Rapid Communications in Mass Spectrometry* 34.S2 2020. e8539 RCM-19-0158.R2, e8539. DOI: https://doi.org/10.1002/rcm.8539 (return page 11).

[Arm08] S. Armenta, S. Garrigues, and M. de la Guardia. "Green Analytical Chemistry". *TrAC Trends in Analytical Chemistry* 27.6 2008, pp. 497–511. DOI: https://doi.org/10.1016/j.trac.2008.05.003 (return pages xxiii, 8).

[Ast19] F.W. Aston. "A positive ray spectrograph". *The London, Edinburgh, and Dublin Philosophical Magazine and Journal of Science* 38.228 1919, pp. 707–714. DOI: 10.1080/14786441208636004 (return page 10).

[Bal19] Nicolai Zederkopff Ballin and Kristian Holst Laursen. "To target or not to target? Definitions and nomenclature for targeted versus non-targeted analytical food authentication". *Trends in Food Science & Technology* 86 2019, pp. 537–543. DOI: https://doi.org/10.1016/j.tifs.2018.09.025 (return page 8).

[Bas19] Aarti Bashyal et al. "Top-Down Analysis of Proteins in Low Charge States". *Journal of the American Society for Mass Spectrometry* 30.4 2019, pp. 704–717. DOI: 10.1007/s13361-019-02146-1 (return page 10).

[Ber98] D. J. Berkeland et al. "Minimization of ion micromotion in a Paul trap". *Journal of Applied Physics* 83.10 1998, pp. 5025–5033. DOI: 10.1063/1.367318 (return pages 33, 54, 81).

[Ber18] Laurent Bernier et al. "Gas Flow and Ion Transfer in Heated ESI Capillary Interfaces". *Journal of the American Society for Mass Spectrometry* 29.4 2018. PMID: 29468502, pp. 761–773. DOI: 10.1007/s13361-018-1895-0 (return pages 96, 97).

[Ber06] Anders Bertelsen, Solvejg Jørgensen, and Michael Drewsen. "The rotational temperature of polar molecular ions in Coulomb crystals". *Journal of Physics B: Atomic, Molecular and Optical Physics* 39.5 Feb. 2006, pp. L83–L89. DOI: 10.1088/0953-4075/39/5/l02 (return pages xxi, 4).

[BIP19] Bureau International des Poids et Mesures BIPM. *The International System of Units (SI)*. 2019 (return page 7).

[Bla08] Rainer Blatt and David Wineland. "Entangled states of trapped atomic ions". *Nature* 453 2008, pp. 1008–1015. DOI: 10.1038/nature07125 (return pages 18, 19).

[Blo62] N. Bloembergen and P. S. Pershan. "Light Waves at the Boundary of Nonlinear Media". *Phys. Rev.* 128 2 Oct. 1962, pp. 606–622. DOI: 10.1103/PhysRev.128.606 (return page 19).

[Blü89] R. Blümel et al. “Chaos and order of laser-cooled ions in a Paul trap”. *Phys. Rev. A* 40 2 July 1989, pp. 808–823. DOI: 10.1103/PhysRevA.40.808 (return pages 17, 49, 52, 173).

[Bow99] P. Bowe et al. “Sympathetic Crystallization of Trapped Ions”. *Phys. Rev. Lett.* 82 10 Mar. 1999, pp. 2071–2074. DOI: 10.1103/PhysRevLett.82.2071 (return page 16).

[Boy68] G. D. Boyd and D. A. Kleinman. “Parametric Interaction of Focused Gaussian Light Beams”. *Journal of Applied Physics* 39.8 1968, pp. 3597–3639. DOI: 10.1063/1.1656831 (return page 69).

[Bre90] R. G. Brewer et al. “Collision-induced two-ion chaos”. *Nature* 344 90, pp. 305–309. DOI: https://doi.org/10.1038/344305a0 (return pages 17, 81).

[Bro50] Louis de Broglie. *Optique électronique et corpusculaire / M. Louis de Broglie*. French. Paris: Hermann & Cie, 1950 (return page 109).

[Bru66] S. G. Brush, H. L. Sahlin, and E. Teller. “Monte Carlo Study of a One-Component Plasma. I”. *The Journal of Chemical Physics* 45.6 1966, pp. 2102–2118. DOI: 10.1063/1.1727895 (return page 57).

[Bur16] Eric A. Burt et al. “JPL Ultrastable Trapped Ion Atomic Frequency Standards”. *IEEE Transactions on Ultrasonics, Ferroelectrics, and Frequency Control* 63.7 2016, pp. 1013–1021. DOI: 10.1109/TUFFC.2016.2572701 (return page 16).

[Bus06] M. Bussmann et al. “Stopping highly charged ions in a laser-cooled one component plasma of Mg24+ ions”. *International Journal of Mass Spectrometry* 251.2 2006. ULTRA-ACCURATE MASS SPECTROMETRY AND RELATED TOPICS Dedicated to H.-J. Kluge on the occasion of his 65th birthday anniversary, pp. 179–189. DOI: https://doi.org/10.1016/j.ijms.2006.01.042 (return pages xxii, 4, 18).

[Byk19] Dmitry S. Bykov et al. “Direct loading of nanoparticles under high vacuum into a Paul trap for levitodynamical experiments”. *Applied Physics Letters* 115.3 2019, p. 034101. DOI: 10.1063/1.5109645 (return pages xxxi, 179).

[Cam80] J.E. Campana. “Elementary theory of the quadrupole mass filter”. *International Journal of Mass Spectrometry and Ion Physics* 33.2 1980, pp. 101–117. DOI: https://doi.org/10.1016/0020-7381(80)80042-8 (return pages 21, 213).

[Cam84] R. Campargue. “Progress in overexpanded supersonic jets and skimmed molecular beams in free-jet zones of silence”. *The Journal of Physical Chemistry* 88.20 1984, pp. 4466–4474. DOI: 10.1021/j150664a004 (return pages xxvi, 92, 99).

[Cam56] R Campbell. *Théorie générale de l’équation de Mathieu et de quelques autres équations différentielles de la mécanique*. fr. Ed. by Springer. 1956 (return page 17).

[Cap12] Michael Capron. “Étude de l’interaction entre ions multichargés et systèmes complexes d’intérêt biologique : effets de l’environnement à l’échelle moléculaire”. Université de Caen, 2012 (return pages xxi, 4).

[Cas88] R. Casdorff and R. Blatt. “Ordered structures and statistical properties of ion clouds stored in a Paul trap”. *Applied Physics B* 45 1988, pp. 175–182. DOI: 10.1007/BF00695288 (return page 137).

[Cas67] R.A. Cassanova and W.B. Stephenson. “Expansion of a jet into a vacuum”. *Symposium (International) on Combustion* 11.1 1967, pp. 577–587. DOI: https://doi.org/10.1016/S0082-0784(67)80183-8 (return page 101).

[Cha07] C. Champenois et al. “Terahertz frequency standard based on three-photon coherent population trapping”. *Phys. Rev. Lett.* 99 2007, p. 013001 (return pages 18, 19).

[Cha14] C. Champenois et al. “Non-destructive detection method of charged particles without mass limitation”. EP14306498. Priority : 26 Sep. 2014 (return pages xxii, 4).

[Cha08] Caroline Champenois. “Trapping and cooling of ions”. Du 6 au 10 octobre à l’ecole de Physique des Houches, école prédocotorale sur les atomes froids et la condensation de Bose-Einstein, Oct. 2008 (return page 59).

[Chu88] C. Chuangtian et al. *LiB3O5 crystal and its nonlinear optical devices.* Tech. rep. Chinese patent, 1988 (return page 19).

[Cir95] J. I. Cirac and P. Zoller. “Quantum Computations with Cold Trapped Ions”. *Phys. Rev. Lett.* 74 20 May 1995, pp. 4091–4094. DOI: 10.1103/PhysRevLett.74.4091 (return page 18).

[Coh98] Claude N. Cohen-Tannoudji. “Nobel Lecture: Manipulating atoms with photons”. *Rev. Mod. Phys.* 70 3 July 1998, pp. 707–719. DOI: 10.1103/RevModPhys.70.707 (return page 59).

[Col19a] Mathieu Collombon. “Résonance noire à trois photons sur un nuage d’ions calcium confinés”. Thèse. Aix-Marseille Université (AMU) ; Laboratoire PIIM, Feb. 2019 (return page 79).

[Col19b] Mathieu Collombon et al. “Phase transfer between three visible lasers for coherent population trapping”. *Optics Letters* 44.4 Feb. 2019, pp. 859–862. DOI: 10.1364/OL.44.000859 (return page 19).

[DEl89] Christopher F. D’Elia, James G. Sanders, and Douglas G. Capone. “Analytical chemistry for environmental sciences. A question of confidence”. *Environmental Science & Technology* 23.7 1989, pp. 768–774. DOI: 10.1021/es00065a005 (return pages xxiii, 8).

[Dan16] Georgios P. Danezis et al. “Food authentication: Techniques, trends and emerging approaches”. *TrAC Trends in Analytical Chemistry* 85 2016. On-site and In-vivo Instrumentation and Applications, pp. 123–132. DOI: https://doi.org/10.1016/j.trac.2016.02.026 (return pages xxiii, 8–11).

[Daw70] G. A. Dawson. “The Rayleigh instability of water drops in the presence of externalelectric fields”. 75.3 1970, pp. 701–705. DOI: https://doi.org/10.1029/JC075i003p00701 (return page 91).

[Daw76] Peter H Dawson. *Quadrupole mass spectrometry and its applications*. eng. Ed. by Springer. 1976. DOI: https://doi.org/10.1016/C2013-0-04436-2 (return page 33).

[Deh67] H.G. Dehmelt. “Radiofrequency spectroscopy of stored ions I: storage”. *Advances in Atomic and Molecular Physics* 3 1967, pp. 53–72. DOI: https://doi.org/10.1016/S0065-2199(08)60170-0 (return pages 15, 17, 18).

[Dem18] A. J. Dempster. “A new Method of Positive Ray Analysis”. *Phys. Rev.* 11 4 Apr. 1918, pp. 316–325. DOI: 10.1103/PhysRev.11.316 (return page 10).

[Die87] F. Diedrich et al. “Observation of a Phase Transition of Stored Laser-Cooled Ions”. *Phys. Rev. Lett.* 59 26 Dec. 1987, pp. 2931–2934. DOI: 10.1103/PhysRevLett.59.2931 (return page 78).

[Dol68] Malcolm Dole et al. “Molecular Beams of Macroions”. *The Journal of Chemical Physics* 49.5 1968, pp. 2240–2249. DOI: 10.1063/1.1670391 (return pages 91, 98, 100, 101).

[Dou11] T.J. Dougherty and M.J. Pucci. *Antibiotic Discovery and Development*. SpringerLink : Bücher. Springer US, 2011 (return page 6).

[Dou05] Donald J. Douglas, Aaron J. Frank, and Dunmin Mao. "Linear ion traps in mass spectrometry". *Mass Spectrometry Reviews* 24.1 2005, pp. 1–29. DOI: https://doi.org/10.1002/mas.20004 (return page 23).

[Dru13] Olaf H. Drummer and Dimitri Gerostamoulos. "Forensic drug analysis". In: *Forensic Drug Analysis*. Ed. by Olaf H Drummer and Dimitri Gerostamoulos. United Kingdom: Future Science, LTD, Oct. 2013, pp. 2–9. DOI: 10.4155/ebo.13.48 (return pages xxiii, 8).

[Dub96a] Daniel H. E. Dubin. "Effect of correlations on the thermal equilibrium and normal modes of a non-neutral plasma". *Phys. Rev. E* 53 5 May 1996, pp. 5268–5290. DOI: 10.1103/PhysRevE.53.5268 (return page 57).

[Dub96b] Daniel H. E. Dubin and J. P. Schiffer. "Normal modes of cold confined one-component plasmas". *Phys. Rev. E* 53 5 May 1996, pp. 5249–5267. DOI: 10.1103/PhysRevE.53.5249 (return page 57).

[Eat07] William A. Eaton et al. "Evolution of allosteric models for hemoglobin". *IUBMB Life* 59.8-9 2007, pp. 586–599. DOI: https://doi.org/10.1080/15216540701272380 (return page 6).

[Esc03a] J. Eschner. "Sub-wavelength resolution of optical fields probed by single trapped ions: Interference, phase modulation, and which-way information". *Eur. Phys. J. D* 22 2003, pp. 341–345. DOI: http://dx.doi.org/10.1140/epjd/e2002-00235-7 (return page 59).

[Esc03b] Jürgen Eschner et al. "Laser cooling of trapped ions". *J. Opt. Soc. Am. B* 20.5 May 2003, pp. 1003–1015. DOI: 10.1364/JOSAB.20.001003 (return page 18).

[Far93] R. T. Farouki and S. Hamaguchi. "Thermal energy of the crystalline one-component plasma from dynamical simulations". *Phys. Rev. E* 47 6 June 1993, pp. 4330–4336. DOI: 10.1103/PhysRevE.47.4330 (return page 57).

[Fen89] JB Fenn et al. "Electrospray ionization for mass spectrometry of large biomolecules". *Science* 246.4926 1989, pp. 64–71. DOI: 10.1126/science.2675315 (return pages xxvi, 11, 85).

[Fen90] John B. Fenn et al. "Electrospray ionization–principles and practice". *Mass Spectrometry Reviews* 9.1 1990, pp. 37–70. DOI: https://doi.org/10.1002/mas.1280090103 (return pages 11, 85, 89).

[Fil21] Igor Filippov and Mikhail Sudakov. "Analysis of electric fields in mass spectrometry". *International Journal of Mass Spectrometry* 467 2021, p. 116620. DOI: https://doi.org/10.1016/j.ijms.2021.116620 (return page 23).

[Foo05a] C. J. Foot. "Atomic physics". In: Oxford University Press, 2005. Chap. VIII.1 - Doppler-free laser spectroscopy (return page 59).

[Foo05b] C. J. Foot. "Atomic physics". In: Oxford University Press, 2005. Chap. IX - Laser cooling and trapping (return page 59).

[Fra61] P. A. Franken et al. "Generation of Optical Harmonics". *Phys. Rev. Lett.* 7 4 Aug. 1961, pp. 118–119. DOI: 10.1103/PhysRevLett.7.118 (return page 19).

[Geb15] Florian Gebert et al. "Precision Isotope Shift Measurements in Calcium Ions Using Quantum Logic Detection Schemes". *Phys. Rev. Lett.* 115 5 July 2015, p. 053003. DOI: 10.1103/PhysRevLett.115.053003 (return page 36).

[Ger92] D. Gerlich. “Inhomogeneous rf fields: a versatile tool for the study of processes with slow ions”. *Advances in Chemical Physics Series* 82 1992. Ed. by Cheuk-Yiu Ng and Michael Baer, pp. 1–176. DOI: https://doi.org/10.1002/9780470141397.ch1 (return pages 16, 17).

[Gie21] Jan Gieseler et al. “Optical tweezers — from calibration to applications: a tutorial”. *Adv. Opt. Photon.* 13.1 Mar. 2021, pp. 74–241. DOI: 10.1364/AOP.394888 (return pages xxxi, 179).

[Gim14] Natalia Gimelshein et al. “Numerical Modeling of Ion Transport in an ESI-MS System”. *Journal of the American Society for Mass Spectrometry* 25 2014, pp. 820–831. DOI: 10.1007/s13361-014-0838-7 (return pages 95–97, 101, 213).

[Gli03] G. Glish and R. Vachet. “The basics of mass spectrometry in the twenty-first century”. *Nat. Rev. Drug. Discov.* 2 2003, pp. 140–150 (return pages xxiii, 9).

[Gor54] J. P. Gordon, H. J. Zeiger, and C. H. Townes. “Molecular Microwave Oscillator and New Hyperfine Structure in the Microwave Spectrum of NH_3”. *Phys. Rev.* 95 1 July 1954, pp. 282–284. DOI: 10.1103/PhysRev.95.282 (return page 19).

[Grä69] G Gräff, E Klempt, and G Werth. “Method for measuring the anomalous magnetic moment of free electrons”. *Z. Physik* 222 1969, pp. 201–207. DOI: https://doi.org/10.1007/BF01392119 (return page 15).

[Gri18] J. David Griffiths. “Introduction to quantum mechanics”. In: Cambridge University Press, 2018. Chap. X - The adiabatic approximation. DOI: 10.1017/9781316995433 (return pages 28, 193).

[Gun82] W.F. van Gunsteren and H.J.C. Berendsen. “Algorithms for brownian dynamics”. *Molecular Physics* 45.3 1982, pp. 637–647. DOI: 10.1080/00268978200100491 (return page 142).

[Hab85] H. Haberland, U. Buck, and M. Tolle. “Velocity distribution of supersonic nozzle beams”. *Review of Scientific Instruments* 56.9 1985, pp. 1712–1716. DOI: 10.1063/1.1138129 (return pages 100, 102).

[Hal98] S Halas and T Durakiewicz. “Temperature distribution along a metal filament heated in vacuum by DC current”. *Vacuum* 49.4 1998, pp. 331–336. DOI: https://doi.org/10.1016/S0042-207X(97)00170-X (return pages 74, 75).

[Hän80] T.W. Hänsch and B. Couillaud. “Laser frequency stabilization by polarization spectroscopy of a reflecting reference cavity”. *Optics communications* 1980. DOI: https://doi.org/10.1016/0030-4018(80)90069-3 (return pages 69, 213).

[Hän75] T.W. Hänsch and A.L. Schawlow. “Cooling of gases by laser radiation”. *Optics Communications* 13.1 1975, pp. 68–69. DOI: https://doi.org/10.1016/0030-4018(75)90159-5 (return page 18).

[Har10] M. M. Harb et al. “Transfer-matrix-based method for an analytical description of velocity-map-imaging spectrometers”. *Review of Scientific Instruments* 81.12 2010, p. 125111. DOI: 10.1063/1.3505799 (return pages 108, 110, 112).

[Har77] R. L. Hartman, N. E. Schumaker, and R. W. Dixon. “Continuously operated (Al,Ga)As double-heterostructure lasers with 70 °C lifetimes as long as two years”. *Applied Physics Letters* 31.11 1977, pp. 756–759. DOI: 10.1063/1.89537 (return page 19).

[Hay20] A.C. Hayes and E. Gooden M.E. ans Henry. “Plasma stopping-power measurements reveal transition from non-degenerate to degenerate plasmas”. *Nat. Phys.* 16 2020, pp. 432–437. DOI: 10.1038/s41567-020-0790-3 (return page 163).

[Hec10] Jeff Hecht. “A short history of laser development”. *Appl. Opt.* 49.25 Sept. 2010, F99–F122. DOI: 10.1364/AO.49.000F99 (return page 18).

[Her49] Conyers Herring and M. H. Nichols. “Thermionic Emission”. *Rev. Mod. Phys.* 21 2 Apr. 1949, pp. 185–270. DOI: 10.1103/RevModPhys.21.185 (return page 75).

[Het15] M. Hettrich et al. “Measurement of Dipole Matrix Elements with a Single Trapped Ion”. *Phys. Rev. Lett.* 115 14 Oct. 2015, p. 143003. DOI: 10.1103/PhysRevLett.115.143003 (return pages 35, 36).

[Hil16] Laurent Hilico. “NON-LASER COOLING TECHNIQUES”. In: *Trapped Charged Particles : A Graduate Textbook with Problems and Solutions*. Ed. by Martina Knoop, Niels Madsen, and R. C. Thompson. WORLD SCIENTIFIC (EUROPE), 2016. Chap. CHAPTER SEVEN, pp. 147–159. DOI: 10.1142/9781786340139_0007 (return page 17).

[Hil14] Laurent Hilico et al. “Preparing single ultra-cold antihydrogen atoms for free-fall in GBAR”. *International Journal of Modern Physics: Conference Series* 30 2014, p. 1460269. DOI: 10.1142/S2010194514602695 (return pages xxii, 4, 180).

[Hil98] G. C. Hilton et al. “Impact energy measurement in time-of-flight mass spectrometry with cryogenic microcalorimeters”. *Nature* 391 1998 (return page 10).

[Hin06] F Hinterberger. “Ion optics with electrostatic lenses” 2006. DOI: 10.5170/CERN-2006-012.27 (return page 107).

[Hof05] E Hoffmann and V Stroobant. *Spectrométrie de masse*. fr. Ed. by Dunod. 2005. DOI: https://www.dunod.com/sciences-techniques/spectrometrie-masse-cours-et-exercices-corriges (return pages 10, 15).

[Höl79] J. Hölzl and F. K. Schulte. “Work function of metals”. In: *Solid Surface Physics*. Ed. by Josef Hölzl, Franz K. Schulte, and Heribert Wagner. Berlin, Heidelberg: Springer Berlin Heidelberg, 1979, pp. 1–150. DOI: 10.1007/BFb0048919 (return page 72).

[Hor02] L. Hornekær and M. Drewsen. “Formation process of large ion Coulomb crystals in linear Paul traps”. *Phys. Rev. A* 66 1 July 2002, p. 013412. DOI: 10.1103/PhysRevA.66.013412 (return pages 55, 78).

[Hsi77] J. J. Hsieh and C. C. Shen. “Room-temperature cw operation of buried-stripe double-heterostructure GaInAsP/InP diode lasers”. *Applied Physics Letters* 30.8 1977, pp. 429–431. DOI: 10.1063/1.89411 (return page 19).

[Hus18] Audric Husson. “Deceleration of antiprotons from CERN’s ELENA synchrotron and transport of antimatter beams throughthe GBAR experiment”. Thèse. Universite Paris Saclay, Dec. 2018 (return page 180).

[Iri76] J. V. Iribarne and B. A. Thomson. “On the evaporation of small ions from charged droplets”. *The Journal of Chemical Physics* 64.6 1976, pp. 2287–2294. DOI: 10.1063/1.432536 (return page 91).

[IUP97a] Compiled by A. D. McNaught IUPAC and A. Wilkinson. “Compendium of Chemical Terminology, 2nd ed. (the "Gold Book")” 1997. DOI: https://doi.org/10.1351/goldbook.M04002 (return page 5).

[IUP97b] Compiled by A. D. McNaught IUPAC and A. Wilkinson. “Compendium of Chemical Terminology, 2nd ed. (the "Gold Book")” 1997. DOI: https://doi.org/10.1351/goldbook.A00139 (return page 98).

[Joo86] G. Joos and I.M. Freeman. *Theoretical Physics*. Dover Books on Physics. Dover Publications, 1986 (return page 7).

[Kal21] D Kalincev et al. “Motional heating of spatially extended ion crystals”. *Quantum Science and Technology* 6.3 May 2021, p. 034003. DOI: 10.1088/2058-9565/abee99 (return page 81).

[Kam17] M. R. Kamsap et al. “Experimental demonstration of an efficient number diagnostic for long ion chains”. *Phys. Rev. A* 95 1 Jan. 2017, p. 013413. DOI: 10.1103/PhysRevA.95.013413 (return pages 16, 54).

[Kam15] Marius Romuald Kamsap. “Horloge micro-onde à ions : analyse et transport d’un nuage d’ions dans un piège à plusieurs zones”. Thèse. Aix-Marseille Université (AMU), Dec. 2015 (return pages 16, 45, 54, 56).

[Kar89] Michael Karas et al. “Laser Desorption/Ionization Mass Spectrometry of Proteins of Mass 100 000 to 250 000 Dalton”. *Angewandte Chemie International Edition in English* 28.6 1989, pp. 760–761. DOI: https://doi.org/10.1002/anie.198907601 (return page 11).

[Kar13] Pavel Karban et al. “Numerical solution of coupled problems using code Agros2D”. *Computing* 95 2013, pp. 381–408. DOI: 10.1007/s00607-013-0294-4 (return pages 108, 113–115).

[El-70] A.B. El-Kareh and J.C.J. El-Kareh. “VI - The Electrostatic Unipotential Lens”. In: *Electron Beams, Lenses, and Optics*. Ed. by A.B. El-Kareh and J.C.J. El-Kareh. Academic Press, 1970, pp. 185–245. DOI: https://doi.org/10.1016/B978-0-12-238001-3.50010-3 (return page 108).

[Kas50] A. Kastler. “Quelques suggestions concernant la production optique et la détection optique d’une inégalité de population des niveaux de quantification spatiale des atomes. Application à l’expérience de Stern et Gerlach et à la résonance magnétique”. *Journal De Physique Et Le Radium* 11 1950, pp. 255–265. DOI: 10.1051/jphysrad:01950001106025500 (return page 18).

[Kei17] David Z. Keifer and Martin F. Jarrold. “Single-molecule mass spectrometry”. *Mass Spectrometry Reviews* 36.6 2017, pp. 715–733. DOI: https://doi.org/10.1002/mas.21495 (return pages xxiii, 10–12).

[Kel01] A. Kellerbauer et al. “Buffer gas cooling of ion beams”. *Nuclear Instruments and Methods in Physics Research Section A: Accelerators, Spectrometers, Detectors and Associated Equipment* 469.2 2001, pp. 276–285. DOI: https://doi.org/10.1016/S0168-9002(01)00286-8 (return pages 17, 18).

[Kno04] M. Knoop et al. “Metastable level lifetimes from electron-shelving measurements with ion clouds and single ions”. *The European Physical Journal D - Atomic, Molecular and Optical Physics* 29.2 May 2004, pp. 163–171. DOI: 10.1140/epjd/e2004-00022-6 (return page 19).

[Kno16] Martina Knoop. “RADIOFREQUENCY TRAPS”. In: *Trapped Charged Particles : A Graduate Textbook with Problems and Solutions*. Ed. by Martina Knoop, Niels Madsen, and R. C. Thompson. WORLD SCIENTIFIC (EUROPE), 2016. Chap. II, pp. 35–53. DOI: 10.1142/9781786340139_0002 (return pages xxiv, xxv, 25, 187, 188).

[Kon19] Panagiotis Kondylis et al. “Analytical Techniques to Characterize the Structure, Properties, and Assembly of Virus Capsids”. *Analytical Chemistry* 91.1 2019, pp. 622–636. DOI: 10.1021/acs.analchem.8b04824 (return pages xxiii, 8–10).

[Kon06] Nikolai Konenkov et al. “Linear Quadrupoles with Added Hexapole Fields”. *Journal of the American Society for Mass Spectrometry* 17.8 2006, pp. 1063–1073. DOI: https://doi.org/10.1016/j.jasms.2006.03.013 (return page 23).

[Kre05] A. Kreuter et al. “Experimental and theoretical study of the $3d\ ^2D$–level lifetimes of $^{40}Ca^+$”. *Phys. Rev. A* 71 3 Mar. 2005, p. 032504. DOI: 10.1103/PhysRevA.71.032504 (return page 35).

[Let77] V. S. Letokhov, V. G. Minogin, and B. D. Pavlik. “Cooling and capture of atoms and molecules by a resonant light field”. *Soviet Physics JETP* 45 1977. DOI: 10.1103/physreva.90.063407 (return page 64).

[Li75] Jun Li et al. “Effect of Chemical Additive on Fixed Abrasive Polishing of LBO Crystal with Non-water Based Slurry”. *Int. J. of Chemical, Nuclear, Materials and Metallurgical Engin.* 20 1975. DOI: 10.3969/j.issn.1001-9731.2016.02.011 (return page 69).

[Lie08] H. Liebl. *Applied charged particle optics.* Ed. by Springer. Springer, 2008. DOI: https://doi.org/10.1007/978-3-540-71925-0 (return pages 108, 110–112).

[Lip04] Christopher A. Lipinski. “Lead- and drug-like compounds: the rule-of-five revolution”. *Drug Discovery Today: Technologies* 1.4 2004, pp. 337–341. DOI: https://doi.org/10.1016/j.ddtec.2004.11.007 (return page 6).

[Liv04] R.G. Livesey. “Solution methods for gas flow in ducts through the whole pressure regime”. *Vacuum* 76.1 2004, pp. 101–107. DOI: https://doi.org/10.1016/j.vacuum.2004.05.015 (return pages 95, 96).

[Mai61] T. H. Maiman et al. “Stimulated Optical Emission in Fluorescent Solids. II. Spectroscopy and Stimulated Emission in Ruby”. *Phys. Rev.* 123 4 Aug. 1961, pp. 1151–1157. DOI: 10.1103/PhysRev.123.1151 (return page 19).

[Maj05] F. G. Major, V. N. Gheorghe, and G Werth. “The Paul trap”. In: *Charged Particle Traps : Physics and Techniques of Charged Particle Field Confinement*. Ed. by F. G. Major, V. N. Gheorghe, and G Werth. Springer, Berlin, Heidelberg, 2005. Chap. 2, pp. 17–49. DOI: https://doi.org/10.1007/b137836 (return pages 25, 187, 188).

[Mar95] R. E. March and F. A. Londry. “Theory of quadrupole mass spectrometry”. In: *Practical aspects of ion trap mass spectrometry*. Ed. by R. E. March and J. F. Todd. Vol. 1. CRC Press, 1995. Chap. 2, pp. 25–48. DOI: https://doi.org/10.1002/(SICI)1096-9888(199704)32:4<351::AID-JMS512>3.0.CO;2-Y (return page 17).

[Mar10] M. Marciante et al. “Ion dynamics in a linear radio-frequency trap with a single cooling laser”. *Phys. Rev. A* 82 3 Sept. 2010, p. 033406. DOI: 10.1103/PhysRevA.82.033406 (return pages 137, 147).

[Mar11] Mathieu Marciante. “Dynamique d’ions en pièges radio-fréquences”. Thèse. Université de Provence - Aix-Marseille I, June 2011 (return page 147).

[Mar21] C. Markert et al. “Observation of charged droplets from electrospray ionization (ESI) plumes in API mass spectrometers”. *Anal. Bioanal. Chem.* 413 2021, pp. 5587–5600. DOI: 10.1007/s00216-021-03452-y (return page 97).

[McL47] Norman William McLachlan. *Theory and application of mathieu functions*. Ed. by Owford. 1947 (return pages xxv, 17, 24, 25, 187–189).

[Mee12] Sebastiaan Y. T. van de Meerakker et al. “Manipulation and Control of Molecular Beams”. *Chem. Rev.* 112 2012, pp. 4828–4878. DOI: https://doi.org/10.1021/cr200349r (return page 180).

[Meh14] K. K. Mehta et al. “Ion traps fabricated in a CMOS foundry”. *Applied Physics Letters* 105.4 2014, p. 044103. DOI: 10.1063/1.4892061 (return page 17).

[Mik14] M Mikulewicz, K Chojnacka, and M Szynkowska. “How Toxicology Impacts Other Sciences”. In: *Encyclopedia of Toxicology 3rd Edition*. Ed. by Philip Wexler. 2014. DOI: https://doi.org/10.1016/B978-0-12-386454-3.00456-5 (return pages xxiii, 8).

[Mon65] Jacques Monod, Jeffries Wyman, and Jean-Pierre Changeux. “On the nature of allosteric transitions: A plausible model”. *Journal of Molecular Biology* 12.1 1965, pp. 88–118. DOI: https://doi.org/10.1016/S0022-2836(65)80285-6 (return page 6).

[Mor04] Giovanna Morigi and Shmuel Fishman. “Dynamics of an ion chain in a harmonic potential”. *Phys. Rev. E* 70 6 Dec. 2004, p. 066141. DOI: 10.1103/PhysRevE.70.066141 (return page 16).

[Mor06] A. Mortensen et al. “Observation of Three-Dimensional Long-Range Order in Small Ion Coulomb Crystals in an rf Trap”. *Phys. Rev. Lett.* 96 10 Mar. 2006, p. 103001. DOI: 10.1103/PhysRevLett.96.103001 (return page 57).

[Mor07] Anders Mortensen et al. “Radio frequency field-induced persistent long-range ordered structures in two-species ion Coulomb crystals”. *J. Phys. B: At. Mol. Opt. Phys.* 40 2007, F223–F229. DOI: 10.1088/0953-4075/40/15/f01 (return page 57).

[Mou86] P. F. Moulton. “Spectroscopic and laser characteristics of Ti:Al2O3”. *J. Opt. Soc. Am. B* 3.1 Jan. 1986, pp. 125–133. DOI: 10.1364/JOSAB.3.000125 (return page 19).

[Mül04] Rolf Mülhaupt. “Hermann Staudinger and the Origin of Macromolecular Chemistry”. *Angewandte Chemie International Edition* 43.9 2004, pp. 1054–1063. DOI: https://doi.org/10.1002/anie.200330070 (return page 5).

[Nak00] Shuji Nakamura, G Fasol, and S.J. Pearton. *The blue laser diode: the complete story*. eng. Ed. by Springer. 2000. DOI: 10.1007/978-3-662-04156-7 (return page 19).

[Nak97] Shuji Nakamura et al. “Room-temperature continuous-wave operation of InGaN multi-quantum-well structure laser diodes with a lifetime of 27 hours”. *Applied Physics Letters* 70.11 1997, pp. 1417–1419. DOI: 10.1063/1.118593 (return page 19).

[Nam14] Y. S. Nam, E. B. Jones, and R. Blümel. “Analytical mean-field scaling theory of radio-frequency heating in a Paul trap”. *Phys. Rev. A* 90 1 July 2014, p. 013402. DOI: 10.1103/PhysRevA.90.013402 (return pages xxii, xxv, xxxi, 4, 17, 52, 54, 171, 173, 180, 213).

[Neu78] W. Neuhauser et al. “Optical-Sideband Cooling of Visible Atom Cloud Confined in Parabolic Well”. *Phys. Rev. Lett.* 41 4 July 1978, pp. 233–236. DOI: 10.1103/PhysRevLett.41.233 (return page 18).

[Neu80] W. Neuhauser et al. “Localized visible Ba^+ mono-ion oscillator”. *Phys. Rev. A* 22 3 Sept. 1980, pp. 1137–1140. DOI: 10.1103/PhysRevA.22.1137 (return page 18).

[Nie10] Michael A. Nielsen and Isaac L. Chuang. *Quantum Computation and Quantum Information: 10th Anniversary Edition*. Cambridge University Press, 2010. DOI: 10.1017/CBO9780511976667 (return page xxv).

[Not56] Wayne B. Nottigham. *Thermionic emission*. Tech. rep. Research laboratory of electronics, MIT, 1956 (return page 75).

[Off08] D. Offenberg et al. “Translational cooling and storage of protonated proteins in an ion trap at subkelvin temperatures”. *Phys. Rev. A* 78 6 Dec. 2008, p. 061401. DOI: 10.1103/PhysRevA.78.061401 (return page 18).

[Olv21] F.W.J. Olver et al. *NIST Digital Library of Mathematical Functions*. 2021 (return pages 27, 213).

[Oos13] Patrick H. Oosthuizen and William E. Carscallen. *Introduction to compressible fluid flow*. Ed. by CRC Press. 2013 (return page 100).

[Opi03] Christiane A. Opitz et al. "Damped elastic recoil of the titin spring in myofibrils of human myocardium". *Proceedings of the National Academy of Sciences* 100.22 2003, pp. 12688–12693. DOI: 10.1073/pnas.2133733100 (return page 7).

[Ott09] R Otto et al. "How can a 22-pole ion trap exhibit ten local minima in the effective potential?" *Journal of Physics B: Atomic, Molecular and Optical Physics* 42.15 July 2009, p. 154007. DOI: 10.1088/0953-4075/42/15/154007 (return page 16).

[Ott08] R. Otto et al. "Nonstandard Behavior of a Negative Ion Reaction at Very Low Temperatures". *Phys. Rev. Lett.* 101 6 Aug. 2008, p. 063201. DOI: 10.1103/PhysRevLett.101.063201 (return page 16).

[Pal09] T. N. Palmer. "Edward Norton Lorenz. 23 May 1917 – 16 April 2008". *Biographical Memoirs of Fellows of the Royal Society* 55 2009, pp. 139–155. DOI: 10.1098/rsbm.2009.0004 (return page 133).

[Pau58] W. Paul, O. Osberghaus, and E. Fischer. "Ein Ionenkäfig". *Forschungsberichte des Wirtschafts- und Verkehrsministerium Nordrhein-Westfalen, Westdeutscher Verlag Köln-Opladen* 415 1958, pp. 1–67. DOI: 10.1007/978-3-663-04689-9 (return page 15).

[Pau53] W. Paul and H. Steinwedel. "Ein neues Massenspektrometer ohne Magnetfeld". *Z. Naturforsch. A* 8 1953, p. 448 (return page 15).

[Pau48] Linus Pauling. "Nature of Forces between Large Molecules of Biological Interest". *Nature* 161.4097 May 1948, pp. 707–709. DOI: 10.1038/161707a0 (return page 6).

[Pay17] Susan Payne. "Chapter 4 - Methods to Study Viruses". In: *Viruses*. Ed. by Susan Payne. Academic Press, 2017, pp. 37–52. DOI: https://doi.org/10.1016/B978-0-12-803109-4.00004-0 (return page 9).

[Ped10] J. Pedregosa-Gutierrez et al. "Anharmonic contributions in real RF linear quadrupole traps". *International Journal of Mass Spectrometry* 293 June 2010. See also erratum at : http://www.sciencedirect.com/science/article/pii/S1387380610001004, p. 57. DOI: 10.1016/j.ijms.2009.12.009 (return pages 24, 186).

[Ped18a] J. Pedregosa-Gutierrez et al. "Correcting symmetry imperfections in linear multipole traps". *Review of Scientific Instruments* 89.12 2018, p. 123101. DOI: 10.1063/1.5075496 (return pages 16, 19).

[Ped18b] J. Pedregosa-Gutierrez et al. "Symmetry breaking in linear multipole traps". *Journal of Modern Optics* 65.5-6 2018, pp. 529–537. DOI: 10.1080/09500340.2017.1408866 (return pages 16, 19).

[Ped21] Jofre Pedregosa-Gutierrez and Jim Dempsey. "Direct N-Body problem optimisation using the AVX-512 instruction set". *ArXiv* 2021 (return pages 133, 141).

[Ped15] Jofre Pedregosa-Gutierrez et al. "Ion transport in macroscopic RF linear traps". *International Journal of Mass Spectrometry* 381-382 2015, pp. 33–40. DOI: https://doi.org/10.1016/j.ijms.2015.03.008 (return pages 19, 139, 146).

[Pen14] Wen-Ping Peng, Szu-Wei Chou, and Avinash A. Patil. "Measuring masses of large biomolecules and bioparticles using mass spectrometric techniques". *Analyst* 139 14 2014, pp. 3507–3523. DOI: 10.1039/C3AN02329J (return page 10).

[Pio19] A. Piovesan, M.C. Pelleri, and F. Antonaros. “On the length, weight and GC content of the human genome”. *BMC Res Notes* 12.106 2019. DOI: https://doi.org/10.1186/s13104-019-4137-z (return page 7).

[Poi21] A. Poindron et al. “Non-destructive detection of large molecules without mass limitation”. *The Journal of Chemical Physics* 154.18 2021, p. 184203. DOI: 10.1063/5.0046693 (return pages v, xxvii, 18, 139–141, 151).

[Poi18] Adrien Poindron. “Giant molecule detector based on laser cooled trapped $^{40}Ca^{+}$ ions”. MA thesis. Université Aix-Marseille, 2018 (return pages 38, 69).

[Pre89] J.D. Prestage, G.J. Dick, and L. Maleki. “New Ion Trap for Frequency Standard Applications”. *J. Appl. Phys.* 66 1989, p. 1013. DOI: https://doi.org/10.1063/1.343486 (return page 15).

[Pre99] J.D. Prestage, R.L. Tjoelker, and L. Maleki. “Higher pole linear traps for atomic clock applications”. In: *Proceedings of the 1999 Joint Meeting of the European Frequency and Time Forum and the IEEE International Frequency Control Symposium (Cat. No.99CH36313)*. Vol. 1. 1999, 121–124 vol.1. DOI: 10.1109/FREQ.1999.840723 (return page 16).

[Pre91] J.D. Prestage et al. “Ultra-stable Hg^{+} trapped ion frequency standard”. *Proceedings of the 45th Annual Symposium on Frequency Control 1991* 1991, pp 572–581. DOI: 10.1109/FREQ.1991.145953 (return pages 18, 19).

[Pre07] John D. Prestage and Gregory L. Weaver. “Atomic Clocks and Oscillators for Deep-Space Navigation and Radio Science”. *Proceedings of the IEEE* 95.11 2007, pp. 2235–2247. DOI: 10.1109/JPROC.2007.905130 (return page 16).

[Rah86] A. Rahman and J. P. Schiffer. “Structure of a One-Component Plasma in an External Field: A Molecular-Dynamics Study of Particle Arrangement in a Heavy-Ion Storage Ring”. *Phys. Rev. Lett.* 57 9 Sept. 1986, pp. 1133–1136. DOI: 10.1103/PhysRevLett.57.1133 (return page 137).

[Ram13] Michael Ramm et al. “Precision Measurement Method for Branching Fractions of ExcitedP1/2States Applied toCa+40”. *Physical Review Letters* 111.2 July 2013. DOI: 10.1103/physrevlett.111.023004 (return page 35).

[Rap17] Bastian E. Rapp. “Chapter 9 - Fluids”. In: *Microfluidics: Modelling, Mechanics and Mathematics*. Ed. by Bastian E. Rapp. Micro and Nano Technologies. Oxford: Elsevier, 2017, pp. 243–263. DOI: https://doi.org/10.1016/B978-1-4557-3141-1.50009-5 (return page 93).

[Ray82] John William Strutt Lord Rayleigh. “XX. On the equilibrium of liquid conducting masses charged with electricity”. *The London, Edinburgh, and Dublin Philosophical Magazine and Journal of Science* 14.87 1882, pp. 184–186. DOI: 10.1080/14786448208628425 (return page 91).

[Rei08] Martin Reiser. “Beam Optics and Focusing Systems without Space Charge: Sections 3.1 - 3.5”. In: *Theory and Design of Charged Particle Beams*. John Wiley & Sons, Ltd, 2008. Chap. 3, pp. 51–103. DOI: https://doi.org/10.1002/9783527622047.ch3a (return page 116).

[Ric19] Franscesco Ricci. “Levitodynamics toward force nano-sensors in vacuum”. Universitat Politècnica de Catalunya. Institut de Ciències Fotòniques., 2019 (return pages xxxi, 179).

[Roo99] Ch. Roos et al. “Quantum State Engineering on an Optical Transition and Decoherence in a Paul Trap”. *Phys. Rev. Lett.* 83 23 Dec. 1999, pp. 4713–4716. DOI: 10.1103/PhysRevLett.83.4713 (return page 18).

[Rot09] B Roth and S Schiller. “Sympathetically Cooled Molecular Ions: From Principlesto First Applications”. In: *Cold molecules : theory, experiment, applications*. Ed. by V Krems, C Stwalley, and B Friedrich. CRC Press, 2009. Chap. 18, pp. 651–703. DOI: https://doi.org/10.1201/9781420059045 (return page 18).

[Rot05] B. Roth et al. “Production of large molecular ion crystals via sympathetic cooling by laser-cooled Ba^+”. *Journal of Physics B: Atomic, Molecular and Optical Physics* 38.20 Sept. 2005, pp. 3673–3685. DOI: 10.1088/0953-4075/38/20/004 (return page 18).

[Ryj05] Vladimir L. Ryjkov, XianZhen Zhao, and Hans A. Schuessler. “Simulations of the rf heating rates in a linear quadrupole ion trap”. *Phys. Rev. A* 71 3 Mar. 2005, p. 033414. DOI: 10.1103/PhysRevA.71.033414 (return pages xxii, 4, 17, 32, 54, 180).

[Sch02a] J. P. Schiffer. “Melting of Crystalline Confined Plasmas”. *Phys. Rev. Lett.* 88 20 May 2002, p. 205003. DOI: 10.1103/PhysRevLett.88.205003 (return pages 57, 58, 196, 213).

[Sch02b] J. P. Schiffer. “Specific heat and latent heat in finite and infinite one-component plasmas”. In: *Non-Neutral Plasma Physics IV: Workshop on Non-Neutral Plasmas, held 30 July - 2 August, 2001 in San Diego, CA*. Ed. by C. Fred Driscoll François Anderegg and Lutz Schweikhard. Vol. AIP Conference Proceedings, Vol. 606, 2002., p.127-134. 2002. DOI: 10.1063/1.1454276 (return page 58).

[Sch00] J. P. Schiffer et al. “Temperature, ordering, and equilibrium with time-dependent confining forces”. *Proceedings of the National Academy of Sciences* 97.20 2000, pp. 10697–10700. DOI: 10.1073/pnas.190320397 (return pages 17, 51).

[Sch88] John P. Schiffer. “Layered structure in condensed, cold, one-component plasmas confined in external fields”. *Phys. Rev. Lett.* 61 16 Oct. 1988, pp. 1843–1846. DOI: 10.1103/PhysRevLett.61.1843 (return page 137).

[Sch15] L. Schmöger et al. “Coulomb crystallization of highly charged ions”. *Science* 347.6227 2015, pp. 1233–1236. DOI: 10.1126/science.aaa2960 (return page 16).

[Sch98] Jocelyn C Schultz, Christopher A Hack, and W.Henry Benner. “Mass Determination of Megadalton-DNA Electrospray Ions Using Charge Detection Mass Spectrometry”. *Journal of the American Society for Mass Spectrometry* 9.4 1998, pp. 305–313. DOI: https://doi.org/10.1016/S1044-0305(97)00290-0 (return page 10).

[Sei06] S. Seidelin et al. “Microfabricated Surface-Electrode Ion Trap for Scalable Quantum Information Processing”. *Phys. Rev. Lett.* 96 25 June 2006, p. 253003. DOI: 10.1103/PhysRevLett.96.253003 (return page 16).

[Sil16] Nicolas Sillitoe et al. “$\bar{H}^+$ Sympathetic Cooling Simulations with a Variable Time Step”. In: *Proceedings of the 12th International Conference on Low Energy Antiproton Physics (LEAP2016)*. 2016. DOI: 10.7566/JPSCP.18.011014 (return pages 145, 146).

[Ske02] Robert D. Skeel and Jesüs A. Izaguirre. “An impulse integrator for Langevin dynamics”. *Molecular Physics* 100.24 2002, pp. 3885–3891. DOI: 10.1080/00268970210000018321 (return page 144).

[Sko17] Michael Skoblin et al. “Gas Flow in the Capillary of the Atmosphere-to-Vacuum Interface of Mass Spectrometers”. *Journal of the American Society for Mass Spectrometry* 28.10 2017. PMID: 28721673, pp. 2132–2142. DOI: 10.1007/s13361-017-1743-7 (return pages 95–97).

[Sko13] D.A. Skoog et al. *Fundamentals of Analytical Chemistry*. Cengage Learning, 2013 (return page 8).

[Sta22] H. Staudinger and J. Fritschi. "Über Isopren und Kautschuk. 5. Mitteilung. Über die Hydrierung des Kautschuks und über seine Konstitution". *Helvetica Chimica Acta* 5.5 1922, pp. 785–806. DOI: https://doi.org/10.1002/hlca.19220050517 (return page 5).

[Sud03] Michael Sudakov and D. J. Douglas. "Linear quadrupoles with added octopole fields". *Rapid Communications in Mass Spectrometry* 17.20 2003, pp. 2290–2294. DOI: https://doi.org/10.1002/rcm.1187 (return pages 16, 23).

[Szy12] B. Szymanski et al. "Large two dimensional Coulomb crystals in a radio frequency surface ion trap". *Applied Physics Letters* 100.17 2012, p. 171110. DOI: 10.1063/1.4705153 (return page 17).

[Tab12] D. A. Tabor et al. "Suitability of linear quadrupole ion traps for large Coulomb crystals". *Applied Physics B* 107.4 May 2012, pp. 1097–1104. DOI: 10.1007/s00340-012-5058-x (return page 38).

[Tan14] Utako Tanaka et al. "Design of a surface electrode trap for parallel ion strings". *Journal of Physics B: Atomic, Molecular and Optical Physics* 47.3 Jan. 2014, p. 035301. DOI: 10.1088/0953-4075/47/3/035301 (return page 17).

[Tit00] Mark A. Tito et al. "Electrospray Time-of-Flight Mass Spectrometry of the Intact MS2 Virus Capsid". *Journal of the American Chemical Society* 122.14 2000, pp. 3550–3551. DOI: 10.1021/ja993740k (return pages xxiii, 7, 8, 11).

[Twe06] Damian Twerenbold. "Cryogenic Detectors: Detection of Single Molecules". In: *eLS*. American Cancer Society, 2006. DOI: https://doi.org/10.1002/9780470015902.a0006203 (return pages 10, 119).

[Vaz95] Gonzalo Vazquez, Estrella Alvarez, and Jose M. Navaza. "Surface Tension of Alcohol Water + Water from 20 to 50 .degree.C". *Journal of Chemical & Engineering Data* 40.3 1995, pp. 611–614. DOI: 10.1021/je00019a016 (return pages 91, 92).

[Ved91] Fernande Vedel. "On the dynamics and energy of ion clouds stored in an R.F. quadrupole trap". *International Journal of Mass Spectrometry and Ion Processes* 106 1991, pp. 33–61. DOI: https://doi.org/10.1016/0168-1176(91)85011-A (return page 40).

[Ved90] Fernande Vedel, Michel Vedel, and Raymond Evans March. "New Schemes for resonant ejection in r.f. quadrupolar ion traps". *International Journal of Mass Spectrometry and Ion Processes* 99.1 1990, pp. 125–138. DOI: https://doi.org/10.1016/0168-1176(90)85025-W (return pages 19, 37, 38).

[Vio16] Arthur Viodé et al. "Coupling of size-exclusion chromatography with electrospray ionization charge-detection mass spectrometry for the characterization of synthetic polymers of ultra-high molar mass". *Rapid Communications in Mass Spectrometry* 30.1 2016, pp. 132–136. DOI: https://doi.org/10.1002/rcm.7426 (return page 11).

[Wan14] Yong Wan et al. "Precision spectroscopy by photon-recoil signal amplification". *Nat. Commun.* 5 3096 2014 (return page 36).

[Wil12] Stefan Willitsch. "Coulomb-crystallised molecular ions in traps: methods, applications, prospects". *International Reviews in Physical Chemistry* 31.2 2012, pp. 175–199. DOI: 10.1080/0144235X.2012.667221 (return pages xxi, 4, 180).

[Wil08] Stefan Willitsch et al. “Cold Reactive Collisions between Laser-Cooled Ions and Velocity-Selected Neutral Molecules”. *Phys. Rev. Lett.* 100 4 Jan. 2008, p. 043203. DOI: 10.1103/PhysRevLett.100.043203 (return pages xxi, xxx, 4, 18, 178).

[Win78] D. J. Wineland, R. E. Drullinger, and F. L. Walls. “Radiation-Pressure Cooling of Bound Resonant Absorbers”. *Phys. Rev. Lett.* 40 25 June 1978, pp. 1639–1642. DOI: 10.1103/PhysRevLett.40.1639 (return pages 18, 59).

[Win87] D. J. Wineland et al. “Atomic-Ion Coulomb Clusters in an Ion Trap”. *Phys. Rev. Lett.* 59 26 Dec. 1987, pp. 2935–2938. DOI: 10.1103/PhysRevLett.59.2935 (return page 137).

[Win75] D.J. Wineland and H. Dehmelt. “Proposed $10^{14}\Delta\nu/\nu$ laser fluorescence spectroscopy on Tl^+ mono-ion oscillator.” *Bull. of the Am. Phys. Soc.* 20 1975 (return page 18).

[Win07] S. Winiwarter et al. “5.22 - Use of Molecular Descriptors for Absorption, Distribution, Metabolism, and Excretion Predictions”. In: *Comprehensive Medicinal Chemistry II*. Ed. by John B. Taylor and David J. Triggle. Oxford: Elsevier, 2007, pp. 531–554. DOI: https://doi.org/10.1016/B0-08-045044-X/00140-1 (return pages 5, 7).

[Wiß16] Walter Wißdorf et al. “Gas Flow Dynamics in Inlet Capillaries: Evidence for non Laminar Conditions”. *Journal of the American Society for Mass Spectrometry* 27.9 2016. PMID: 27245455, pp. 1550–1563. DOI: 10.1007/s13361-016-1415-z (return pages xxvi, 92–97).

[Wol87] Hermann Wollnik. “2 - General Relations for the Motion of Charged Particles in Electromagnetic Fields”. In: *Optics of Charged Particles*. Ed. by Hermann Wollnik. Academic Press, 1987, pp. 27–47. DOI: https://doi.org/10.1016/B978-0-12-762130-2.50005-4 (return page 108).

[Wue59] R. F. Wuerker, H. Shelton, and R. V. Langmuir. “Electrodynamic Containment of Charged Particles”. *Journal of Applied Physics* 30.3 1959, pp. 342–349. DOI: 10.1063/1.1735165 (return page 18).

[Wut92] Max Wutz, Hermann Adam, and Wilhelm Walcher. *Theorie und Praxis der Vakuumtechnik*. Ed. by Springer Verlag. 1992. DOI: 10.1007/978-3-322-87814-4 (return pages 93, 95).

[Zel74] Y. B. Zeldovich. “Cooling with the aid of high-frequency energy”. *JETP Lett.* 19 1974, pp. 74–75 (return page 18).

[Zwi99] Günter Zwicknagel, Christian Toepffer, and Paul-Gerhard Reinhard. “Stopping of heavy ions in plasmas at strong coupling”. *Physics Reports* 309.3 1999, pp. 117–208. DOI: https://doi.org/10.1016/S0370-1573(98)00056-8 (return pages 164, 179).

Index

S

T

V

Copyright Permissions

- Figure In.2 reproduced with permission from:
  Richard Wheeler, licensed under CC BY-SA 3.0, https://en.wikipedia.org/wiki/File:1GZX_Haemoglobin.png.
- Figure I.1 reproduced with permission from:
  US Patent US2939952A (Expired), https://patents.google.com/patent/US2939952A/en.
- Figure I.2 reproduced and adapted with permission from:
  Arian Kriesch Akriesch, licensed under CC BY 2.5. https://commons.wikimedia.org/wiki/File:Paul-Trap.svg, https://commons.wikimedia.org/wiki/File:Penning_Trap.svg.
- Figure 1.1 reproduced with permission from:
  J.E. Campana. “Elementary theory of the quadrupole mass filter”. *International Journal of Mass Spectrometry and Ion Physics* 33.2 1980, pp. 101–117. DOI: https://doi.org/10.1016/0020-7381(80)80042-8.
- Figure 1.4a reproduced and adapted with permission from:
  F.W.J. Olver et al. *NIST Digital Library of Mathematical Functions*. 2021.
- Figure 3.1 reproduced with permission from:
  Y. S. Nam, E. B. Jones, and R. Blümel. “Analytical mean-field scaling theory of radio-frequency heating in a Paul trap”. *Phys. Rev. A* 90 1 July 2014, p. 013402. DOI: 10.1103/PhysRevA.90.013402.
- Figure 3.4 and D.1 reproduced and adapted with permission from:
  J. P. Schiffer. “Melting of Crystalline Confined Plasmas”. *Phys. Rev. Lett.* 88 20 May 2002, p. 205003. DOI: 10.1103/PhysRevLett.88.205003.
- Figure 4.7 produced with permission from:
  Alexander Franzen, licensed under CC BY-NC 3.0, http://www.gwoptics.org/ComponentLibrary/.
- Figure 4.7 produced with permission from:
  Natalia Gimelshein et al. “Numerical Modeling of Ion Transport in an ESI-MS System”. *Journal of the American Society for Mass Spectrometry* 25 2014, pp. 820–831. DOI: 10.1007/s13361-014-0838-7, arxiv version https://arxiv.org/abs/1311.5172.
- Figure 4.8 reproduced with permission from:
  T.W. Hänsch and B. Couillaud. “Laser frequency stabilization by polarization spectroscopy of a reflecting reference cavity”. *Optics communications* 1980. DOI: https://doi.org/10.1016/0030-4018(80)90069-3.

- Figure 5.1 and its caption reproduced with permission from:
  Andreas Dahlin, licensed under CC BY 2.0. https://en.wikipedia.org/wiki/File:ESI_positive_mode_(21589986840).jpg.

Résumé

Une nouvelle application pour un ensemble d'ions piégés refroidis par laser est proposée pour la détection non-destructive de molécules géantes. Dans cette application, un ion moléculaire est injecté dans un ensemble d'ions Ca^+. Le signal de détection est attendu dans la fluorescence de l'ensemble d'ions susceptible de varier après la perturbation induite par la molécule. Dans ce manuscrit, les éléments nécessaires à la conception, la réalisation et le maniement d'un prototype sont présentés, ainsi que les résultats expérimentaux et numériques permettant de valider le concept et d'étudier les conditions de fonctionnement. La thèse est organisée en trois parties. La première partie présente les aspects fondamentaux du piégeage des ions et de leur refroidissement par laser, en mettant l'accent sur le cas non-adiabatique et le comportement de plusieurs ions. Les principes et résultats expérimentaux sont également exposés. La deuxième partie traite des aspects fondamentaux et expérimentaux de la source moléculaire d'ionisation par électrospray ainsi que des éléments de guidage des particules chargées qui lui sont rattachés. Cette partie est l'occasion de faire le point sur les avancées récentes dans des systèmes similaires. La troisième partie présente les simulations de dynamique moléculaire réalisées afin de reproduire numériquement l'interaction ainsi que d'étudier le comportement des ions piégés. Grâce aux simulations, nous mettons en évidence les rôles clés de l'interaction coulombienne combinée au chauffage radiofréquence dans le mécanisme de déstabilisation du nuage conduisant à la détection. Les conditions favorisant la détection sont étudiées, ainsi que certains aspects du piégeage des ions comme le chauffage par radiofréquence.

Mots clés : détection non-destructive ; molécules géantes ; refroidissement laser ; ions confinés ; chauffage radio-fréquence ; dynamique moléculaire.

Abstract

A new application for a laser-cooled trapped ion ensemble is proposed for the non-destructive detection of giant molecules. In this application a molecular ion is injected into a Ca^+ ion ensemble. The detection signal is expected in the fluorescence of the ion set which may vary after the perturbation induced by the molecule. In this manuscript, the necessary elements for the design and handling of a prototype are presented, as well as experimental and numerical results to validate the concept and to study the operating conditions. The thesis is organised in three parts. The first part presents the fundamental aspects of ion trapping and laser cooling, with an emphasis on the non-adiabatic case the behaviour of more than one ions. Experimental principles and results are also exhibited. The second part deals with the fundamental and experimental aspects of the electrospray ionisation molecular source and its attached guiding elements for charged particle. This part is the opportunity to sum up the recent advances in similar systems. The third part presents the molecular dynamics simulations conducted in order to numerically reproduce the interaction as well as to study the behaviour of the trapped ions. With the simulations, we highlight the key roles of the Coulomb interaction combined with radio-frequency heating in the cloud destabilisation mechanism leading to detection. The conditions favouring detection are studied, as well as certain aspects of ion trapping such as radio-frequency heating.

Keywords: non-destructive detection ; giant molecules ; laser cooling ; trapped ions ; radio-frequency heating ; molecular dynamics.